School of Civil and Mechanical Engineering

Ultrasonic Monitoring of Corrosion in Reinforced Concrete with Top-Bar Defects

Yikuan Wang

0000-0002-9342-9214

This thesis is presented for the Degree of

Doctor of Philosophy

of

Curtin University

October 2021

Copyright notice

Declaration

To the best of my knowledge and belief this thesis contains no material previously published by any other person except where due acknowledgment has been made.

This thesis contains no material which has been accepted for the award of any other degree or diploma in any university.

Signature: ………………………………………….

Date: 01/10/2021 ………………………..

Abstract

Corrosion is the predominant cause of deterioration of reinforced concrete structures, especially to those in marine environment. Latest studies have revealed that the quality of the steel-concrete interface significantly affects the concrete corrosion process. Interfacial defects in reinforced concrete lead to earlier corrosion initiation and a higher corrosion rate of steel reinforcement. Interfacial voids are generated underneath the horizontal reinforcement with more than 305 mm concrete cast below in deep beam structures, e.g., wall, due to the top-bar effect. Reinforced concrete with top-bar defects always shows a lower chloride threshold, higher corrosion rate, more aggressive corrosion activity, and a different corrosion pattern of steel rebar, making the condition assessment, structural health monitoring, and service life prediction of the structures a challenging task. Obtaining knowledge of the corrosion process would be of particular importance for integrity assessment and lifecycle management of reinforced concrete structures with top-bar defects. Conventional techniques such as visual inspection and half-cell potential have been extensively employed in the industry for condition assessment of reinforced concrete structures. These methods are labour intensive, time-consuming, lack of accuracy, and unable to quantify the corrosion process. Several ultrasonic wave-based structure health monitoring techniques have been developed for corrosion monitoring in the past decades. However, all these studies are conducted based on the assumption that the reinforced concrete has a good bond. Using the developed ultrasonic wave-based algorithm to monitor the corrosion process of reinforced concrete with top-bar defects may lead to a false interpretation of the results, resulting in a false estimation of the severity of concrete corrosion.

In this study, a new ultrasonic guided wave-based algorithm is developed to (i) monitor concrete setting, (ii) detect top-bar defects, and (iii) monitor the corrosion process of reinforced concrete with top-bar defects using PZT wafers that are mounted on the ends of the reinforcement. Reinforced concrete wall structures are cast vertically, aiming to create interfacial defects owning to the top-bar effect. The specimens are sawed to inspect the cross-section, and interfacial voids are visually observed underneath the reinforcements at an elevation of 300 mm and above. The ultrasonic results

show that the amplitude of the signal increases with the elevation of the bars. Nonlinear feature o the signal shows good detectability of top-bar effects. An increasing difference between high-frequency component and low-frequency component is observed between bottom bar and top bars, which can be utilized for a reference-free detection of top-bar effects in hardened reinforced concrete. The algorithm is extended to monitor the corrosion process of reinforced concrete. A clear difference in the pattern of the ultrasonic signals is detected in reinforced concrete with and without top-bar defects that are subjected to corrosion. This observation reveals the influence of the top-bar effect on the corrosion process and ultrasonic waves propagating in the waveguide. The destructive tests conducted at the end of the experiments reveal that top-bar specimens have a significant loss of mass, strength, and strain than the bars with a good bond.

A hybrid technique, which consists of electrochemical techniques, ultrasonic guided wave-based technique, and Synthetic Aperture Focusing Technique (SAFT)-based ultrasonic imaging technique, is proposed to provide comprehensive information about the corrosion process of reinforced concrete with and without top-bar defects. Electrochemical techniques such as half-cell potential and linear polarization resistance are employed to measure the probability of corrosion and the corrosion rate of the reinforced concrete. Contact transducers are used to excite and receive the guided waves. Surface-seeking mode and core-seeking mode are carefully selected to evaluate the deterioration of bond and bar, respectively. The pattern of the guided waves in reinforced concrete with top-bar defects shows a clear difference from that in reinforced concrete with a good bond. The images of the cross-section of the reinforced concrete reconstructed by SAFT clearly identify the initiation and the propagation of the cracks before any corrosion signs appear on the surface of the concrete. The combined results successfully differentiate the reinforced concrete with and without top-bar defects and provide comprehensive information on the corrosion process of the reinforced concrete.

To Beloved Zhujing

Acknowledgement

This project is supported by the Australian Research Council through Discovery Project grant DP160104731. I would like to thank Australia government, Australian Research Council and Curtin University for their support of my research.

I am sincerely grateful to my supervisor, Prof. Abhijit Mukherjee, for his invaluable guidance, mentoring and support of my PhD candidature at Curtin University.

I wish to express my sincere gratitude to my co-supervisor, Dr Dhami Navdeep, for her experiences and guidance that have helped me expand my thought.

I also wish to express my sincere gratitude to the principal investigator of this project, Prof. Arnaud Castel, for his guidance and experiences of the Top-bar effect, which is the focus of this project.

I wish to thank all lab staff for their assistance in conducting experiments at the Civil Engineering Lab, Curtin University.

I wish to thank all staff members in School of Civil and Mechanical Engineering, Cutin University. Special thanks to Ms. Cheryl Cheng, for her exceptional assistance in ordering all necessary material for my study and arranging milestone presentations for me.

I would also like to express my gratitude to all my colleagues, Navdeep, Subhra, Jay, Elaheh, Nimrat, Sakshi, Asha, Sakshi, Hector, Aprana, Raja, Abijit, and Anaut. Special Thank to my Lab buddy Nimrat. Thank you for the wonderful time we spend together.

Last but not least, I would like to express my Heartfelt gratitude to my parents, Yumei Li and Yujun Wang, my girlfriend, Dr. Zhujing Zhang, for their encouragement, support and unconditional love.

This work is dedicated to my parents and my girlfriend.

Yikuan Wang

October 2021

Attributes

This thesis contains one chapter that in publication form. The co-authors of this chapter are hereby acknowledged for their contribution. The signed attribution statements have been included as follows:

Attribution statement for Chapter 5: Detection of Top-Bar Effect in Reinforced Concrete Using Guided Ultrasonic Waves

STATEMENT OF AUTHORSHIP

Title	Detection of Top-Bar Effect in Reinforced Concrete Using Guided Ultrasonic Waves
Status	✓ Published ☐ Accepted by the Journal ☐ Submitted in a Journal ☐ Unsubmitted work in manuscript style
Publication details	Wang, Y., A. Mukherjee and A. Castel (2021). "*Detection of Top-Bar Effect in Reinforced Concrete Using Guided Ultrasonic Waves*." Journal of Structural Engineering **147**(4): 04021032.

Principal Author

Name of principle author				
Yikuan Wang				
Contribution				
Concept and design	Data acquisition and Methods	Data Manipulation	Interpretation and Discussion	Write-up
X	X	X	X	X
Certification				
This published paper presents original research I conducted during my HDR candidature and is not subjected to any obligations or contractual agreement with a third party that would constrain its inclusion in this thesis. I am the primary author of this paper.				

Signature
I acknowledge the contribution stated above are accurate to the best of my knowledge

Co-authorship agreement

By signing the statement of authorship agreement, each author agrees that their contribution stated by the principal author is accurate and they grant permission to the candidate to include this work in his/ her thesis.

Name of co-author 1 and the corresponding author				
Professor Abhijit Mukherjee (Principal supervisor)				
Contribution				
`Concept and design	Data acquisition and Methods	Data Manipulation	Interpretation and Discussion	Write-up
X		X	X	X
Signature *I acknowledge the contribution stated above are accurate to the best of my knowledge*				

Name of co-author 2				
Professor Arnaud Castel				
Contribution				
Concept and design	Data acquisition and Methods	Data Manipulation	Interpretation and Discussion	Write-up
			X	X

Signature *I acknowledge the contribution stated above are accurate to the best of my knowledge*

Table of Contents

List of Tables

List of Tables

Abbreviations

ToF	Time of Flight
PZT	Lead zirconate titanate, Piezo material
NDT	Nondestructive testing
SHM	Structural health monitoring
STFT	Short-Time Fourier Transform
FFT	Fast Fourier Transform
TI	Transmission index
DI	Damage index
S-C	Steel-concrete
DC	Direct Current
LPR	Linear polarization resistance
HCP	Half-cell potential
ACI	American concrete institute
AS	Australian standard

Chapter 1

1. Introduction

1.1. Motivation

The degradation of civil infrastructures, such as buildings, bridges, and historical monuments, has increased public and government concerns worldwide due to the social and economic cost by the aging or failure of these structures. In Australia, 47 billion AUD worth of civil infrastructure assets managed by 230 of the 562 local councils are in poor condition and require refurbishment and upgrade (Australian Local Government Association 2015). It is reported that in New South Wales alone, more than 6.3 billion AUD are required to restore the functionality of infrastructure assets to an acceptable condition, and an additional 14.6 billion AUD would be required to replace the infrastructures that are in poor conditions due to improper maintenance (Dollery, Byrnes et al. 2007). Therefore, long-term strategic planning is required for ongoing maintenance and renewal of the existing and further civil infrastructures to maintain their functionality, integrity, and durability during service life. Among all the causes that lead to the degradation of civil infrastructures, corrosion of the reinforcement is the principle cause of the deterioration of reinforced concrete infrastructures. Corrosion due to chloride contamination is especially critical for Australian civil infrastructures, as all Australia's major cities but Canberra are coastal cities. Hence, most critical civil infrastructures are located in the marine environment where the salinity is high. As a result, they are particularly vulnerable to chloride-induced corrosion.

Currently, visual inspection, which visually checks any sign of defects that appeared on the surface of the structures, remains the most commonly used technique for civil infrastructure inspection. Dye penetrant inspection can be employed to better visualize the microcracks on the surface of the structures. These approaches are generally time-consuming, labor-intensive, sensitive to ambient conditions, and the application is limited to the accessibility of the inspection regions. More importantly, they can only be used to detect the defects that are on or grows to the surface of the structures. Hence they cannot be used to detect the incipient defects. Electrochemical techniques, such as half-cell potential and linear polarization resistance, have been extensively employed to evaluate corrosion of reinforced concrete in the field. These methods enable instant detection of the corrosion rate and the probability of the corrosion of the structures. However, the accuracy of these methods is influenced by the condition of the structures, such as the thickness of the concrete cover, moisture content and chloride content n the concrete cover, and the condition of the environment, e.g., temperature and humidity. Most importantly, they cannot be used to quantify the corrosion process. In the recent 20 years, ultrasonic wave-based methods have been intensively employed by researchers to detect and monitor defects in metallic, composite, and reinforced concrete structures. Numerous ultrasonic wave-based algorithms have been proposed, making it possible to detect incipient defects in the structures and monitor the development of the defects. Ultrasonic guided wave-based techniques have been extensively employed to monitor the corrosion of reinforced concrete (Sharma and Mukherjee 2010, Sharma, Sharma et al. 2018a, Dixit and Gupta 2021). In general, the deterioration of the steel bar leads to a reduction in the signal strength due to the increased attenuation and reflections, while the deterioration of the bond results in an increment in the signal strength as the debond deters the energy leakage from the bar to the surrounding concrete. The deterioration of the steel bar and the steel-concrete bond can be evaluated by analyzing the changes in the guided waves and mapping the pattern of guided waves onto the well-defined corrosion process of reinforced concrete. All these experiments are conducted assuming that the steel bars are fully bonded with the surrounding concrete and only pores generated during casting exist between the bars and the concrete. Corrosion of reinforced concrete initiates at the location where the steel bar is contacted with soluble chloride ions in the pores. Rusts first fill up the pores, build up compressional stress on the surrounding concrete, and eventually initiates cracks once the compressional stress exceeds the bearing capacity of the concrete.

However, apart from the pores that cumulated around the embedded bar, numerous studies have reported the presence of interfacial voids underneath the horizontal reinforcement (Arthur 1946, Jeanty, Mitchell et al. 1988, Mohammed, Otsuki et al. 1999, Wang, Mukherjee et al. 2021). During the setting of reinforced concrete, coarse aggregates settle due to gravity, pushing air bubbles and water moving upwards. Part of the water and air strapped underneath the horizontal rebars. Interfacial voids are formed underneath the reinforcements once the concrete is hardened. This phenomenon is known as the top-bar effect. According to American Concrete Institute (ACI) building code 440.1R-06, "Top-bar" is defined as the horizontal reinforcements with more than 12 in (305 mm) of concrete below at the time of embedment (ACI-Committee-440 2006). The top-bar defect leads to loss of bond at the bottom side of the steel-concrete interface. A safety factor of 1.3 is recommended to compensate the bond loss for horizontal reinforcements with top-bar defects in normal vibrated concrete. However, recent experimental studies have reported the observation of top-bar defects at a much lower elevation (260 mm) than the defined one in ACI 440 (Nasser, Clément et al. 2010, Zhang, Castel et al. 2011). Solely depend on the standard may lead to underestimating the severity of the top-bar effect that may endanger the integrity and functionality of the structures. Other studies have reported a less severe top-bar effect in self-compacting concrete (Chan, Chen et al. 2003, Hossain and Lachemi 2008, Trezos, Sfikas et al. 2014). Top-bar defects are observed at a much higher elevation. It may lead to an overestimation of the top-bar effect. Hence, it is important to detect the presence of top-bar defects to ensure the integrity and functionality of the structures.

The corrosion process of reinforced concrete with top-bar defects has been intensively studied in the past decades (Mohammed, Otsuki et al. 1999, Castel, Vidal et al. 2003, Zhang, Castel et al. 2011, Zhang, François et al. 2020, Cai, Zhang et al. 2020b). The results indicate that the top-bar effect has a significant effect on the corrosion process of reinforced concrete. A more severe generalized corrosion is observed at the bottom half of the bar in concrete with top-bar defects, while localized corrosion is observed in concrete with a good bond. The corrosion rate increases the elevation of the reinforcement and is proportional to the severity of top-bar defects (Soylev and François 2003, Söylev and François 2005). Top-bar defect leads to a much earlier depassivation of the protective firm around the bar and thus results in an earlier corrosion initiation (Zhang, Castel et al. 2011). Hence, an early detection of the top-bar defects and continuous monitoring of the corrosion process of reinforced concrete with top-bar defects is of particular importance for maintaining the structure and preventing structural failure.

1.2. Scope of work

Extensive studies have been conducted to evaluate the corrosion process of reinforced concrete with and without top-bar defects using various methods. Yet none of them evaluates the corrosion of reinforced concrete with top-bar defect nondestructively. The principal objective of the present study is to develop a nondestructive method to monitor the corrosion process of reinforced concrete with top-bar defects. Prior to corrosion monitoring, detection of the presence of top-bar defects in reinforced concrete is very important. Knowing the presence of top-bar defects can help better interpret the ultrasonic results in reinforced concrete. In addition, developing a nondestructive method to monitor concrete setting is also important, which is very helpful for in-field application.

To fulfills above objectives and the research gaps identified in the section 2.6, the present project has been extended to the following key tasks:

1. To create reinforced concrete with natural top-bar defects.
2. To develop an algorithm for detecting the top-bar defects and monitoring concrete corrosion.
3. To investigate the feasibility of exciting guided waves using the PZT wafers mounted to the ends of the rebars and use it to evaluate various types of steel reinforcement.
4. To detect top-bar defects in reinforced concrete using guided waves excited by surface-mounted PZT wafers.
5. To monitor the hydration process of cement paste and reinforced concrete using guided waves excited by surface-mounted PZT wafers.
6. To monitor the corrosion process of reinforced concrete using guided waves excited by surface-mounted PZT wafers.
7. To compare the signals and the pattern of signals in reinforced concrete with and without top-bar defects subjected to accelerated corrosion.

8. To develop a combined technique, consisting of electrochemical techniques, ultrasonic guided wave-based technique, and ultrasonic imaging technique, to provide more comprehensive information about the condition of reinforced concrete under chloride attack.

1.3. Thesis outline

The thesis consists eight chapters. The scheme of each chapter is provided below:

Chapter 1: introduces the motivation of this study, the objectives, and the contents of each chapter.

Chapter 2: presents a brief literature review of the topics that are closely related to this study. The literature review focuses on four topics, corrosion of reinforced concrete, top-bar effect in reinforced concrete, conventional methods for concrete corrosion assessment, and ultrasonic methods for concrete corrosion detection and monitoring. The corrosion process of reinforced concrete is introduced, followed by the mechanism of steel bar corrosion in reinforced concrete. The formation of top-bar defects is explained in detail, and the effects of top-bar defects on the properties of reinforced concrete are discussed. A brief literature review of experimental studies on investigating the corrosion process of reinforced concrete with top-bar defects is presented. The principle of conventional methods for concrete corrosion assessment is discussed, and the applications of these methods for concrete corrosion assessment are presented. The principle of guided wave propagation in cylindrical bodies is discussed, followed by a review of the key wave parameters for damage detection. The applications of using guided waves to evaluate bar deterioration, detect the debonding of the S-C interface, and monitor concrete corrosion is presented. Synthetic Aperture Focusing Technique (SAFT)-based ultrasonic imaging technique for crack detection is also discussed. This chapter concludes with the research gap.

Chapter 3: presents the proposed methods for guided wave-based structural health monitoring method for detecting top-bar defects and monitoring concrete corrosion. The specimens are designed to create top-bar defects. The configuration of the specimens and the concrete mix design are presented. The set-up of the accelerated corrosion is presented, and the electrochemical assessment and ultrasonic monitoring systems are discussed. The selection of excitation waves for PZT-based and contact transducer-based systems is discussed, followed by the proposed damage index for detection of top-bar defects and the transmission index for monitoring concrete corrosion.

Chapter 4: assesses the effectiveness of using guided waves for monitoring cement hydration and concrete setting. Guided waves are sent through both plain bars and deformed bars to validate the robustness of the proposed method for concrete setting monitoring in different types of waveguides. A prototype of a cast-in compact PZT wafer-based transducer is proposed. The transducer is first employed to monitor the setting of cement paste, along with temperature measurements and penetration tests for comparison purposes. Then the transducer is used to monitor the setting of concrete. The results are presented and discussed.

Chapter 5: presents an experimental study of using guided shear waves for the detection of top-bar defects. A reinforced concrete wall structure is cast vertically, aiming to create natural top-bar defects. PZT wafers are permanently bonded to the ends of the bars using superglue. The creation of top-bar defects is evaluated, and the curing process is monitored. Both linear and nonlinear damage features of the received signals are extracted, and the results are discussed.

Chapter 6: extends the proposed method used in Chapter 5 to monitor the corrosion of reinforced concrete with and without top-bar defects. The specimens are subjected to anodic current to accelerate the corrosion process. Two sets of specimens, each consisting of one reinforced concrete with top-bar defects and one controlled specimen with good bond, are corroded to two milestones, termed as surface stain and surface cracking, which are the two critical signs of concrete corrosion in visual inspection. Guided waves through the steel bars are recorded every 20 hours. The proposed transmission index is employed to evaluate the residual signal strength. The pattern of the TI is analyzed and mapped onto the theoretical corrosion process of the reinforced concrete for interpretation. The results in reinforced concrete with and without top-bar defects are compared. A clear difference in the pattern of the TI is observed.

Chapter 7: a hybrid technique, consisting of electrochemical methods, ultrasonic guided waves, and ultrasonic imaging, is proposed to evaluate the life cycle of reinforced concrete. Contact transducers are employed to excite and capture the guided waves in the steel bar. Two wave modes, termed surface-seeking mode and core-seeking mode, are carefully selected based on their mode shape and being employed to evaluate the changes in the S-C interface and the bar, respectively. The guided waves are first employed to monitoring the setting of the reinforced concrete. Then they are used to monitoring the corrosion of a 24 mm diameter steel round bar to invesitgate the effects of bar deterioration on the two modes. Finally, the guided waves are employed to monitor the corrosion of the embedded bars. Electrochemical techniques, such as HCP and LPR, are employed to detect the probability of corrosion and corrosion rate. The SAFT-based ultrasonic imaging technique is used to visualize the cross-section of the specimen, aiming to detect the initiation of cracks, quantify the size of the cracks and monitor the propagation of the cracks. The results are first presented and discussed separately to compare the pros and cons. Then the useful information extracted using different techniques is combined to provide more comprehensive inofrmation of the corrosion process of the reinforced concrete specimens. The difference of the specimen with and without top-bar defects is also identified and discussed.

Chapter 8: concludes the thesis with a summary of key findings of the work and contributions of this work to the development of ultrasonic wave-based structural health monitoring of corrosion process in reinforced concrete, especially in reinforced concrete with top-bar defects. Recommendations for future works are presented.

Reference

ACI-Committee-440 (2006). "440.1R-06: Guide for the Design and Construction of Structural Concrete Reinforced with FRP Bars." Technical Documents.

Arthur, P. C. (1946). "Comparative Bond Efficiency of Deformed Concrete reinforcing Bars." Journal of Research of the National Bureau of Standards **37**(RP 1755): 399-407.

Australian Local Government Association. (2015). "NATIONAL State of the Assets 2015: Roads and Community Infrastructure Report." from http://alga.asn.au/?ID=13900&Menu=50,577.

Cai, Y., W. Zhang, C. Yang, R. François, L. Yu, M. Chen, H. Chen and H. Yang (2020). "Evaluating the chloride permeability of steel–concrete interface based on concretes of different stability." Structural Concrete **n/a**(n/a).

Castel, A., T. Vidal, R. François and G. Arliguie (2003). "Influence of steel–concrete interface quality on reinforcement corrosion induced by chlorides." Magazine of Concrete Research **55**(2): 151-159.

Chan, Y.-W., Y.-S. Chen, Chen and Y.-S. Liu (2003). "Development of Bond Strength of Reinforcement Steel in Self-Consolidating Concrete " ACI structural journal **100**(4): 490-498.

Dixit, M. and A. K. Gupta (2021). "A Review of Different Assessment Methods of Corrosion of Steel Reinforcement in Concrete." Iranian Journal of Science and Technology, Transactions of Civil Engineering.

Dollery, B., J. Byrnes and L. Crase (2007). "The Infrastructure Crisis in Australian Local Government: A Proposed Federal Asset Fund Solution." Australasian Journal of Regional Studies **13**(1): 3-19.

Hossain, K. M. A. and M. Lachemi (2008). "Bond Behavior of Self-Consolidating Concrete with Mineral and Chemical Admixtures." Journal of Materials in Civil Engineering **20**(9): 608-616.

Jeanty, P. R., D. Mitchell and M. S. Mirza (1988). "Investigation of "Top Bar" Effects in Beams." Structural Journal **85**(3).

Mohammed, T. U., N. Otsuki and M. Hisada (1999). "Corrosion of Steel Bars with Respect to Orientation in Concrete." ACI Materials Journal **96**(2): 154-159.

Nasser, A., A. Clément, S. Laurens and A. Castel (2010). "Influence of steel–concrete interface condition on galvanic corrosion currents in carbonated concrete." Corrosion Science **52**(9): 2878-2890.

Sharma, A., S. Sharma, S. Sharma and A. Mukherjee (2018). "Monitoring invisible corrosion in concrete using a combination of wave propagation techniques." Cement and Concrete Composites **90**: 89-99.

Sharma, S. and A. Mukherjee (2010). "Longitudinal guided waves for monitoring chloride corrosion in reinforcing bars in concrete." Structural Health Monitoring **9**(6): 555-567.

Soylev, T. A. and R. François (2003). "Quality of steel–concrete interface and corrosion of reinforcing steel." Cement and Concrete Research **33**(9): 1407-1415.

Söylev, T. A. and R. François (2005). "Corrosion of Reinforcement in Relation to Presence of Defects at the Interface between Steel and Concrete." Journal of Materials in Civil Engineering **17**(4): 447-455.

Trezos, K. G., I. P. Sfikas and C. G. Pasios (2014). "Influence of water-to-binder ratio on top-bar effect and on bond variation across length in Self-Compacting Concrete specimens." Cement and Concrete Composites **48**: 127-139.

Wang, Y., A. Mukherjee and A. Castel (2021). "Detection of Top-Bar Effect in Reinforced Concrete Using Guided Ultrasonic Waves." Journal of Structural Engineering **147**(4): 04021032.

Zhang, R., A. Castel and R. François (2011). "Influence of steel-concrete interface defects owing to the top-bar effect on the chloride-induced corrosion of reinforcement." Magazine of Concrete Research **63**(10): 773-781.

Zhang, W., R. François, Y. Cai, J.-P. Charron and L. Yu (2020). "Influence of artificial cracks and interfacial defects on the corrosion behavior of steel in concrete during corrosion initiation under a chloride environment." Construction and Building Materials **253**: 119165.

Chapter 2

2. Literature Review

2.1. Introduction

This chapter presents a literature review on four topics closely related to this project: corrosion of reinforced concrete, top-bar effect in reinforced concrete, conventional assessment method for concrete corrosion, and ultrasonic methods for detection concrete defects and monitoring concrete corrosion. The state of concrete corrosion expressed as a function of service life is discussed. The widely adapted three-stage corrosion-inducing cracking model has been introduced to better understand the corrosion process of reinforced concrete. The general mechanism of steel bar corrosion in concrete and the mechanism of corrosion in a chloride environment is discussed to provide an in-depth understanding of the corrosion of steel bars. The top-bar effect in reinforced concrete is discussed. The formation of top-bar defects is explained, and the impact of top-bar defects on reinforced concrete is discussed, followed by the review of corrosion of reinforced concrete with top-bar effects. The effects of top-bar defects on the concrete corrosion process are presented. Conventional concrete corrosion methods that are being used both in the field and in the laboratory are introduced. The applications of these methods are discussed, and the limitations are presented. The main drawback of these methods lies in the requirement of accessibility to the inspection area, time-consuming, and they cannot provide quantitative estimation of the corrosion process.

In contrast, the ultrasonic wave-based technique has been reported to be sensitive to concrete corrosion and able to quantify the corrosion process. The applications of ultrasonic waves for detecting concrete corrosion are briefly discussed. Based on the literature reviews, two research gaps are identified, (1) nondestructive evaluation of top-bar effect in reinforced concrete and (2) nondestructive monitoring of corrosion in reinforced concrete with top-bar defects.

2.2. Corrosion of reinforced concrete

Reinforced concrete infrastructures are expected to maintain functionality and the integrity throughout their service life without any structural failure. However, few causes can endanger the functionality and integrity of the structure, shorten the service life, and eventually result in severe economic and social costs. The causes include but are not limited to improper design, overloading, deterioration of reinforcements, and cracking and spalling of concrete. Among these, corrosion-induced concrete defects have been the primary cause of degradation of reinforced concrete structures infrastructures (Zhao and Jin 2016). In general, the embedded rebar is protected by the concrete cover due to the alkaline environment. The dissolution of calcium hydroxide in the pore solution leads to the alkalinity (PH>12.5) of the concrete cover (Bertolini, John et al. 2013). The high alkalinity passivates the rebar and forms a protective oxide layer on the surface of the rebar. This layer is only 10-15 nm thick and mainly consists of ferrous oxides and oxyhydroxides (Elsener and Rossi 2018). Two major causes can break down the protective layer and induce corrosion in reinforced concrete, which are (i) carbonation of the concrete cover and (ii) chloride attack on the steel rebar.

Carbon dioxide in the atmosphere can penetrate the concrete by absorption into the capillary pores on the surface and then diffuses in depth through pores networks and internal cracks in concrete (Šavija and Luković 2016). The calcium hydroxide presented in the pore solution can react with the carbon dioxide, leading to the formation of carbon carbonate in the pores. This tends to neutralize the alkalinity of the concrete cover. This reaction initiates at the surface of the concrete cover and propagates gradually in depth until reaching the rebar. Carbonation brings down the PH value of the concrete cover from above 12.5 to 9. The protective layer is no longer stable. Depassivation of rebar occurs, and once the protective layer is destroyed, corrosion initiates. This is known as the carbonation of concrete (Bertolini, John et al. 2013). Carbonation occurs over the entire concrete cover. Therefore, carbonation-induced corrosion may occur over the whole surface of the reinforcement that contacts with the carbonated concrete. Hence, carbonation of concrete results in generalized corrosion, where a large area of the surface of the bar is corroded. The generated rusts induce uniform expansive stress on the surrounding concrete and lead to cracking and spalling of the concrete cover(Angst, Elsener et al. 2012).

Chloride attack on the rebar is the primary cause for corrosion of concrete structure globally. The main sources of chloride ions in concrete are (i) chloride contaminated concrete mix and (ii) penetration of chloride ions from the atmosphere, especially in the marine environment. Modern design standards of concrete structures employ restrictions on the total amount of chloride in newly constructed concrete structures, aiming to eliminate the chloride-induced corrosion due to chloride ions in the concrete mixture. The limits of soluble chloride content in various types of concrete structures recommended by ACI 318 are summarised in Table. 2-1.

Table. 2-1 Limits of water-soluble chloride ion in new construction in ACI 318(ACI-Committee-318 2019)

Type of structure	Maximum allowable chloride (% by weight of cement)
Prestressed concrete	0.06
RC exposed to chloride in service	0.15
RC protected from moisture in service	1.00
Other RC construction	0.30

The penetration of chloride from the environment is the primary source of chloride in concrete. The chloride ions can transfer to the embedded rebar through interconnected pores in the concrete cover by capillary suction, diffusion, and permeation. The chloride ions accumulate in the pores around the rebar, and the chloride content in these pores increases with the increasing transportation of chloride ions from the environment. Once the chloride content exceeds the chloride threshold value, depassivation of rebar occurs. According to American Concrete Institute (ACI 2001) and Australian Standards AS2758.1-2014 (AS/NZS 2014), a chloride threshold level (CTL) of 0.2% of concrete mass is considered to dissolve the passive form. Unlike carbonation that depassivates the whole surface of the rebar, depassivation of embedded rebar only occurs at the location in contact with pores where the chloride content exceeds its threshold value. This leads to a localized breakdown of the protective form. The depassivated area acts as the anode, and the intact area acts as the cathode. Macrocells with a high corrosion rate are formed to accelerate the corrosion process (Warkus and Raupach 2010). The growth of localized pits can significantly reduce the cross-section of the rebar even before visual signs (stain and cracks) are observed on the concrete cover. This significantly reduces the material properties of the rebar and endangers the safety of the structure although the structure looks intact.

2.2.1. States of concrete corrosion

The corrosion states in reinforced concrete can be expected as a function of service time. As proposed by Tuutti (Tuutti 1982), a time-dependent state of concrete corrosion is illustrated in Fig. 2-1. The corrosion of concrete can be divided into two distinct periods, namely the initial period, t_i and the propagation period, t_p. The former one corresponds to the period that the corrosive agents propagate from the atmosphere to the rebar and gradually depassivate and break down the protective layer on the rebar. During this period, the carbon dioxide continuously carbonates the concrete cover layer by layer and reduces the PH value. The progress of carbonation grows in depth until it reaches the rebar. While in the marine environment, the chloride ions propagated through the interconnected pores in the concrete cover. The chloride content continuously buildup in the pores around the rebar and gradually depassivate the bar and eventually destroy the protective layer. The propagation period initiates at the breakdown of the protective layer, followed by the initiation of corrosion. It is completed until the degree of damage reaches the limits per design standards. The corrosion is in an active state during this stage.

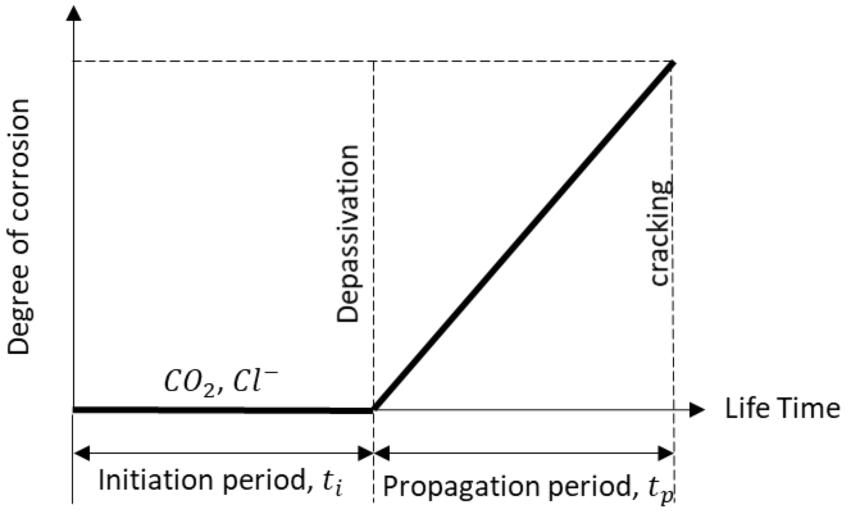

Fig. 2-1 Time-dependent states of concrete corrosion (Tuutti 1982).

Liu and Weyers (Liu and Weyers 1998) proposed a three-stage corrosion-induced cracking model, as shown in Fig. 2-3, that better defines the mechanism of corrosion-induced cracking in reinforced concrete (Caré, Nguyen et al. 2008, Wong, Zhao et al. 2010, Zhao, Ding et al. 2014). The three stages are the corrosion products filling stage, the concrete cover stressing stage, and the concrete cover cracking stage. Following the breaking down of the protective layer, corrosion initiates on the surface of the rebar. At stage 1, the generated rusts fill in the pores and microcracks in the concrete around the bar. It is assumed that no pressure is generated by the rusts. In stage 2, as more rusts are generated, the pores and the microcracks around the bar are filled with rusts. Expansive pressure is generated by the excess rust and applied to the surrounding concrete. The pressure increases with the generation of rusts. When the expansion pressure overcomes the bearing capacity of the surrounding concrete, cracks initiate at the steel-concrete interface and propagates towards the concrete surface. During the propagation of the crack in the concrete cover, rusts continuously fill in the crack gap that further extends it until the crack appears on the surface of the concrete.

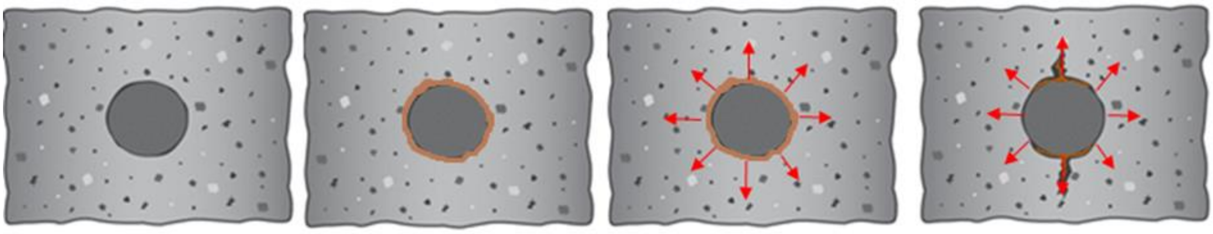

Fig. 2-2 The three-stage corrosion-inducing cracking model of reinforced concrete. (a) Intact. (b) Stage 1: Filling. (c) Stage 2: Stressing. (d) Stage 3: Cracking (CivilEngineeringForum 2017)

2.2.2. Mechanism of steel bar corrosion in concrete

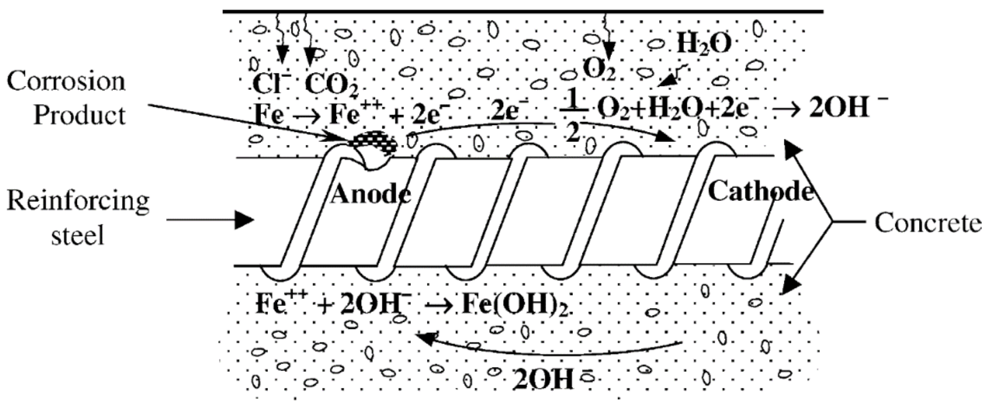

Fig. 2-3 Schematic illustrations of steel reinforcement corrosion in concrete (Ahmad 2003).

The corrosion of concrete reinforcements is an electrochemical process. The process consists of the dissolution of metal (steel/iron) at the anode of the bar and the reduction of oxidants at the cathode as illustrated in Fig. 2-3. This process can occur between different bars or in the same bar between the depassivated part (anode) and the passive part (cathode). The iron loses electrons to form ferrous ions (Fe^{2+}) at the anodic site:

Anode: $Fe \rightarrow Fe^{2+} + 2e^{2-}$ 2-1

The pore solution in the surrounding concrete of the bar acts as the electrolyte, allowing the electron and ions movement between anode and cathode. At the cathode, the dissolved oxygen receives electrons produced at the anodic site to form hydroxyl ions (OH^-). Hence the cathodic reaction depends on the availability of O_2:

Cathode: $H_2O + \frac{1}{2}O_2 + 2e^- \rightarrow 2OH^-$ 2-2

The hydroxyl ions at the cathode and the ferrous ion at the anode induces an electrode potential difference. To restore the electrical neutrality, the hydroxyl ions transfer through the electrolyte to the anode, where the hydroxyl ions are combined with ferrous ions to produce ferrous hydroxide:

$Fe^{2+} + 2OH^- \rightarrow Fe(OH)_2$ 2-3

The ferrous hydroxide can be further oxidized by the dissolved oxygen to form ferrous oxide-hydroxide and transfers to a more stable form hydrated ferric oxide (rust):

$4Fe(OH)_2 + H_2O + O_2 \rightarrow 4Fe(OH)_3$ 2-4

$4Fe(OH)_3 \rightarrow Fe_2O_3 \cdot 2H_2O$ 2-5

For chloride-induced corrosion, iron reacts with chloride ions in the pore solution with the absence of oxygen to form a soluble ferrous-chloride complex at the anode:

Anode: $Fe + 2Cl^- \rightarrow (Fe^{2+} + 2Cl^-) + 2e^{2-}$ 2-6

Ferrous-chloride complex migrates from the anode to the cathode with a higher concentration of oxygen. It reacts with the hydroxyl ions to form ferrous hydroxide.

Cathode: $(Fe^{2+} + 2Cl^-) + 2e^{2-} + 2H_2O \rightarrow Fe(OH)_2 + 2H^+ + 2Cl^-$ 2-7

Ferrous hydroxide is oxidized to form rusts on the surface of the rebar as per Eq.2-4 and Eq.2-5.

2.3. Top bar effect in reinforced concrete

2.3.1. Effects of top-bar defects on concrete

The bond between steel reinforcements and surrounding concrete is of paramount importance for reinforced concrete structures. However, there are several situations where the bond is deficient. Interfacial voids underneath the horizontal rebars have been observed in deep beams or wall structures (Jeanty, Mitchell et al. 1988, Mohammed, Otsuki et al. 1999, Chan, Chen et al. 2003, Soylev and François 2003, Castel, Vidal et al. 2006, Nasser, Clément et al. 2010, Zhang, Castel et al. 2011). During the concrete setting process, coarse aggregates settle due to gravity, pushing water, air, and fine aggregates moving upwards. A small portion of the air bubbles and water is trapped underneath horizontal reinforcements. Once the concrete is hardened, voids are formed underneath the horizontal reinforcements. (Söylev and François 2006). This phenomenon is known as the "top-bar" effect. The interfacial voids formed due to top bar effect is known as top bar defect. The top-bar effect significantly reduces bond strength in deep reinforced concrete structures, such as wall and deep beam (Mohammed, Otsuki et al. 1999). The effects of the orientation of casting and elevation of rebars on the characteristics of the bond have been reported since the 1910s (Jeanty, Mitchell et al. 1988). The change in the bond quality with the position of the reinforcement in normal vibrated concrete (NVC) structures has been investigated using pull-out tests. The results indicated that the bond efficiency of the top bars was around two-thirds of that of the bottom bars, where good bonds were expected (Arthur 1946). Based on this result, the top-bar effect was first included in the American Concrete Institute(ACI) building code in 1951 (Wan, Petrou et al. 2002). ACI building code 440 (ACI-Committee-440 2006) defines "top-bar" as horizontal reinforcements with 12 in (305 mm) and more concrete below it. A safety factor has been introduced to compensate for the bond strength loss due to the top-bar effects. The factor of safety was first defined as 1.4 in 1971. In the 1980s, an experimental investigation was conducted on full-scale reinforced concrete beams, concluding that the top-bar effect resulted in a 22% reduction of the bond strength (Jeanty, Mitchell et al. 1988). Based on these findings, the safety factor was reduced from 1.4 to 1.3 in 1989 (Wan, Petrou et al. 2002), which is still in use. Recent lab-based experiments report the observation of the top-bar effect underneath the horizontal rebars in NVC at an elevation of 260 mm (Nasser, Clément et al. 2010, Zhang, Castel et al. 2011). Hence, the ACI building code can serve as reliable guidance for defining top-bar in NYC, but it may lead to underestimating top-bar effect in lower elevation bars (<305 mm).

A number of studies have reported the observation of top-bar effect in self-compacting concrete (SCC) (Chan, Chen et al. 2003, Soylev and François 2003, Castel, Vidal et al. 2006, Esfahani, Lachemi et al. 2008, Hossain and Lachemi 2008, Valcuende and Parra 2009, Hassan, Hossain et al. 2010). These studies focus on detecting the top-bar effect by analyzing the bond strength. Benefiting from the uniform compaction throughout the depth of the concrete member, SCC significantly reduces the top-bar effect comparing to NVC. Significant wider voids are observed in SCC, although the size of the voids in SCC and NVC are equivalent (Castel, Vidal et al. 2006). The top-bar induced reduction in the bond strength in SCC was less than that in NVC (Hossain and Lachemi 2008, Valcuende and Parra 2009, Hassan, Hossain et al. 2010). A reduced safety factor,1.25, has been proposed in case of high viscosity power type SCC compared to 1.3 for NVC recommended in ACI building code. The effects of the water-cement ratio on the intensity of the top-bar effect in SCC has been explored experimentally (Trezos, Sfikas et al. 2014). The top-bar effect appears to be more intense with increasing w/c ratio in SCC. For the same w/c ratio and similar compressive strength, less intensive top-bar effect is observed in SCC than in NVC. Another study has reported that the bond strength in SCC is 20% lower than that in NVC. (Esfahani, Lachemi et al. 2008). Therefore, an additional factor of safety of 1.3 has been suggested for all top bars in SCC. Evidently, the method to offset the consequences of the top-bar effect in reinforced concrete structures has been to employ the safety factors.

2.3.2. Effects of top-bar defects on concrete corrosion

The influences of the top-bar effect on the long-term performance of reinforced concrete have been intensively investigated (Angst, Geiker et al. 2019). The severity of the chloride-induced corrosion of the top cast bars is worse than that of bottom casted bars. Mohammed et.al (Mohammed, Otsuki et al. 1999) has reported the observation of severe corrosion on the bottom half of the bar at a chloride concentration of 0.2 % of cement mass while the top half remains intact at a chloride concentration of 0.4 %, although it has passed the chloride value recommended by the latest ACI building code and Australian Standard. Significant amount of microcell and microcell corrosion occurred within the interfacial voids due to top bar effect, creating deep localised pits on the surface of the bar(Mohammed, Otsuki et al. 2002). Prepassivation of the bars before embedding using cement paste coat was found to be an effective method to delay early corrosion, especially top casted bars (Mohammed and Hamada 2006). Castel et al. (Castel, Vidal et al. 2003) evaluated the degree of corrosion in a 14-year-old and a 17-year-old concrete beam that undergoing wetting and drying cycle in an aggressive environment. The results indicate that parameters of pore solution do not solely determine the critical chloride threshold content, e.g. [Cl-]/[OH-] ratio or total chloride content, but also strongly depend on the steel-concrete interface condition. The actual chloride threshold reduces with the increasing size of the interfacial voids. This conclusion is confirmed by a recent study focusing on the exploring the relationship between chloride threshold and steel-concrete interface using back scattered electron microscopy (Kenny and Katz 2020). As the distance between the steel bar and concrete solid (thickness of pores or voids) decreases, the chloride threshold increases.

The corrosion rate increases with the elevation of the reinforcing bar (Soylev and François 2003) and is proportional to the micro-defects owning to the top-bar effect (Söylev and François 2005). Shi and Ming (Shi and Ming 2017) employed electrochemical impedance spectroscopy (EIS) and X-ray computed tomography (X-CT) to nondestructively evaluate the corrosion behavior of the top bar and bottom part of the top cast bar in a chloride environment. The top bar effect resulted in the formation of loose and porous defects underneath horizontally casted bars. Thus, more severe active corrosion was observed at the bottom surface than the top surface. The results were later confirmed by scanning electron microscopy (SEM) and energy dispersive X-ray spectrometry (EDS). It was concluded that the top bar effect caused a gradually loose of protective firm due to depletion of $Ca(OH)_2$ layer and the voids allows the accumulation of chloride ions than accelerate the corrosion process.

Higher chloride permeability was observed in specimens with top bar defects than the controlled specimens, and in specimens with top bar defects, the permeability in the bottom part of the bar was higher than that in the top (Zhang, François et al. 2020, Cai, Zhang et al. 2020a, Cai, Zhang et al. 2020b). The permeability increases with the elevation of the bar. The chloride penetration depth increased from 13.73 mm to 23.85 mm when the height of the bar increases from 50 mm to 850 mm. Although a higher concentration of chloride ions was found at the top side of the rebar, corrosion always initiated at the bottom side due to top-bar defects (Zhang, François et al. 2020).

Nasser et al. (Nasser, Clément et al. 2010) evaluated the influence of S-C interface quality on the galvanic current in macrocell corrosion of reinforced concretes. The mass loss of the reinforcements and the macrocell corrosion current density in specimens with interfacial defects were 56% and 200% more than that of the specimens without.

Zhang et.al (Zhang, Castel et al. 2009, Zhang, Castel et al. 2011) observed generalized corrosion on the bottom surface of the rebar influenced by the top-bar effect, and specimens with good bonds showed a typical localized pitting corrosion pattern. It has been observed that the top-bar effect accelerates the corrosion rate of the rebar. The polarisation resistance (R_p) of specimens with top-bar defects reduced between 9-17 weeks at chloride content of 0.5-0.8% of the cement mass, while in specimens with good bond, it fell after 29 weeks at a chloride content of 0.9%. Therefore, early detection of the top-bar defects and continuous monitoring of the corrosion process is paramount for maintaining reinforcement concrete structures and preventing structural failure.

2.4. Conventional inspection and condition assessment methods for corrosion detection and monitoring

Several conventional methods are already being employed to detect and monitor corrosion in reinforced concrete in the laboratory and in field. The term corrosion detection is defined as the detection of instant corrosion activity while corrosion monitoring is defined as continuous monitoring of progression of corrosion in reinforced concrete.

2.4.1. Visual inspection

Routine inspection of concrete structures is performed as part of the asset maintenance and management to ensure the structures' integrity, safety, and serviceability. Visual inspection is the most commonly used approach to assess the condition of the structures. The purpose of visual inspection is to provide an initial diagnosis of the condition of the assessed structures. The assumption is that the signs of defects, such as cracks, rust stains, and watermarks, appear on the reinforced concrete surfaces and can be observed visually. Inspectors conduct the inspections prepare an inspection survey based on their observation according to the recommended guidelines by national and local authorities. Examples of such guidelines are ACI 311.4R Guide for Concrete Inspection reported by American Concrete Institute and the bridge inspection procedure manual established by the Department of Transport of NSW. These guidelines discuss the necessity of concrete structure inspection and recommend plans for inspection activities and the methods of implementing the plans (ACI 2000). However, the reliability of the survey highly depends on the inspectors' judgement(Moore, Phares et al. 2001). The process of visual inspection is labor-consuming, time-consuming, and even causes injury.

Corrosion of reinforcing bar in concrete leads to rust stains and cracks on the surface of concrete structures. The visual inspection concerning the corrosion of concrete focuses on locating these signs. As discussed in the previous section, the rust stains and corrosion-induced cracks only appear on the surface of the concrete when the corrosion is at an advanced stage (Bertolini, Elsener et al. 2014). Severe corrosion may occur inside the concrete, although no signs of corrosion are visually observed on the concrete surface. This leads to the underestimation of concrete corrosion. Hence, advanced techniques are required to indicate the occurrence of corrosion in the concrete before any visual signs are observed. Corrosion in reinforced concrete is an electrochemical process. Hence electrochemical techniques are effective to assess the corrosion of the concrete by identifying the possible location and severity of the corrosion.

2.4.2. Electrochemical techniques

2.4.2.1. Half-cell potential

The hall-cell potential (HCP) technique is widely adopted to detect the possibility of the occurance of corrosion in concrete structures in the field and in the laboratory. (Verma, Bhadauria et al. 2014, James, Bazarchi et al. 2019, Rodrigues, Gaboreau et al. 2021).

Fig. 2-4 shows the schematic of the half-cell potential setup recommended by ASTM C876 (ASTM 2015). The corrosion potential of the corroding concrete is measured as the potential difference between the targeting area of the rebar and the reference electrode with a voltmeter. A metal rod is immersed in saturated copper sulfate solution, saturated calomel solution, and silver-chloride solution to form a copper-sulfate electrode (CSE), a saturated calomel electrode (SCE), and a silver-chloride electrode, respectively. The electrode is placed on the surface of the concrete cover with a wet sponge in between to provide good electrolytic contact between the concrete and the electrode. The solution used to wet the sponge has a similar PH as that in the pores to reduce junction potentials created by the difference between the pore solution and the sponge solution (Angst, Vennesland et al. 2009). The negative side of the voltmeter is connected to the reinforcing bar. Hence, it requires local drilling of the concrete cover to access the embedded bar. This requires knowing in advance the location of the bar.

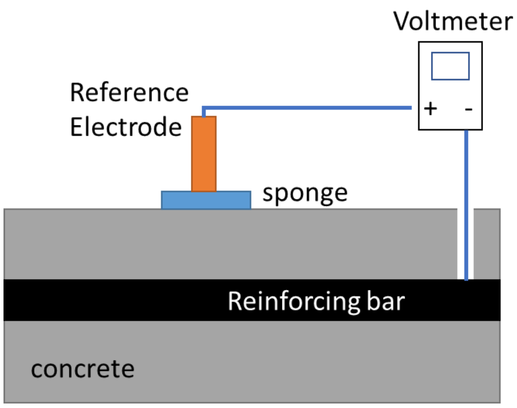

Fig. 2-4 Schematic of the half-cell potential measurement setup

For reinforced concrete structures exposed to the atmosphere, the interpretation of the measured corrosion potential is recommended by ASTM C876, as summarized in Table. 2-2. It returns the probability of corrosion activity at the location of measurement. For values larger than -200 mV/CSE, the probability of corrosion of the reinforcement is < 10%. The steel bar is believed to be in its passive state. As the corrosion initiates and proceeds, the potential becomes more negative. For values lower than -350 mV/CSE, the probability of concrete corrosion is > 90%. The values in between indicate an uncertain probability, hence unable to detect probability. The interpretation of the measured potential is based on the absolute values of the measured potential in the early version of ASTM C876. The measurement is usually performed with a single electrode at a large grid spacing (0.5m to 2m). This is known as point measurements (Elsener, Andrade et al. 2003). However, the absolute values of the potential readings are not only influenced by the corrosion state, but also facts such as depth of concrete cover, moisture content of the concrete, and PH of the pore solution. Potential gradients instead of absolute values are recommended by RILEM (Elsener, Andrade et al. 2003) as a better method to locate the areas of corrosion activity. This method requires potential reading of the entire area of the inspected surface with a multiple wheel arrangement and a smaller grid spacing. The smaller the grid spacing, the more precise the location of the corrosion. The potential readings are usually represented in colour plots or equipotential contour plots to generate a potential map. The colour squares or the contour lines indicate the measured potential and illustrate the potential shift at different locations of the scanning surface.

Table. 2-2 interpretation of measured HCP according to ASTM C876.

Potential (mV/CSE)	Probability of steel corrosion activity
>-200	Less than 10%
-200 - -350	Uncertain
<-350	More than 90%

The corrosion activity strongly influences the HCP in the concrete. However, other facts can influence it, which can lead to a false interpretation of the potential readings. The facts that influence the HCP readings are extensively investigated (Elsener, Andrade et al. 2003, Pour-Ghaz, Isgor et al. 2009, Yodsudjai and Pattarakittam 2017):

Concrete cover: The HCP varies with the depth of concrete cover. The Utah Department of Transportation Research Division has reported that the HCP became less negative as the thickness of the concrete cover decreased from 2.5 into 2.0 in (63.5 mm to 50.8 mm) or increased to 3.0 in (76.2 mm). The experiment conducted by Yodsudjai and Pattarakittam (Yodsudjai and Pattarakittam 2017) showed that the HCP with a cover of 25 mm was lower than that of 50 mm but higher than that of 100 mm. Hence, it is suggested that the concrete cover shows no definite influence on the measurement of potential. The concrete cover shows a clear effect on the potential difference between the cathode and anode of the potential circuit. As the depth of the concrete cover increases, the potential distribution becomes flatter, and the potential difference reduces.

Concrete resistivity: The corrosion rate of the reinforcement is significantly influenced by concrete resistivity (Ghods, Isgor et al. 2007). The increase of concrete resistivity shifts the potential of the cathode to more positive values and the potential of the anode to more negative values. The increase in resistivity affects the cathode more than the anode. This increases the potential difference between the cathode and anode. In concrete with low resistivity, the potential distribution on the concrete surface is similar to the potential distribution at the steel-concrete interface. The difference in the potential distribution between the surface and the interface increases with the increasing resistivity. Hence, the detection of concrete becomes more challenging as the concrete resistivity increases.

Moisture content: The moisture content of the concrete cover directly affects the concrete resistivity. The concrete resistivity becomes lower as the moisture content increases. Hence, the HCP reduces with increasing moisture content. The HCP values of wet specimens are higher than those of dry ones. This is because the current can easily flow between points in a wet condition, resulting in a lower difference of HCP. While in dry conditions, the current is difficult to flow, leading to a higher difference of HCP (Vennesland, Raupach et al. 2007).

Chloride content: The HCP decreases with the increasing chloride content in concrete. In the presence of both moisture content and chloride contamination, it is reported that the moisture content has a more substantial effect on the concrete resistivity than the chloride content (Hunkeler 1996). Thus, moisture content has more influence on the HCP of the concrete than chloride content.

Oxygen content: Oxygen concentration in concrete does not significantly affect HCP measurement unless the concrete is a complete lack of oxygen. A very low or none oxygen content in the concrete cover may lead to a very negative potential (Aanrade and Martinez. 2010).

Interpretation of HCP measurements allows the identification of the probability of corrosion activity and detection of the possible location of the corrosion. However, the HCP is not correlated directly with the rate of corrosion. Therefore, it is unable to detect the corrosion rate of rebars.

2.4.2.2. Concrete resistivity

Concrete resistivity is the ability of the concrete to resist the charge transfer. It is the ratio between the impressed voltage and the resulting current. The dimension of resistivity is multiplied by the length of the specimen (two probes configuration) or the probe spacing (four probes configuration. Thus, the unit of concrete resistivity is Ω m. The initial concrete resistivity varies between 10 and 10^6 Ω m. This is because the resistivity of the concrete is affected by several factors, such as the w/c ratio, the composition of the concrete, and the curing conditions. All these factors can result in considerable variation in the porosity of the concrete (Presuel-Moreno, Wu et al. 2013, Azarsa and Gupta 2017). High initial resistivity is generally found in dry concrete and concrete with a low w/c ratio. This is because the electrical current (ions transfer between electrodes) is transferred through the pore solutions in concrete. Dry concrete lacks pore solutions while a concrete with low w/c ratio results in concrete with low porosity, reducing the ions transfer.

The Four-point Wenner array probe technique is the most common method to measure concrete resistivity. Fig. 2-5 illustrates the principle of concrete resistivity measurement using the four-point Wenner probe technique. The Wenner probe consists of four equally spaced electrodes that are placed on the surface of the concrete. The two outer electrodes induce current flow at a frequency of 50 Hz – 1 kHz(Rodrigues, Gaboreau et al. 2021). The two inner electrodes measure the resulting potential. Conducting liquid is usually applied between the tip of the electrodes and the surface of the concrete to improve the contact for a more accurate measurement.

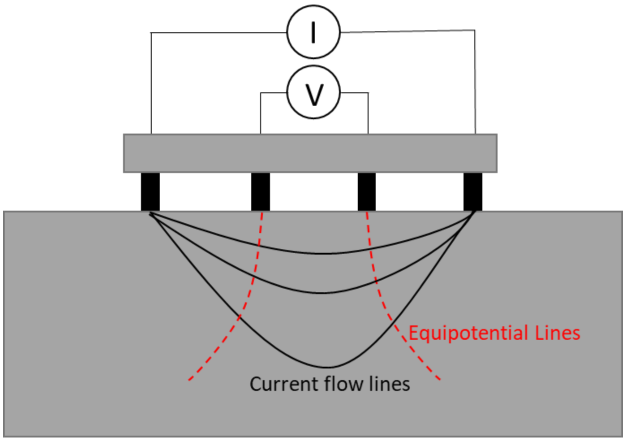

Fig. 2-5 Schematic of the Four-point Wenner array probe technique (Rodrigues, Gaboreau et al. 2021)

The concrete resistivity ρ can be determined by:

$$\rho = ka\frac{V}{I} \qquad 2\text{-}8$$

Where k is the geometry factor (2π for semi-infinite media such as concrete slab), a is the spacing between the electrodes, V is the measured potential, and I is the induced current.

The correlation between the measured concrete resistivity and the corrosion of reinforcing bars has been intensively investigated. The results are summarised in Table. 2-3 (Daniyal and Akhtar 2019). The correlation between the concrete resistivity and the corrosion severity varies significantly with studies. It has been mentioned previously that concrete resistivity is affected by many factors. Hence, this method cannot be used with complete confidence unless these factors are considered when analyzing the corrosion activity.

Table. 2-3 Correlation between concrete resistivity and corrosion severity (Daniyal and Akhtar 2019).

Corrosion severity in terms of concrete resistivity (kΩ cm)			Reference
Low	Moderate	High	
> 12	5–12	< 5	(CAVALIER, VASSIE et al. 1981)
> 8.5	6.5–8.5	< 6.5	(Hope, Ip et al. 1985)
> 30–40	7–30	< 7	(López and González 1993)
> 100	20–100	< 20	(Andrade and Alonso 1996)
> 30	10–30	< 10	(Morris, Vico et al. 2002)
> 100–200	10–100	< 10	(González, Miranda et al. 2004)
> 12	8–12	< 8	(Smith, Schokker et al. 2004)

2.4.2.3. Linear polarization resistance

The polarization resistance technique is the only available method to measure the corrosion rate in reinforced concrete. Polarization resistance is the resistance of the reinforcement to oxidation during polarization owning to the applied external potential. The word corrosion rate here refers to two different meanings: the average corrosion rate and the instantaneous corrosion rate:

Average corrosion rate: This is the engineering value required for service life calculation and prediction of structural degradation evaluation. It is the average value of mass loss or cross-section loss over a long period. If the time for rebar to depassivate is unknown, the calculated average value may contain an error that leads to a false estimation of the corrosion rate.

Instantaneous corrosion rate (I_{corr}): The polarization resistance is directly related to the corrosion current. Hence, it can be determined by polarization resistance (R_p) measurement. Polarization resistance devices can directly measure the polarization resistance of the concrete (e.g. potentiostat). The estimation of instantaneous corrosion rate is straightforward and reliable but only applicable for general corrosion attach. Environmental aspects such as temperature and moisture can influence the estimation of corrosion rate. Thus, these aspects need to take into account for a more accurate estimation.

The linear polarization resistance method applies potential sweep on the reinforcement around its open circuit potential in the cathodic direction or the anodic direction and records the induced current. A potential current density curve can be generated using the induced potential and the resulting current, where the x-axis is the current (mA), and the y-axis is the potential (mV). The slope of the step-in potential (ΔE) and the resulting current density (ΔI) can be sued to represent the polarization resistance (R_p) (Stern and Geaby 1957):

$$R_p = \frac{\Delta E}{\Delta I} \qquad \text{2-9}$$

The rate of the potential sweep is an essential parameter for the accurate estimation of the polarization resistance. A sweep rate of 2.5 – 10 mV/min can provide a reliable evaluation of R_p for active corrosion in concrete (Andrade and Alonso 2004), and 0.6V/h (10 mV/min) is the commonly recommended value by ASTM G5 (ASTM 2014).

The corrosion rate (I_{corr}) is inversely proportional to the corrosion resistivity:

$$I_{corr} = \frac{B}{R_p} \qquad \text{2-10}$$

Where B is the Stern–Geary constant, the value of B is assumed to be 26 mV for actively corroding rebar and 52 mV for passive rebar (Millard, Law et al. 2001).

The corrosion current density (i_{corr}) can be expressed as:

$$i_{corr} = \frac{I_{corr}}{A} \qquad \text{2-11}$$

Where A is the area of the surface of the rebar that gets polarised. Polarization occurs typically over a small area of the rebar. Precise measurement of the value of A can provide an accurate estimation of i_{corr}.

The interpretation of the LPR results is recommended by RILEM TC 154-EMC (Andrade and Alonso 2004). The measured corrosion density in mA/cm^{2,} the corresponding corrosion rate in mm/year, and the corrosion level of the rebar are summarized in Table. 2-4. For the value of i_{corr} less than 0.1 mA/cm^2, the corrosion level of the rebar is negligible. Thus the rebar is believed to be in its passive state. For values of i_{corr} between 0.1 - 0.2 mA/cm^2, the state of the rebar transfers from passive to active corrosion. Hence, the depassivation of the rebar occurs, and corrosion initiates. For values of i_{corr} between 0.1 - 0.5 mA/cm^2, the corrosion initiates bur the corrosion level is low with a corrosion rate of 0.001 - 0.005 mm/year. For values of i_{corr} between 0.5 - 01 mA/cm^2, the corrosion level increases to moderate, and the corrosion rate increases to 0.005 – 0.010 mm/year. For values of i_{corr} above 1 mA/cm^2, the corrosion level is high, and the corrosion rate is above 0.010 mm/year. It is reported (Andrade and Alonso 2004) that a value of i_{corr} above 1 mA/cm^2 is rarely recorded in an actual structure. The most common values of i_{corr} for active corrosion lies between 0.1 - 1 mA/cm^2.

Table. 2-4 Typical values of corrosion current density, icorr, related to the rate of corrosion activity (Andrade and Alonso 2004).

Corrosion current density i_{corr} (mA/cm^2)	Corrosion Rate V_{corr} (mm/year)	Corrosion Level
≤ 0.1	≤ 0.001	Negligible
0.1 – 0.5	0.001-0.005	Low
0.5 - 1	0.005-0.010	Moderate
> 1	> 0.010	Hight

Linear polarization resistance measurement is typically conducted using the three-electrode system. The schematic of the three-electrode LPR system is presented in Fig. 2-6. A three-electrode system consists of a reference electrode (RE), a counter electrode (CE), a working electrode (WE), and a potentiostat. The RE (as described in 2.4.2.1) is placed on the surface of the concrete. A wet sponge is placed between the RE and the concrete to ensure good electrolyte contact. The CE is generally stainless steel that closes the electrical circuit. The CE is usually placed in the vicinity of the RE. The rebar is used as the WE. Since the rebar is embedded in the concrete, local drilling of the concrete cover is requisite to assess the rebar. Studies (Andrade, Soler et al. 1995, Rengaraju, Neelakantan et al. 2019) have revealed the location and type of the RE, the geometry and the material of the CE, and the material of the embedded electrode (rebar) can influence the measurement. Hence, the description of the configuration, especially the information of the three electrodes, should be provided in the experimental studies (Burkan, Ueli et al. 2019).

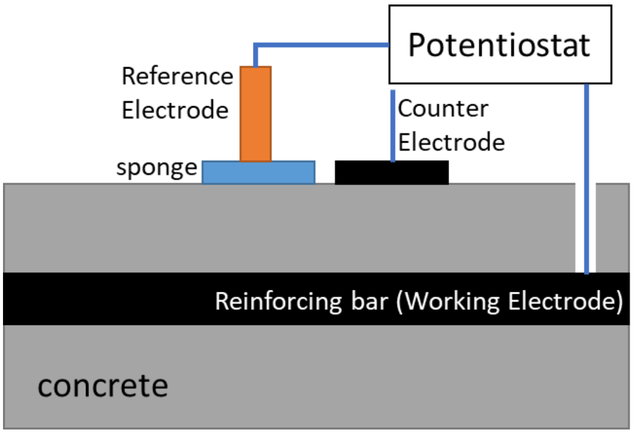

Fig. 2-6 Schematic of the three-electrode LPR measurement setup (Rodrigues, Gaboreau et al. 2021).

A lab-based experiment study by Millard et al. (Millard, Law et al. 2001)has reported the influences of the ambient environmental conditions on the LPR corrosion rate measurement of reinforced concrete exposed to carbonation corrosion. The influence of two conditions, relative humidity, and temperature are evaluated:

Relative Humidity (RH): The specimens undergo drying and wetting cycles between 60 % and 90% RH at an interval of 24 Hours. The RH in the concrete remains steady in all specimens depict of the variation in the external RH. The RH shows very little influence on the polarization resistance measurement in carbonated concrete. A more recent study conducted by the authors (Law, Cairns et al. 2004) indicates that the RH can have a pronounced effect on the

LPR measurement in the concrete under chloride attack. This is because the local environment within the chloride-induced pits is very sensitive to the local moisture content.

Temperature: The ambient temperature has a significant effect on corrosion activity. The internal temperature of the concrete increases with the increasing ambient temperature. A clear increasing trend of the corrosion rate was observed with an increasing ambient temperature. The corrosion current density increases from 0.5 mA/cm^2 to 1.5 mA/cm^2 between 16 °C to 21°C.

2.5. Ultrasonic methods for reinforced concrete corrosion monitoring

2.5.1. Guided wave propagation in cylindrical bodies

Ultrasonic guided waves are capable of detecting damages in cylindrical structures like rods. The governing equation for propagation of elastic waves in isotropic media can be expressed as (Ostachowicz, Kudela et al. 2012):

$$(\lambda + \mu)\nabla(\nabla \cdot u) + \mu\nabla 2u = \rho\,\ddot{u} \qquad \text{2-12}$$

Where λ and μ are Lamé parameters that specific to materials, u refers to the displacement field vector, ∇ is the Laplace operator and ρ is the mass density.

The equation of motion in cylindrical bodies can be derived in cylindrical coordinates (x, r, θ). The displacement field vector u can be expressed as the sum of the irrotational vector field u_ϕ and the solenoidal vector field u_r using Helmholtz decomposition. It is assumed that the displacement field vector is generated by the scalar potential ϕ and vector potential $H = (H_x, H_r, H_\theta)$ (Ostachowicz, Kudela et al. 2012):

$$u = u\varphi + uH = \nabla\varphi + \nabla \times H, \nabla \cdot H = 0 \qquad \text{2-13}$$

The displacement components can be expressed as (Ostachowicz, Kudela et al. 2012):

$$u_x = \frac{\partial\phi}{\partial x} + \frac{1}{r}\frac{\partial(rH_\theta)}{\partial r} + \frac{1}{r}\frac{\partial H_r}{\partial\theta} \qquad \text{2-14}$$

$$u_r = \frac{\partial \phi}{\partial r} + \frac{1}{r}\frac{\partial H_x}{\partial \theta} - \frac{\partial H_\theta}{\partial x}$$

$$u_\theta = \frac{1}{r}\frac{\partial \phi}{\partial \theta} + \frac{\partial H_r}{\partial x} - \frac{\partial H_x}{\partial r}$$

For longitudinal elastic waves in cylindrical structures like rods, the analysis can be simplified by the assumption of rotational symmetry of the cross-section with regard to the x-axis. Thus, the displacement and stress components are independent of the rotational angle θ. The displacement component u_θ and the deformation components $\gamma_{x\theta}$ and $\gamma_{r\theta}$ are equal to zero, thus (Ostachowicz, Kudela et al. 2012):

$$u_\theta = \gamma_{x\theta} = \gamma_{r\theta} = 0 \qquad \text{2-15}$$

Because of this symmetry, the potential vector H only contains one nonzero component H_θ and the H_x and H_r components are equal to zero. Thus, the displacement field vector can be simplified as (Ostachowicz, Kudela et al. 2012):

$$u_x = \frac{\partial \phi}{\partial x} + \frac{1}{r}\frac{\partial (rH_\theta)}{\partial r}$$

$$u_r = \frac{\partial \phi}{\partial r} - \frac{\partial H_\theta}{\partial x} \qquad \text{2-16}$$

By substituting the relationships in 2-16 into equation 2-12, equations of two independent motions can be expressed (Ostachowicz, Kudela et al. 2012):

$$C_L \nabla^2 \phi = \ddot{\phi}$$

$$C_S\,(\nabla^2 H_\theta - \frac{H_\theta}{r^2}) = \ddot{H}_\theta \qquad \text{2-17}$$

Where C_L is the longitudinal wave velocity and C_S is the shear wave velocity (Ostachowicz, Kudela et al. 2012):

$$C_L = \sqrt{\frac{\lambda + 2\mu}{\rho}} \qquad C_S = \sqrt{\frac{\mu}{\rho}} \qquad \text{2-18}$$

For (Ostachowicz, Kudela et al. 2012):

$$\frac{\partial}{\partial r}\nabla^2 H_\theta = \nabla^2 \frac{\partial H_\theta}{\partial r} - \frac{1}{r^2}\frac{\partial H_\theta}{\partial r} \qquad \text{2-19}$$

By substituting (Ostachowicz, Kudela et al. 2012):

$$H_\theta = \frac{\partial \psi}{\partial r} \qquad \text{2-20}$$

Equation 2-17 can be simplified into (Ostachowicz, Kudela et al. 2012):

$$C_L \nabla^2 \phi = \ddot{\phi} \qquad C_S \nabla^2 \psi = \ddot{\psi} \qquad \text{2-21}$$

Equation 2-16 can also be expressed as (Ostachowicz, Kudela et al. 2012):

$$u_x = \frac{\partial \phi}{\partial x} - \frac{\partial^2 \psi}{\partial r^2} - \frac{1}{r}\frac{\partial \psi}{\partial r} \qquad u_r = \frac{\partial \phi}{\partial r} - \frac{\partial^2 \psi}{\partial x \partial r} \qquad \text{2-22}$$

The nonzero components of the displacement field are (Ostachowicz, Kudela et al. 2012):

$$\varepsilon_{xx} = \frac{\partial u_x}{\partial x} \qquad \text{2-23}$$

$$\varepsilon_{rr} = \frac{\partial u_r}{\partial r}$$

$$\varepsilon_{\theta\theta} = \frac{u_r}{r}$$

$$\gamma_{xr} \frac{\partial u_r}{\partial x} + \frac{\partial u_x}{\partial r}$$

Using Hooke's Law, the stress field can be expressed (Ostachowicz, Kudela et al. 2012):

$$\sigma_{xx} = 2\mu\varepsilon_{xx} + \lambda(\varepsilon_{xx} + \varepsilon_{rr} + \varepsilon_{\theta\theta})$$

$$\sigma_{rr} = 2\mu\varepsilon_{rr} + \lambda(\varepsilon_{xx} + \varepsilon_{rr} + \varepsilon_{\theta\theta}) \qquad \text{2-24}$$

$$\sigma_{\theta\theta} = 2\mu\varepsilon_{\theta\theta} + \lambda(\varepsilon_{xx} + \varepsilon_{rr} + \varepsilon_{\theta\theta})$$

$$\tau_{xr} = \mu\gamma_{xr}$$

Pochhammer (Pochhammer 1876) developed the Pochhammer frequency equation for analyzing wave propagation in cylindrical structures. The equation has been employed to predict the axial and radial amplitude distribution of the longitudinal waves in the cylinder to obtain the dispersion curves (Ostachowicz, Kudela et al. 2012):

$$\frac{2\alpha}{a}(\beta^2 + k^2)J_1(\alpha a)J_1(\beta a) - (\beta^2 - k^2)J_0(\alpha a)J_0(\beta a) - 4k^2\alpha\beta J_1(\alpha a)J_0(\beta a) = 0 \qquad \text{2-25}$$

Flexural waves propagating in a rod are dependent on the circumferential angle θ. All the components of the displacement vector are nonzero. Thus, the displacement vectors for flexural waves are (Ostachowicz, Kudela et al. 2012):

$$u_x = U_x(r)\, cos\, \theta e^{i(kx-\omega t)}$$

$$u_r = U_r(r)\, sin\, \theta e^{i(kx-\omega t)} \qquad \text{2-26}$$

$$u_\theta = U_\theta(r)\, cos\, \theta e^{i(kx-\omega t)}$$

The functions U_x, U_r and U_θ can be expressed as (Ostachowicz, Kudela et al. 2012):

$$U_x(r) = ikAJ_1(\alpha r) - \frac{C}{r}\frac{\partial}{\partial r}[rJ_2(\beta r)] - \frac{C}{r}J_2(\beta r)$$

$$U_r(r) = A\frac{\partial}{\partial r}J_1(\alpha r) + \frac{B}{r}J_1(\beta r) + ikCJ_2(\beta r) \qquad \text{2-27}$$

$$U_\theta(r) = -\frac{A}{r}J_1(\alpha r) + ikCJ_2(\beta r) - B\frac{\partial}{\partial r}J_1(\beta r)$$

2.5.2. Wave parameters for damage detection

The characteristics of the guided waves can be altered due to the presence of damage in the waveguide. Several wave parameters have been employed to detect the altered characteristics of the guided waves. The word 'damage' in structural health monitoring refers to the state of the structure that is different from the pristine state ('benchmark'). Hence, a damage event is detected by comparing the current state of the structure to its benchmark (Su and Ye 2009).

Two basic configurations of signal actuator and receiver are used in guided wave-based damage identification, namely pitch-catch and pulse-echo, as shown in Fig. 2-7.

In the pitch-catch configuration, the damage is always assumed to present on or in the close vicinity of the wave path. The diagnostic wave excited by the signal actuator on one side of the damage interact with the damage. This alters (increases) the length of the wave path. The wave diffracts from the side of the damage and being received by the signal receiver at the other side of the damage. The changes in the wave parameters, especially the Time-of-Flight (ToF) and the signal strength can be detected. However, this method cannot be used to locate the damage unless multiple sensor paths, known as a sensor network, are used.

In pulse-echo configuration, the signal actuator and the receiver are placed on the same side of the damage. The diagnostic wave first passes the signal receiver and then interacts with the damage. The wave can be reflected from the damage and captured by the signal receiver. This wave is known as the reflected wave. The ToF of the reflected waves can be used to locate the damage.

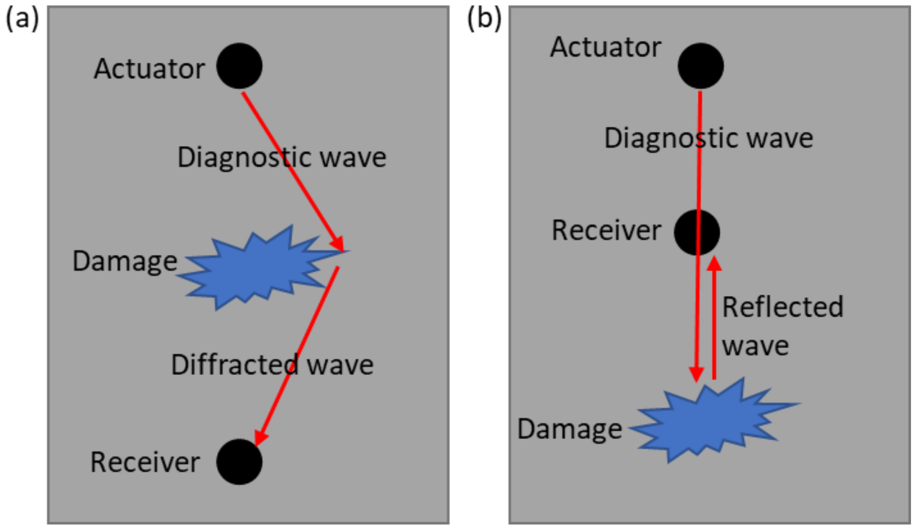

Fig. 2-7 Configuration of actuator and receiver in (a) pitch-catch and (b) pulse-echo.

2.5.2.1. Signal strength

The signal strength is one of the most straightforward parameters of the guided wave. The peak-to-peak voltage of the signal (Sharma and Mukherjee 2013) and the total energy around the excitation frequency (Miller, Kundu et al. 2013)are usually used to analyze the signal strength. The signal strength varies significantly with different types of defects. For corrosion in reinforcing bars, the bar deterioration significantly increases the attenuation of the guided wave. Hence, the signal strength reduces with increasing exposure to corrosion. While for debonding detection, energy leakage from the waveguide to the surrounding materials is impeded due to the discontinuities in the bond. More energy is retained in the waveguide and thus, the signal strength increases with the increasing debonding. The major drawback of damage detection using signal strength is that the amplitude of the signal is highly dependent on the contact between the transducer and the hosting structure. For a contact transducer, the applied pressure on the transducer can significantly influence the amplitude of the exciting signal (Majhi, Mukherjee et al. 2021). Transducers can be permanently mounted to the host structures using adhesives to eliminate the coupling issue. However, the bond between the transducer and the host structure weakens with time due to the vibration of the transducer and the degradation of the adhesive. This may affect the records and lead to false data interpretation.

2.5.2.2. Time of flight (ToF)

ToF is the time taken for the guided wave to travel from the actuator to the receiver. Guided wave is multi-modal, and each mode travels at a different velocity even at the same excitation frequency. The velocity of the modes is dominated by the geometry and properties of the waveguide and the excitation frequency. For a known specimen and excitation frequency, the velocity of the modes remains constant, and thus, ToF can be used to identify the modes of the wave packets in the received signals. Damage can increase the wave path and therefore increase the ToF. If a sensor network is employed, multiple wave paths can be obtained. The difference in the ToF in all paths can be used to locate the damage through triangulation (Hu, Cai et al. 2012).

2.5.2.3. Frequency profile

The frequency of excitation is an essential factor for damage detection as it dominates the propagation of the guided waves. In general, the presence of defects such as cracking and debonding does not alter the dominant frequency of the received signal. A recent study (Majhi, Mukherjee et al. 2019) has reported a shift from high frequency to low frequency in the received signal in a steel rod with increasing exposure to corrosion. Hence, the frequency shift in the frequency profile of the received signal can be employed to monitor the bar deterioration. The interaction between the incident wave and the defects may generate harmonics at multiple frequencies of the excitation. This additional component in the frequency profile can be used to detect damages, especially for microscopic defects that cannot be detected by the linear waves.

2.5.2.4. Damage induced nonlinearity

Compared to the parameters derived from the linear guided wave, the nonlinear waves are more sensitive to minor defects and can detect incipient defects. The incident ultrasonic waves open and close such defects, leading to higher harmonic generation (Richardson 1979). When ultrasonic waves encounter an imperfect bonded interface, the tensile part of the wave opens the interface and reflects the waves, while the compressional part closes the interface, allowing the wave to transmit. The repetition of the closing and opening of the interface generates higher harmonics leading to localized nonlinearity. This is known as contact acoustic nonlinearity (CAN). The ToF of the CAN have been extensively employed to detect and locate incipient defect like fatigue cracks in metallic structures(Guyer and Johnson 2009, Chao, Ming et al. 2013, Hong, Su et al. 2014, Su, Zhou et al. 2014, Hong, Su et al. 2015, Wang, Guan et al. 2017).

2.5.3. Deployment of sensors

2.5.3.1. Surface contact

The transducers can be either in contact with the surface of the host structures using coupling agents (Fig. 2-8 (a)) (Sharma and Mukherjee 2015, Bhalla, Sharma et al. 2018) or permanently mounted to the structures using glue/epoxy (Fig. 2-8 (b)) (Sohn, Dutta et al. 2011, Wang, Guan et al. 2017). Surface contact is a widely employed deployment of sensors by researchers (Sharma and Mukherjee 2010, Sun and Zhu 2020) to contact ultrasonic evaluation due to its convenience in accessibility, attachment, maintenance, reparation, and replacement. The employment of coupled transducers is flexible. They can either be used to excite longitudinal guided waves to evaluate the change in the waveguide (Sharma and Mukherjee 2010)or to excite bulk waves that travel through a thick structure, e.g. concrete, to evaluate the condition deep inside the structure (Majhi, Mukherjee et al. 2021). The main drawback of the coupled transducer is the signal strength of the excitation highly depend on the contact between the transducer and the host structure. Any change in the size of the contact area or the contact pressure can cause a change in the signal strength, which may lead to a false diagnosis (Majhi, Mukherjee et al. 2021).

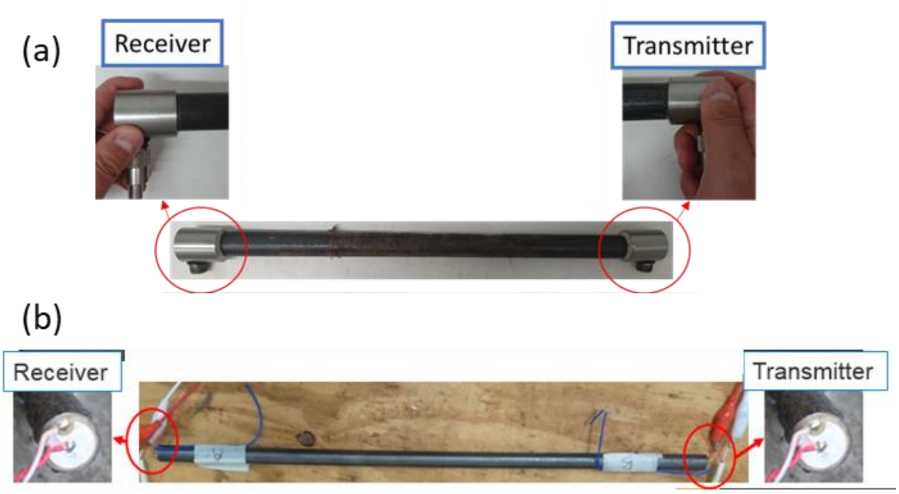

Fig. 2-8 Surface mounted transducers (a) coupled and (b) mounted.

Benefiting from the small size and cheap price, PZT wafers can be permanently mounted to the host structure, allowing permanent monitoring of the structure (Wang, Guan et al. 2017). Since the wafers are permanently mounted, the effect of contact can be eliminated. The wafers have been extensively used to monitor debonding (Zima and Rucka 2018), delamination (Sohn, Dutta et al. 2011) and cracking (Wang, Guan et al. 2017)in laminates or plates. The wafers can generate elastic waves that travel at the surface of the structure, limiting its application to evaluate the condition inside the structures. Therefore, they are commonly used to evaluate laminates, plates and the upper surface of structures. In addition, the surface contacted transducers are exposed to ambient noise and environmental degradation, which may lead to a low signal-noise ratio and durability of the transducers.

2.5.3.2. Embedded

By embedding the transducers in the structures, it allows isolation of the transducers from the ambient noise and environmental degradation, leading to high SNR, good durability and extend the service life of the transducers (Su and Ye 2009). An embedded transducer normally consists of a PZT wafer covered with resin, epoxy or grout to protect it from damage or short circuit. These small embedded transducers that are placed in reinforced concrete structures are known as smart aggregates (Zhang, Li et al. 2022). They have been employed by researchers to monitor concrete setting (Qin and Li 2008), concrete cracking (Feng, Kong et al. 2015), delamination (Jiang, Wang et al.

2021) and evaluate mechanical properties of concrete (Zhang, Hou et al. 2018). Although embedding provides protection to the transducers, it also limits access to the transducers. The main disadvantage is that it is difficult to access, maintain and replace the transducers. Other than this, precise placement and alignment of transducers are required.

2.5.4. Guided wave-based damage detection

Corrosion of reinforced concrete is a very complex process. It can be assumed to be a superposition of three phenomena, bar deterioration, debonding of the steel-concrete interface, and concrete cracking. These phenomena can initiate at a different time of exposure to corrosion and eventually occur simultaneously, resulting in severe corrosion defects.

2.5.4.1. Detection of bar deterioration using guided waves

Once the passive protective film on the steel bar is destroyed, localized corrosion occurs on the surface of the bar. This leads to bar deterioration that reduces the material properties of the steel reinforcement. The guided wave-based method utilizing wave characteristics, such as the amplitude of the signal (Sharma and Mukherjee 2010, Zhao, Durham et al. 2019, Durham, Zhao et al. 2020), ToF (Amjad, Yadav et al. 2015, Farhidzadeh and Salamone 2015, Zhao, Durham et al. 2019) and frequency (Farhidzadeh and Salamone 2015, Majhi, Mukherjee et al. 2019) has been reported to be sensitive to deterioration of rod structures such as steel rebar. Longitudinal guided waves were employed by Sharma and Mukherjee (Sharma and Mukherjee 2010) to detect rebar deterioration. The pitting corrosion was simulated by notches with symmetrical 0%, 20%, 40%, and 60% diameter reduction in the middle of the bar. Both pitch-catch and pulse-echo configurations were used to receive the direct transmitted and damage reflected signals. It was reported that the amplitude of the reflected signal increased while the amplitude of the transmitted signals reduced with the increasing size of the notch. The interaction between guided waves and rebar damage simulated by partial removal of different lengths of rebar section was experimentally studied (Lu, Li et al. 2013). It was found that the captured signals could not be compared straightforwardly because the responses of the guided waves vary with individual rebar, although they were almost identical. Amjad et al. (Amjad, Yadav et al. 2015) also indicated that the reduction in amplitude of the transmitted signal could be caused by corrosion as well as the contact/bonding between the sensor and the host structure. To counter these issues, a ToF-based technique was proposed to monitor the corrosion-induced deterioration of reinforcing bars. The ToF of the transmitted signal was not affected by the contact/debonding. Therefore it could serve as a more reliable technique for quantitative measurement of rebar corrosion. It has been demonstrated that the ToF of the L (0,1) mode shown good sensitivity to the corrosion of reinforcing bars, and the corrosion-induced ToF variation matched closely with the theoretical dispersion curves. However, ToF is not sensitive to early stages of corrosion. Majhi et al. (Majhi, Mukherjee et al. 2019) proposed a time-frequency method that combines both time and frequency information for monitoring the corrosion of reinforcing bars. It was demonstrated that the higher order modes attenuated faster than the lower order modes with the progression of corrosion. Sriramadasu et al. (Sriramadasu, Banerjee et al. 2019) proposed a non-dimensional scatter coefficient, defined as the ratio of the energy of the scattered wave modes to the energy of the directly transmitted wave, to detect the pitting corrosion in rebar, which was simulated by scraping off the material from the surface of the rebar. The amplitude of the directly transmitted signal was not affected much by the pitting corrosion, but the amplitude of the damage scattered signal varies significantly with the location and size of the pits. It was observed that the scatter coefficient increases with the size of the pits, and the increment is more significant when the location of the pit is closer to the signal receiver. A similar experiment has been conducted by Zhao et al (Zhao, Durham et al. 2019). Guided waves in pulse-echo configuration have been employed to detect corrosion damage simulated by removing material from the surface of the rebar. The amplitude of the damage echoed signal increased, and the amplitude of the rod-end echoed signal decreased with increasing cross-sectional losses. The Location of the damage was identified using the ToF of the damage echoed signals. The attenuation of longitudinal, flexural and torsional modes in an embedded rebar were investigated. Clay was wrapped around the bar to absorb the energy leaked from the rebar while propagating. It was observed that the longitudinal modes attenuated much lower than the flexural and torsional modes. The longitudinal mode was more pronounced to monitoring corrosion of rebar.

2.5.4.2. Detection of debonding using guided waves

Debonding of the steel-concrete interface occurs with the generation of rust between the steel and the surrounding concrete. The size of debonding increases with increasing exposure to corrosion, leading to a gradual loss of bond. Ultrasonic guided wave-based technique has been intensively employed to detect the debonding in multilayer structures such as debonding of the steel-concrete interface (Na, Kundu et al. 2003, Sharma and Mukherjee 2010), debonding of FRP rode-concrete interface (Jiang, Kong et al. 2017), debonding of the steel-grout interface (Zima and Rucka 2018) and delamination of composite laminates (Ren and Lissenden 2013). The concrete bonded to the reinforcement acts as an attenuating medium for the waves travelling through the reinforcement. Waves continue leaking from the steel bar to the surrounding concrete while propagating in the bar. The debonding leads to the breakage of the contact between the reinforcement and the concrete and impedes the energy leakage. Therefore, wave characteristics such as amplitude (Na, Kundu et al. 2003, Wu and Chang 2006a, Gu, Luo et al. 2016, Jiang, Kong et al. 2017) and attenuation (Wu, Chan et al. 2015, Sun and Zhu 2020) has been employed to evaluate the size of the debonding. The guided waves are sensitive to changes of the waveguide, especially the change in the bonding condition (bounded bar to debonded bar or vise versa). Wave can be diffracted and reflected from where the bonding condition changes. Hence, the velocity (Zima and Rucka 2018, Zima and Kędra 2019)and the ToF (Wang, Zhu et al. 2009) have been used to locate the debonding.

Na et al. (Na, Kundu et al. 2003) evaluated the feasibility of detecting steel-concrete interface delamination using longitudinal guided waves and nonaxisymmetric guided waves. The longitudinal guided wave was excited using transducers that direct contact with the bar ends while the nonaxisymmetric guided waves were launched at the surface of the reinforcement and the surface of the concrete by transducers with a special coupler. The peak-to-peak voltage increased with increasing debonding. The nonaxisymmetric guided waves excited at the surface of the bar significantly outperformed the other two arrangements. However, when the steel bar was not accessible. The nonaxisymmetric guided waves excited at the surface of the concrete that could deliver desirable results were more useful.

Wu and Change (Wu and Chang 2006b) have proposed a guided wave-based algorithm to detect debonding in reinforced concrete using embedded PZT wafers in pith catch configuration. The algorithm has been experimentally validated to detect debonding reinforced concrete samples (Wu and Chang 2006a). Piezoelectric (PZT) discs were mounted to the surface of the rebar using epoxy and embedded in the concrete. The amplitude of the signals increased as the debonding increased. While the ToF of the signal remained steady for debond size up to 101.6 mm. A slight drop in the ToF was observed for a debond size of 203.2 mm. Hence, it was concluded the amplitude of the signal was more sensitive to incipient debonding than the ToF.

Wang et al. (Wang, Zhu et al. 2009) have conducted an experimental study to detect debonding in reinforced concrete using a pitch-catch configuration with both direct transmitted waves and bar-end reflected waves taking into account. PZT strip sensors were bonded to the surface of the embedded bars. Three wave packets were identified in the received signal where Wave 1 was the incident wave from the actuators, and Wave 2 and 3 were the reflected waves by the two ends of the rebar. It was found that the time interval between Wave 1 and 3 could be used to locate the debonding while the amplitude ratio of Wave 1 and 3 could be employed to estimate the debonding damage index. The amplitude and the ToF of Wave 1 could be used to estimate the length of the debonding.

Sharma and Mukherjee (Sharma and Mukherjee 2010) have employed longitudinal guided waves to monitor corrosion-induced steel-concrete debonding both by simulated debonding and accelerated corrosion. It was reported that the amplitude of the L (0,1) mode continued to drop with increasing simulated debonding. In case of accelerated corrosion, the pattern was more complicated. In the beginning, the formation of rusts caused debonding. Less energy leaked into the surrounding concrete due to the local breakage of the bond, leading to an increment in the amplitude of the transmitted signals. However, at advanced corrosion, the amplitude continuously falls due to the formation of pits and surface irregularities. Thus, they concluded that it is essential to investigate bars undergoing natural corrosion, and simulation was insufficient to estimate the natural corrison process.

Wu et al. (Wu, Chan et al. 2015) have investigated bond deterioration at the steel-concrete interface due to split failure using PZT based system with improved sensor design. Bond deterioration index BDI was proposed to identify the change in the signal's attenuation and estimate the bond length. The BDI increased with applied pullout loading. This indicated a reduction in attenuation of the guided waves propagating in steel rebar by the surrounding concrete, caused by the bond deterioration due to split failure.

An active PZT-based pitch-catch approach was performed to access the debond between the steel and concrete in static, quasi-static, and continuous loading states (Gu, Luo et al. 2016). In the static state, the debonding was simulated by wrapping PVC pipe over the steel bar. The amplitude of the transmitted signal increased as debond enlarged. In quasi-static state, debond was created by bending test and a notch was pre-set to in the tensile side of the specimen to induce cracks. The test was paused at every load step for recording signals. In the initial stage, micro-cracking initiated from the notch and propagated through the cross-section of the specimen. The amplitude remained steady as the debonding created by the macro cracking was negligible. As the loading increased, the bar began to slip away from the bonded concrete. This led to debonding, resulting in an increment in the amplitude. In the continuous test, the signals were recorded during the bending test to simulate the situation in the field. The amplitude of the pitch-catch ultrasonic signals was interfered with by the AE signals emitted from the damage. Yet the amplitude of the ultrasonic signals showed an increasing tendency, which indicated a slow degradation of the bond. The formation of macro cracking and integral slipping of the bar were clearly identified.

Jiang et al. (Jiang, Kong et al. 2017) have investigated the influence of debonding on wave leakage from waveguide to surrounding concrete. PZT wafer was mounted to the surface of an FRP bar as the signal actuator. Two smart aggregates were cast in the concrete to measure the wave leaked into the concrete. Pullout tests were conducted to create debonding owning to bond slippage. The amplitude of the signal shown a decreasing trend with the increasing debonding. A wave packet-based damage index that evaluation the residual energy of the signals that leaked into the concrete was proposed. With increasing debonding, the values of the DI increased. The initial debonding and the fully debonding stages were clearly identified using the proposed DI.

Zima and Rucha (Zima and Rucka 2018) have employed the pulse-echo method to investigate debonding between steel bar and grout. Two micro-size plate PZT transducers were mounted to the same end of the bar, one as actuator and one as the receiver. It was reported that the average propagation velocity of the damage reflected wave increased with the increasing size of debonding. As the debonding increased, the distance between the actuator and debonding reduced, the length of the wave path, from the actuator to debonding then reflected to the receiver, reduced. Therefore, the ToF of the debond reflected wave was reduced. The proposed method was further validated in a reinforced concrete specimen with simulated single and multiple debonding (Zima and Kędra 2019). It was observed that regardless of the numbers of debonding, single or multiple, the velocity of the reflected waves was affected by the total length of debonding.

Sun and Zhu (Sun and Zhu 2020) have employed high order longitudinal mode L (0,8) to evaluate different bonding conditions (solid, honeycomb, and void) of reinforced concrete during setting, curing, and cured. The attenuation of the captured signals was calculated and used to evaluate the bonding conditions. It was reported that the attenuation values of the solid, honeycomb and void concrete specimens showed clear differences in setting, curing, and cured stages. A normalized attenuation with respect to the effective bonding length was proposed. It was found that the normalized attenuation was almost identical in all specimens, validating that the attenuation difference was caused by the difference in energy leakage from the defect regions. Hence, attenuation of high order longitudinal mode could be used to evaluate the bonding conditions.

2.5.4.3. Monitoring corrosion of reinforced concrete using guided waves

The investigation conducted by Sharma and Mukherjee (Sharma and Mukherjee 2010) has compared the guided wave results of simulated and real corrosion of reinforced concrete. The results revealed that the simulated corrosion could well represent the incipient stage of corrosion. However, at the advanced stage of corrosion, the guided waves in reinforced concrete subjected to actual corrosion shown a more complex phenomenon, which was failed to be represented by simulated corrosion. Therefore, to have a realistic estimation of corrosion, simulated corrosion is not sufficient. It is indispensable to conduct experimental investigations of reinforced concrete undergoing actual corrosion. The sensitivity of the guided wave-based method for corrosion monitoring in reinforced concrete structures has been extensively reported (Dixit and Gupta 2021, Fan and Shi 2021). Most of the studies utilize the amplitude of the guided waves excited either by contact transducer (Sharma and Mukherjee 2010, Sharma and Mukherjee 2011) at the bar ends or PZT wafers mounted on the surface of the rebars (Sriramadasu, Lu et al. 2019, Sriramadasu, Banerjee et al. 2020). ToF of the guided waves has also been utilized to monitor corrosion, benefiting from its independence of contact condition between transducers and the host structure (Miller, Kundu et al. 2013).

Ervin and Resis (Ervin and Reis 2008) have employed guided longitudinal modes in both low (<200 kHz) and high (2-8 MHz) frequencies to monitor corrosion of reinforced mortar specimens. The effect of the ribs of the rebar on the guided waves was identified experimentally. It was found that the effect of ribs on guided waves was negligible if the wavelength was much longer than the dimension of the ribs. At higher frequencies, where the axial displacement of the wave mode was concentrated at the center of the bar, the guided wave was less affected. Other than these two conditions, the reinforcing ribs led to the attenuation of guided waves. The L (0,1) mode at low frequencies was attenuated as rusts initially cumulated between the steel and the mortar. The initially cumulated rusts increase the contact between the steel and mortar, causing more energy to leak into the surrounding mortar. Once the pressure built up and crack initiated, the signal began to gain strength. This indicated that the attenuation of the L (0,1) mode was closely related to the contact and the pressure caused by the cumulated rusts. The attenuation of the L (0,9) mode at high frequencies increased with increasing mass loss, indicating the sensitivity of the L (0,9) mode to monitor the bar deterioration during uniform corrosion. Hence, it was concluded that the higher frequencies were more suitable to monitor bar deterioration while lower frequencies were more suitable to detect the rust accumulation at the steel mortar interface (Ervin, Kuchma et al. 2009).

Li et al. (Li, Zhang et al. 2014)have employed longitudinal L (0,1) mode at 40 kHz to evaluate the corrosion of ribbed bars in concrete subjected to different levels of corrosion. The pattern of the amplitude in all specimens matched, validating the repeatability of the results. Hence, it was concluded that the longitudinal guided wave-based method could be a reliable corrosion detection method.

Sharma's group has extensively studied guided longitudinal wave-based corrosion monitoring in reinforced concrete undergoing accelerated corrosion. The mode shape of the waves modes was analyzed, and the wave modes for signal excitation were carefully selected based on their axial displacement distribution, total energy density, and attenuation (Sharma and Mukherjee 2010). Two wave modes, namely core-seeking and surface-seeking mode, were employed. The core seeking mode was the L (0,7) at 1 MHz with its axial displacement and total energy density concentrated around the center of the bar. Hence it was more suitable to detect bar deterioration due to corrosion. While the surface-seeking mode (L (0,1) mode at 100 kHz) had a significant amount of axial displacement and total energy density on the surface of the bar, hence it was suitable to detect bonding conditions at the steel-concrete interface.

It was reported that the amplitude of the core-seeking mode first remained steady in the first 6 days of corrosion and then continuously fell throughout the entire period. The incipient formation of localized pits did not distort the waveguide. Hence it did not affect the core-seeking mode. As the pits grew larger and deeper, the bar deteriorated, guided waves reflected from the pits, reducing the transmitted signals. The amplitude of the surface-seeking mode was complex. Initially, the formation of rust at the steel-concrete interface caused debonding, resulting in an increase in the amplitude due to the impeding of energy leakage. At an advanced stage of corrosion, the amplitude continuously fell due to the formation of pits and surface irregularities.

The proposed methods were then employed to monitoring reinforced concrete corrosion in an oxide and a chloride environment (Sharma and Mukherjee 2011). The oxide corrosion mainly affected the surface of the bar, while the chloride corrosion led to pitting in the bar. Hence, the surface-seeking mode was more suitable to monitor incipient oxide corrosion in reinforced concrete. In chloride corrosion, the core-seeking first raised and then fell, indicating the formation of delamination followed by severe loss of material from the bar. With the core-seeking mode, the amplitude fell with the increasing corrosion exposure, indicating the continuous formation of pits in the bar. In oxide corrosion, the rate of corrosion was slower. The signal strength of the surface-seeking mode gradually reduced, indicating the slow bond deterioration. The formation of pits was insignificant. Therefore the amplitude of the core-seeking mode dropped slowly with increasing corrosion.

A detailed investigation has been conducted to evaluate the guide wave-based corrosion monitoring technique in varying environments (with/without chloride) (Sharma and Mukherjee 2013). Embedded bars are corroded to different stages in the presence and absence of chloride. The ultrasonic voltage ratio was correlated with destructive parameters, such as mass loss, tensile stress, and bond strength to predict the level of bar deterioration. A mapping between the physical condition of the reinforcement with the voltage ratios was attempted, indicating the guided wave was a promising and effective method to monitor corrosion of reinforced concrete under varying environments.

A combination of wave propagation techniques has been proposed to better monitor invisible corrosion in concrete (Sharma, Sharma et al. 2018a, Sharma, Sharma et al. 2018b). Active guided wave method, passive acoustic emission measurement, and half-cell potential measurements were combined to provide detailed information about the corrosion. Although HCP measurement could not quantify the corrosion, it indicated the probability of the corrosion. Hence it could validate that AE signals were originating from corrosion. The pattern of the core-seeking and the surface-seeking mode of the guided waves could successfully reflect the deterioration of the bar and the bond. However, it could not detect the initial corrosion formation and the corrosion-induced cracking in the concrete body. On the other hand, AE measurement could successfully detect and locate the corrosion initiation and monitor the crack propagation in the concrete cover. By utilizing the combined technique, the corrosion initiation, bar deterioration, bond deterioration, and corrosion-induced cracking in reinforced concrete could be monitored comprehensively.

Most of the studies on guided wave-based corrosion monitoring in reinforced concrete were conducted by measuring the amplitude of the signal, Miller et al. (Miller, Kundu et al. 2013) proposed a new guided wave-based corrosion monitoring method by measuring the change in the TOF of the guided waves as the specimens were loaded laterally. The pattern of signal loss and ToF changes with increasing corrosion matched with each mother. The main advantage of the ToF-based method was it was not influenced by the bond condition between the transducers and the host structures, while the amplitude of the signal was not only affected by the corrosion of the bar but also depended on the bonding condition of the transducer. When subjected to lateral loading, the ToF variation was different from corroded and intact rebars, from where the corrosion level can be obtained by measuring the ToF shift.

Talakokula and Bhalla (Talakokula and Bhalla 2015) compared the sensing capability of the surface-mounted and embedded PZT patches in detecting chloride-induced concrete corrosion. It was found that the embedded sensor in the vicinity of the rebar was susceptible to the corrosion initiation stage where the ingression of chloride ions into concrete occurred, while the surface-mounted PZT sensors shown comparatively less sensitivity. Once the depassivation of rebar occurred, embedded sensors became less effective, but the surface-mounted PZT sensors varied significantly with increasing corrosion during the corrosion propagation and cracking of concrete stages. It was concluded that the same PZT sensors could be either surface mounted to the bar or embedded in the vicinity of the bar, and the two types of arrangement should be employed simultaneously for comprehensive monitoring of concrete corrosion.

Sriramadasu et al.(Sriramadasu, Lu et al. 2019, Sriramadasu, Banerjee et al. 2020) have investigated the corrosion of reinforced concrete using flexural modes induced by PZT strips mounted to the surface of the rebar. It was reported that the flexural mode showed better sensitivity to the surface condition of the bar than the longitudinal modes. It was susceptible to the corrosion initiation phase. The pattern of the amplitude variation with increasing corrosion clearly indicated the different phases of corrosion. During the initial phase of corrosion, the diameter of the rebar increases due to the formation of rusts. This led to increased stress transferred from the rebar to the surrounding concrete. As a result, the amplitude of the flexural mode was reduced with corrosion during this stage. In the corrosion progress phase, debonding occurred at the steel-concrete interface, impeding the stress transfer. Thus the amplitude of the signal increased with increasing debonding. During the cracking phase, the rebar deteriorated, and deep pits formed. The signal experienced strong attenuation and reflection. As a result, the amplitude of the signal reduced with increasing corrosion.

2.5.5. Ultrasonic imaging of invisible cracking in reinforced concrete using SAFT reconstruction

The cracking of reinforced concrete initiates from the steel-concrete interface and propagates towards the concrete cover. Concrete cracking can only be confirmed when surface stains or surface cracks are visually observed. However, severe cracking has been generated at this stage, not only endangers the integrity of the structure but also provides quick access of chloride ions and moistures to the rebar and further induce corrosion. Hence, it is essential to detect and monitor the propagation of the invisible cracking before it reaches the concrete cover. Ultrasonic imaging of the concrete cross-section can provide information about the location of the embedded steel reinforcements and crack generated in the concrete. The most adopted ultrasonic imaging technique is the point-to-point pulse-echo scanning on the surfaces of the structure with the piezo-electric transducer. Such a system was developed but mainly used for medical applications in the early 1940s and employed for materials testing in the 1970s (Krautkrämer, Seiger et al. 1990). The inhomogeneous property of reinforced concrete makes ultrasonic imaging a challenging task. The acoustic properties of pores and aggregates are much different from those of cement matrix, resulting in strong wave scattering and mode conversion. The strong attenuation of the pulse signal and structural noise can mask the reflected signals from the objects of interest. Low-frequency transducers with short impulse responses were developed in the 1990s, making the application of ultrasonic imaging of concrete structures using a single (A-scan) or multiple (B-scan) measurements possible (Schickert 2005). The influence of structural noise on imaging of concrete cross-section was critical and thus complicating the interpretation of the results. To counter these drawbacks and to enhance the imaging precision, a postprocessing image reconstruction algorithm, known as Synthetic Aperture Focusing Technique (SAFT), has been extensively employed to reconstruct the image of the cross-section of reinforced concrete (Schickert 2005, Spies, Rieder et al. 2012, Ghosh, Kumar et al. 2020, Majhi, Mukherjee et al. 2021). The algorithm focuses ultrasonic signals captured at numerous aperture points to any points of the reconstructed image by coherent superposition (Schickert, Krause et al. 2003). The early application of the SAFT method for concrete imaging has been extensively reported in review papers (Schickert 2005, Spies, Rieder et al. 2012) and journal papers (Beniwal and Ganguli 2015, Majhi, Mukherjee et al. 2021). The latest applications of the SAFT method for concrete imaging are summarized and discussed below.

Shokouhi et al. (Shokouhi, Wolf et al. 2014) have employed multisensory low-frequency (central frequency of 50 kHz) ultrasonic testing to detect and characterize shallow and deep delamination in reinforced concrete using SAFT reconstructed B-, C-, and D-scans. Deep delamination at a depth > 100 mm could be directly detected using the SAFT method, while shallow delamination at a depth < 100 mm could not be detected. This was because the reflection from the shallow delamination interfered with the surface waves and the direct incident waves from transducer to receiver, known as the near-surface effect of ultrasound. However, the shallow delamination could be evaluated indirectly by the missing reflections from the bottom boundary of the specimen and distortion of the near-surface effect. The SAFT method was then employed to evaluate the delamination in an actual structure, a section of the deck of a demolished concrete bridge. The actual location of delamination measured from the cores extracted from the location of interest matched well with the reconstructed imaging of the concrete cross-section, indicating the SAFT-based technique is a promising method for in-depth testing of the concrete structure.

The limitation of the aperture of traditional SAFT-based technique has been identified as the impedance to a quantitative interpretation. To counter this limitation, Hoegh and Khazanovich (Hoegh and Khazanovich 2015) have proposed an enhanced SAFT algorithm, termed SAFT-EPan reconstruction, by assuming the shift factor for placement of individual scan to be within a certain range, rather than knowing the precise shift between scans. Based on the concept that the inclusions and defects within a certain region resulted in similar relative reflectivity, regardless of the location of the scans, the placement of each scan could be determined using the proposed procedure incorporating a similarity of overlapping regions. The proposed method was experimentally validated by a full-scale controlled test on PCC slabs. Comparing to the traditional SAFT method, The proposed method had demonstrated an improved resolution of the reconstructed imaging and a more reliable characterization of inclusions and defects, especially when robotic precision of scan placement was not feasible.

Choi et al. (Choi, Bittner et al. 2016) have compared the reconstructed images using tomography and SAFT using different measuring methods. Air-coupled and dry-point ultrasonic measurements have been conducted to evaluate the inclusions and defects in reinforced concrete structures. The embedded voids in the reinforced concrete could be successfully detected using air-coupled ultrasonic tomograms. The microcracks within the concrete were difficult to identify but could be detected in some cases. The reconstructed image using dry-point measurement clearly identified the location of the reflectors, such as rebars and voids. However, defects below densely spaced rebars could not be detected due to the shallowing effect. Microcracks could not be detected because they could not provide sufficient reflections. In terms of reconstruction techniques, SAFT based technique could successfully detect the location of the embedded rebars, but tomogram images failed to do so. Tomograms showed superior performance for the isolated concrete elements containing densely spaced rebars, while the SAFT technique showed superior performance for thickness measurement of the concrete element with low rebar volumes. The two imaging techniques have shown distinct characteristics. Thus the employment of the imaging technique depended on the type of concrete element of interest and the type of embedded targets.

Tseng et al. (Tseng, Chang et al. 2018) have compared the performance of using two modern techniques, total focusing method (TFM) and phased array method (PA), on the SAFT-based image reconstruction of reinforced concrete. PA method showed superior performance in detecting targets smaller than aggregates under noisy and low signal-noise ratio conditions but at a shallow depth (< 300mm) due to the high attenuation of ultrasonic waves in concrete. TFM method outperformed in detecting targets larger than the side of aggregates in concrete as it improved the image quality by employing a large number of SNR corrected data. Hence, TFM overwhelmed PA in a high SNR environment. Hence, the PA method was recommended for detecting small targets at shallow depth, while the TFM method was suggested to evaluate large targets.

Ghosh et al. (Ghosh, Kumar et al. 2020) have proposed a new SAFT imaging algorithm to detect corrosion-induced damage in concrete using the combination of compressional wave and planner Rayleigh wave. Compressional wave-based SAFT imaging illustrated the images of the rebar exposed to increasing corrosion exposure. In the pristine condition, the full rebar was visible. As the corrosion process proceeded, the corrosion-affected portion of the rebar disappeared from the image. The rebar was disappeared entirely from the image at an advanced stage of corrosion. Rayleigh wave traveled near the surface of the concrete. Thus the Rayleigh wave-based SAFT imaging was capable of detecting the near-surface cracks. As the rebar started to disappear from the compressional wave-based SAFT imaging, the cracks began to appear in the Rayleigh wave-based SAFT image. Hence, the Rayleigh wave-based SAFT method could be employed to perform an initial detection of near-surface cracks, followed by a more comprehensive compressional wave-based SAFT imaging of the condition of the embedded rebar.

Zatar et al (Zatar, Nguyen et al. 2020) have performed a lab-based experiment to detect multiple debonding, voids, and honeycombs in concrete slabs with multiple embedded rebars using a commercially available ultrasonic pitch and catch (UPC) device. The reinforcements and different types of damages could be interpreted based on the specific spectrum of the reconstructed SAFT images and the waveform in the vertical direction.

Majhi et al. (Majhi, Mukherjee et al. 2021) have proposed an algorithm to improve the quality of SAFT images obtained from a reduced data set by processing through three-step cascading filters. The images were first processed by the spatial apodization (SA) filter to control the spatial directivity of the received signals. Then, a contrast improvement (CI) filter was employed to enhance the contrast of the embedded objects by modifying the reflection intensity and thus reduced the noises generated by the reflections from the aggregates. At last, a moving average-based reflection localization (RL) filter was used to further improve the location of the rebar. It has been demonstrated experimentally that, compared to the conventional SAFT method, the proposed algorithm produced a much cleaner image with a considerably reduced data set, making it a promising algorithm for imaging heterogeneous materials.

2.6. Research gap

The effect of the casting direction and the elevation of the reinforcement on bond characteristics were identified in the early 1910s, later termed the Top-bar effect and included in the American Concrete Institute (ACI) building code 440 in 1951. The top-bar is the horizontal reinforcement with more than 12 in (305 mm) of the concrete cast below. Interfacial defects form underneath the rebar during casting and lead to poorer bond strength. A factor of safety of 1.3 has been recommended to compensate for the loss of the bond strength in normal vibrated concrete due to the top-bar effect. However, literature reviews have elucidated that the decisive thickness of concrete, 12 in (305 mm), may not work in all cases. Zhang et al. (Zhang, Castel et al. 2011) has reported the observation of interfacial defect at an elevation of 260 mm in normal vibrated concrete, while numerous studies have indicated a less intensive top-bar effect in self consolidated concrete. Interfacial defects are observed at a higher elevation (> 305 mm). Simply relying on the elevation suggested by ACI 400 may lead to underestimating or overestimating the severity of the top-bar effect in reinforced concrete, resulting in a poorer design and unnecessary cost of money. However, the candidate is unaware of any study hitherto on detection of top-bar effect nondestructively.

Corrosion of reinforced concrete leads to deterioration of steel reinforcements, debonding of the steel-concrete interface, and cracking in the concrete body, resulting in a significant reduction of the integrity and safety of the reinforced concrete structures. Studies (Nasser, Clément et al. 2010, Zhang, Castel et al. 2011) have reported a significantly different corrosion pattern of reinforced concrete with interfacial defects owning to the top-bar effect. Significant generalized corrosion has been observed underneath the rebars due to the presence of interfacial void, while mild localized pitting corrosion is randomly distributed around the surface of the bars with a good bond. Earlier corrosion initiation is observed in concrete with top-bar, but the crack initiation is postponed. Therefore, an early diagnosis of corrosion initiation, crack initiation, and continuous monitoring of the corrosion process is critical for maintaining and preventing the failure of reinforced concrete structures with top-bar defects.

Ultrasonic wave-based corrosion monitoring method has been found to be a reliable nondestructive technique for corrosion detection and monitoring in civil infrastructure. Guided waves generated by PZT wafers that are mounted to the surface of the rebars have been extensively employed to evaluate the deterioration of steel reinforcements and the debonding of the steel-concrete interface. PZT wafers are cheap, robust, and small in size, allowing them to be easily installed on the embedded rebar for corrosion monitoring (Su, Ye et al. 2006). In contrast, contact ultrasonic transducers can be employed to evaluate the bar deterioration and debonding using specific wave modes and frequencies. However, all the studies employing the ultrasonic method for concrete corrosion monitoring have been conducted, assuming that the reinforced concrete has a good steel-concrete bond. As it has been revealed that reinforced concrete affected by top-bar defect showing a completely different corrosion pattern. It is critical to developing an ultrasonic wave-based SHM algorithm to monitor the corrosion of reinforced concrete with interfacial defects owning to the top-bar effect. Therefore, two research gaps have been identified with the literature review:

- Development of nondestructive evaluation method for detecting top-bar defects in reinforced concrete. PZT wafers feature small size and robustness against environmental degradation, can be permanently mounted to the surface of the embedded horizontally spaced steel reinforcements. Ultrasonic signals can be continuously sent through the bars before, during, and after concrete casting, providing comprehensive information on how the cement hydration affects the signals propagating in steel bars and identifying top-bar defects. The corrosion process of reinforced concrete with top-bar defects is completely different from that of reinforced concrete with a good bond. It is of particular importance to confirm where there is a top-bar defect or not, as it requires a different algorithm to interpret the ultrasonic results.
- Development of nondestructive structure health monitoring method for monitoring corrosion process of reinforced concrete with top-bar defects. Both PZT wafer-based and contact transducer-based techniques have been developed and extensively applied to monitor the corrosion process of reinforced concrete. However, all these studies are conducted based on the assumption that the reinforced concrete has a good steel-concrete bond. Since the corrosion pattern of the reinforced concrete with top-bar defects is different, its effects on the characteristics of the ultrasonic signal propagating in the bars may be different. It is essential to identify how the corrosion pattern owning to the top-bar effect influences the guided waves and utilize this information to monitor the corrosion of reinforced concrete with top-bar defects. Ultrasonic scanning techniques can also be used to monitor corrosion-induced cracking. By reconstructing images of the cross-section of the reinforced concrete using ultrasonic signals, it can visualize the embedded objects in the cross-section, allowing locating the embedded rebars, detection of crack initiation, quantifying the size of the cracks, and monitoring the propagation of the cracks before corrosion signs are observed on the concrete cover.

2.7. Summary

The literature review briefly summarized a great number of literature and studies related to the corrosion of reinforced concrete, the top-bar effect, and concrete corrosion assessment and monitoring techniques. The states of concrete corrosion and the mechanism of corrosion caused by chloride attack are discussed in detail. The interfacial defect known as the top-bar effect is discussed. Studies on the top-bar effect and its influence on the corrosion of reinforced concrete are summarised and discussed. The literature review enlightened that several techniques, visual inspection and electrochemical techniques, have already been employed in the field to assess the condition of the reinforced concrete and to detect corrosion. However, these methods are not capable of detecting incipient corrosion and quantify the corrosion.

On the other hand, the ultrasonic wave-based technique shows excellent sensitivity to concrete corrosion and has the potential to quantify the corrosion of reinforced concrete. The theory of guided wave propagation in cylindrical bodies, such as rods, is explained in detail. The wave parameters that extensively employed to detect defects in reinforced concrete are explained. The latest experimental studies on guided wave-based monitoring of bar deterioration, debonding at the steel-concrete interface, and the corrosion process of reinforced concrete are presented. SAFT-based ultrasonic imaging technique to detect invisible cracking in concrete is also discussed. The literature review is concluded by presenting the research gaps.

Reference

ACI-Committee-318 (2019). Building code requirements for structural concrete (ACI 318-019) and Commentary on Building Code Requirements for Structural Concrete (ACI 318R-19). Farmington Hills, Mich., Farmington Hills, Mich. : American Concrete Institute.

ACI, A. C. I. (2000). "311.4R-1:Guide for Concrete Inspection." Technical Documents.

ACI, A. C. I. (2001). "222R-01: Protection of Metals in Concrete Against Corrosion." Technical Documents.

Ahmad, S. (2003). "Reinforcement corrosion in concrete structures, its monitoring and service life prediction—a review." Cement and Concrete Composites **25**(4): 459-471.

Amjad, U., S. K. Yadav and T. Kundu (2015). "Detection and quantification of diameter reduction due to corrosion in reinforcing steel bars." Structural Health Monitoring **14**(5): 532-543.

Andrade, C. and C. Alonso (1996). "Corrosion rate monitoring in the laboratory and on-site." Construction and Building Materials **10**(5): 315-328.

Andrade, C. and C. Alonso (2004). "Test methods for on-site corrosion rate measurement of steel reinforcement in concrete by means of the polarization resistance method." Materials and Structures **37**(9): 623-643.

Andrade, C., L. Soler, C. Alonso, X. R. Nóvoa and M. Keddam (1995). "The importance of geometrical considerations in the measurement of steel corrosion in concrete by means of AC impedance." Corrosion Science **37**(12): 2013-2023.

Angst, U., B. Elsener, A. Jamali and B. Adey (2012). "Concrete cover cracking owing to reinforcement corrosion – theoretical considerations and practical experience." Materials and Corrosion **63**(12): 1069-1077.

Angst, U., Ø. Vennesland and R. Myrdal (2009). "Diffusion potentials as source of error in electrochemical measurements in concrete." Materials and Structures **42**(3): 365-375.

Angst, U. M., M. R. Geiker, M. C. Alonso, R. Polder, O. B. Isgor, B. Elsener, H. Wong, A. Michel, K. Hornbostel, C. Gehlen, R. François, M. Sanchez, M. Criado, H. Sørensen, C. Hansson, R. Pillai, S.

Mundra, J. Gulikers, M. Raupach, J. Pacheco and A. Sagüés (2019). "The effect of the steel–concrete interface on chloride-induced corrosion initiation in concrete: a critical review by RILEM TC 262-SCI." Materials and Structures **52**(4): 88.

Arthur, P. C. (1946). "Comparative Bond Efficiency of Deformed Concrete reinforcing Bars." Journal of Research of the National Bureau of Standards **37**(RP 1755): 399-407.

ASTM (2014). G5-14e1: Standard Reference Test Method for Making Potentiodynamic Anodic Polarization Measurements. West Conshohocken, PA, ASTM International.

ASTM (2015). C876-15 Standard Test Method for Corrosion Potentials of Uncoated Reinforcing Steel in Concrete. West Conshohocken, PA, ASTM International.

AS/NZS, Aggregates and rock for engineering purposes Concrete aggregates. 2014, Standards Australia: Australia. p. 25.

Azarsa, P. and R. Gupta (2017). "Electrical Resistivity of Concrete for Durability Evaluation: A Review." Advances in Materials Science and Engineering **2017**: 8453095.

Baolin Wan, M. F. P. K. A. H. and A. H. Aly (2002). "Top Bar Effects in Prestressed Concrete Piles." ACI Structural Journal **99**(2): 208-214.

Beniwal, S. and A. Ganguli (2015). "Defect detection around rebars in concrete using focused ultrasound and reverse time migration." Ultrasonics **62**: 112-125.

Bertolini, L., B. Elsener, P. Pedeferri, E. Redaelli and R. B. Polder (2014). Corrosion of Steel in Concrete : Prevention, Diagnosis, Repair. Weinheim, GERMANY, John Wiley & Sons, Incorporated.

Bertolini, L., W. John, amp and Sons (2013). Corrosion of steel in concrete : prevention, diagnosis, repair / Luca Bertolini ... [et al.]. Weinheim, Weinheim : Wiley-VCH.

Burkan, I., A. Ueli, G. Mette, H. Ceki, H. Carolyn, P. Jose, T. David, T. David and V. Pavan (2019). "Recommended practice for reporting experimental data produced from studies on corrosion of steel in cementitious systems." RILEM Technical Letters **4**(0).

Cai, Y., W. Zhang, C. Yang, R. François, L. Yu, M. Chen, H. Chen and H. Yang (2020). "Evaluating the chloride permeability of steel–concrete interface based on concretes of different stability." Structural Concrete **n/a**(n/a).

Cai, Y., W. Zhang, L. Yu, M. Chen, C. Yang, R. François and K. Yang (2020). "Characteristics of the steel-concrete interface and their effect on the corrosion of steel bars in concrete." Construction and Building Materials **253**: 119162.

Caré, S., Q. T. Nguyen, amp, Amp, Apos, V. Hostis and Y. Berthaud (2008). "Mechanical properties of the rust layer induced by impressed current method in reinforced mortar." Cement and Concrete Research **38**(8): 1079-1091.

Castel, A., T. Vidal, R. François and G. Arliguie (2003). "Influence of steel–concrete interface quality on reinforcement corrosion induced by chlorides." Magazine of Concrete Research **55**(2): 151-159.

Castel, A., T. Vidal, K. Viriyametanont and F. Raoul (2006). "Effect of Reinforcing Bar Orientation and Location on Bond with Self-Consolidating Concrete." ACI Structural Journal **103**(4): 559-567.

CAVALIER, P., P. VASSIE and TRRL (1981). "INVESTIGATION AND REPAIR OF REINFORCEMENT CORROSION IN A BRIDGE DECK." Proceedings of the Institution of Civil Engineers **70**(3): 461-480.

Chan, Y.-W., Y.-S. Chen, Chen and Y.-S. Liu (2003). "Development of Bond Strength of Reinforcement Steel in Self-Consolidating Concrete " ACI structural journal **100**(4): 490-498.

Chao, Z., H. Ming, S. Zhongqing, W. Qiang and C. Li (2013). "Evaluation of fatigue cracks using nonlinearities of acousto-ultrasonic waves acquired by an active sensor network." Smart Materials and Structures **22**(1): 015018.

Choi, H., J. Bittner and J. S. Popovics (2016). "Comparison of Ultrasonic Imaging Techniques for Full-Scale Reinforced Concrete." Transportation Research Record **2592**(1): 126-135.

CivilEngineeringForum. (2017). "CARBONATION AND CORROSION." from https://www.civilengineeringforum.me/carbonation-and-corrosion/.

Daniyal, M. and S. Akhtar (2019). "Corrosion assessment and control techniques for reinforced concrete structures: a review." Journal of Building Pathology and Rehabilitation **5**(1): 1.

Dixit, M. and A. K. Gupta (2021). "A Review of Different Assessment Methods of Corrosion of Steel Reinforcement in Concrete." Iranian Journal of Science and Technology, Transactions of Civil Engineering.

Durham, N., J. Zhao, G. Bridges and D. Thomson (2020). "Acoustic guided wave detection of grounding rod corrosion: equivalent circuit model and implementation." Smart Materials and Structures **29**(5): 055040.

Elsener, B., C. Andrade, J. Gulikers, R. Polder and M. Raupach (2003). "Half-cell potential measurements—Potential mapping on reinforced concrete structures." Materials and Structures **36**(7): 461-471.

Elsener, B. and A. Rossi (2018). Passivation of Steel and Stainless Steel in Alkaline Media Simulating Concrete. Encyclopedia of Interfacial Chemistry. K. Wandelt. Oxford, Elsevier**:** 365-375.

Ervin, B. L., D. A. Kuchma, J. T. Bernhard and H. Reis (2009). "Monitoring Corrosion of Rebar Embedded in Mortar Using High-Frequency Guided Ultrasonic Waves." Journal of Engineering Mechanics **135**(1): 9-19.

Ervin, B. L. and H. Reis (2008). "Longitudinal guided waves for monitoring corrosion in reinforced mortar." Measurement Science and Technology **19**(5): 055702.

Fan, L. and X. Shi (2021). "Techniques of corrosion monitoring of steel rebar in reinforced concrete structures: A review." Structural Health Monitoring **0**(0): 14759217211030911.

Farhidzadeh, A. and S. Salamone (2015). "Reference-free corrosion damage diagnosis in steel strands using guided ultrasonic waves." Ultrasonics **57**: 198-208.

Ghods, P., O. B. Isgor and M. Pour-Ghaz (2007). "A practical method for calculating the corrosion rate of uniformly depassivated reinforcing bars in concrete." Materials and Corrosion **58**(4): 265-272.

Ghosh, D., R. Kumar, A. Ganguli and A. Mukherjee (2020). "Nondestructive Evaluation of Rebar Corrosion Induced Damage in Concrete through Ultrasonic Imaging." Journal of Materials in Civil Engineering **32**(10): 04020294.

Gu, A., Y. Luo and B. Xu (2016). "Continuous condition monitoring of reinforced concrete using an active diagnosis method." Structural Health Monitoring **15**(1): 104-112.

Guyer, R. A. and P. A. Johnson (2009). Nonlinear Elasticity and Nondestructive Evaluation and Imaging. Nonlinear Mesoscopic Elasticity. Weinheim, WILEY-VCH Verlag GmbH & Co. KGaA: 323-367.

Hassan, A. A. A., K. M. A. Hossain and M. Lachemi (2010). "Bond strength of deformed bars in large reinforced concrete members cast with industrial self-consolidating concrete mixture." Construction and Building Materials **24**(4): 520-530.

Hoegh, K. and L. Khazanovich (2015). "Extended synthetic aperture focusing technique for ultrasonic imaging of concrete." NDT & E International **74**: 33-42.

Hong, M., Z. Su, Y. Lu, H. Sohn and X. Qing (2015). "Locating fatigue damage using temporal signal features of nonlinear Lamb waves." Mechanical Systems and Signal Processing **60-61**: 182-197.

Hong, M., Z. Su, Q. Wang, L. Cheng and X. Qing (2014). "Modeling nonlinearities of ultrasonic waves for fatigue damage characterization: Theory, simulation, and experimental validation." Ultrasonics **54**(3): 770-778.

Hope, B. B., A. K. Ip and D. G. Manning (1985). "Corrosion and electrical impedance in concrete." Cement and Concrete Research **15**(3): 525-534.

Hossain, K. M. A. and M. Lachemi (2008). "Bond Behavior of Self-Consolidating Concrete with Mineral and Chemical Admixtures." Journal of Materials in Civil Engineering **20**(9): 608-616.

Hu, N., Y. Cai, G. Zhu, C. Tsuji, Y. Liu, Alamusi and Y. Cao (2012). "Characterization of damage size in metallic plates using Lamb waves." Structural Health Monitoring **11**(2): 125-137.

Hunkeler, F. (1996). "The resistivity of pore water solution—a decisive parameter of rebar corrosion and repair methods." Construction and Building Materials **10**(5): 381-389.

James, A., E. Bazarchi, A. A. Chiniforush, P. Panjebashi Aghdam, M. R. Hosseini, A. Akbarnezhad, I. Martek and F. Ghodoosi (2019). "Rebar corrosion detection, protection, and rehabilitation of reinforced concrete structures in coastal environments: A review." Construction and Building Materials **224**: 1026-1039.

Jeanty, P. R., D. Mitchell and M. S. Mirza (1988). "Investigation of "Top Bar" Effects in Beams." Structural Journal **85**(3).

Jiang, T., Q. Kong, D. Patil, Z. Luo, L. Huo and G. Song (2017). "Detection of Debonding Between Fiber Reinforced Polymer Bar and Concrete Structure Using Piezoceramic Transducers and Wavelet Packet Analysis." IEEE Sensors Journal **17**(7): 1992-1998.

Kenny, A. and A. Katz (2020). "Steel-concrete interface influence on chloride threshold for corrosion – Empirical reinforcement to theory." Construction and Building Materials **244**: 118376.

Krautkrämer, J., H. Seiger, H. Krautkrämer, J. D. Hislop, W. Grabendörfer, R. Frielinghaus, W. Kaule, L. Niklas, U. Opara and U. Schlengermann (1990). Ultrasonic Testing of Materials. Berlin, Heidelberg, GERMANY, Springer Berlin / Heidelberg.

Law, D. W., J. Cairns, S. G. Millard and J. H. Bungey (2004). "Measurement of loss of steel from reinforcing bars in concrete using linear polarisation resistance measurements." NDT & E International **37**(5): 381-388.

Li, D., S. Zhang, W. Yang and W. Zhang (2014). "Corrosion Monitoring and Evaluation of Reinforced Concrete Structures Utilizing the Ultrasonic Guided Wave Technique." International Journal of Distributed Sensor Networks **10**(2): 827130.

Liu, Y. and R. Weyers, E (1998). "Modeling the Time-to-Corrosion Cracking in Chloride Contaminated Reinforced Concrete Structures." Materials Journal **95**(6): 675-680.

López, W. and J. A. González (1993). "Influence of the degree of pore saturation on the resistivity of concrete and the corrosion rate of steel reinforcement." Cement and Concrete Research **23**(2): 368-376.

Lu, Y., J. Li, L. Ye and D. Wang (2013). "Guided waves for damage detection in rebar-reinforced concrete beams." Construction and Building Materials **47**: 370-378.

Majhi, S., A. Mukherjee and A. Ganguli (2021). "Enhanced Ultrasonic Imaging in Concrete Structures with Spatial Apodization Filters." Journal of Materials in Civil Engineering **33**(10): 04021266.

Majhi, S., A. Mukherjee, N. V. George and B. Uy (2019). "Corrosion detection in steel bar: A time-frequency approach." NDT & E International **107**: 102150.

Millard, S. G., D. Law, J. H. Bungey and J. Cairns (2001). "Environmental influences on linear polarisation corrosion rate measurement in reinforced concrete." NDT & E International **34**(6): 409-417.

Miller, T. H., T. Kundu, J. Huang and J. Y. Grill (2013). "A new guided wave–based technique for corrosion monitoring in reinforced concrete." Structural Health Monitoring **12**(1): 35-47.

Mohammed, T. U. and H. Hamada (2006). "Corrosion of Horizontal Bars in Concrete and Method to Delay Early Corrosion." ACI Materials Journal **103**(5).

Mohammed, T. U., N. Otsuki, H. Hamada and T. Yamaji (2002). "Chloride-Induced Corrosion of Steel Bars in Concrete with Presence of Gap at Steel-Concrete Interface." ACI Materials Journal **99**(2).

Mohammed, T. U., N. Otsuki and M. Hisada (1999). "Corrosion of Steel Bars with Respect to Orientation in Concrete." ACI Materials Journal **96**(2): 154-159.

Moore, M., B. M. Phares, B. Graybeal, D. Rolander and G. Washer (2001). "Reliability of Visual Inspection for Highway Bridges, Volume I: Final Report."

Morris, W., A. Vico, M. Vazquez and S. R. de Sanchez (2002). "Corrosion of reinforcing steel evaluated by means of concrete resistivity measurements." Corrosion Science **44**(1): 81-99.

Na, W. B., T. Kundu and M. R. Ehsani (2003). "Lamb Waves for Detecting Delamination between Steel Bars and Concrete." Computer-Aided Civil and Infrastructure Engineering **18**(1): 58-63.

Nasser, A., A. Clément, S. Laurens and A. Castel (2010). "Influence of steel–concrete interface condition on galvanic corrosion currents in carbonated concrete." Corrosion Science **52**(9): 2878-2890.

Pochhammer, L. (1876). "Ueber die Fortpflanzungsgeschwindigkeiten kleiner Schwingungen in einem unbegrenzten isotropen Kreiscylinder." **1876**(81): 324-336.

Pour-Ghaz, M., O. B. Isgor and P. Ghods (2009). "Quantitative Interpretation of Half-Cell Potential Measurements in Concrete Structures." Journal of Materials in Civil Engineering **21**(9): 467-475.

Presuel-Moreno, F., Y. Y. Wu and Y. Liu (2013). "Effect of curing regime on concrete resistivity and aging factor over time." Construction and Building Materials **48**: 874-882.

Ren, B. and C. J. Lissenden (2013). "Ultrasonic guided wave inspection of adhesive bonds between composite laminates." International Journal of Adhesion and Adhesives **45**: 59-68.

Rengaraju, S., L. Neelakantan and R. G. Pillai (2019). "Investigation on the polarization resistance of steel embedded in highly resistive cementitious systems – An attempt and challenges." Electrochimica Acta **308**: 131-141.

Reza Esfahani, M., M. Lachemi and M. Reza Kianoush (2008). "Top-bar effect of steel bars in self-consolidating concrete (SCC)." Cement and Concrete Composites **30**(1): 52-60.

Richardson, J. M. (1979). "Harmonic generation at an unbonded interface—I. Planar interface between semi-infinite elastic media." International Journal of Engineering Science **17**(1): 73-85.

Rodrigues, R., S. Gaboreau, J. Gance, I. Ignatiadis and S. Betelu (2021). "Reinforced concrete structures: A review of corrosion mechanisms and advances in electrical methods for corrosion monitoring." Construction and Building Materials **269**: 121240.

Šavija, B. and M. Luković (2016). "Carbonation of cement paste: Understanding, challenges, and opportunities." Construction and Building Materials **117**: 285-301.

Schickert, M. (2005). "Progress in ultrasonic imaging of concrete." Materials and Structures **38**(9): 807-815.

Schickert, M., M. Krause and W. Müller (2003). "Ultrasonic Imaging of Concrete Elements Using Reconstruction by Synthetic Aperture Focusing Technique." Journal of Materials in Civil Engineering **15**(3): 235-246.

Sharma, A., S. Sharma, S. Sharma and A. Mukherjee (2018). "Investigation of deterioration in corroding reinforced concrete beams using active and passive techniques." Construction and Building Materials **161**: 555-569.

Sharma, A., S. Sharma, S. Sharma and A. Mukherjee (2018). "Monitoring invisible corrosion in concrete using a combination of wave propagation techniques." Cement and Concrete Composites **90**: 89-99.

Sharma, S. and A. Mukherjee (2010). "Longitudinal guided waves for monitoring chloride corrosion in reinforcing bars in concrete." Structural Health Monitoring **9**(6): 555-567.

Sharma, S. and A. Mukherjee (2011). "Monitoring Corrosion in Oxide and Chloride Environments Using Ultrasonic Guided Waves." Journal of Materials in Civil Engineering **23**(2): 207-211.

Sharma, S. and A. Mukherjee (2013). "Nondestructive Evaluation of Corrosion in Varying Environments Using Guided Waves." Research in Nondestructive Evaluation **24**(2): 63-88.

Shi, J. and J. Ming (2017). "Influence of defects at the steel-mortar interface on the corrosion behavior of steel." Construction and Building Materials **136**: 118-125.

Shokouhi, P., J. Wolf and H. Wiggenhauser (2014). "Detection of Delamination in Concrete Bridge Decks by Joint Amplitude and Phase Analysis of Ultrasonic Array Measurements." Journal of Bridge Engineering **19**(3): 04013005.

Smith, K. M., A. J. Schokker and P. J. Tikalsky (2004). "Performance of Supplementary Cementitious Materials in Concrete Resistivity and Corrosion Monitoring Evaluations." ACI Materials Journal **101**(5): 6.

Soylev, T. A. and R. François (2003). "Quality of steel–concrete interface and corrosion of reinforcing steel." Cement and Concrete Research **33**(9): 1407-1415.

Söylev, T. A. and R. François (2005). "Corrosion of Reinforcement in Relation to Presence of Defects at the Interface between Steel and Concrete." Journal of Materials in Civil Engineering **17**(4): 447-455.

Söylev, T. A. and R. François (2006). "Effects of Bar-Placement Conditions on Steel-Concrete Bond." Materials and Structures **39**(2): 211-220.

Spies, M., H. Rieder, A. Dillhöfer, V. Schmitz and W. Müller (2012). "Synthetic Aperture Focusing and Time-of-Flight Diffraction Ultrasonic Imaging—Past and Present." Journal of Nondestructive Evaluation **31**(4): 310-323.

Sriramadasu, R. C., S. Banerjee and Y. Lu (2019). "Detection and assessment of pitting corrosion in rebars using scattering of ultrasonic guided waves." NDT & E International **101**: 53-61.

Sriramadasu, R. C., S. Banerjee and Y. Lu (2020). "Sensitivity of longitudinal guided wave modes to pitting corrosion of rebars embedded in reinforced concrete." Construction and Building Materials **239**: 117855.

Sriramadasu, R. C., Y. Lu and S. Banerjee (2019). "Identification of incipient pitting corrosion in reinforced concrete structures using guided waves and piezoelectric wafer transducers." Structural Health Monitoring **18**(1): 164-171.

Stern, M. and A. L. Geaby (1957). "Electrochemical Polarization: I . A Theoretical Analysis of the Shape of Polarization Curves." Journal of The Electrochemical Society **104**(1): 56.

Su, Z., C. Zhou, M. Hong, L. Cheng, Q. Wang and X. Qing (2014). "Acousto-ultrasonics-based fatigue damage characterization: Linear versus nonlinear signal features." Mechanical Systems and Signal Processing **45**(1): 225-239.

Sun, H. and J. Zhu (2020). "Nondestructive evaluation of steel-concrete composite structure using high-frequency ultrasonic guided wave." Ultrasonics **103**: 106096.

Talakokula, V. and S. Bhalla (2015). "Reinforcement corrosion assessment capability of surface bonded and embedded piezo sensors for reinforced concrete structures." Journal of Intelligent Material Systems and Structures **26**(17): 2304-2313.

Trezos, K. G., I. P. Sfikas and C. G. Pasios (2014). "Influence of water-to-binder ratio on top-bar effect and on bond variation across length in Self-Compacting Concrete specimens." Cement and Concrete Composites **48**: 127-139.

Tseng, C.-W., Y.-F. Chang and C.-Y. Wang (2018). "Total Focusing Method or Phased Array Technique: Which Detection Technique Is Better for the Ultrasonic Nondestructive Testing of Concrete?" Journal of Materials in Civil Engineering **30**(1): 04017256.

Tuutti, K. (1982). Corrosion of steel in concrete. Ph.D, Lund University.

Valcuende, M. and C. Parra (2009). "Bond behaviour of reinforcement in self-compacting concretes." Construction and Building Materials **23**(1): 162-170.

Verma, S. K., S. S. Bhadauria and S. Akhtar (2014). "Monitoring Corrosion of Steel Bars in Reinforced Concrete Structures." The Scientific World Journal **2014**: 957904.

Wang, Y., R. Guan and Y. Lu (2017). "Nonlinear Lamb waves for fatigue damage identification in FRP-reinforced steel plates." Ultrasonics **80**: 87-95.

Wang, Y., X. Zhu, H. Hao and J. Ou (2009). "Guided wave propagation and spectral element method for debonding damage assessment in RC structures." Journal of Sound and Vibration **324**(3): 751-772.

Warkus, J. and M. Raupach (2010). "Modelling of reinforcement corrosion – geometrical effects on macrocell corrosion." Materials and Corrosion **61**(6): 494-504.

Wong, H. S., Y. X. Zhao, A. R. Karimi, N. R. Buenfeld and W. L. Jin (2010). "On the penetration of corrosion products from reinforcing steel into concrete due to chloride-induced corrosion." Corrosion Science **52**(7): 2469-2480.

Wu, F., H.-L. Chan and F.-K. Chang (2015). "Ultrasonic guided wave active sensing for monitoring of split failures in reinforced concrete." Structural Health Monitoring **14**(5): 439-448.

Wu, F. and F.-K. Chang (2006). "Debond Detection using Embedded Piezoelectric Elements for Reinforced Concrete Structures - Part II: Analysis and Algorithm." Structural Health Monitoring **5**(1): 17-28.

Wu, F. and F.-K. Chang (2006). "Debond Detection using Embedded Piezoelectric Elements in Reinforced Concrete Structures - Part I: Experiment." Structural Health Monitoring **5**(1): 5-15.

Yodsudjai, W. and T. Pattarakittam (2017). "Factors influencing half-cell potential measurement and its relationship with corrosion level." Measurement **104**: 159-168.

Zatar, W. A., H. D. Nguyen and H. M. Nghiem (2020). "Ultrasonic pitch and catch technique for non-destructive testing of reinforced concrete slabs." Journal of Infrastructure Preservation and Resilience **1**(1): 12.

Zhang, R., A. Castel and R. François (2009). "The corrosion pattern of reinforcement and its influence on serviceability of reinforced concrete members in chloride environment." Cement and Concrete Research **39**(11): 1077-1086.

Zhang, R., A. Castel and R. François (2011). "Influence of steel-concrete interface defects owing to the top-bar effect on the chloride-induced corrosion of reinforcement." Magazine of Concrete Research **63**(10): 773-781.

Zhang, W., R. François, Y. Cai, J.-P. Charron and L. Yu (2020). "Influence of artificial cracks and interfacial defects on the corrosion behavior of steel in concrete during corrosion initiation under a chloride environment." Construction and Building Materials **253**: 119165.

Zhao, J., N. Durham, K. Abdel-Hadi, C. A. McKenzie and D. J. Thomson (2019). "Acoustic guided wave techniques for detecting corrosion damage of electrical grounding rods." Measurement **147**: 106858.

Zhao, Y., H. Ding and W. Jin (2014). "Development of the corrosion-filled paste and corrosion layer at the steel/concrete interface." Corrosion Science **87**: 199-210.

Zhao, Y. and W. Jin (2016). Steel Corrosion-Induced Concrete Cracking, Elsevier.

Zima, B. and R. Kędra (2019). "Reference-free determination of debonding length in reinforced concrete beams using guided wave propagation." Construction and Building Materials **207**: 291-303.

Zima, B. and M. Rucka (2018). "Guided ultrasonic waves for detection of debonding in bars partially embedded in grout." Construction and Building Materials **168**: 124-142.

Chapter 3

3. Methodology

3.1. Introduction

The methodology for ultrasonic wave-based structural health monitoring (SHM) is presented in this chapter. Firstly, the specimen configuration and the material properties of the samples are summarised, followed by the discussion of the setup of accelerated corrosion. In the real-life, it may take years or even decades for corrosion to initiate on the rebars. To accelerate the corrosion process in the lab, the anodic current is employed. By controlling the amplitude of the current, the mass loss of the rebar can be predicted by Faraday's law. The details of the setup of the corrosion monitoring systems are presented. The setup is only used to monitor the corrosion of the designed specimens, which is simulating a small part of a concrete beam.Four techniques, PZT wafer-based ultrasonic technique, contact transducer-based ultrasonic technique, half-cell potential, and linear polarisation resistance, are employed, and the applications are discussed. The selection of the wave mode, waveform, and excitation frequency is discussed. The dispersion curves generated using DISPERSE® software are presented. Damage indices and a transmission index are proposed to detect the top-bar effect and monitor the corrosion process. The algorism of the damage imaging technique using Synthetic Aperture Focusing Technique (SAFT) is presented.

3.2. Preparation of specimens

Mild steel bars provided by Midalia Steel, Perth, AU are used in this study. Both round and ribbed bars are employed, and the diameters of the bars are 12 mm and 24 mm. The bars are tested to get the material properties using Shimazu 250kN UTM in Civil Engineering Laboratory in Curtin university. The average yield stress and ultimate strength is 343MPa and 505 MPa for 12 mm round bar and 537 MPa and 644 MPa for 12 mm ribbed bar. The bars are processed to a required length in the Civil Engineering workshop at Curtin University. The ends of the bars are machined to have a plain surface to ensure the proper contact for the contact transducers (CT) for longitudinal wave excitation. For 12 mm bars, the ends are further processed using sandpapers to increase the contact area for permanently mounting the PWTs using super glue.

The standard composition of concrete is given in Table. 3-1, was used. Reinforced concrete specimens of various sizes are cast with a proportion of cement, fine and coarse aggregates as 1:1.37:2.77. The water-cement ratio is kept at 0.45. The average slump was found to be 54 ± 2 mm. All specimens are cast vertically, aiming to create the top-bar effect naturally. The fresh concrete was equally divided into four portions and added into the mould one by one. The mould was vibrated on a vibration table after each portion of fresh concrete was added. The moulds are removed once the specimens are hardened, and the specimens are wrapped with moisture-retaining fabrics for water curing. Water is sprayed daily to maintain the moisture of the fabrics for 28 days.

Table. 3-1 Concrete mix design

Mix Component (kg/m3)	
Coarse aggregate (10mm basalt)	1190.50
Fine aggregate (sand)	590.30
OPC (GP cement)	430
Water/binder ratio	0.45
Free water	193.5
Total	2404.3

Four types of RC specimens, namely simulated top-bar (S1), Natural top-bar type 1 (N1), natural top-bar type 2 (N2) and cast-in reinforcement (C1), are used in this study to suit different purposes. The dimensions of specimen N1 are 800 mm × 100 mm × 300 mm as shown in Fig. 3-1. The specimen contains 4 400 mm long round steel bars of diameter 12 mm located at 100 mm, 300 mm, 500 mm, and 700 mm from the bottom of the specimen. The specimen is later sawed to a smaller dimension of 200 mm × 100 mm × 300 mm to conduct corrosion experiments.

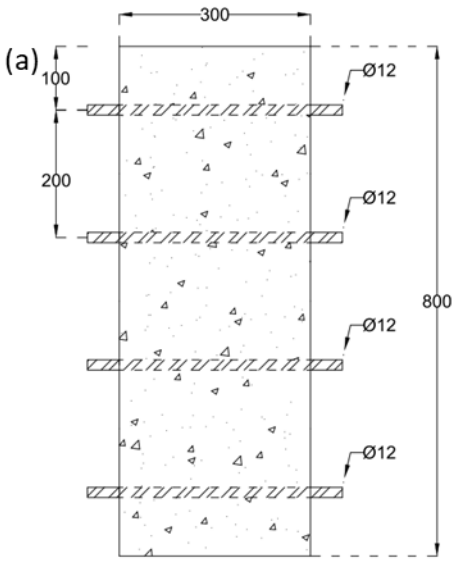

Fig. 3-1 schematic drawing of Natural Top-bar specimen 1 (a) Side view and (b) Front view; all dimensions are in mm.

The dimensions of specimen N2 are 600 mm × 200 mm × 400 mm as shown in Fig. 3-2. The relatively large surface area (200 mm × 400 mm) provides enough area for ultrasonic scanning. Two types of bar are used in this specimen, 12 mm ribbed bars with surface-mounted PWTs and 24 mm plain bars with CT.

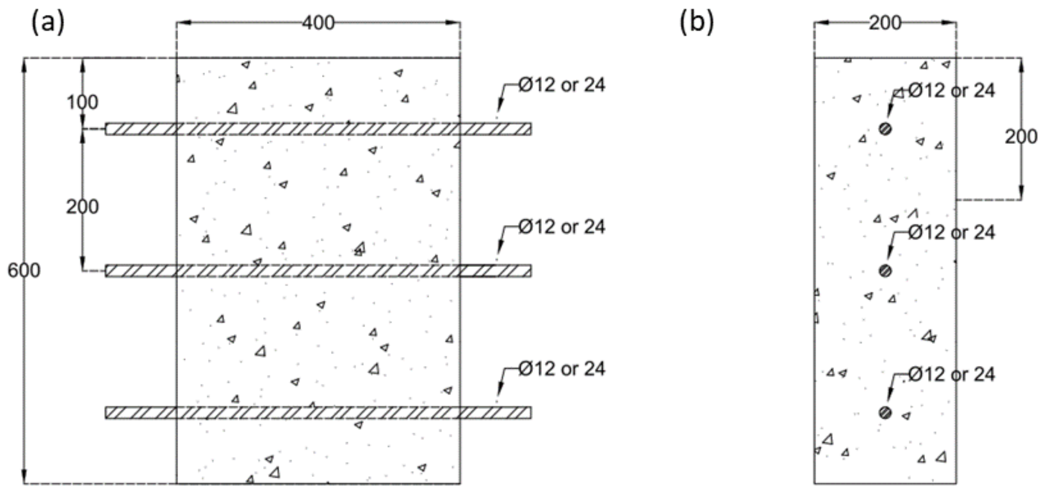

Fig. 3-2 schematic drawings of Natural Top-bar specimen 2 (a) Side view and (b) Front view; all dimensions are in mm.

The dimensions of specimen S1 are 200 mm × 200 mm × 400 mm as shown in Fig. 3-3. The specimen contains 5 bars (round or deformed). To simulate debonding owning to top-bar effect, double-sided tape is attached to the surface of the bottom part of bars, and the top part of the bars remains intact. Fig. 3-3 (c) shows the 12 mm ribbed bars subjected to simulated top-bar effect. The debonding area is 0%, 15%, 30%, 45%, and 60% of the bottom part of the embedded bars. All 5 bars are cast in the same mould. In this case, the material properties of the concrete around different bars are assumed to be identical, hence minimizing the effect of the variation of the properties of the surrounding concrete on ultrasonic wave transmission.

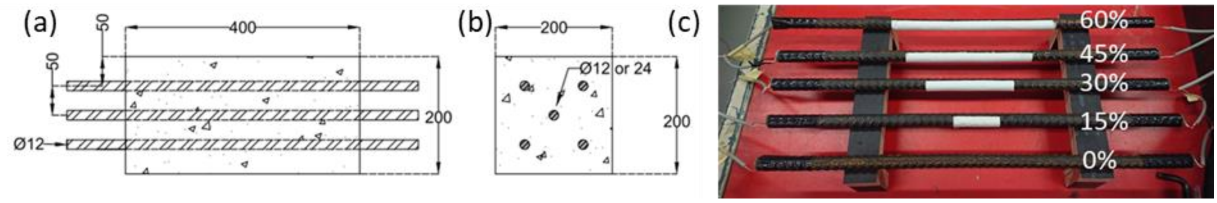

Fig. 3-3 schematic drawings of simulated Top-bar specimen (a) Side view, (b) Front view, and (c) 12 mm ribbed bars with simulated top-bar using double-sided tape

Since specimen C1 contains cast-in bars with attached PZT wafers and the bars are about 100 mm long, there is not specific size for the concrete part as long as it is big enough to contain the bars. the mould for specimen S1 is used to cast most of the specimen C1. In order to perform penetration resistance test using a spring type penetrometer, Specimen C1 is casted in a 9L rectangular plastic basin with a dimension of 340 X 270 X 130 mm. The area of the concrete surface is large enough to perform the resistance test. 100 mm thick mortar is casted around it to provide support to the sides of the basin to resist the expansion of fresh mortar/concrete during penetration resistance test. The bars are casted at the centre of the specimen. The PZT wafers that mounted to the ends of the bars are connected to long cables. The cables are exposed to air allowing connection with the ultrasonic instruments.

3.3. Experiment setup

3.3.1. Setup of accelerated corrosion

3.3.1.1. Bare bars

In natural environments, the corrosion process of reinforced concrete takes several years to occur. In this study, a controlled anodic current technique is employed to accelerate the corrosion process. The 3.5% Sodium Chloride (NaCl) solution was used as the electrolyte to simulate the senility of the coastal environment. The setup of accelerated corrosion of bare bars is shown in Fig. 3-4. A constant current is applied using the DC power supply. The steel bars are used as the anode connected to the positive terminal of the power supply. While the negative terminal is connected to a Zinc screw that merged in the 3.5% NaCl solution, acting as the cathode. The steel bars are inserted into the plastic boxes through circular holes. The gap between the bar and the hole is sealed with removable adhesive (Bostik Blu Tack). All the bars are exposed to accelerated corrosion for 20 hours per day until they reach desired mass loss. The bars are removed from the boxes daily to visually inspect the corrosion, take ultrasonic readings, and measure the mass loss. The corrosion product, $Fe(OH)_3$, is formed at the anode (steel bar) and dissolved in the 3.5% NaCl solution. The mass loss of the anode can be calculated using Faraday's second law of electrolysis given by Equation *3-1*

Mass loss in gram: $\boldsymbol{m} = \frac{\boldsymbol{Mit}}{\boldsymbol{ZF}}$ 3-1

Where M is the molar mass which is 55.845 g/mol for iron. i is the current in Ampere. t is the total time the current was applied in seconds. Z is the number of electrons involved in the reaction, which is 2 for iron. F is Faraday's constant, which is 96,485 Ampere/second.

In Fig. 3-4 (a), the bars are fully merged in the 3.5% NaCl solution. General corrosion is expected, and the reactions occur uniformly over the entire surface of the merged bars. In Fig. 3-4 (b), only the bottom half of the bar is merged in the 3.5% NaCl solution, and the top half is protected by a nonconductive tape. Hence the reactions can only occur on the surface of the bottom half of the bar. This is to simulate the corrosion of the specimen subjected to the top-bar effect.

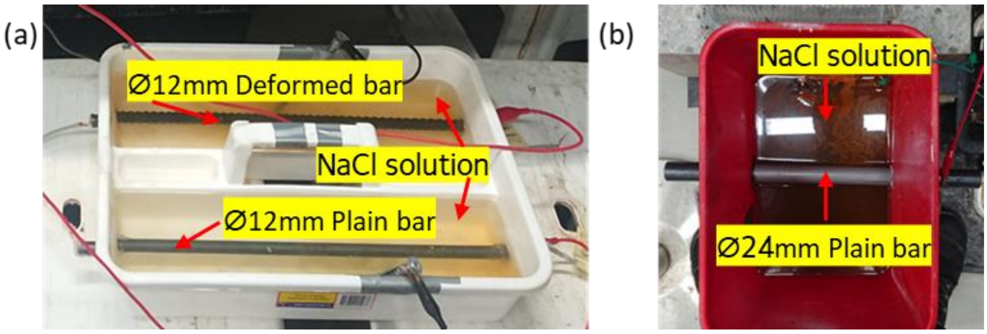

Fig. 3-4 setup of accelerated corrosion for steel bars (a) fully merged in 3.5% NaCl solution and (b) half merged in solution

3.3.1.2. Embedded bars

Two methods are used in this study to create the chloride environment for the rebar in concrete to corroded, namely wet-wrap and pond, as shown in Fig. 3-5. For wet-wrapped specimens, they are first immersed in 3.5% NaCl solution for 48 hours to ensure full saturation of the specimen. One cotton sheet is wrapped around the center part of the specimen, and steel-wire mesh is wrapped around the cotton sheet, as shown in Fig. 3-5 (a). A container is placed at the top of the specimen. The 3.5% NaCl solution keeps dripping on the specimen to keep the specimen saturated and continuously provides Cl^- ions for the reactions. The bar acts as the anode, and the steel-wire mesh is the cathode. The current flows from the embedded bar towards the surrounding concrete surfaces, as shown in Fig. 3-5 (c). A constant voltage DC power supply is used to impress electrical current through the specimen. The imposed voltage varies with the size of the specimens. 5 V voltage is used to corrode small specimens such as specimen type N1, and 10 V is used for specimen Type N2. The impressed current is around 0.04 A for all specimens. The estimated mass loss is 0.04 g/hour according to Equation *3-1*. This allows enough time to capture the entire duration corrosion process using monitoring techniques. Fig. 3-5 (b) shows the setup of corrosion using ponding. A timber frame is mounted on the top surface of the specimen using silicone sealant. The pond is filled with 3.5% NaCl solution. The solution leaks into the specimen and reaches the embedded bar through the pores. The specimen is kept for 48 hours to ensure saturation of NaCl solution within it before imposing an anodic current. The embedded bar is used as the anode. A Zinc screw is merged in the NaCl solution and connected to the negative terminal of the power supply, hence acting as the cathode. In this case, the current flows from the embedded bar to the top surface of the specimen as shown in Fig. 3-5 (d). The concrete cover of the ponded specimens is larger than that of the wrapped ones. Hence the resistance of the ponded specimens is significant. Hence, a constant 15V DC regulated power supplier was employed to impress electrical current through the specimen. The current is around 0.04-0.05 A. The estimated mass loss is 0.04-0.05 g/hours. The relatively slow mass loss allows enough time to capture information about the corrosion process.

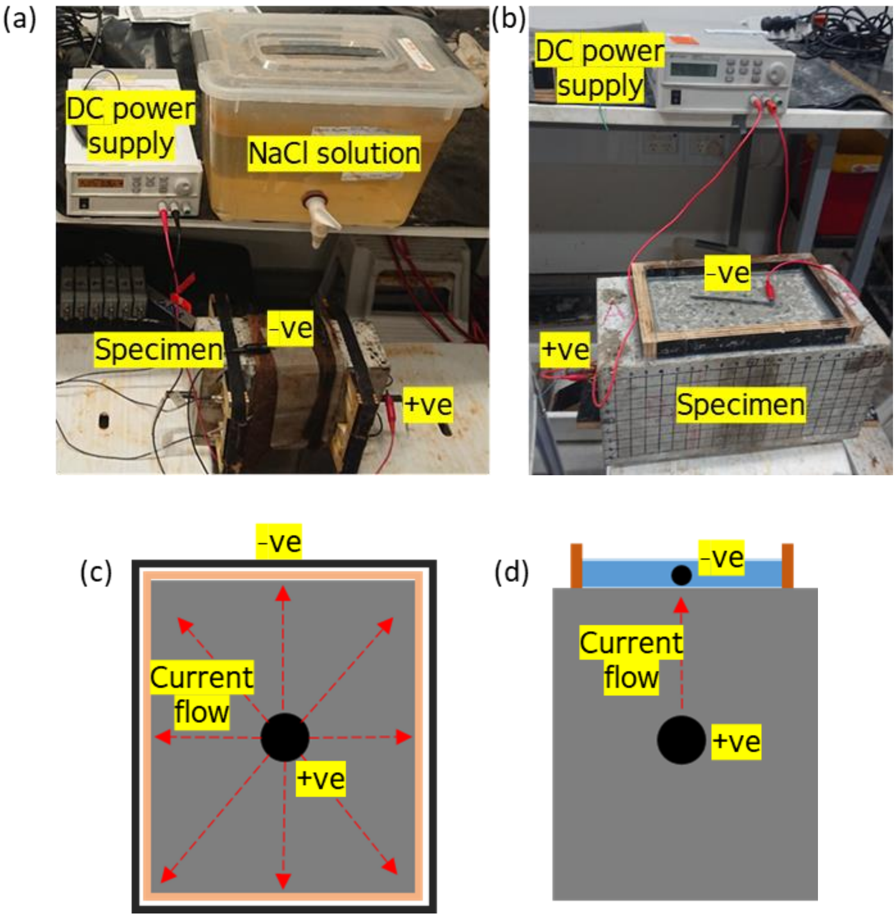

Fig. 3-5 Corrosion set-up for reinforced concrete using (a) wet-wrap and (b) pond; Current flow in reinforced concrete using (c) wet-wrap and (d) pond.

3.3.2. Corrosion Monitoring Set-up

Several concrete corrosion monitoring techniques have been developed in the past decades. In this study, ultrasonic and electrochemical techniques, as shown in Fig. 3-6, are employed to monitor the corrosion process of the specimens.

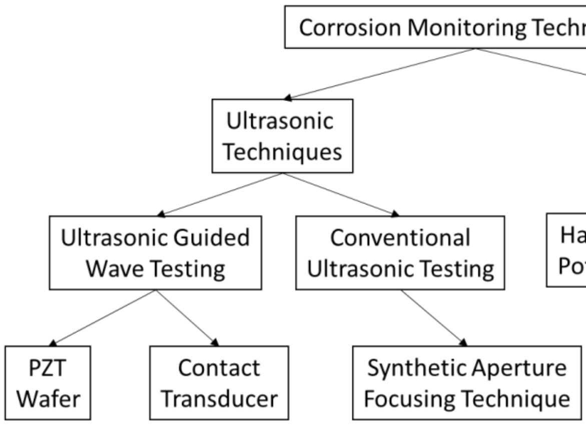

Fig. 3-6 Corrosion monitoring techniques

3.3.2.1. PZT wafer-based ultrasonic testing system

The PZT wafer-based ultrasonic testing system consists of a signal generator (RIGOL DG1032Z), a High Voltage Power Amplifier (Cyprian HVA-400-A), PZT discs (PI PRYY+0220), oscilloscope (PicoScope2204A and 2206B), and a computer as shown in Fig. 3-7. RIGOL DG1032Z arbitrary waveform generator allows user-defined waveform. It features a maximum voltage output of 10 V peak-to-peak, a sample rate of 200 MSa/s, and maximum frequency output of 30 MHz to achieve a good resolution and precision of output signals. In this study, Hanning-windowed sinusoidal tone burst waveforms of various numbers of cycles are used as the excitation signals. The details of the waveforms are discussed in section 3.4.1. The waveforms are first created in Ultra Station, and then transferred to and stored in the signal generator. Cyprian HVA-400-A high-voltage amplifier can deliver excitation signals at both high voltage and high frequency with a maximum output voltage of 400 V_{pp} and maximum output current of $2A_{RMS}$. The voltage gain of the amplifier is fixed at 200 times. Therefore the output voltage is controlled by the output voltage of the signal generator, e.g., 1 V_{pp} output voltage from the signal generator gives a 200 V_{pp} output voltage from the amplifier. The PI

PYRR+0220 PZT wafers are used as both signal transmitter and receiver. The light radial wafer has a diameter of 10 mm and a thickness of 0.5 mm, allowing easy attaching to the limited area without influencing the structural integrity. The resonance frequency of these wafers is found to be around 250 kHz. The wafer features a broad range of extraction frequencies, from Hz to MHz. in this study, the frequency range is from 100 kHz to 1 MHz. The PICOSCOPE 2204A oscilloscope features a bandwidth of 10 MHZ and a maximum sampling rate of 100 MS/s. It has two BNC channels, one is used as the reference, and the other is used to receive signals. The oscilloscope is later upgraded to PICOSCOPE 2206B, with a bandwidth of 50 MHZ and a maximum sampling rate of 500 MS/s, allowing more data points for the same window length.

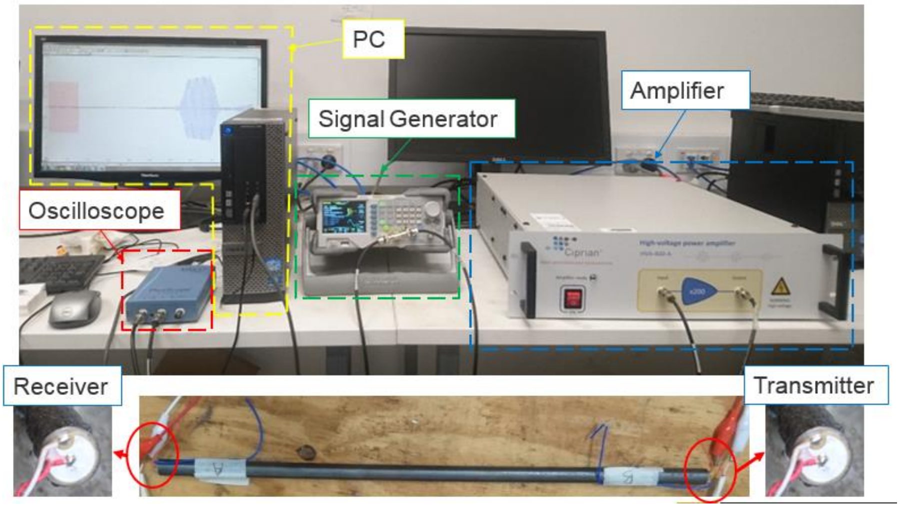

Fig. 3-7 Instruments and experiment setup： PZT wafer-based ultrasonic guided wave.

Fig. 3-8 shows the schematic diagram of the operation of the PZT wafer-based ultrasonic guided wave testing system. The signal is first generated in the signal generator. The signal is transferred to the oscilloscope as the reference signal and the signal amplifier using BNC-to-BNC cables. The signal is amplified 200 times in the signal amplifier and transferred to the signal transmitter using a BNC-to-Clip cable. The electrical signal is converted to a mechanical signal (vibration) by the PZT wafer and transmit through the waveguide. The PZT wafer at the other end of the waveguide receives the vibration and converts it to an electrical signal captured by the oscilloscope and transferred to a PC for data analysis.

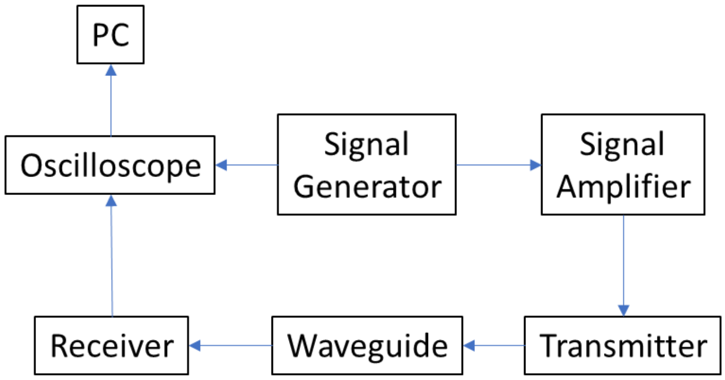

Fig. 3-8 Schematic diagrams of the operation of PZT wafer-based ultrasonic system.

3.3.2.2. CT based ultrasonic testing system

The CT-based ultrasonic testing system consists of a signal pulser/receiver (JSR DPR300 Pulser/Receiver), oscilloscope (PICOSCOPE 2204A), a laptop, and contact transducers, as shown in Fig. 3-9. The JSR DPR300 Pulser/Receiver is an all-in-one instrument that consists of a signal pulser, a signal receiver, frequency filters, and a receiver amplifier. It features a bandwidth of 50 MHz, a build-in adjustable pulse amplitude up to 475 V with a low receiver noise of 49 mV_{pp}, and a maximum receiver gain of 66 dB. The frequency of the signal is controlled by the operating frequency of contact transducers and the build-in low pass and high pass filter. The instrument is controlled by Windows-based software, JSR Control Panel, as shown in Fig. 3-10.

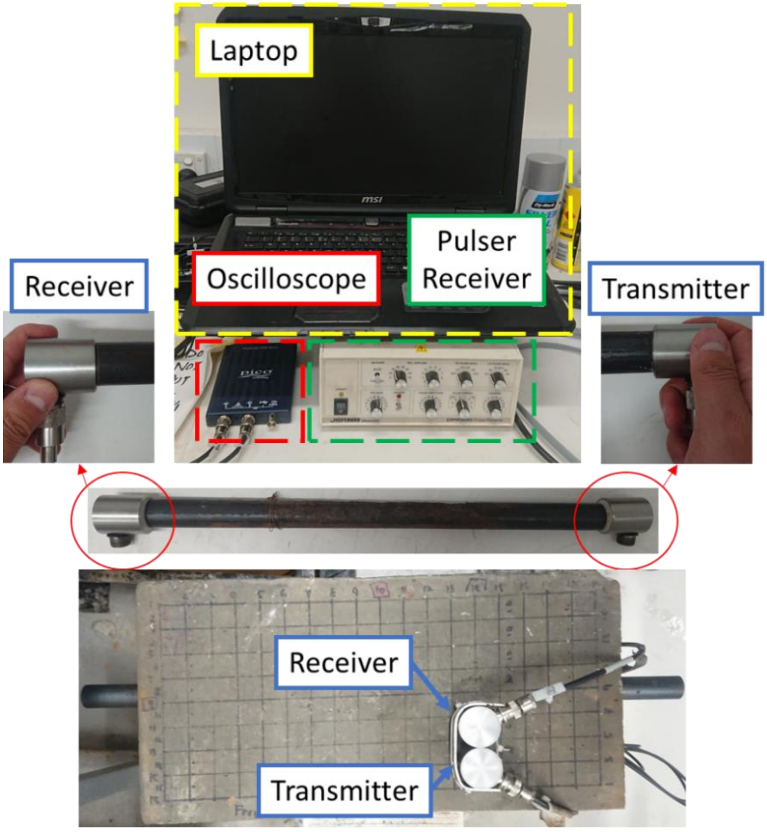

Fig. 3-9 Instruments and experiment setup： CT based ultrasonic guided wave testing.

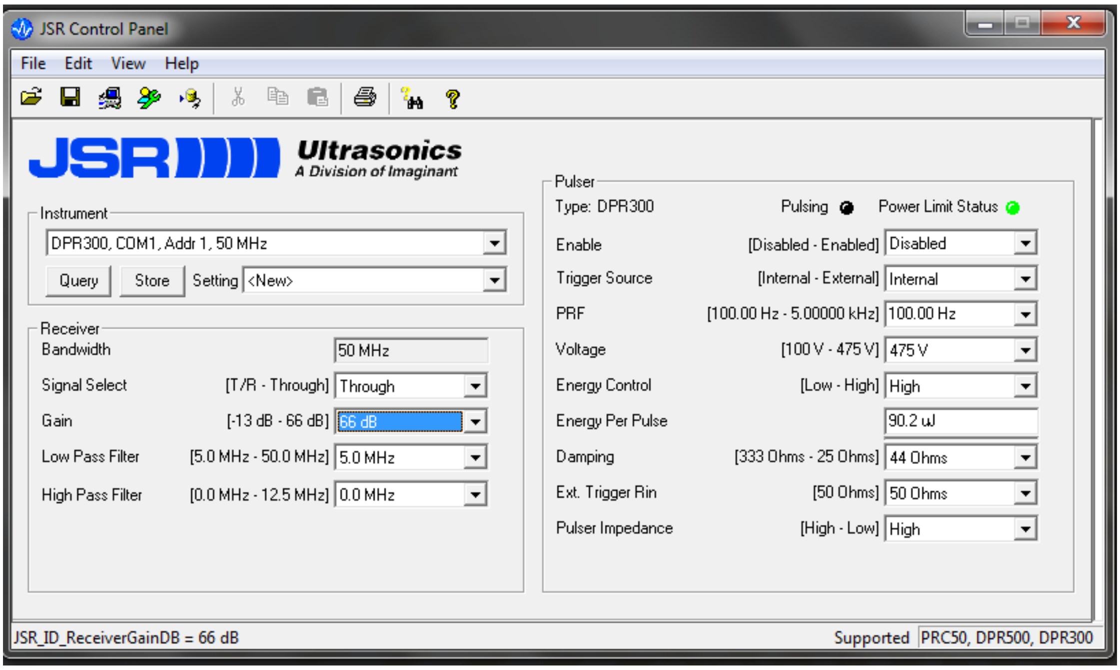

Fig. 3-10 JSR Control Panel

Fig. 3-11 shows the schematic diagram of the operation of the CT-based ultrasonic system. The signal is first generated in the JSR pulser/receiver and then sent to the transmitter using a BNC-TO-BNC cable.

The contact surface is covered with grease to allow better contact between the transducers and the specimen. For guided waves, the signal transfers from the transmitter on one end of the bar to the receiver on the other end. The coupling issue of transducers can significantly influence the received signal. To minimize the effect of the coupling issue, the signal readings are repeated three times, and the strongest signal is used as the final reading. For concrete in-depth scanning, the transmitter and the receiver are tied together. The center-to-center spacing of the transducers is 30 mm. The transducer and the receiver move together along the scanning direction. The applied pressure on the transducers does affect the amplitude of the applied signal and received signal. This may lead to misestimation if applied pressure on transducers varies at different scanning points or at the same location over different times. To counter this issue, one 1 kg steel block is placed on top of the transducers to ensure a constant pressure. All the received signals are first transferred back to JSR pulser/receiver. The received signal undergoes low pass and high pass filters and gets amplified before sending to the oscilloscope. All the data are transferred and stored on a PC for analysis.

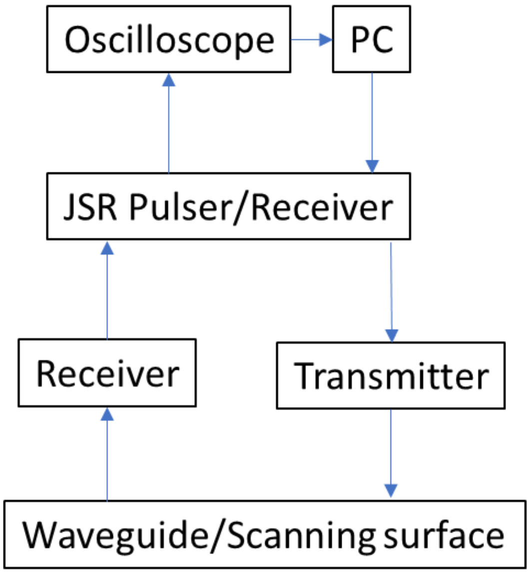

Fig. 3-11 Schematic diagrams of the operation of CT-based ultrasonic system.

4 different types of contact transducers are used in this study as shown in Fig. 3-12. The transducers are, from left to right in Fig. 3-12, ULTRAN GC100-D25-10, Olympus V318 0.5MHZ/.75'', Olympus V303 1.0MHZ/0.5'', and ULTRAN GC200-D25. ULTRAN GC100-D25-10 transducers have a central frequency

of 100 kHz and an active diameter of 25 mm. ULTRAN GC200-D25 transducers have a central frequency of 200 kHz and an active diameter of 25 mm. Olympus V318 0.5MHZ/.75'' transducers have a central frequency of 500 kHz and an active diameter of 0.75 inches (19.05 mm). Olympus V303 1.0MHZ/0.5'' transducers have a central frequency of 1 MHz and an active diameter of 0.5 inches (12.7 mm).

Fig. 3-12 Contact transducers of various frequencies

3.3.2.3. Linear Polarisation Resistance (LPR)

A standard three-electrode electrochemical cell setup is used to perform the linear polarisation resistance measurement, as shown in Fig. 3-13. The three electrodes are the working electrode, the counter electrode, and the reference electrode. The measurements are conducted using EZstat Pro potentiostat. It can control the potential across the reference electrode and the working electrode by sending current from the counter electrode to the working electrode. The steel bar is used as the working electrode, while a stainless-steel plate is used as the counter electrode as stainless steel is stable in acid for the measurement duration. The reactions occurring at the counter electrode do not influence the reactions occurring at the working electrode during electroanalytical experiments. A portable Copper-Copper Sulfate (Ag/AgCl) Reference Electrodes (Tinker & Rasor Model-6-B) is used as the reference electrode. Ag/AgCl solutions are changed every three months to maintain the concentration of Ag elements for reactions.

As anodic current is employed to induce the corrosion, the specimens are discharged and rested for at least 2 hours to achieve the steady-state open circuit potential (OCP) before conducting the electroanalytical experiments. Due to the small size of the specimen, the variation of current potential and current at different scanning points is insignificant. To reduce the experiment time, the scanning point is only at the center of the side surface of the specimens (with respect to the casting director), right above the steel bar.

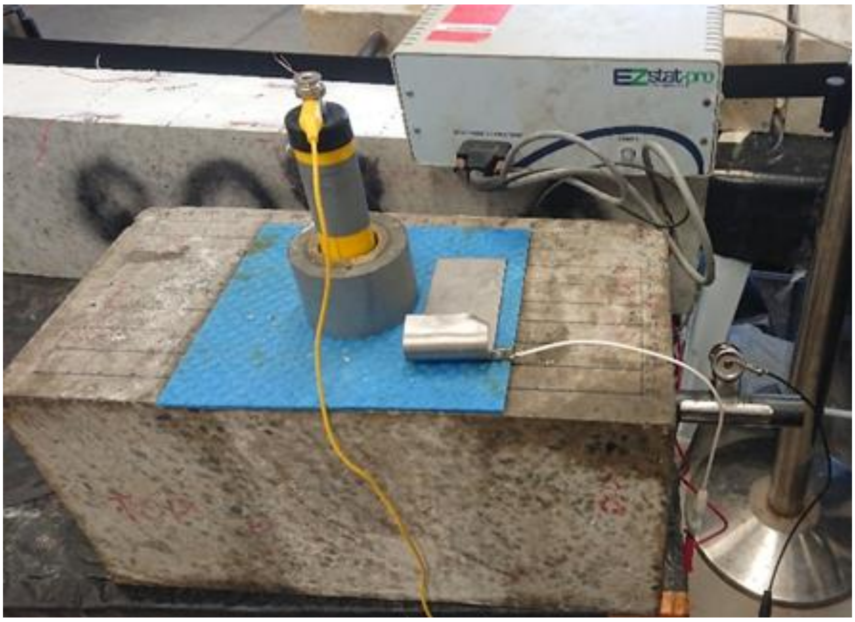

Fig. 3-13 Instruments and experiment setup： linear polarization resistance

The operation of EZstat Pro potentiostat is controlled by NuVant EZware software. The control panel is shown in Fig. 3-14. For a linear polarisation resistance measurement, go to Technique → Sweep Technique → Linear Sweep Voltammetry. The Pretreatment Time (s) is the duration at the Pretreatment Voltammetry (V). The scanning begins at the Initial Potential (V) at a user-defined Scan Rate (V/s) to the First Vertex Potential (V). In this study, the Pretreatment Time is 20 seconds, Pretreatment Voltammetry and the Initial Potential is set to be -1.6 V, the First Vertex Potential is 0.6 V, and the Scan Rate is 0.01 V/s. The Tafel plot and corrosion analysis results can be generated using the built-in data analysis tool, as shown in Fig. 3-15. By defined the surface area, equivalent weight, and density of the working electrode (steel bar), the corrosion potential, the corrosion current, and the corrosion rate can be directly obtained.

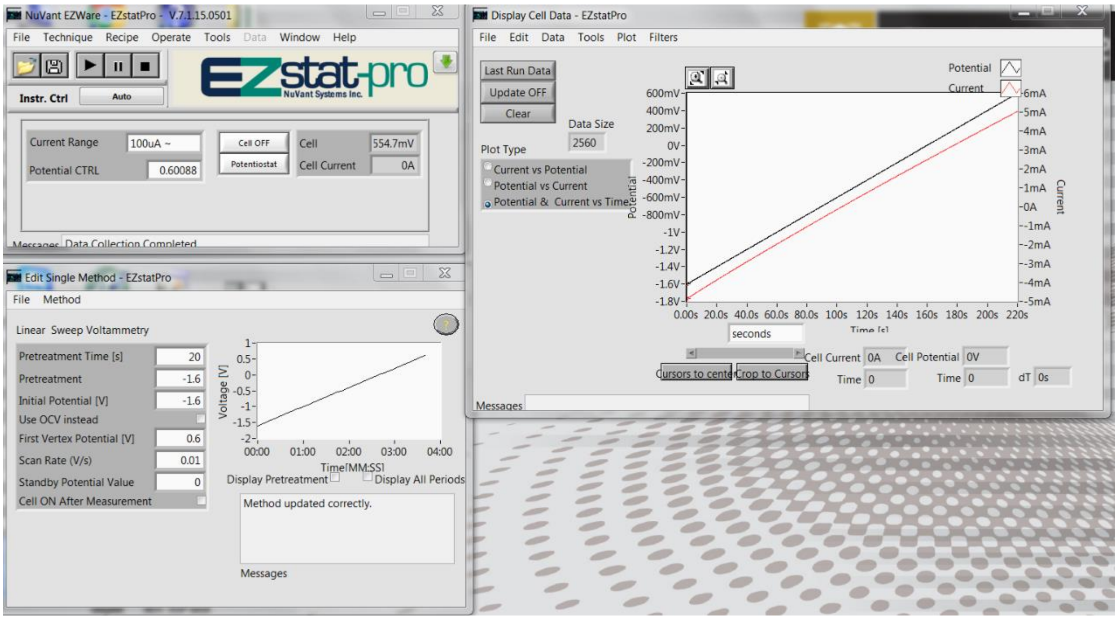

Fig. 3-14 NuVant EZware control panel

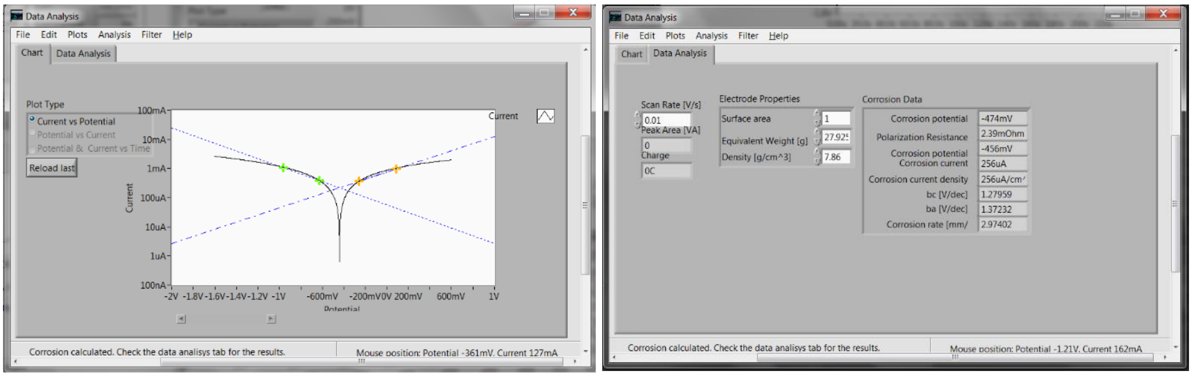

Fig. 3-15 EZware build-in data analysis tool (a) Tafel plot and (b) corrosion analysis results

3.3.2.4. Half-cell potential (HCP)

The same portable Copper-Copper Sulfate Reference Electrodes (Tinker & Rasor Model-6-B) are used to measure the half-cell potential of the specimens. A multimeter (MICRON Q1070A true RMS digital multimeter) is used to measure the DC voltage. The positive side is connected to the steel bar, and the negative side is connected to the electrode. The measurement point is at the center of the side surface, above the steel bar. The specimens are discharged from the DC power supply and rested for at least 2 hours before taking readings.

Fig. 3-16 Instruments and experiment setup: Half-cell potential (HCP)

3.4. Selection of Excitation Signals

In an isotropic cylindric waveguide, waves can propagate in longitudinal, flexural, and torsional modes due to the cylindric boundary and the frequency-dependent properties. Guided waves are dispersive with multiple modes traveling simultaneously at different group velocities and attenuation rates even at the same excitation frequencies. The dispersive characteristics of guided waves complicate the identification of wave modes in a received signal. Hence, knowing the velocity of the wave modes across all frequencies is essential for interpreting the signals. Three essential parameters of the dispersive characteristics of the guided waves are phase velocity, group velocity, and attenuation. These parameters are dominated by the mechanical properties of the medium, the geometry of the medium, and the excitation frequency. The dispersion curves for a normalized radius steel round bar are generated using DISPERSE® software, as shown in Fig. 3-17. The steel bar is modeled as an isotropic cylinder. Longitudinal modes have axial and radial displacement, torsional modes have angular displacement and flexural modes have all three displacements. The three modes are represented by L(a,b), T(a,b), and F(a,b), respectively, where ‘a’ and ‘b’ represent the circumferential displacements and sequential order of mode. Phase velocity is the velocity of a monochromatic wave, while group velocity refers to the velocity of an entire wave packet to propagate through distance. Since accurate tracing of each monochromatic wave is very difficult, the group velocity is used to identify the mode of the wave packets. The dispersion curves are used to help select excitation signals and identify the corresponding wave modes in received signals. The PZT wafer can free vibrate in all directions, while the contact transducer can vibrate in the longitudinal direction. Both longitudinal and flexural waves can be generated in a PZT wafer system, while only longitudinal mode can exist in a contact transducer system. Hence, the criteria for excitation signal varies with the type of transducers.

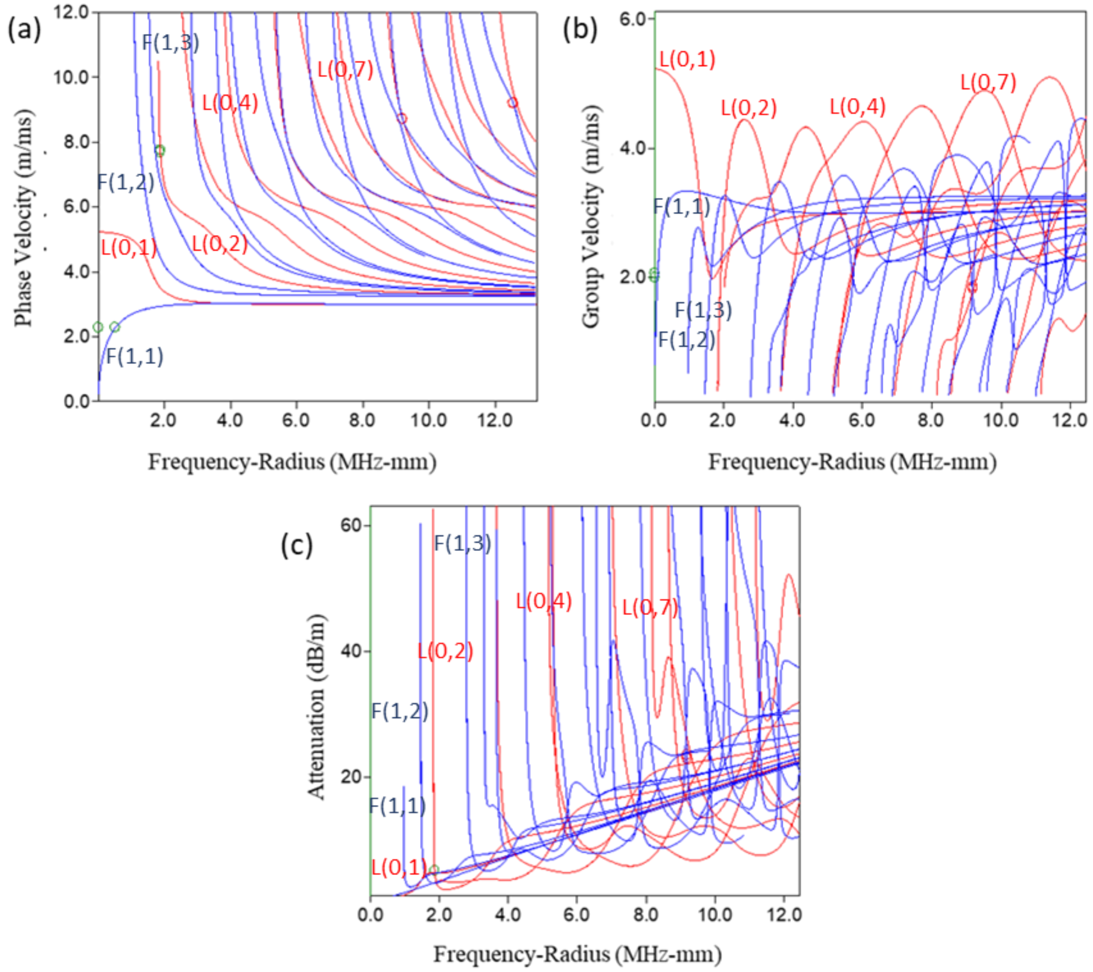

Fig. 3-17 Dispersion curves of guided waves traveling in steel round bar (a) Phase velocity (b) Group velocity and (c) Attenuation

3.4.1. PZT Wafer-based system

A PZT wafer allows user-defined waveform and central excitation frequency. The selection of excitation signal in a PZT wafer system depends on the dispersive characteristics of the excitation as well as the response of the signal at the receiving end. The key characteristics are the amplitude of the signal, the number of wave modes, the group velocity of individual wave mode, the wavelength, and the attenuation. High amplitude allows the signal to evaluate the changes in the waveguide. Low attenuation allows the signal to travel and evaluate a long distance. A lower number of wave modes allows easy identification of wave mode, while a higher number of wave modes gives more information about the waveguide. The group velocity defines the arrival time for each wave mode. If the group velocity for the wave modes is similar, a merged wave packet is expected, which complicates the identification of wave modes. Hence, an optimal excitation signal should feature high amplitude with low attenuation and well-separated wave modes for easy identification.

A 20-cycle Hanning-windowed tone burst is used to excite the guided waves, in considering minimizing the possibility of wave packet overlapping, maximizing the peak amplitude while keeping signal energy more concentrated around the excitation frequency, therefore minimizing wave dispersion. The 20-cycle Hanning-windowed tone burst is the production of a 20-cycle sine and a Hanning function of the same window length, expressed by:

$$\sin 2\pi \mathrm{f t} \times \left(\frac{1}{2} + \frac{1}{2}\cos(2\pi(\frac{\mathrm{t}-\mathrm{t}_{\max}}{\mathrm{t}_{\max}}))\right) \quad (3\text{-}1)$$

$$\mathrm{t}_{\max} = \mathrm{n} \times \frac{1}{\mathrm{f}} \quad (3\text{-}2)$$

Where f is the central excitation frequency, t is the time domain of the waveform, t_{max} is the maximum time of the waveform and n is the number of cycles.

Fig. 3-18 (a) shows a typical 20-cycle Hanning-windowed tone burst at 350 kHz. The total time window of the excitation signal is 5.8E-5 s. The corresponding frequency domain of the excitation is shown in Fig. 3-18 (b). The bandwidth of the signal is 100 kHz, the effective frequency range is from 300 kHz to 400 kHz, and most of the energy is concentrated around 350 kHz.

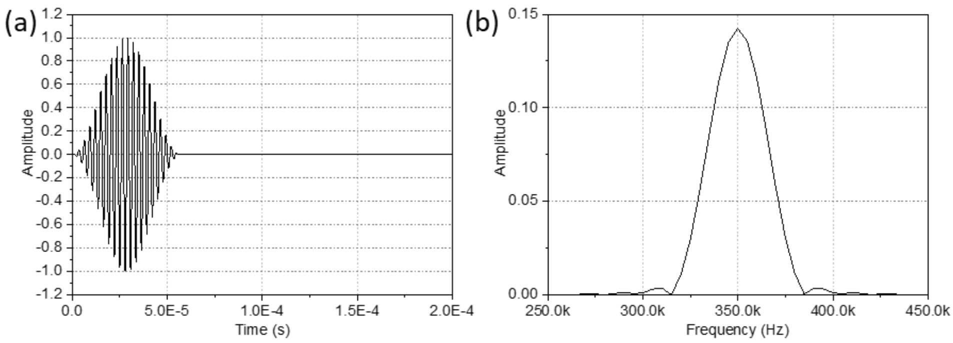

Fig. 3-18 20-cycle Hanning-windowed tone burst (a) time domain and (b) frequency domain

Fig. 3-19 (a) shows the received signal in the time domain in a round steel bar with a 400 mm length and a 12 mm diameter using the 20-cycle Hanning-windowed tone burst at 350 kHz. Three wave packets can be clearly identified, among which the third wave packet has the strongest signal amplitude. The wave modes can be identified by referring to the dispersion curve for a 12 mm steel round bar around 350 kHz, as shown in Fig. 3-19 (b). The group velocity of the wave packet is first calculated directly from the time signal. The group velocity and the frequency are used to locate the wave modes. In general, the measured group velocity is lower than the theoretical group velocity. Hence, the wave mode has a slightly higher group velocity in the dispersion curve. The first wave packet is L (0,2) mode traveling at 3561 m/s. The second wave packet is a merged mode of F (1,3) and F (1,1) traveling at 2881 m/s, which is slightly slower than the theoretical group velocity of 3200 m/s. The third wave packet consists of 3 wave modes, F (1,2), L (0,1), and L (0,3). The dispersion curve shows that the group velocity of these three modes at 350 kHz is similar. The measured group velocity of this wave packet is 2258 m/s, while the theoretical value is between 2295 m/s and 2424 m/s.

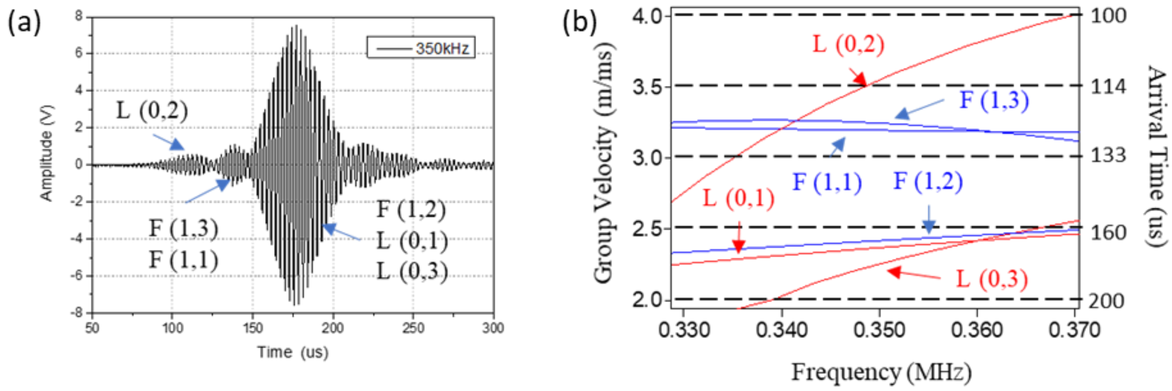

Fig. 3-19 Typical received signal at 350 kHz in a 12 mm steel round bar (a) time domain and (b) Dispersion curve around 350 kHz.

The theoretical resonance frequency of the PZT wafer is 200 kHz. A preliminary study has been conducted to find the actual resonance frequency by checking the sound level due to ultrasonic vibration. A wafer is attached to a steel bar, and a frequency sweep from 100 kHz to 1 MHZ is applied to the wafer. The sound of the vibration reaches a peak between 230 kHz to 250 kHz.

Theoretically, excite the signal on the PZT wafer at its resonance frequency can achieve the highest vibration amplitude. However, the response of the excitation signal may vary due to many criteria, such as the geometry of the waveguide, attenuation and dispersive characteristics of the wave, and the variation in PZT wafer and waveguide. To counter the uncertainty caused by these issues, a frequency sweep from 200 kHz to 1 MHz is employed to excite signals in all PZT wafer-based systems. A narrowband tone burst features high energy concentration around the excitation frequency to reduce the effects of wave dispersion and to achieve precise response, while a broadband signal can provide comprehensive information of the evaluated structure. A frequency sweep using a narrowband signal can give comprehensive information over a wide frequency range by generating precise information at individual frequencies.

Fig. 3-20 shows the Damage index of signals at various frequencies in a 12 mm round steel bar using frequency sweep from 200 kHz to 1 MHz at an exciting voltage of 200 V_{pp}. The damage index is generated using the total energy of the signal around the excitation frequency. The details are discussed in section 3.5.1. Two peaks can be clearly identified, one at 250 kHz, which is the resonance frequency of the wafer, and the second peak is around 350 kHz which gives the strongest response. The frequency sweep is employed throughout the entire duration of the experiments. Two features, DI of the signal at the strongest frequency and frequency shift of the entire frequency range, are extracted to evaluate the change in the waveguide during the experiments.

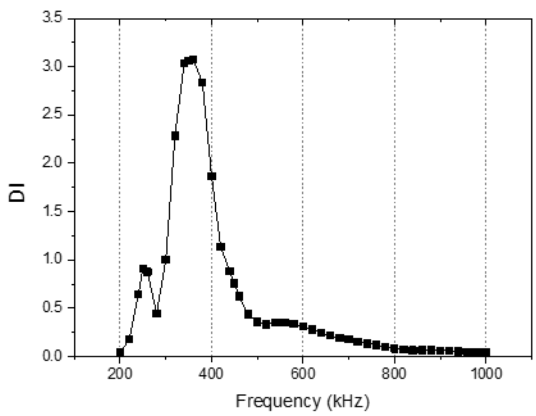

Fig. 3-20 DI of frequency sweep signals in a 12 mm steel round bar

3.4.2. Contact Transducer-based system

A contact transducer allows exciting signals in one direction. By keeping the contact transducer parallel to the longitudinal direction of the waveguide, guided longitudinal waves can be generated. The longitudinal modes can be selected using different excitation frequencies. The selection of the excitation frequency is based on two criteria, the dispersion characteristics of the signal and the corresponding mode shape. For an embedded steel bar, energy leakage at the steel-concrete interface and energy degradation due to corrosion-induced bar deterioration play an important role. The energy variation is contributed by the combined effects of steel-concrete interface delamination and bar deterioration. The core-seeking mode features low attenuation, high excitation frequency, and its total energy density and axial displacement are concentrated in the middle of the bar. It is sensitive to the change in the waveguide, thus being used to monitor bar deterioration. A surface-seeking mode, featuring low attenuation, low excitation frequency with displacement and energy concentrated on the surface of the bar, is sensitive to variation in the steel-concrete interface. Hence it is used to monitor the corrosion-induced interface debonding (Sharma and Mukherjee 2013). Unlike the PZT wafer that allows user-defined excitation frequency, each contact transducer only has a specific working frequency. The available transducers in the Ultrasonic lab, Curtin University are 100 kHz, 200 kHz, 500 kHz, 1 MHz, and higher. Hence the excitation frequencies are chosen from these.

A contact transducer sends a pulse through the waveguide. Accurately estimate the group velocity is very difficult. Hence, the phase velocity is used to identify the wave modes. The dispersion curves of a 24 mm diameter round steel bar are shown in Fig. 3-21. By calculating the wave velocity of the received signal and referring to the phase velocity dispersion curve, it is found that the 100 kHz transducer generates L (0,1) mode, the 500 kHz transducer generates L (0,4) mode, and the 1 MHz transducer generates L (0,7) mode. The attenuation of these modes at the excitation frequency is low, at 1 dB/m, 2.5 dB/m and 4.9 dB/m, respectively.

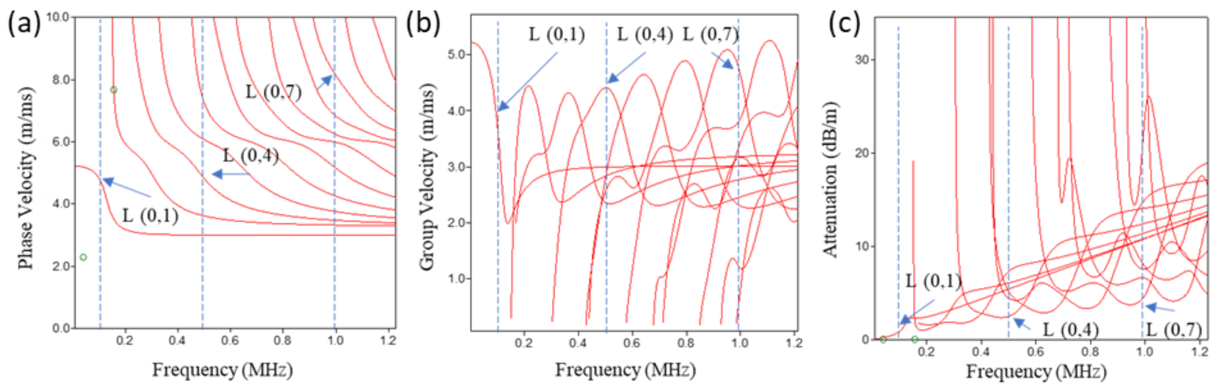

Fig. 3-21 Dispersion curves for 24 mm round steel bar (a) Phase velocity (b) Group velocity and (c) Attenuation

Fig. 3-22 shows the mode shape of the wave modes at the excitation frequency. The mode shape indicates the distribution of the axial displacement and the total energy density along the radius of the bar. For L (0,7) mode at 1 MHz as shown in Fig. 3-22 (a), the axial displacement and the total energy density are concentrated around the central of the bar and negligible near the surface of the bar. Therefore, it is more sensitive to the change of the bar (e.g. material loss) due to corrosion and not sensitive to the change near the surface (e.g. steel-concrete interface delamination). Hence, this mode is used as the core-seeking mode to monitor the bar deterioration due to corrosion. In contrast, L (0,1) mode at 100 kHz has a significant amount of axial displacement and energy at the surface, making it sensitive to the delamination of the steel-concrete interface due to corrosion. Meanwhile, there is a considerable amount of axial displacement and energy along the entire radius of the bar, from the surface to the core. It can also provide information about the bar deterioration but less sensitivity than the L (0,7) mode. Hence, the L (0,1) mode is mainly used as the bond-seeking mode to monitor the steel-concrete interface delamination.

The axial displacement and the total energy density of L (0,4) mode at 500 kHz show a different pattern. These two components are concentrated at two locations, near the surface, and middle of the surface and the core. In this case, this mode is sensitive to both surface delamination and bar deterioration. Hence, this mode is used to monitor the combined effect of surface delamination and bar deterioration due to corrosion.

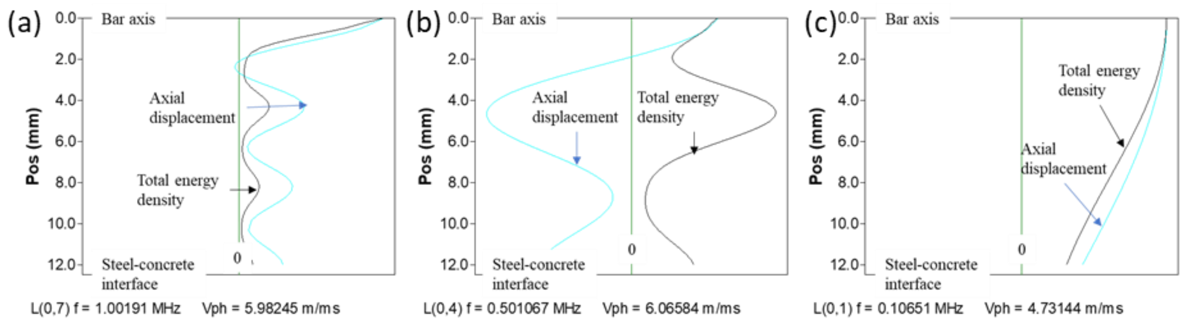

Fig. 3-22 Mode shape of (a) L (0,7) at 1 MHz, (b) L (0,4) at 500 kHz and (c) L (0,1) at 100 kHz

3.5. Damage index

3.5.1. Damage Index (DI) for Top-bar detection

Wave energy is one of the most straightforward linear features of ultrasonic waves. In a reinforced concrete structure, the material properties change due to concrete setting, and the interface quality between steel and concrete can significantly influence the magnitude of the scattered guided wave energy (Sharma and Mukherjee 2010). A linear damage index is developed to evaluate the deviation in the wave energy of captured ultrasonic signal with regard to its benchmark (bar in air), as

$$DI_{linear}(i) = \frac{A_1(i)}{A_1(0)} \quad (3\text{-}3)$$

$$A_1 = \sum_{f_0-\frac{B}{2}}^{f_0+\frac{B}{2}} A(f) \quad (3\text{-}4)$$

$$\mathrm{A(f) = FFT(f(x))} \quad (3\text{-}5)$$

where $A_1(i)$ is the wave energy of the signals around the excitation frequency at time i. f_0 is the excitation frequency. B is the bandwidth of the signal. FFT stands for Fast Fourier Transform. A(f) and f(x) is the signal in frequency and time domain. Due to the formation of interface debonding, fewer energy leaks into the surrounding concrete, more wave energy can be captured, resulting in a greater DI_{linear}.

A nonlinear damage index is also developed using the nonlinear features extracted from the ultrasonic signals. For ultrasonic waves traveling in a medium, the nonlinearity, originates from the material, geometric and instrumental nonlinearity, may exist even in its intact state. To minimize the effects of these nonlinearity sources and emphasize CAN, an amplitude ratio of high frequency component to excitation frequency component is employed. The nonlinear damage index is established as the correlation between the amplitude ratio of the current state and that of its intact state, as:

$$DI_{nonlinear}(i) = \frac{A_2(i)/A_1(i)}{A_2(0)/A_1(0)} \quad (3\text{-}6)$$

$$A_2 = \sum_{2f_0-\frac{B}{2}}^{2f_0+\frac{B}{2}} A(f) \quad (3\text{-}7)$$

where $A_2(i)$ is the wave energy of the signals around $2f_0$ at the time i. In case of the wave traveling in a bar embedded in concrete with good interface quality, the high frequency component experiences strong attenuation, resulting in a smaller $DI_{nonlinear}$. For wave traveling in bar embedded in concrete with interface debonding, CAN get generated, resulting in a greater $DI_{nonlinear}$.

The linear DI is employed in Chapter 5 to detect the presence of the top-bar effect by comparing the amplitude of the received signal over setting time with its benchmark (bar in air). In RC with a good bond between steel and concrete, the waves travel in-between the S-C interface, leading to strong attenuation. In addition, the waves continuously leak from the bar to the surrounding concrete through the S-C interface while propagating. This leads to a continuous drop in the amplitude of the received signal. In RC with top-bar defects, the attenuation and leakage are expected to be less due to the presence of the voids owning to the top-bar effect. The voids separate the concrete from the bar, hence deterring the wave leakage. As the elevation of the bars increases, a more severe top-bar effect is expected and thus the size of the voids increases with the elevation. Fewer waves can leak into the surrounding concrete. Therefore, greater linear DI, DIlinear, are expected at a higher elevation of the bars, indicating a more severe top-bar effect. However, the linear DI requires a benchmark to compare with, which is the linear DI of a known good bond. If the linear DI is greater than the benchmark, there is a high possibility that the specimen has top-bar defects.

The nonlinear DI, on the other hand, is a self-referenced indicator of the top-bar effect. The voids owning to the top-bar effect allows the generation of contact acoustic nonlinearity (CAN). Hence, the nonlinear component of the received signals is expected to increase in RC with the top-bar effect. In

RC with a good bond, it is well known that high frequencies experience more attenuation than low frequencies and no CAN is expected to generate. The nonlinear component of the received signals is expected to reduce in RC with a good bond. One of the main drawbacks of measuring nonlinearity is that it is very weak, less than 1% of the amplitude of the linear component. Signal processing is required to filter the raw signal and isolate the nonlinear components.

3.5.2. Transmission Index (TI)

The energy of the transmitted wave is one of the most straightforward metrics for monitoring the condition of the waveguide. In a reinforced concrete structure, the deterioration of the steel-concrete interface bond and distortion of the reinforcing bar due to corrosion can significantly influence the magnitude of the transmitted energy. The norm of the transmitted energy is measured by recording the transmitted time signals successively as the specimens are exposed to corrosion. Fast Fourier Transform is applied on the time signals as:

$$\mathrm{A}(F_I) = \mathrm{FFT}(\mathrm{f}(\mathrm{x})) \qquad (3\text{-}8)$$

Where $A(F_i)$ is the Fast Fourier Transform of the ith time signal $f(t)_i$

The norm of energy is computed over a frequency window ω±B/2.

$$E_i = \sum_{\omega-B/2}^{\omega+B/2} A(F_i) \qquad (3\text{-}9)$$

Where ω is the excitation frequency and B is the bandwidth

The transmission index is calculated as 1's complement of the ratio of the ith energy norm (E_i) and the initial energy norm E_0.

$$TI(i) = 1 - \frac{E_i}{E_0} \qquad (3\text{-}10)$$

A frequency sweep has been conducted from 200 kHz to 600 kHz at an interval of 20 kHz to determine the best excitation frequency ω.

Fig. 3-23 shows a typical excitation signal and received signal in an intact specimen at a central frequency of 350 kHz. The effective frequency range is 300 kHz to 350 kHz with a central excitation frequency, ω, of 350kHz, and the bandwidth of excitation signal, B, is 100 kHz as shown in Fig. 3-23 (b). Hence, the amplitude of the FFT of the received signal from 300 kHz to 350 kHz is summed up to obtain the TI, as shown in Fig. 3-23 (d).

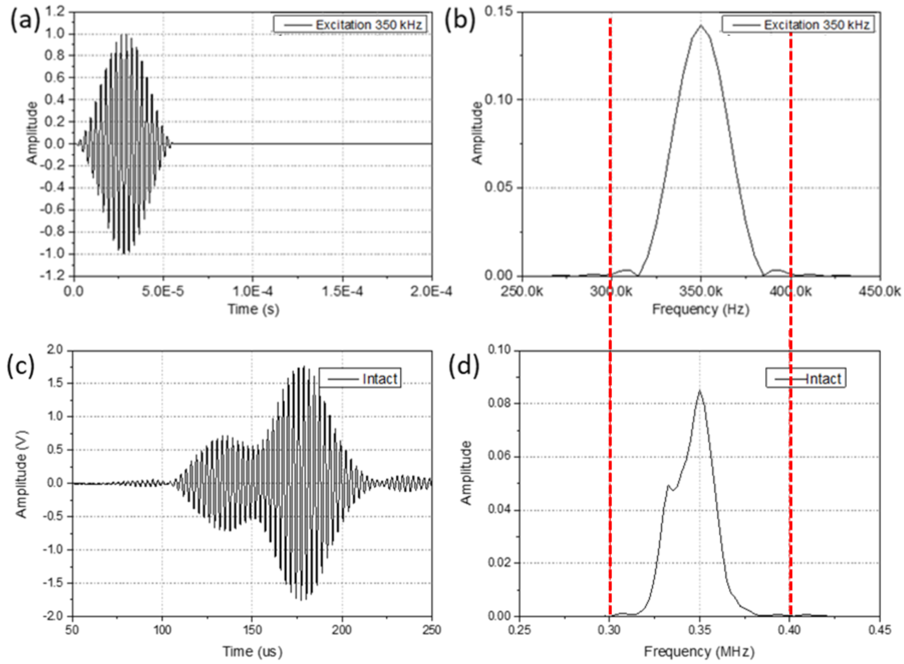

Fig. 3-23 (a) Excitation signal in the time domain at 350 kHz, (b) Excitation signal at frequency domain, (c)a typical received time signal in an intact specimen, and (d) received signal at frequency domain.

The TI measures the residual strength of the signal, which is employed to monitor concrete setting in Chapter 4 and monitor concrete corrosion in Chapter 6 and 7. During concrete setting, the material properties of the concrete continue to change. This strongly influences the amplitude of the waves propagating in the bar. The presence of the surrounding material (fresh concrete) increases the attenuation and the leakage of the guided waves, leading to a reduced TI. As the material property increases with setting, the TI continues to drop. Micro-cracks and voids may form around the bars, deterring the leakage, which may temporarily increase the TI. By measuring the variation in the TI, the setting of concrete can be monitored.

In case of corrosion, it leads to changes in the S-C interface and deterioration of the bar. The rusts are expected to first fill the voids which increase the contact between the steel and concrete. This leads to increased leakage of waves, lower TI is expected. Then the rusts intrude the S-C interface and cause debonding. This leads to a reduction in wave leakage, hence the TI increases. At the advanced stage of corrosion, surface irregularity and pits formed in the bar. The guided waves are strongly distorted by the irregularity and some of the waves can be reflected by the pits, which leads to a reduced TI. by referencing the variation in TI, the state of the bar and the surrounding concrete can be identified, and the corrosion process can be monitored.

3.5.3. Damage Imaging using Synthetic Aperture Focusing Technique (SAFT)

The grids lines are marked on the side surface of the specimen at an interval of 10 mm in both directions. A pair of 200 kHz transducers in tie-together mode with a center-to-center spacing of 30 mm are moving simultaneously in steps of 10 mm along the marked lines. The waveform $f_i(t)$, as shown in Fig. 3-24 (a), acquired using the tie-together transducers are used to generate SAFT images of the cross-section of the specimens. By calculating the time of flight (ToF) of the wave packet, the near-surface effect, the reflection from the bar, and the reflection from the bottom boundary of the specimen can be identified.

Assuming the cross-section of the specimen of dimension m×n is discretized into a square grid of m rows and n columns as shown in Fig. 3-24 (b). The ToF of the signal from the transmitter T_i to the receiver R_i via the pixel P_{jk} is calculated as

$$ToF_{jk}^{i} = \frac{\sqrt{(x_{jk}-x_T^i)^2+(y_{jk})^2}+\sqrt{(x_{jk}-x_R^i)^2+(y_{jk})^2}}{V} \quad (3\text{-}11)$$

Where x_{jk} and y_{jk} are the location of the pixel in the x- and y-axis. x_T^i and x_R^i are the location of the transmitter and receiver. V is the velocity of the compressional wave propagating in the specimens.

The image intensity I_{jk} accumulated at the pixel P_{jk} corresponding to N numbers of scanning point is calculated as:

$$I_{jk} = \sum_{i=1}^{N} f_i\left(ToF_{jk}^{i}\right) \quad (3\text{-}12)$$

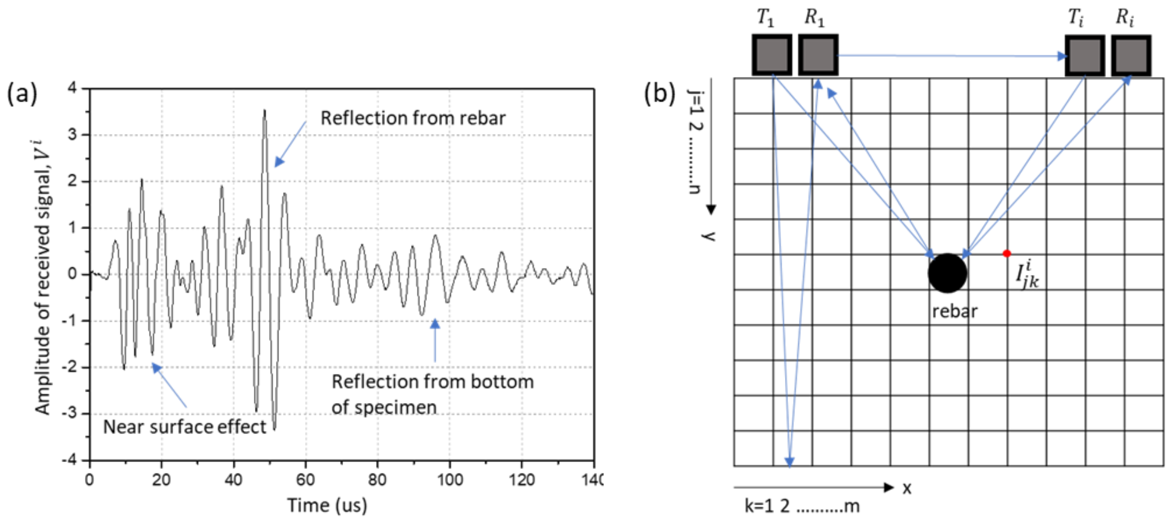

Fig. 3-24 (a) a typical received waveform and (b) SAFT-based imaging algorithm

The constructed imaging using a single waveform is shown in Fig. 3-25 (a). The cross-section of the specimen is $200\ mm \times 200\ mm$. The depth of the image is extended to 250 mm to show the reflection from the bottom boundary. Three clear regions can be identified. A group of curved lines underneath the transmitter and receiver indicates the near-surface effect. The second group of curve lines indicates the reflection from the possible location of the steel bar. The location of the steel bar can be anywhere on the curved line. The third group of the curved line represents the reflection from the bottom boundary of the bar. A new image is constructed using multiple waveforms by employing SAFT, as shown in Fig. 3-25 (b). The top 50 mm of the image is occupied by the near-surface effect. A scattered field at the center of the image is highlighted, which is mapped with the location of the steel bar in the specimen. At the bottom part of the image, two scattered fields can be identified. These are the reflection from the bottom boundary of the specimen. It is also noticed that there is a gap between these scatter fields, right under the location of the steel bar. This is because the waves are blocked by the rebar and reflected to the top surface. No waves can pass the steel bar and propagate to the bottom. Hence, any objects, e.g., other steel bars and cracks, underneath the steel bar cannot be detected. Therefore, these objects will be missed in the image.

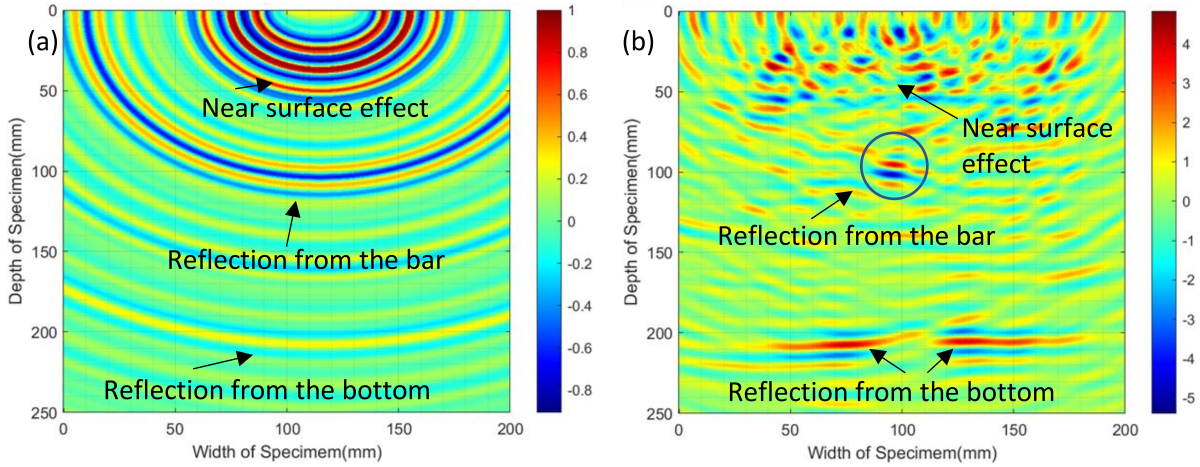

Fig. 3-25 Image of cross-section using (a) single waveform and (b) SAFT

3.5.4. Penetration resistance test

A spring-type penetrometer, as shown in Fig. 3-26, is used to detect the initial set and final set of the cement paste according to ASTM C403. The penetration resistance of the setting cement paste is measure in kilogram-force and the maximum reading of the penetrometer is 140 kgf. The area of the penetration needle shank is 32, 65, 161, 323, and 645 mm2, giving a measurement of the penetration resistance of up to 42.88 MPa. The initial and final set occur when the penetration resistance reading equals or exceeds 3.5 MPa and 27.6 MPa, respectively.

3.5.5. Temperature measurement

One of the key phenomena of cement hydration and concrete setting is the release of heat. The temperature of the cement/concrete changes during hydration. By measuring the change in the temperature, it allows the monitoring of cement hydration process. a needle type thermometer is used to measure the temperature of the cement and concrete during setting, as shown in Fig. 3-26. The room temperature and the temperature of the specimen is measure during setting, providing a supporting information of the hydration process as well as for comparison purpose. The four stages can be estimated using the temperature measurement, which can be used to validate the efficiency of the guided wave results.

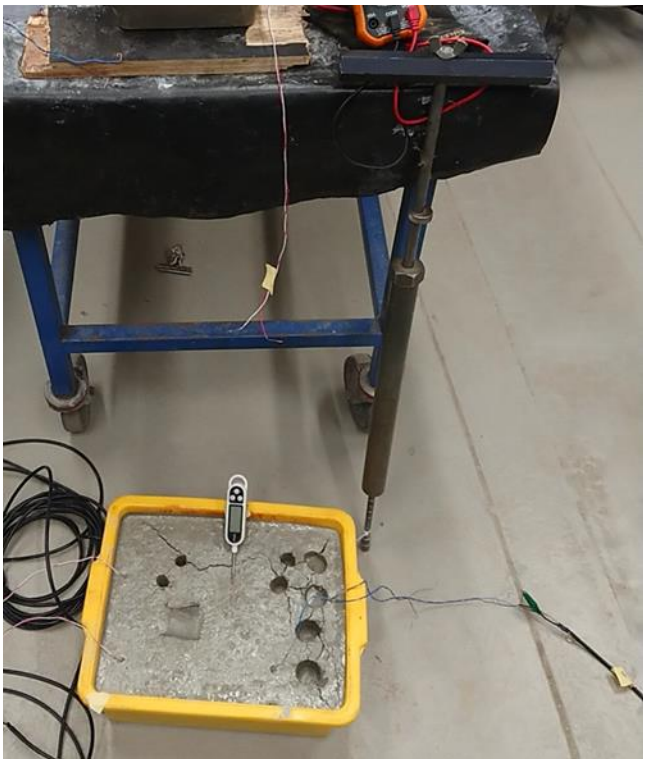

Fig. 3-26 Penetration resistance test using spring type penetrometer

3.6. Summary

This chapter discussed the experiments performed to detect debonding owning to top-bar effect and access corrosion of reinforced concrete in detail. The experiments specimens include 1) vertically cast reinforced concrete samples that are embedded with steel bars of various types and diameters and 2) small concrete samples that are embedded with plain bars and ribbed bars subjected to various lengths of artificial debonding as well as short plain bars that are cast in the concrete.

The setup of accelerated corrosion is discussed in detail. Accelerated corrosion using anodic current is employed to corrode the bare and embedded bars. Wet-wrap and pond on the top surface are used to keep the specimens saturated in a wet environment with chloride ions for chloride-induced corrosion. The wet-wrap specimens allow a random location of corrosion initiation and direction of crack propagation. While the ponded specimens, by controlling the direction of current flow, the crack propagation direction is predictable.

Two types of piezoelectric sensors, PZT wafers, and contact transducers, are used to generate and capture the guided waves through the bars and the bulk waves through concrete. PZT wafers feature small size and broadband of user-defined excitation frequency, but the output voltage is relatively low. While the contact transducers feature high output voltage, but the excitation frequency is pre-defined.

Four techniques, PZT wafer-based ultrasonic technique, contact transducer-based ultrasonic technique, half-cell potential, and linear polarisation resistance, are employed in this study. PZT wafer-based ultrasonic-based technique is used to detect the guided waves to access the existence of top bar effect and concrete corrosion through steel bars. Contact transducer-based ultrasonic technique is used to excite and detect the longitudinal guided waves to access the corrosion of the embedded bars and exciting bulk waves through concrete to monitor the concrete cracking using Synthetic Aperture Focusing Technique (SAFT). Half-cell potential and linear polarization resistance are commonly used electrochemical methods to monitor concrete corrosion. These techniques are used to detect the severity of the concrete corrosion and the probability of the occurrence of the corrosion. These techniques are employed simultaneously to monitor the concrete corrosion to provide more information about the corrosion process.

The wave energy is used as the key feature to detect the top-bar effect and the corrosion of the bare bars and embedded bars. A linear and a nonlinear damage index (DI) is proposed to detect the existence of the top-bar effect. While a transmission index (TI) is proposed to monitor the corrosion of both bare bars and embedded bars in concrete.

Reference

Sharma, S. and A. Mukherjee (2010). "Longitudinal guided waves for monitoring chloride corrosion in reinforcing bars in concrete." Structural Health Monitoring **9**(6): 555-567.

Sharma, S. and A. Mukherjee (2013). "Nondestructive Evaluation of Corrosion in Varying Environments Using Guided Waves." Research in Nondestructive Evaluation **24**(2): 63-88.

Chapter 4

4. Guided wave-based monitoring of concrete hydration.

4.1. Introduction

Concrete is made of water, cement and aggregates. The water and cement bind together through multiple chemical reactions to form a glue that is adhered to the aggregates to form a solid concrete. This chemical process is known as cement hydration. The procedure of cement hydration can be represented in five distinct stages, known as Pre-induction stage (I), Induction stage (II), Acceleration stage (III), Deceleration stage (IV), and Steady state (V) (Marchon and Flatt 2016). In stage 1, the hydrolysis of the cement component occurs rapidly, leading to rapid heat generation. The temperature increases several degrees within this period, normally 15 mins. In stage 2, the reaction is slow. Therefore the temperature grows slowly. As a result, the concrete remains in a plastic state. Stage 2 can last for 1-4 hours. This stage is crucial for construction as it allows the concrete to be transported and poured into mould without difficulty. The setting initiates at the end of this stage. In stage 3, the chemical reactions occur rapidly, and the temperature of the concrete increases rapidly. The maximum temperature occurs at the end of this stage. This is the main stage for concrete to gain stiffness and strength during the concrete setting, usually between 4-10 hours. The final set of cement and the initiation of concrete hardening occurs in this stage. In stage 4, the rate of the reaction is slow, and the temperature reduces. The concrete becomes rigid solid. The concrete continues to harden and gain strength with time. Stage 5 refers to the curing period of the concrete. The concrete continues to gain strength as long as the water is provided.

This chapter outlines the experimental study to monitor the concrete hydration process using the proposed ultrasonic methods. The guided waves are monitored through both plain bars and deformed bars with surface-mounted PZT wafers at the ends of the bars. In congest with the temperature measurement, the ultrasonic results are used to detect the four stages of cement hydration. The influence of top-bar defects on the propagation of guided waves in reinforced concrete is also investigated. To better control the severity of the top-bar defects, artificial top-bar defects are employed instead of natural ones. The debonding owning to top bar effect is simulated by mounted thick double-sided tape on the bottom part of the bars. The size of the debonding is summarized in Table. 4-1. The designation specimen follows the order [Bar type] [Length of debonding (in %)]. Bar type is denoted by letters P and D, where P is plain bar and D is deformed bar. The length of debonding is denoted by the letter D followed by numerals, where D stands for debonding. For example, PD0 means a plain bar with 0% debonding.

Table. 4-1 Specimens with artificial debonding.

Specimen	Bar type	Size of debonding
PD0	12mm plain	0%
PD15	12mm plain	15%
PD30	12mm plain	30%
PD45	12mm plain	45%
PD60	12mm plain	60%
DD0	12mm deformed	0%
DD15	12mm deformed	15%
DD45	12mm deformed	45%
DD60	12mm deformed	60%

A cast-in concrete hydration sensor is proposed in this chapter. The sensor allows the generation and acquisition of both guided waves through reinforcement and bulk waves through concrete. The sensor is employed to monitor the hydration of both cement paste and concrete specimens. Temperature measurements are employed to monitor the temperature change of the hydration. Penetration resistance test is also used to detect the time of the initial set and final set of the cement paste. The results are compared with those in specimens with through-thickness bar (section 4.2 and 4.3) evaluate the capability of the sensor for cement/concrete hydration monitoring.

4.2. Monitoring concrete setting through plain bar using PZT wafers

The size of the debonding formed at the steel-concrete interface owning to the top-bar effect is difficult to control and measure non-destructive. To evaluate the effect of the debonding size on the top-bar effect on the concrete setting, all the plain bars are subjected to artificial debonding. Thick form double-sided tapes are attached to the bottom part of the plain bar to simulate the debonding formed by the top-bar effect. The sizes of the debonding are equal to 0%, 15%, 30%, 45%, and 60% of the bottom half of the embedded part of the bar. A frequency sweep from 200 kHz to 600 kHz has been employed to evaluate the bond development during the 13 hours concrete setting period. The TI proposed in section 3.5.1 is employed to monitor the signal strength variation due to the bond development during the concrete setting period.

4.2.1. Frequency response of the signal

The TI at various excitation frequencies is presented in Fig. 4-1. It is observed that, for the bar in air scenario, the signal strength varies significantly with the excitation frequencies, even at the same excitation voltage. The overall pattern of the TI variation is similar in all 5 bars, with a slight difference in the frequency that gives the peak signal strength. Two rising and falling fluctuations can be clearly identified, one between 200kHz to 260 kHz and the other one is between 280 kHz to 450 kHz. Significant variation of the TI occurred within these two frequency ranges. The TI variation is not significant after 450 kHz. Therefore, the pattern of the TI over various frequencies can be divided into three zones.

Zone 1 has a frequency range of 200 kHz to 260 kHz with a peak at 240 kHz, which is close to the resonance frequency of the PZT wafer. The amplitude of TI in all bars decreased with the concrete setting, but the change in the fluctuation of the TI was insignificant. The amplitude of the TI reduced sharply in the first 5.5 hours, but the variation was insignificant afterward.

Zone 2 has a frequency range of 280 kHz to 450 kHz with a peak amplitude of around 350 kHz. For the specimen with no debonding, the amplitude of all frequencies dropped gradually in the first 5.5 Hours while maintained the shape of the fluctuation. The fluctuation was insignificant afterward. For the specimen PD15, the shape of the fluctuation remained unchanged for 7.5 hours and then flatted. For specimen PD30, the shape of the fluctuation remained throughout the entire period of the concrete setting, but the relative amplitude of the fluctuation was reduced compared to that in the bar in air. As the size of the debonding further increases, the relative amplitude of the fluctuation was getting closer to that in the bar in air.

Zone 3 has a frequency range of 450 kHz and 600 kHz. The fluctuation of the amplitude of the TI was insignificant in all specimens. In a specimen with no and low debonding, Fig. 4-1 (a) and (b), the fluctuation of the TI showed a falling trend once the fresh concrete was poured into the mould. Then the fluctuation gradually became a rising trend as the concrete setting processed. By contrast, the variation in the TI fluctuation was low in the specimen with a larger size of debonding. The larger the size of the debonding, the more stable the trend of the TI fluctuation. Hence, like zone 2, the shape of the TI fluctuation was getting closer to that in the bar in air as the size of the debonding increased.

The maximum amplitude variation during concrete setting occurred in zone 2 for all specimens. It was noted that the amplitude of TI dropped significantly once fresh concrete was poured into the mould. The amplitude dropped by 70%, 62%, 88%, 89% and 93% for PD0, PD15, PD30, PD45 and PD60, respectively. In general, the amplitude dropped more significantly for specimens with a larger size of debonding. In contrast, during the setting period, from freshly poured concrete (I hour) to hardened concrete (13 hours), the amplitude reduction during this period was 99%, 99%, 95%, 95%, and 76%, respectively. Hence, the variation in the amplitude of TI decreased with the increasing size of debonding. This is because the bond strength change dominates the TI variation due to the concrete setting. As the bond strength increased, the attenuation of waves increased, and the leakage of energy from bar to concrete increased. Hence, the total energy that reached the receiver was reduced, leading to falling TI. However, due to the presence of the debonding, the effects of the bond development on the wave propagating in the steel bar were reduced. As the size of debonding increased, the effect of the bond strength on the propagating wave was further reduced. An extreme case was 100% debonding, where the embedded bar was equivalent to the bar in air. Therefore, the variation of the amplitude of TI was lower in specimens with larger debonding.

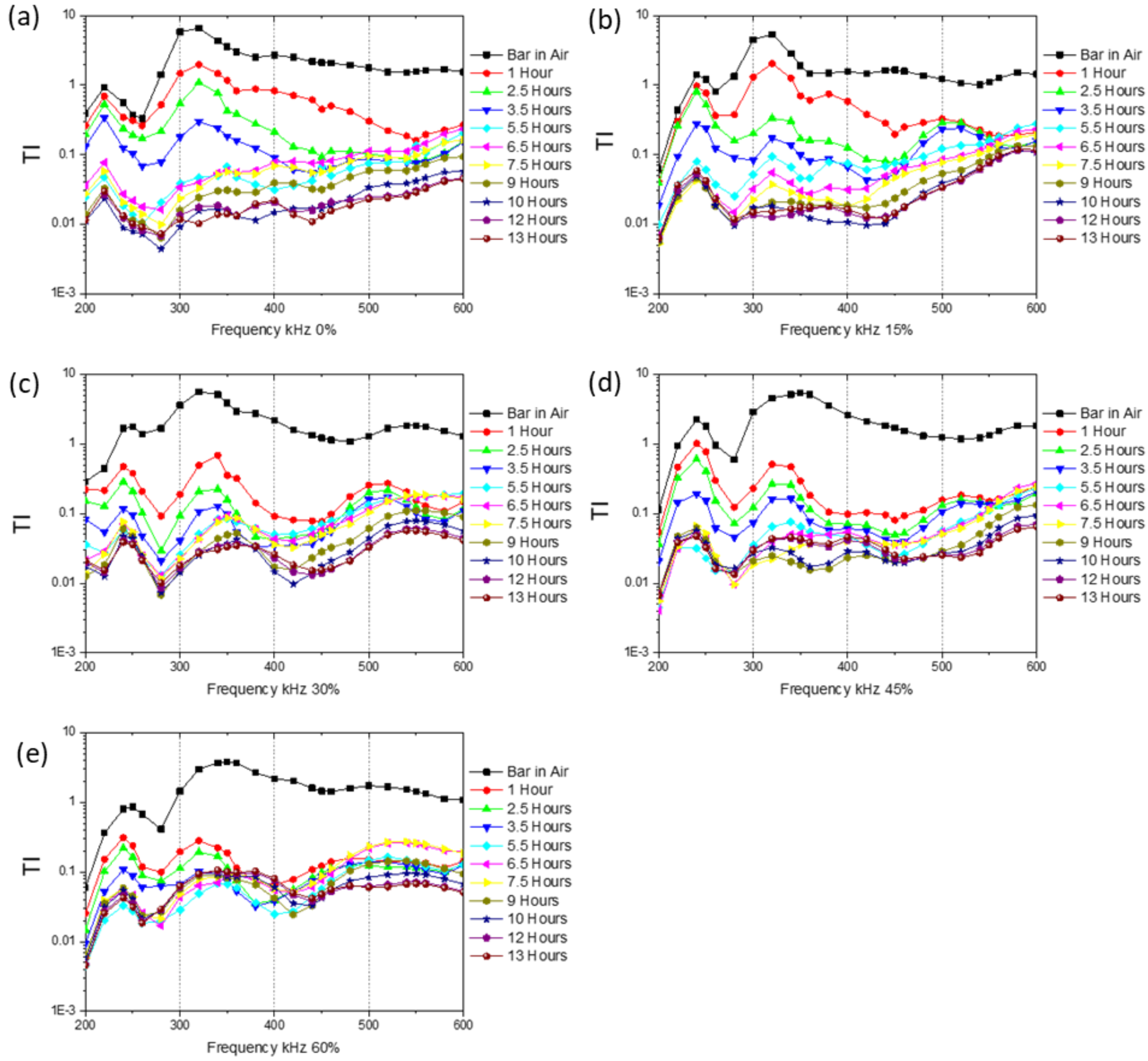

Fig. 4-1 Frequency sweep results in plain bar subjected to artificial debonding (a) 0% debonding (b) 15% debonding (c) 30% debonding (d) 45% debonding and (e) 60% debonding

4.2.2. Selection of excitation frequency for concrete setting monitoring

The excitation frequency dominates the characteristics of the propagating wave. The criteria of selecting an optimal frequency are high signal strength, low wave complicity, well-separated wave modes. The mode shape of the wave is also essential. It defines the sensitivity of the mode to the variation on the surface of the bar and in the bar. The received signals are analyzed based on the criteria. 3 frequencies, 240 kHz, 320 kHz, and 600 kHz, are selected to monitor the concrete setting.

Fig. 4-2 (a) shows a typical received signal of 240 kHz in the bar in air. By referring to the dispersion curves for the 12 mm diameter plain bar, two wave modes, F (1,1) mode and F (1,2) mode, can be clearly identified. The first wave packet is F (1,1) mode and the second wave packet is mode F (1,2). The signal strength of these two modes is similar. The peak to peak voltage of F (1,1) and F (1,2) modes is 2.5 V and 3 V, respectively. Fig. 4-2 (b) and (c) show the mode shape of F (1,1) mode and F (1,2) mode at 240 kHz. F (1,1) mode shows a significant amount of axial displacement at the surface and no axial displacement around the core of the bar. The energy density of F (1,1) mode is uniformly distributed along the bar radius but peaked at the surface. Hence, this mode is sensitive to the variation near the surface of the steel bar. Therefore, it is sensitive to the bond development at the steel-concrete interface.Similarly, F (1,2) mode has a significant axial displacement and energy density near the surface. Hence, it is also sensitive to the bond strength development at the steel-concrete interface. Therefore, these modes are surface-seeking modes.

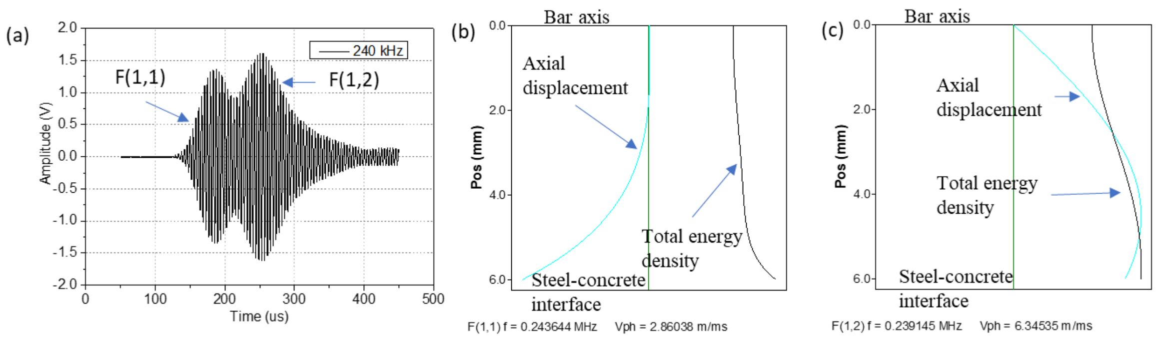

Fig. 4-2 (a) Typical received signal in Time domain at 240 kHz and (b) mode shape of F(1,1) and (c) mode shape of F(1,2) at 240 kHz

Fig. 4-1 (a) shows a typical received signal of 320 kHz in the bar in air. The first wave packet, F (1,3) mode, has a peak to peak voltage of 1 V. While the second wave packet, F (1,2) mode, has a peak to peak voltage of 8 V. Therefore, the F (1,2) mode dominates the total signal strength of the signal at 320 kHz. It is also noted that there is a third wave packet arriving at 350 us in the received signal.

However, the ToF of this wave packet neither match with any direct transmitted wave mode at 320 kHz in the dispersion curve nor match with the reflection of mode F (1,3). The source of this wave packet remains unclear. Fig. 4-3 (b) and (c) show the mode shape of the F (1,3) mode and F (1,2) mode at 320 kHz. F (1,3) mode shows a significant amount of axial displacement and energy density near the surface of the bar. Hence, this mode is sensitive to the development of bonds at the steel-concrete interface. F (1,2) mode also shows a significant amount of energy density at the surface of the bar. The axial displacement is peaked in between the surface and the core of the bar. Hence, F (1,2) mode is also sensitive to the development of the bond. Therefore, these modes are surface-seeking modes.

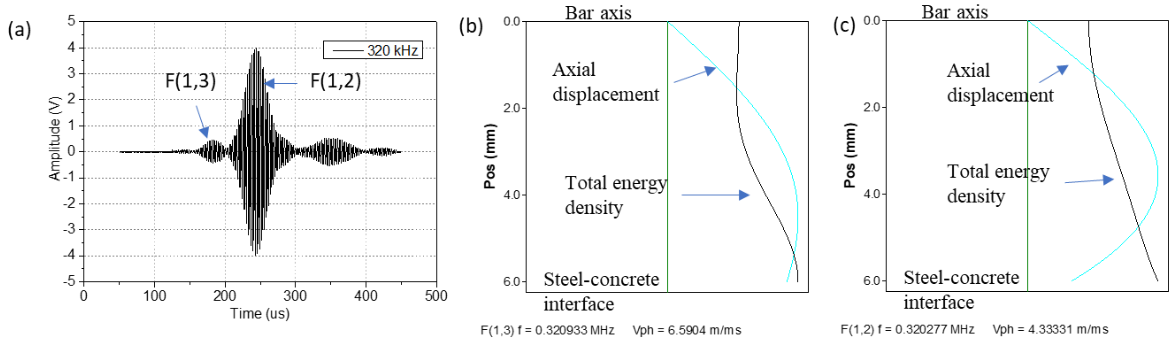

Fig. 4-3 (a) Typical received signal in Time domain at 320 kHz and (b) mode shape of F(1,1) and (c) mode shape of F(1,2) at 320 kHz.

Fig. 4-4 (a) shows a typical received signal of 600 kHz in the bar in air. Unlike the previous two signals where flexural modes are generated, the signal excited by high frequency can generate longitudinal modes. The first wave packet is L (0,3) mode, which is also the strongest mode. L (0,3) mode at a high frequency of 600 kHz has a significant amount of loss of signal strength due to material absorption. Hence, the peak to peak voltage of the signal at 600 kHz is around 1.6 V, which is the lowest among the three selected frequencies. Fig. 4-4 (b) shows the displacement mode shape and energy density distribution of L (0,3) mode at 600 kHz. The energy density and the axial displacement are concentrated around the core of the bar, and the surface components are relatively low. Hence, it is more sensitive to the change of the bar and not the change in the steel-concrete interface. However, there would not be any geometry change or mass loss of the bar during the concrete setting period.

The main contribution of the variation in the bar should be the vibration restriction of the bar and energy loss due to the "clamping" of the hardening concrete. Hence, L (0,3) mode at 600 kHz is more sensitive to the development of the strength of the surrounding concrete. This mode is a core-seeking mode.

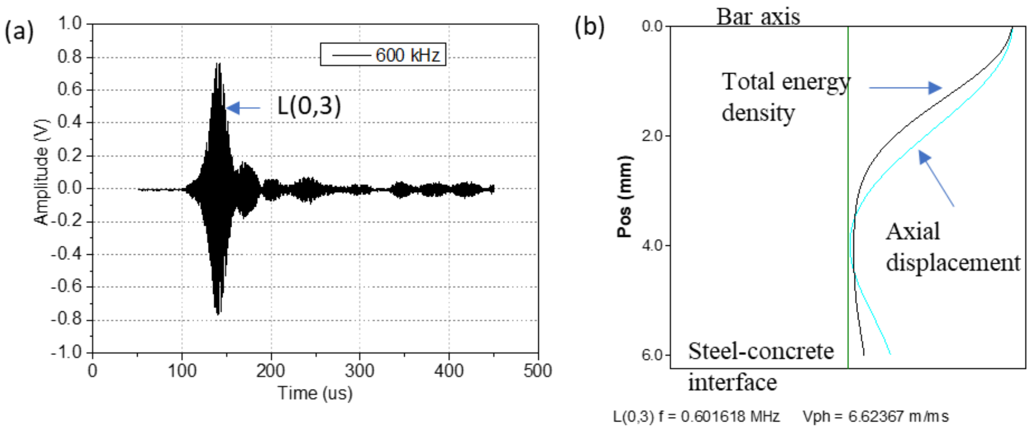

Fig. 4-4 (a) Typical received signal in Time domain at 600 kHz and (b) mode shape of L(0,3) at 600 kHz

4.2.3. Monitoring concrete setting using selected signals

The amplitude ratio of TI indicating the relationship between the TI of received signals over the setting period and the TI of the signal in the benchmark (bar in air) is employed to investigate the TI variation due to concrete setting over time. The amplitude ratio of TI of signals at 240 kHz, 320 kHz, and 600 kHz received in specimen PD0, PD15, PD30, PD45, and PD60 are plotted and compared in Fig. 4-5.

Fig. 4-5 (a) shows the amplitude ratio of TI at 240 kHz received in specimen PD0 to PD60. When fresh concrete is poured into the mould, the TI of signals reduces by 30% to 70%. It is noted that the TI of signal in specimen PD0 and PD15 drops the least, around 35%. The amplitude ratio of the TI of the signals continues to fall sharply until 5.5 hours after concrete pouring. The TI of all specimens drops by 96% to 99%. The difference in the amplitude of TI in all specimens is marginal, although the maximum size of the debonding is 60% of the bottom surface of the bar, which is 30% of the total embedded surface. At this stage, the concrete begins to stiffen. Hence, it is believed that the concrete is transferred from a plastic state to a setting state. The formation of the bond at the steel-concrete interface is initiated. The bond strength and the strength of the surrounding concrete starts to increase. The amplitude of TI becomes steady afterward until the concrete is completely hardened. The amplitude ration of TI of signal in specimen with 0% debonding is the lowest among all the bars at 2.4%, while the amplitude ration of signal in specimen PD60 is the highest, at 5.3%. The amplitude ratio of the signal in specimens PD30 and PD45 is similar to that in specimen PD0. It is also noted that the amplitude ratio of the signal in specimen PD15 is the second-highest among all the specimens. The pattern of the amplitude ratio variation in specimen PD15 is different from the others between 5.5 hours and 13 hours. The amplitude ratio of the signal in specimen PD15 continues to go down from 5.5 hours to 7.5 hours. Then it begins to increase at a slow rate until 13 hours. While in other specimens, the amplitude ratio increases from 5.5 hours to 7.5 hours, then it starts to reduce at a slow rate until 13 hours.

Fig. 4-5 (b) shows the amplitude ratio of TI at 320 kHz received in specimen PD0 to PD60. For specimen PD0, the amplitude ratio drops by 70% after the concrete is poured into the mould. The amplitude ratio continues to drop throughout the entire setting period. The amplitude ratio reduces sharply by 99.3% in the first 5.5 hours. Then the amplitude ratio continues to drop at a slower rate. The amplitude ratio drops by 99.8% when the concrete is completely hardened in the 13th hour. A similar pattern is observed in the amplitude ratio of specimen PD15. The amplitude ratio drops by 62% after pouring concrete and by 99.3% when the concrete is hardened. The amplitude ratio of specimens PD30, PD45, and PD60 shows a different pattern. When the fresh concrete is poured into the mode, the amplitude ratio of these three specimens drops by 90%. It is noted that the reduction of the amplitude ratio for these specimens is almost identical, although the difference in the size of the debonding is significant. However, the pattern of the amplitude ratio variation due to the concrete setting for these specimens is different. For specimen PD30, the amplitude continues to drop by 99.5% until the 10th hour and becomes steady afterward. For specimen PD45, the amplitude ratio drops by 99.5% at the 7.5th hour, and then it begins to rise slowly and reaches 0.96% at the 13th hour. The amplitude ratio of specimen PD60 drops by 98.4% at the 5.5th hour, and then it starts to rise by 1.6% until the 10th hour. Since then, the amplitude ratio has remained steady until the 13th hour. At the 13th hour, when the concrete specimen is hardened, the amplitude ratio of the signal increases with the size of the debonding. The amplitude ratio of specimen PD0 is the lowest among all the specimens at about 0.15%, and the value increases to 0.27%, 0.47%, 0.96%, and 3.1% for specimen PD15, PD30, PD45, and PD60, respectively. Fig. 4-5 (c) shows the amplitude ratio of TI at 600 kHz received in specimen PD0 to PD60. It is noted that the pattern of the amplitude ratio variation in specimen PD0, PD30, PD45, and PD60 is similar, while the amplitude ratio for specimen PD15 shows a slightly different pattern. The amplitude of the signal drops significantly when the fresh concrete is poured into the mould. The TI drops by 83% to 89%. The TI of signal in specimen PD0 reduces the least among all the specimens. A similar phenomenon is observed in signals at 240 kHz and 320 kHz. The amplitude of the ratio continues to drop by 2% to 7% until 3.5th hour before it begins to rise. It is noted that, between 1 hour and 3.5 hours, the reduction of the amplitude of the ratio decreases with the increasing size of debonding. The amplitude of the ratio drops by 7.5%, 3.6%, 2.8%, 2.2% and 1.6% for PD0, PD15, PD30, PD45 and PD60, respectively. The amplitude of the ratio increases by 6% and 8% between the 3.5th hour to 6.5th hour. The amplitude falls sharply from 3.6% to 7.5% until the 10th hour. Since then, the amplitude ratio for signals in all specimens has remained steady until the 13th hour. The amplitude ratio of the signal in specimen PD0 is the lowest among all the specimens at about 2.9%, and the amplitude ratio in specimen PD15 is the highest at 8.1%. The amplitude ratio in all other bars varies between 3.2% to 4.7%. The amplitude ratio variation in specimen PD15 is different from the other specimens. It is recalled that for the signal at 240 kHz, the amplitude ratio variation in specimen PD15 is also different from the other. If specimen PD15 is not considered, the amplitude ratio increases with the size of the debonding.

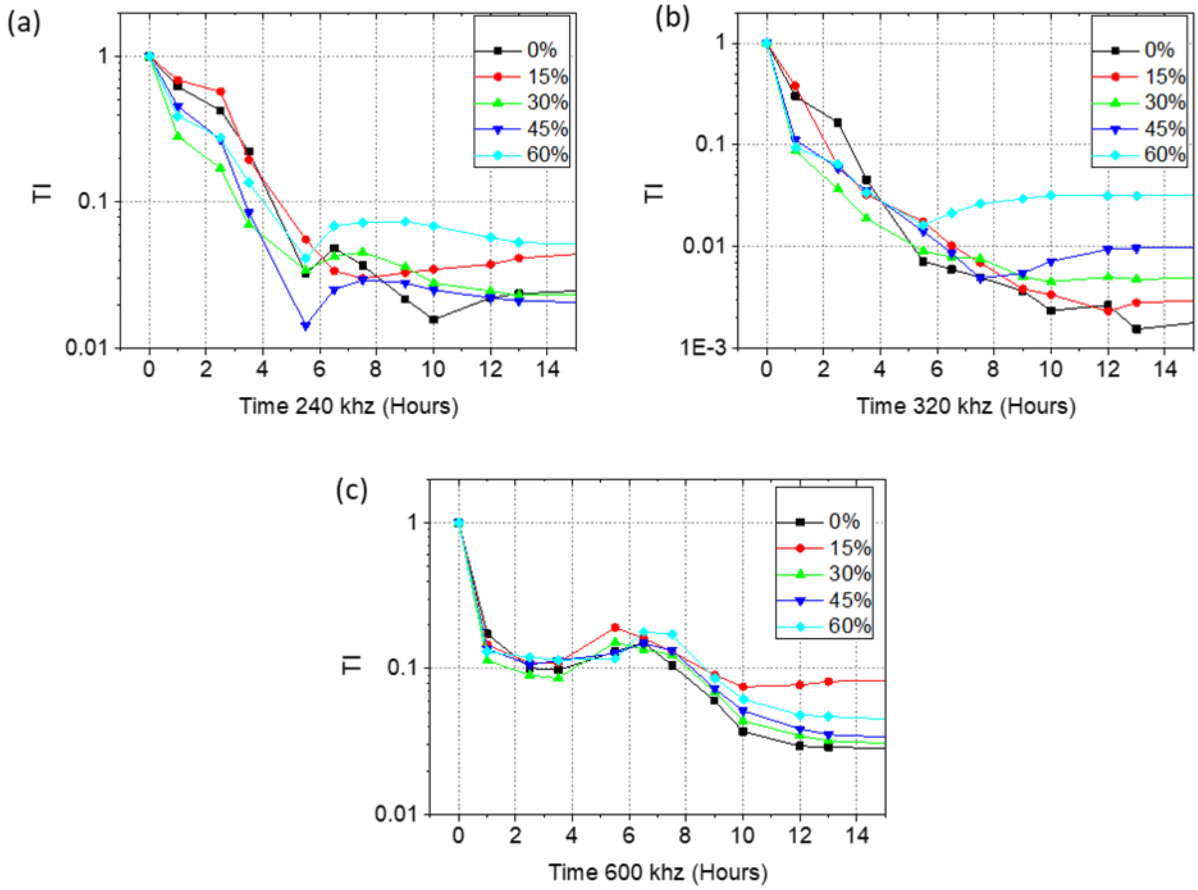

Fig. 4-5 Amplitude ratio of TI of signals at different times after pouring concrete in specimens with various lengths of debonding at (a) 240 kHz (b) 320 kHz, and (c) 600 kHz.

A needle-type thermometer was cast in the concrete to measure the temperature inside the concrete during the setting period. The room temperature was maintained at 23 °C. The internal temperature of the concrete over the setting period is plotted in Fig. 4-6. The temperature of the concrete at the pre-induction period was not measured. In the first 3 hours after pouring, the concrete temperature increased slowly and approaching room temperature. The temperature grew rapidly from 5.5 hours and peaked at 10 hours. The temperature reduced slowly between 10 hours and 13 hours.

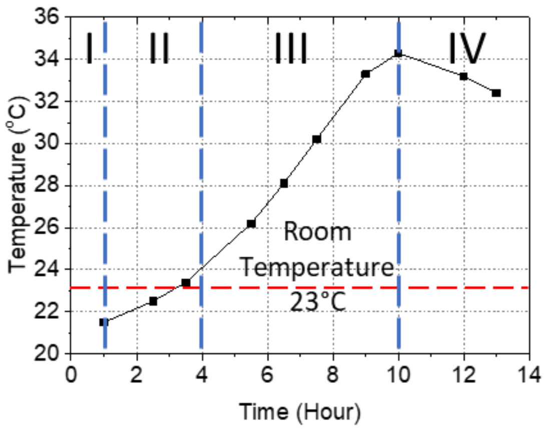

Fig. 4-6 Temperature variation during the concrete setting period

The signals at different excitation frequencies show different behaviors in responding to the concrete setting. Fig. 4-7 shows the ratio of TI of the signal at 240 kHz and 600 kHz in specimen PD0. The amplitude ratio of the signal at 240 kHz drops significantly in the first 5.5 hours of the concrete setting period, and the variation is negligible afterward. The amplitude ratio of the signal at 600 kHz first drops and then increases between 1-5.5 hours. The amplitude ratio drops sharply between 5.5-13 hours. Hence, the signal at 240 kHz is sensitive to monitor the early stage of the concrete setting (Stage 2), and the signal at 600 kHz is sensitive to monitor the hardening of the concrete (stage 3).

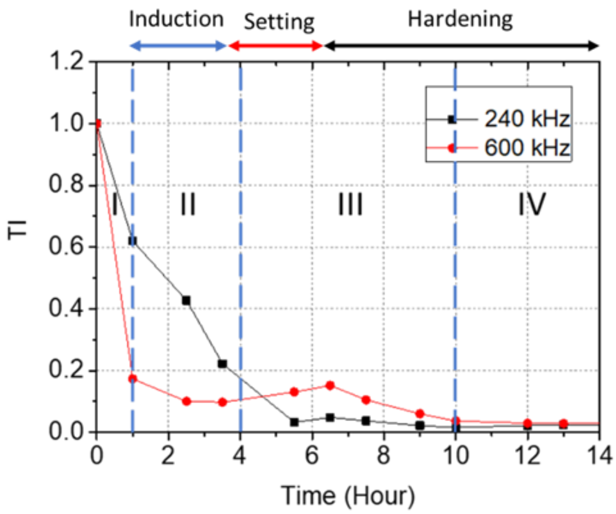

Fig. 4-7 Ratio of TI of signal at 240 kHz and 600 kHz in specimen PD0

Stage 1 (0-1 hours): The pre-induction stage (Stage 1) occurs during the first hour. The ratio of TI of the signal at both frequencies drops significantly in this stage. The ratio of TI of the signal at 240 kHz and 600 kHz drops by 38% and 83%, respectively. In stage 1, the condition of the waveguide changes from bar in air to embedded bar in fluid cement paste. The attenuation of the signal and the damping ratio at the surface of the bar increases dramatically. Therefore, the signal strength of the received signal drops significantly, leading to a sharply reduced ratio of TI. It is noted that the ratio of TI of the signal at 600 kHz drops much more than that of the signal at 240 kHz. This is because the axial displacement and energy density of the modes in the signal at 240 kHz is concentrated at the surface of the bar, while those of the modes in the signal at 600 kHz are concentrated at the center of the bar. The signal at 240 kHz is sensitive to the change at the surface of the bar, hence sensitive to the development of the bond at the steel-concrete interface. The signal at 600 kHz, on the other hand, is mainly affected by the energy leakage from the bar to the surrounding material, hence sensitive to the strength of the surrounding concrete. In stage 1, the concrete is still in its fluid state, the bond at the steel-concrete interface is weak, leading to a slight reduction in the ratio of TI. While for the signal at 600 kHz, the surrounding material changed from air to fluid concrete, the strength of the surrounding material increases dramatically. Hence, a significant amount of energy leaks into the concrete, leading to a sharp reduction of the ratio of TI.

Stage 2 (1-4 hours): The dormant stage (Stage 2) occurs between 1 to 4 hours after pouring concrete. The chemical reactions occur slowly at a steady level. The internal temperature of concrete grows slowly and approaches the room temperature at a rate of 0.5°C per hour. As a result, the concrete paste remains in a fluid state. The amount of hydrated concrete increases slowly with time, leading to a slow stiffening of concrete paste. Hence, the strength of the concrete paste increases at a slow rate. Due to the large size of the specimen and the difficulty to access the ultrasonic instrument and needle penetrometer at the same time, a concrete surface puncture is performed using a sewing needle to measure the relative resistance of the cement paste. The needle can be easily pricked into the concrete paste, although the resistance increases with time. Hence, it is believed that the setting of concrete paste occurs but has not yet reached its initial set.

As for the ultrasonic measurement, the ratio of TI of the signal at 240 kHz, which is sensitive to the variation on the surface of the bar, drops significantly from 63% at 1 hour to 22% at 3.5 hours. It indicates the occurrence of the setting of concrete paste, leading to a continuous stiffening of concrete paste and the development of the bond between steel and concrete. On the other hand, the ratio of TI of the signal at 600 kHz drops from 17% to 9.8% from 1 hour to 3.5 hours. The stiffening of the concrete paste leads to the increased strength of the surrounding concrete. However, the chemical reaction in stage 2 is slow. The strength increment is not significant. In addition, the concrete paste remains soft. Therefore, the energy leakage slowly increases with time, leading to a slight reduction in the ratio of TI. It is also noted that the reduction of the ratio of TI is much smaller compared to that in stage 1. This is because the strength variation of the surrounding material in stage 2 is much smaller than that in stage 1. The effect of the surrounding material in stage 2 is weaker than that in stage 1.

Stage 3 (4-10 hours): The acceleration stage occurs between 4 hours and 10 hours after pouring concrete. The concrete temperature increases rapidly by 1.8°C per hour, indicating a significant increment of the rate of the chemical reactions. The concrete paste stiffens at a fast rate, the state of the concrete paste changes from fluid to solid at the end of this stage. The initial set and final set occur during this stage, followed by the initiation of concrete hardening. The concrete surface puncture test shows that the needle cannot prick into the concrete after 6.5 hours. Hence, it is believed that the concrete has passed its final set, and the initiation of the hardening process has begun.

The ratio of TI of the signal at 240 kHz continues to drop sharply from 22% to 3.3% from 3.5 hours to 5.5 hours. Then the ratio remains steady between 5.5 hours and 10 hours, indicating the final set has been taken place, and the hardening of the concrete has begun. During the concrete setting period, from 1 to 5.5 hours, the surrounding concrete paste changes from fluid to solid, and the bond at the steel-concrete interface changes from soft bond to solid bond. Therefore, the damping ratio of the concrete paste increases significantly with time, the attenuation of surface seeking modes continues to rise, leading to a reduction of the ratio of TI. Hence, it is concluded that the signal can successfully monitor concrete setting by measuring the variation in the ratio TI due to the development of the bond between steel and concrete. When the concrete is hardened, the bond strength at the interface and the strength of the concrete continue to increase. However, the signal can no longer detect the variation in the strength of the bond and the concrete. Hence, the surface seeking modes can be used as an indicator to monitor concrete setting and detect the initiation of concrete hardening.

The ratio of TI at 600 kHz first increases from 9.8% to 15% between 3.5 hours to 6.5 hours. How the setting process, between initial set and initiation of the concrete hardening, affects the waveguide and the characteristics of the core-seeking mode remain unclear. However, it is recalled that the ratio of TI in all five specimens increased during this period. The repeatability of this phenomenon is confirmed. This phenomenon can be used to estimate the time of the final set and the initiation of concrete hardening. The ratio drops by 11.3% from 6.5 hours to 10 hours. During this time, the solid concrete continues to harden and gain strength. More energy is leaked into the surrounding concrete with time, result in a continuous reduction in the ratio of TI. Hence, the core seeking mode can serve as an indicator of concrete hardening at an early stage.

Stage 4 (10 – 13 hours): The concrete hydration reaches the deceleration stage after 10 hours. The temperature of the concrete starts to reduce, indicating the slowing down of the chemical reactions. The ratio of TI of the signal at both frequencies becomes steady. Both core seeking mode and surface seeking mode can no longer capture the strength variation, although the concrete continues to gain strength with time. At this stage, the concrete has gained enough stiffness and strength to stand alone without the mould. The concrete can be removed from the mould and subjected to curing to gain full strength.

4.3. Monitoring concrete setting through deformed bar using PZT wafers

In the previous discussion (section 4.2.3), the signals are excited using surface-mounted PZT wafers and transmitted through a round steel bar. In the form of the ratio of DI, the signal strength of signals varies with the setting and hardening of the fresh concrete. Hence, the ultrasonic method can be used to monitor the concrete setting. Deformed bars, instead of round bars, are more commonly used as concrete reinforcement. The ribs on the surface of the bars can increase the bond between steel and concrete and minimize the bar slippage. The increased complexity of the geometry of the bar due to the presence of ribs can significantly influence the characteristics of the guided waves. Hence, it is essential to investigate how deformed bar affects the guided wave and to validate the capability of the proposed ultrasonic method to monitor the concrete setting using deformed bars as a waveguide. Artificial debonding is also employed to simulate the top-bar effect. The size of the debonding is equal to 0%, 15%, 30%, 45%, and 60% of the bottom half of the embedded part of the bar.

4.3.1. Frequency response of the signal

A frequency sweep from 200 kHz to 600 kHz has been performed to evaluate the frequency response of the signals in deformed steel bars. The TI at various excitation frequencies in deformed bars with different degrees of debonding is presented in Fig. 4-8. The pattern of the TI variation in deformed bars is similar to that in plain bars. The amplitude of the TI in deformed bars is smaller than that in plain bars. This is because the attenuation rate of waves in a deformed bar is much higher than that in a plain bar. In addition, the waves experience strong reflection and deflection due to the presence of the ribs, resulting in smaller transmitted energy. Hence, the TI is smaller. Three zones can be identified based on the fluctuation in the TI.

Zone 1 is between 200 kHz and 260 kHz, with a peak at around 220 kHz, close to the wafer's resonance frequency. The variation in the shape of the TI fluctuation is insignificant. The peak frequency remains at 220 kHz throughout the entire setting period. The amplitude of the TI decreases with the concrete setting. The reduction rate varies significantly at different stages of the setting. For specimen DD0 and DD15, the amplitude drops significantly in the first 5 hours after pouring concrete, and the variation of the amplitude is insignificant afterward. For specimens DD45 and DD60, the amplitude of TI varies significantly with time.

Zone 2 is between 260 kHz and 400 kHz, with a peak amplitude of around 300 kHz. For specimen DD0, the amplitude of all frequencies drops significantly within the first 5 hours. The shape of the fluctuation is flattened after 5 hours, indicating that the attenuation of the signal at the frequency in zone 2 increases dramatically with the concrete setting. For specimens DD15 and DD45, the shape of the fluctuation is flattened after 9 hours. While for specimen DD60, the shape of the fluctuation remained throughout the entire period of the concrete setting, a clear peak can still be identified when the concrete is hardened. Hence, it is concluded that the attenuation of the signal at the frequencies within zone 2 increases with the concrete setting, but the increment in the attenuation decreases with the size of the debonding.

Zone 3 is between 400 kHz and 600 kHz, with a peak at 500 kHz. The fluctuation varies a lot in different specimens, even in the bar in air state. For specimen DD0, a clear peak can be identified at around 500 -520 kHz. The shape of the fluctuation remains constant throughout the entire setting period, with a slight shift in the peak frequency to 500 kHz. For specimen DD15, a peak can also be identified at 500 kHz, but the fluctuation is much smaller than that in DD0. The peak frequency shifts to 480 kHz at the end of the setting period. For specimen DD45, the fluctuation is insignificant, the amplitude of the TI does not vary significantly with frequencies. A clear peak is observed after 8 hours, with a peak frequency at around 460 kHz. For specimen DD60, the fluctuation in the TI is insignificant, but a clear peak can be observed at 500 kHz. The peak frequency shifts to 460 kHz at the end of the setting. Hence, in zone 3, a peak frequency shift to the lower range is observed, and the amplitude of the shift increases with the size of the debonding.

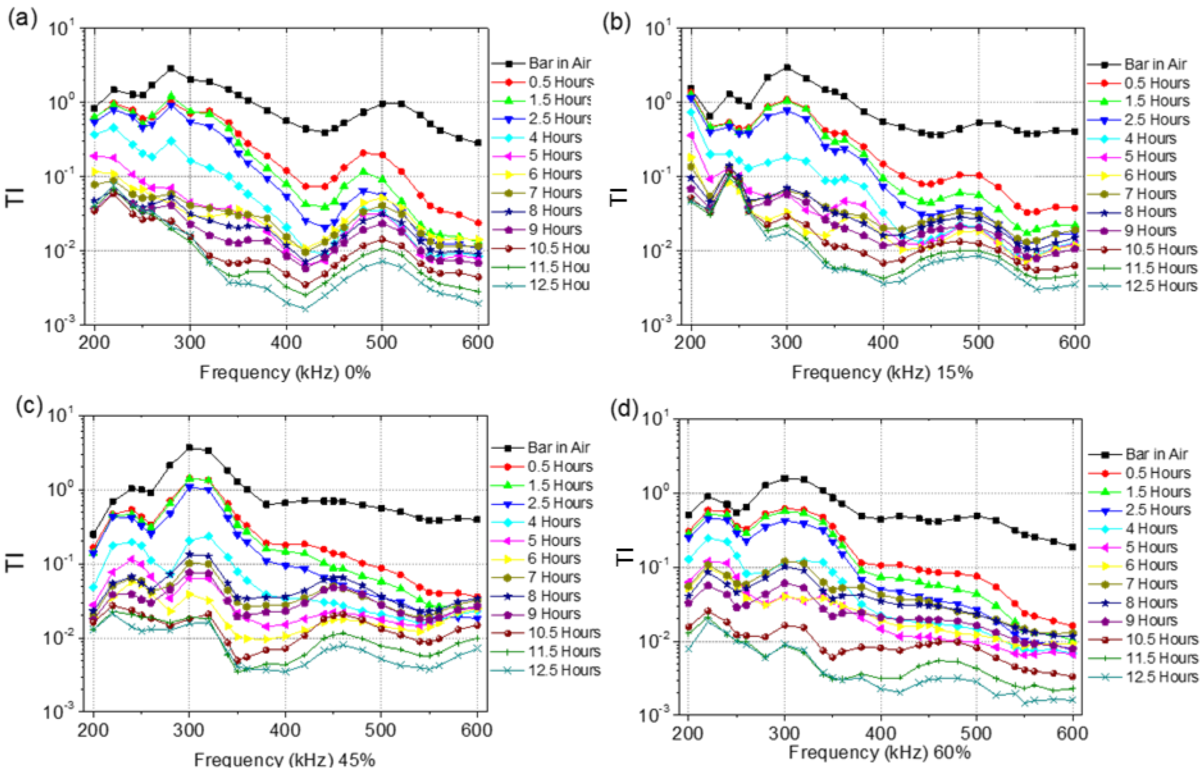

Fig. 4-8 Frequency sweep results in deformed bars subjected to artificial debonding (a) 0% debonding (b) 15% debonding (c) 45% debonding and (d) 60% debonding

The maximum amplitude reduction due to concrete setting occurred in zone 2 for all specimens. Similar to the TI in plain bars, the amplitude of TI dropped significantly when concrete was poured into the mould. The amplitude dropped by 65%, 62.5%, 61.3% and 61.1% for DD0, DD15, DD45 and DD60, respectively. The amplitude reduction was less with the increasing size of debonding. However, the difference is insignificant. The amplitude reduction of DD0 was only 3.9% more than that of DD60, although the size of debonding is equal to 30% of the total area of the embedded bar. The amplitude further dropped by 97.9%, 98.4%, 98.9%, and 97.5% between 1 hour (liquid state) and 13 hours (solid-state) for the specimens. The amplitude reduction is significant in all. The effect of the concrete setting on the waveguide and the wave propagating in the waveguide can be clearly monitored. However, the difference in the amplitude reduction between this period is also insignificant. The amplitude of DD60 was only 0.4% less than that of DD0. The amplitude reduction of DD15 and DD45 was 0.5% and 1% more than that of DD0. Hence, the TI reduction at the end of the setting cannot accurately indicate the difference in the size of the debonding.

4.3.2. Selection of excitation frequency for concrete setting monitoring

Fig. 4-9 shows the variation of the TI of signal in specimen DD0 over the concrete setting period at frequencies from 200 kHz to 600 kHz. The TI of signals at all frequencies reduces with time at a different reduction rate. Two patterns of the TI variation due to concrete setting can be observed. One is at frequencies from 200 kHz to 260 kHz, the amplitude of the TI continuously reduces over time, and the amplitude becomes steady after 10 hours. The other one is between 280 kHz and 600 kHz. The amplitude shows a clear decreasing-increasing-decreasing trend. The increment occurs between the 5th hour and the 6th hour after pouring concrete.

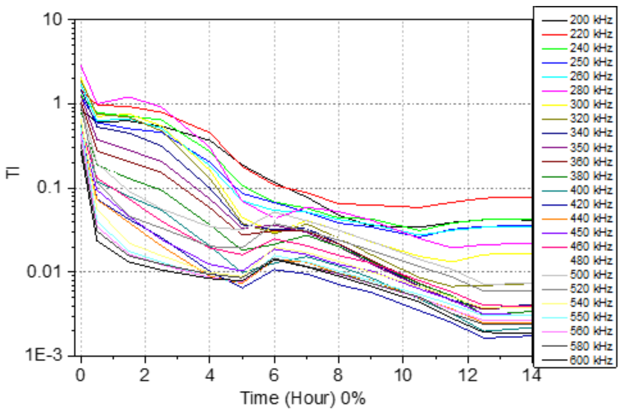

Fig. 4-9 The variation of TI of signals at various frequencies during the concrete setting period

The presence of the ribs on the surface of the bar complicates the geometry of the bar. It is difficult to generate the dispersion curves for a deformed bar and estimate the mode shape of the corresponding wave mode. Hence, the main selection criteria for an optimal signal are signal strength and wave complicity. It is recalled that, in Fig. 4-8, the maximum amplitude of TI occurs at around 300 kHz for all four specimens. Hence, the signal excited at 300 kHz is used to monitor the concrete setting. The transmitted signals in the bar in air are presented in Fig. 4-10. Three wave packets can be observed in all specimens. Since the dispersion curves of the ribbed bar are unavailable, it is unable to identify the mode of these wave packets. Hence, these wave packets are termed mode 1, mode 2, and mode 3. The three modes merged to a different extent. Hence the arrival time of the mode is measured from the peak point of the wave packet. Mode 1 is the first received wave packet, the amplitude of mode is the lowest among all three modes. The arrival time of mode 1 is about 150 us. Mode 2 has the highest amplitude. Therefore, it dominates the TI of the signal. The arrival time of mode 2 is around 200 us. Mode 3 arrives the last, but the amplitude of this mode is much larger than mode 1. The arrival time for mode 3 varies significantly in different specimens, from 230 to 250 us.

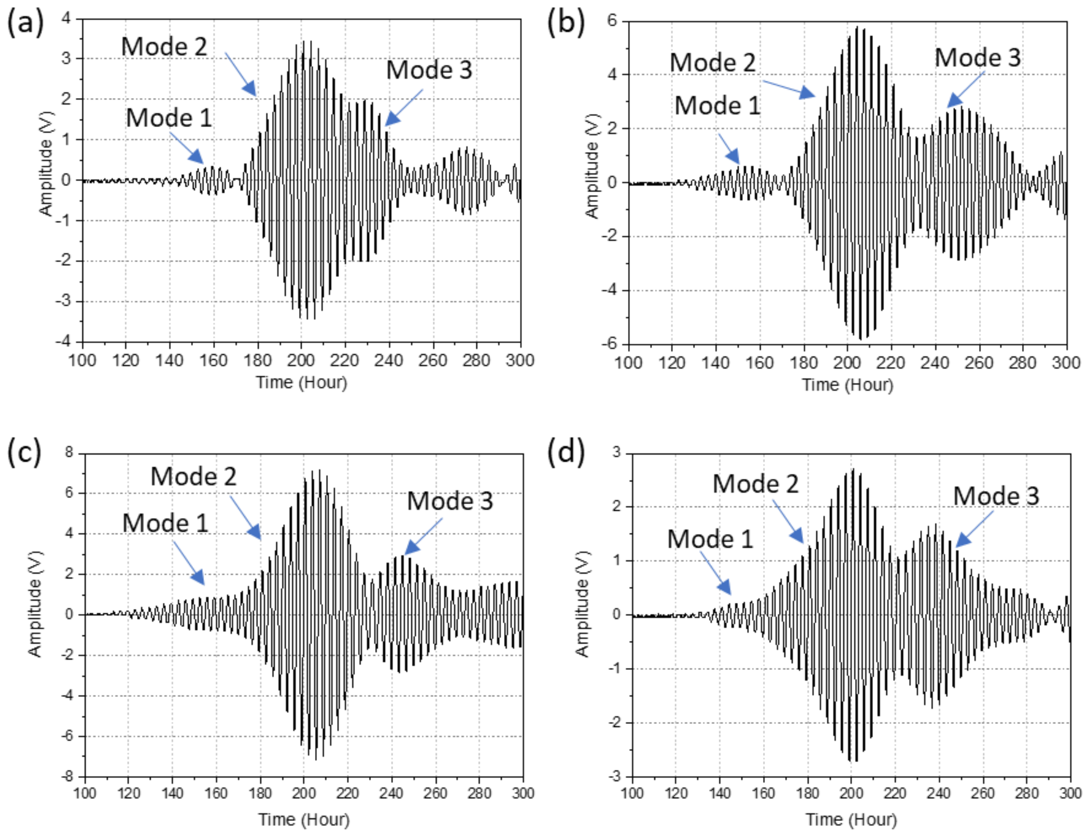

Fig. 4-10 Received signal in bar in air in specimen (a) DD0, (b) DD15, (c) DD45 and (d) DD60.

4.3.3. Monitoring concrete setting using selected signals

Two needle-type thermometers are cast in the concrete specimen to measure the temperature during the setting period. One is cast at 10 mm in the concrete to measure the temperature near the surface, and the other is cast at 150 mm in the concrete to measure the temperature at the center of the specimen. The room temperature varies between 19°C and 20°C during the setting period. The surface and internal temperature of the concrete are plotted in Fig. 4-11. In the first 4 hours after pouring concrete, the temperature increases slowly and approaches room temperature. During this period, the temperature near the concrete surface and at the center of the concrete is almost identical. The temperature grows rapidly from the 5th hour to the 11.5th hour then the growth slows down. During this period, the difference in the surface and internal temperature increases with time. Hence, stage 1 is between 0 hours and 0.5 hours. Stage 2 is between 0.5 hours and 4 hours. stage 3 begins after 4 hours and finishes at 11.5 hours. Stage 4 occurs after 11.5 hours.

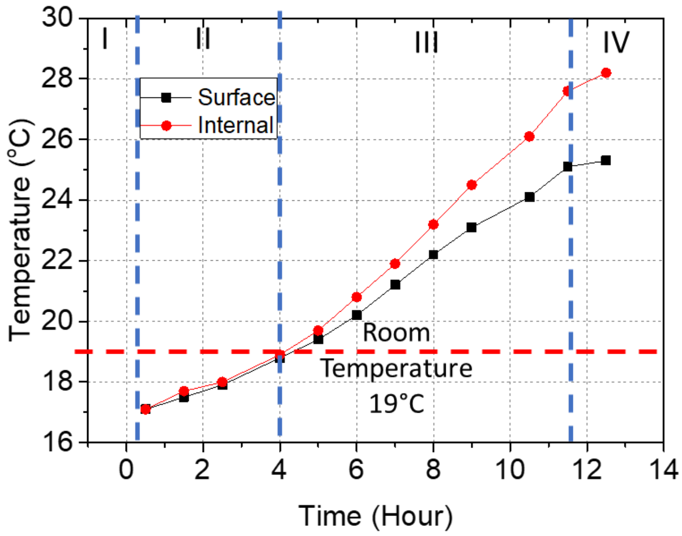

Fig. 4-11 Temperature variation in concrete with the deformed bar during the concrete setting period

As described in section 5.3.3, a needle penetration test is used to evaluate the stiffness of the concrete to identify the initial and final set of the concrete. The needle can fully prick into the concrete in the first 3 hours. As the stiffness of the concrete grows over time, the length of the needle that can penetrate the concrete reduces. The resistance increases rapidly between 4 hours and 6 hours. At the 6th hour, only the tip of the needle can pierce into the concrete. Hence, it is concluded that the initial set occurs around the 4th hour, and the final set occurs around the 6th hour.

The ratio of TI of the signal at 300 kHz in specimen DD0, DD15, DD45, and DD60 are plotted ad compared in Fig. 4-12.

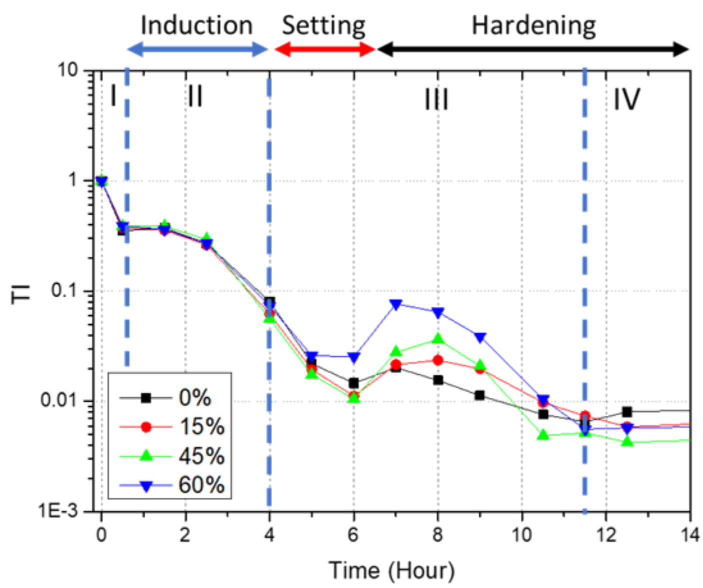

Fig. 4-12 Ratio of TI of signals at 300 kHz in specimens with various lengths of debonding.

Stage 1 (0-0.5 hours): The pre-induction stage (Stage 1) occurs during the first 0.5 hours. The waveguide condition changes from the bar in air to the bar embedded in the fluid concrete paste during this stage. The attenuation of the signal and the damping ratio at the steel-concrete interface increases dramatically. Hence, the signal strength of the received signal drops significantly, leading to a sharp reduction in the ratio of TI. The TI of signals dropped by 64.8%, 62.5%, 61.3%, and 61.1% for specimen DD0, DD15, DD45, and DD60, respectively. The TI of the signal increases with the size of the debonding. However, the difference is insignificant. The amplitude profiles of the time signals of two extreme cases, specimen DD0 and DD60, before and after pouring concrete are shown in Fig. 4-13. The amplitude of mode 1 in DD0 increases by 30%, but the arrival time of the peak is delayed. This is because the signal experiences strong dispersion due to the presence of the concrete. Mode 1 and mode 2 are merged, resulting in an increased amplitude. While the amplitude of mode 1 in DD60 reduces by 27.5%. The amplitude of mode 2 and mode 3 in DD0 reduces by 61.3% and 62%, and the amplitude of mode 2 and mode 3 in specimen DD60 decreases by 53.5% and 80.4%, respectively. Hence, these two modes are sensitive to the bond change at the steel-concrete interface.

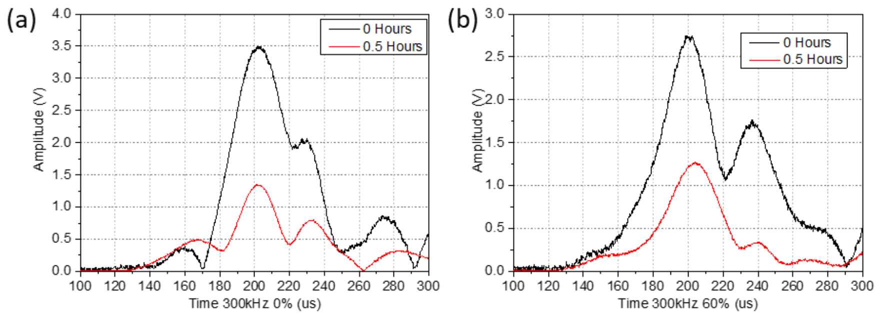

Fig. 4-13 Amplitude profiles of time signals in specimen (a) DD0 and (b) DD60 in stage 1

Stage 2 (0.5-4 hours): The dormant stage (Stage 2) occurs between 0.5 to 4 hours after pouring concrete. During this stage, the chemical reaction occurs slowly at a steady rate. The temperature of the concrete paste grows slowly at an average rate of 0.5°C /hour to approach the room temperature. As a result, the concrete paste remains in fluid (plastic) state. It is noted that the temperature increasing rate between 2.5 and 4 hours is more significant than that before 2.5 hours, indicating the speed up of cement hydration. However, the needle can easily penetrate the concrete paste. The resistance to needle penetration increases slightly with time. Hence it is concluded that the cement hydration process occurs but not yet reached its initial set.

As for the ultrasonic results, it is noted that the variation of the ratio of TI of all specimens is almost identical between 0.5 hours to 5 hours, regardless of the size of the debonding. The ratio of TI remains steady between 0.5 hours and 1.5 hours. The amplitude of mode 1 and mode 2 in specimen DD0 remains unchanged, but mode 3 increases by 21%, as shown in Fig. 4-14 (a). The effect of this increment in mode 3 on the signal strength is insignificant. In specimen DD60, the amplitude of mode1 remains unchanged. The peak amplitude of mode 2 and mode 3 reduces by 7% and 33.3%. The amplitude of mode 3 is much smaller than that of mode 2. Therefore, the reduction in the signal strength is not significant. During this period, the amount of hydrated cement is negligible. The stiffness of the concrete paste remains unchanged. The attenuation of the signal does not vary with time during this period. As a result, the TI remains steady.

The ratio of TI drops sharply from 1.5 hours to 4 hours. The ratio of TI drops by 9.3% to 10.3%. It indicates the occurrence of the setting of concrete, leading to the generation of hydrated cement. The concrete paste begins to stiffen, and the bond between steel and concrete paste starts to develop. As a result, the transmitted signal experience increasing attenuation and dispersion. More energy of the signal leaks into the surrounding concrete paste. These contribute to the reduction in the ratio of TI. During this period, the amplitude of all modes drops continuously with time, among which the amplitude of mode 2 drops the most. The amplitude in specimen DD0 drops by 57.6%, 84.4%, and 74.3% for mode 1, mode 2, and mode 3, respectively. While the amplitude in specimen DD60 drops by 41.8%, 80.3%, and 72.5% for mode 1, mode 2, and mode 3, respectively.

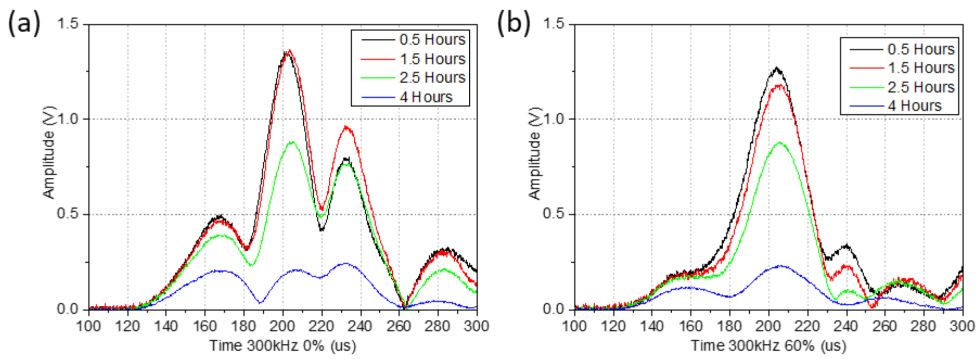

Fig. 4-14 Amplitude profiles of time signals in (a) specimen DD0 and (b) DD60in stage 2

Stage 3 (4-10 hours): The acceleration stage occurs between 4 and 11.5 hours after pouring concrete. The internal temperature of the concrete increases rapidly at a rate of 1.2°C/hour, indicating the acceleration of cement hydration. The concrete paste stiffens at a fast rate. During this stage, the concrete paste lost its plasticity with time and transferred from fluid paste to hardened solid. It is noted that the surface and internal temperature curves start to slip after the 4th hour. This is because the surface temperature is dominant by both the heat generated by cement hydration and the room temperature. The heat generated via cement hydration increases the temperature of the concrete, while the relatively low room temperature keeps the concrete cool. The chemical reactions occur at an increasing rate. More heat can be generated over time to increase the temperature of the concrete while the room temperature is steady at around 19°C. The difference between the surface and internal temperature increases with time. The stiffness of the cement paste increases significantly after 4 hours, and the concrete becomes solid at 6 hours that the needle cannot prick into the concrete. Hence, it is believed that the initial and final set occurs between 4-6 hours and the hardening of the solid concrete begins at the 7th hour.

The ratio of TI continues to drop by 6.6%, 5.1%, 4.6%, and 4.8% for DD0 to DD60 from the 4th hour to the 6th hour indicating the stiffening of the concrete paste due to the accelerated cement hydration. Then a sudden increment in the ratio of TI in all specimens is observed at the 7th hour. The ratio of TI increases by 0.6%, 1.0%, 1.7%, and 5.1% for DD0 to DD60 from 6 hours to 7 hours. The increment of the ratio of TI is more significant in specimen with a larger size of debonding. The same phenomenon is observed in specimen with plain bars. Hence, the sudden jump in the ratio of TI can be used to identify the completion of concrete setting and the initiation of concrete hardening.

For the variation in the time signals, the amplitude of the modes continues to reduce from the 4th hour to the 6th hour and then increases from the 6th hour to the 7th hour in specimen DD0. The amplitude reduces by 77.7%, 74.6%, and 90.3% for mode 1, mode 2, and mode 3 at the 6th hour. From the 6th hour to the 7th hour, the amplitude of mode 1 continues to drop by 27%, but mode 2 and mode 3 increases by 47% and 53%. For specimen DD60, the amplitude of mode 1 first drops by 37.7% from the 4th hour to the 6th hour and then increases by 22.1% from the 6th hour to the 7th hour. Mode 2 and mode 3 are merged at the 5th and the 6th hour, make it difficult to distinguish the wave modes. During the 7th hour, the amplitude of mode 2 and mode 3 increases dramatically that even higher than the amplitude of the modes during the 4th hour.

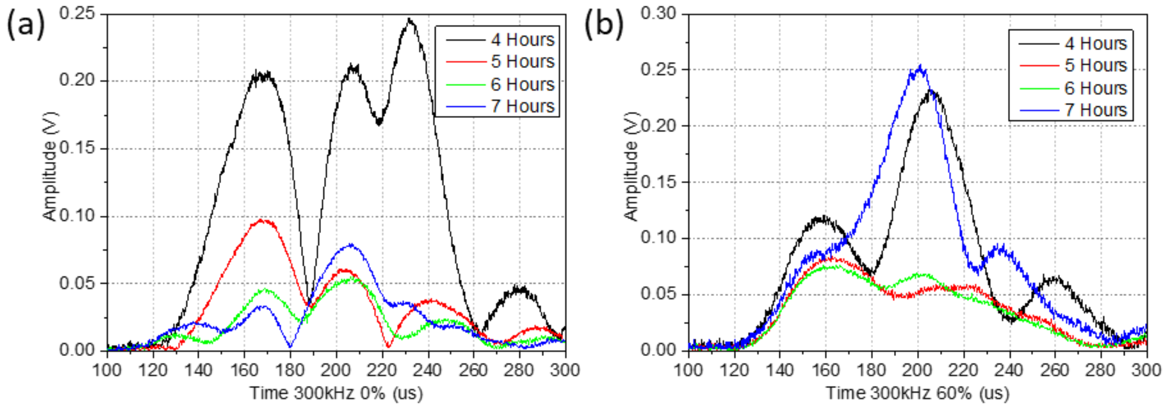

Fig. 4-15 Amplitude profiles of time signals in (a) specimen DD0 and (b) DD60in stage 3 -setting

The ratio of TI in specimen DD0 and DD60 drops continuously from 2% at the 7th hour to 0.7% at the 11.5th hour. While the ratio of TI in specimen DD15 and DD45 first increases 0.2% and 0.9%, then drops by 1.6% and 3.1 %, respectively. During this period, the concrete becomes solid, and the strength of the solid concrete increases due to the continuous hardening. More energy leaks into the concrete from the waveguide, leading to a continuous reduction in the strength of the received signals. Therefore, the ratio of TI reduces with time during this stage.

Fig. 4-16 show the amplitude profiles of the time signals in specimen DD0 and DD60 from the 7th hour to 11.5th hour. It is noted that, in specimen DD0, the amplitude of mode 1, mode 2, and mode 3 reduces by 19.6%, 80.7%, and 41.4%, respectively. While the amplitude of the modes drops by 75.4%, 95.9%, and 92.6%, respectively. The amplitude of mode 2 drops the most in all specimens regardless of the size of the debonding. Hence, mode 2 is sensitive to the hardening of the concrete.

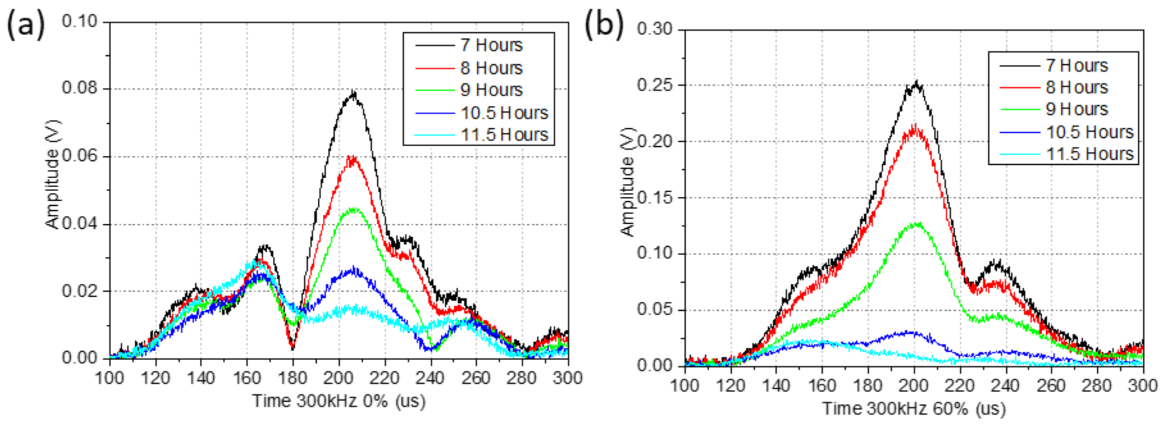

Fig. 4-16 Amplitude profiles of time signals in (a) specimen DD0 and (b) DD60in stage 3 -hardening

Stage 4 (11.5 – 12.5 hours): The concrete hydration reaches the deceleration stage after 11.5 hours. The temperature increment slows down at a rate of 0.6°C/hour, similar to the rate during stage 2. It indicates the slowing down of the concrete hydration. At this stage, the concrete has gained enough stiffness and strength to stand alone without the mould. The ratio of the TI in all specimens becomes steady. It is known that the concrete continuously gains strength during stage 4 and 28 days of curing. Hence, guided waves are no longer sensitive to detect the strength variation in the surrounding concrete.

Fig. 4-17 shows the Amplitude profiles of the time signals in specimen DD0 and DD60 from 11.5th hour and 12.5th hour. For specimen DD0, the amplitude of mode 1 becomes dominant, and the amplitude remains steady, and the amplitude of mode 2 and mode 3 increases by 16.6% and 52.2% during this period. As a result, the total energy of the signal does not vary significantly with time. For specimen DD60, mode 1 dominates the received signal while mode 2 and mode 3 almost disappear. The two Amplitude profiles in Fig. 4-17 (b) are almost identical. Hence, it further confirms that the signals become steady during stage 4, and it can be used to identify the time to safely remove the mould without damage the integrity of the concrete.

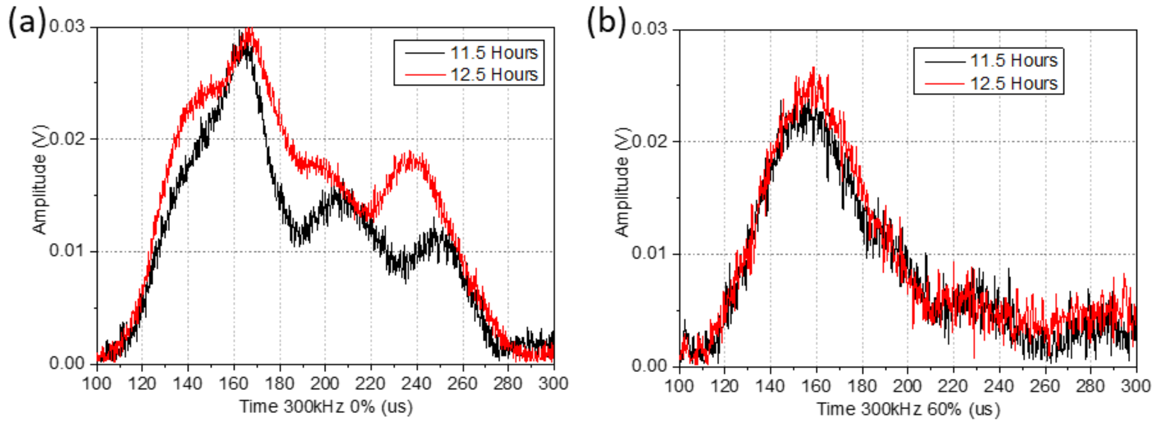

Fig. 4-17 Amplitude profiles of time signals in (a) specimen DD0 and (b) DD60in stage 4

4.4. Monitoring the setting of cement paste and concrete using cast in PZT based transducer.

The guided wave-based technique has been proved to be an effective method to monitor the setting of concrete reinforced with both plain bar and deformed bar in the previous sections. The steel bars in these specimens are partially embedded in concrete with two ends exposed to air. However, the reinforcements are fully embedded in concrete in civil infrastructure for protection purposes. Furthermore, a strong reflection of guided waves occurs at the exposed bar to the embedded bar interface, leading to reduced strength of the transmitted signal. In addition, the reinforcements in civil infrastructures are usually meters in length, and the hooks are used at the ends for anchoring purposes. Hence, the guided wave will experience strong attenuation while traveling in long bars and even disappear due to the increased attenuation when fresh concrete is poured into the mould or during the setting period.

To overcome these drawbacks, a compact PZT wafer-based transducer is proposed to monitor concrete setting, as shown in Fig. 4-18. The transducer consists of 4 PZT wafers and 2 mild steel plain bars. The steel bars are 12 mm in diameter and 100 mm in length. The spacing between the bars is fixed as 70 mm using cable ties. Both ends of the bars are machined to a smooth surface for attaching PZT wafers. The surface of the PZT wafer is fully covered with a layer of superglue and a layer of silicone gel to protect it from damage and short-circuit when cast in fresh concrete. The transducer features the function of both guided wave systems and smart aggregates. The signal can be excited at one end of the bar, and the transmitted signal can be received at the other end of the same bar. The same technique used in 4.2 can be employed here to monitor the concrete setting. The relatively short length of the bar can significantly reduce the attenuation of the transmitted signals, leading to a strong transmitted signal.

The signal can also be excited in one bar and received from the other bar. The signal can transmit between bars in two ways. One is that the wafer vibrates the concrete paste/hardened concrete. The signal transmits through concrete directly from one wafer as bulk waves and is received by the other. The other way is that the waves first travel in the steel bar as the guided wave. The waves continuously leak into the surrounding concrete when traveling. Part of the leaked waves can transmit into the other bar and being received the wafer. It is known that the waves can leak in all directions, and the damping ratio of the concrete is high. The wave leakage between the two bars is not significant. Hence, the received signal is dominated by the bulk waves.

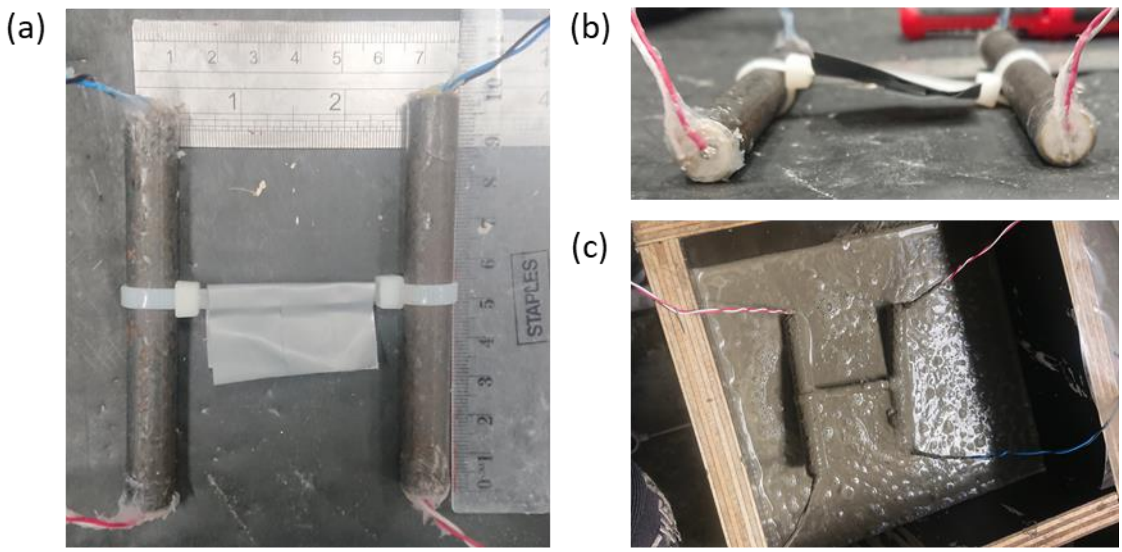

Fig. 4-18 Cast in PZT transducer (a) top view with dimensions, (b) side view and (c) transducer in fresh concrete.

The phenomenon that the TI rises after the final set of the concrete specimens is repeatedly observed in the previous tests. In order to investigate the cause of this phenomenon, more specifically, whether it is the cement hydration or the binding of aggregates that cause the TI rise, a cement paste specimen of the same size and water-cement ratio as the concrete specimen is used. A short bar with PZT wafers attached at both ends is cast in a cement paste, and the guided waves are excited on and received by the cast-in PZT wafers. Another advantage of using a cement paste is that standard cement setting tests can be employed to detect the initial set and the final set of the specimen. A spring-type penetrometer, as shown in Fig. 4-19, is used to detect the initial set and final set of the cement paste according to ASTM C403. The penetration resistance of the setting cement paste is measure in kilogram-force and the maximum reading of the penetrometer is 140 kgf. The area of the penetration needle shank is 32, 65, 161, 323, and 645 mm^2, giving a measurement of the penetration resistance of up to 42.88 MPa. The initial and final set occur when the penetration resistance reading equals or exceeds 3.5 MPa and 27.6 MPa, respectively.

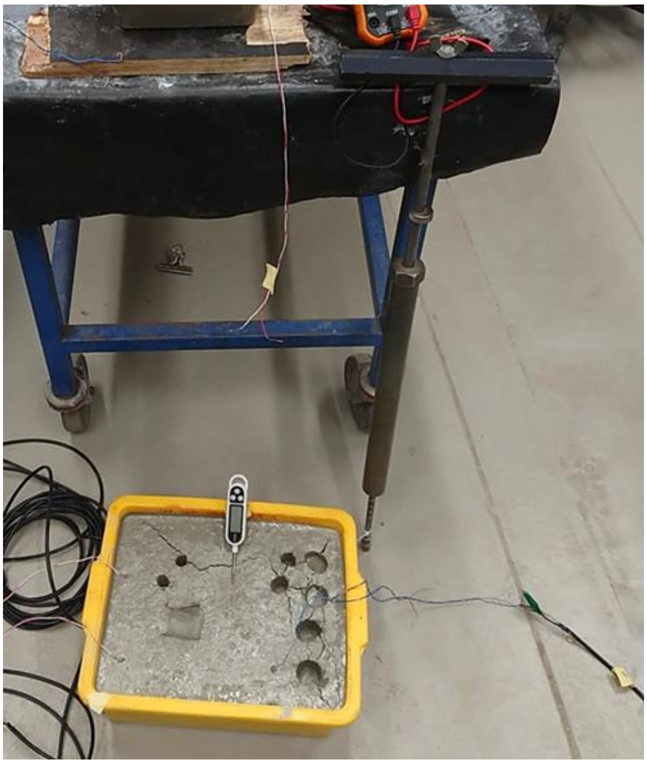

Fig. 4-19 spring type penetrometer

4.4.1. Frequency response of signals

4.4.1.1. Cement paste

Due to the small size of the waveguide, a 10-cycle Hanning-windowed sinusoidal tone burst is used as the input signal to reduce the wavelength of the signal while maintaining high signal strength. Fig. 4-20 shows the frequency response of the signal in the bar cast in the cement paste. It is noted that even in the bar in air, the frequency response of the signals in this bar is different from that in the bar cast in concrete. This phenomenon is observed in all the conducted experiments. The frequency response of the signals varies from bar to bar, although the bars are the same type with the same length and diameter. Hence, obtaining the frequency response of the signals in the bar of interest before casting is essential for selecting excitations and reinforcement monitoring. It is recommended first to check the frequency response of the signals and use the bars with similar responses as the waveguide. However, for concrete setting monitoring, it is observed that the amplitude of the signal is dominating the setting monitoring through the waveguide. Hence, the frequency response of signals does not significantly affect the ability of guided waves for setting monitoring.

The frequency response of signal in bar cast in cement paste shows a clear 2 zones. Zone 1 has a frequency range from 200 kHz to 400 kHz with a peak at 270 kHz, and zone 2 has a frequency range from 400 kHz to 600 kHz with a peak at 530 kHz. At the end of the experiment, the peak frequency slowly shifts from 270 kHz to 250 kHz in zone 1 and from 530 kHz to 550 kHz in zone 2. In general, the amplitude decreases with the setting of cement paste, and the fluctuation of the frequency response remains similar throughout the setting period. Hence, the peak frequencies, 270 kHz and 530 kHz, are used to monitor the setting of the cement paste.

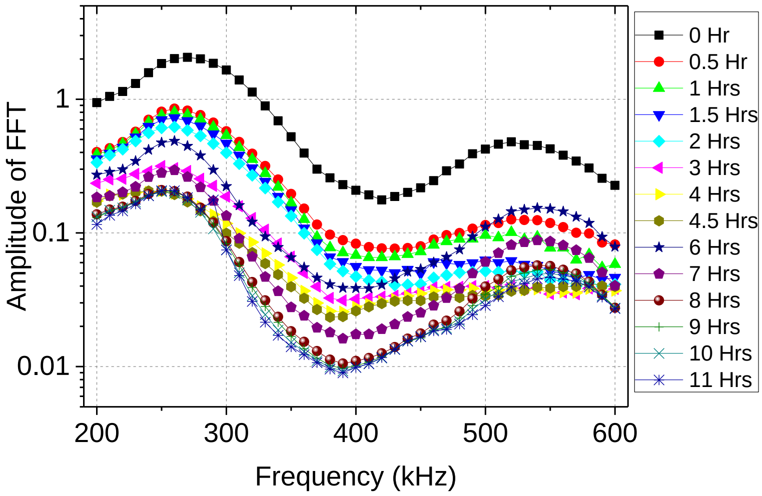

Fig. 4-20 Frequency sweep results of guided wave in plain bar cast in cement paste.

4.4.1.2. Concrete

The TI of signals at various excitation frequencies during the setting period is presented in Fig. 4-21. It is noted that, in the bar in air scenario, the TI of the signals varies significantly with the excitation frequency. Three zones can be identified. The TI in zone 1 increases sharply from 200 kHz and peaks at 250 kHz. Then the TI reduces slightly to 260 kHz. The TI in zone 2 first increases from 280 kHz and peaks at around 320 kHz, then the TI reduces sharply to 450 kHz. The TI in zone 3 first reduces from 460 kHz to 540 kHz. Then it becomes steady at excitation frequency between 550 kHz and 600 kHz.

Zone 1 has a frequency range from 200 kHz to 260 kHz with a peak at 250 kHz, which is close to the resonance frequency of the PZT wafer. The difference in TI of the signal at the frequency from 240 kHz to 260 kHz is insignificant. The amplitude of TI decreases with the concrete setting while the frequency of the peak shifts from 250 kHz to 230 kHz when the concrete is hardened at 12.5 hours. it is also noted that the amplitude of the TI reduces sharply in the first 4 hours by about 72.2%, while the TI reduction between 4 hours and 12.5 hours is only about 7.6%.

Zone 2 has a frequency range from 280 kHz to 450 kHz, with a peak at 330 kHz. The TI reduces sharply by 90% in the first 8 hours then the TI reduction slows down. The TI reduces about 3.4% from 8 hours to 12.5 hours. The peak of the frequencies first shifts to a higher frequency at 340 kHz at 6 hours. Then, the peak frequency continuously reduces from 6 hours to 12.5 hours. The frequency of the peak at 12.5 hours is 320 kHz. It is also noted that the rising and falling fluctuation in zone 2 is getting flattened over time.

Zone 3 has a frequency range from 460 kHz to 600 kHz. The TI reduces significantly when fresh concrete is poured into the more, i.e., the condition of waveguide changes from the bar in air to the embedded bar. The variation of TI during the setting period (12.5 hours) is insignificant. The fluctuation of TI with excitation frequency remains steady, continuously reducing from 460 kHz to 540 kHz and constant between 560 kHz to 600 kHz.

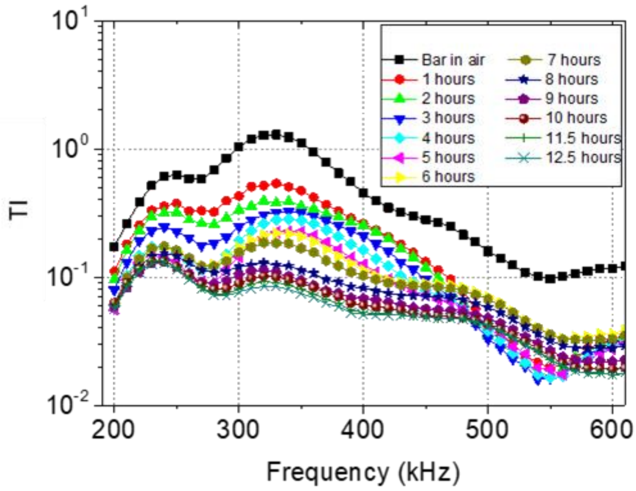

Fig. 4-21 Frequency sweep results of guided wave in plain bar cast in concrete

Fig. 4-22 shows the TI variation of bulk waves through concrete at different excitation frequencies. The range of the frequency sweep is between 200 kHz and 400 kHz. In contrast to the TI of guided waves, the TI of the bulk waves increases with the concrete setting. Only the TI variation for the signal between 8 hours and 12.5 hours is presented. The PZT wafer records no signal at any frequencies within the first 8 hours after pouring concrete. The Pattern of the TI can be divided into 2 zones, one is between 200 kHz and 280 kHz, and the other one is between 300 kHz and 400 kHz.

Zone 1 has a frequency range of 200 kHz to 280 kHz. The amplitude of the TI increases with a concrete setting. The change in the shape of the fluctuation in this zone is insignificant, and a clear rising and falling fluctuation are observed throughout this period. The peak frequency is 250 kHz at 8 hours, and then the peak frequency shifts to 240 kHz at 12.5 hours when the concrete is hardened. The TI increases sharply from 8 hours to 10 hours by 3.7 times. Then the TI increment slows down, and the TI increases by 1.7 times from 10 hours to 12.5 hours.

Zone 2 has a frequency range from 300 kHz to 400 kHz. Initially, the fluctuation of the TI at various frequencies is negligible. This is because the amplitude of the signal is similar to the amplitude of the noise. At this stage, the TI of the signal is significantly influenced by the amplitude of the noise, although a noticeable wave packet can be observed in the signals as the concrete continues to get hardened with time, the amplitude of the signal increases leading to a higher signal-to-noise ratio. The amplitude of the signal dominates the amplitude of the TI. The influence of the frequency response on the amplitude of TI is getting more and more significant. Hence, a rising and falling fluctuation in the TI is getting more significant with time.

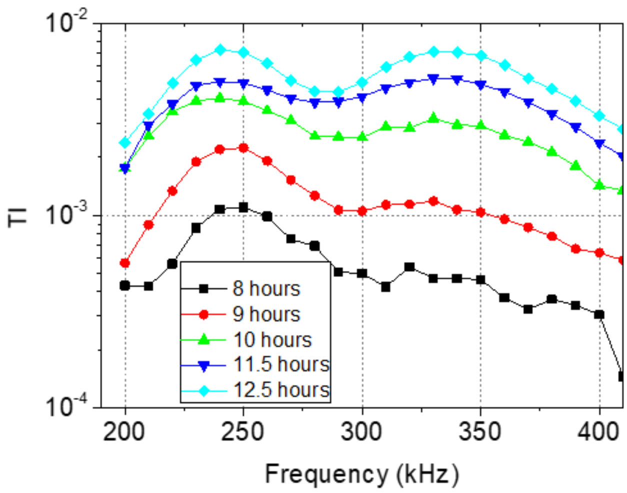

Fig. 4-22 Frequency sweep results of the bulk waves through concrete

4.4.2. Selection of excitation frequency

4.4.2.1. Cement

By analyzing the frequency response of the signal in bar cast in cement paste, it was found that the signal at the frequencies 270 kHz and 530 kHz had the strongest amplitude, and the signals remained strong throughout the setting process of the cement paste. Fig. 4-23 shows the time signal at 270 kHz and 530 kHz in the bar in air scenario. By referring to the dispersion curves of a 12 mm diameter round steel bar, it was identified that the wave packet in the time signal at 270 kHz was the F (1,2) mode.

This mode dominated the time signal, disregard the co-existence of L (0,1) mode, F (1,1) mode, F (1,2) mode, and F (1,3) mode in time signal at 270 kHz. While in time signal at 530 kHz, 3 wave packets were observed, the first one was L (0,2) mode, the second one was a merged F (1,1) mode, and F (1,2) mode and the third one was F (1,3) mode. According to the dispersion curves, the group velocity of F (1,1) mode and F (1,2) mode at 530 kHz was almost identical. Hence the two modes were well merged to form one wave packet. It was also noted that part of the F (1,3) mode was merged into the second wave packet.

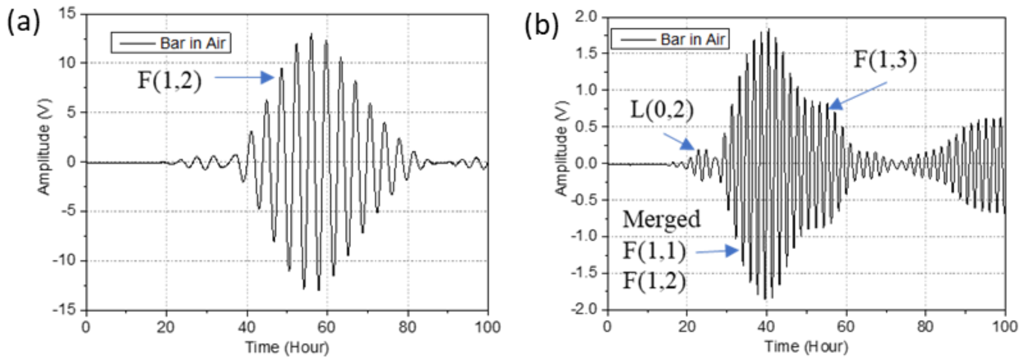

Fig. 4-23 Time signal at (a) 270 kHz and (B) 530 kHz in the bar in air.

Fig. 4-23 shows the mode shape of F (1,1) mode at 270 kHz. F (1,1) mode shows a significant amount of axial displacement near and peaked at the surface of the bar while no axial displacement around the inner radius (0-3 mm) of the bar. The energy density of F (1,1) mode is uniformly distributed along the bar radius. The energy density slightly increases with radius in the inner 5 mm of the bar radius, and the peak energy density is at the surface. Therefore, F (1,1) mode at 270 kHz is sensitive to the bond development near the surface of the bar.

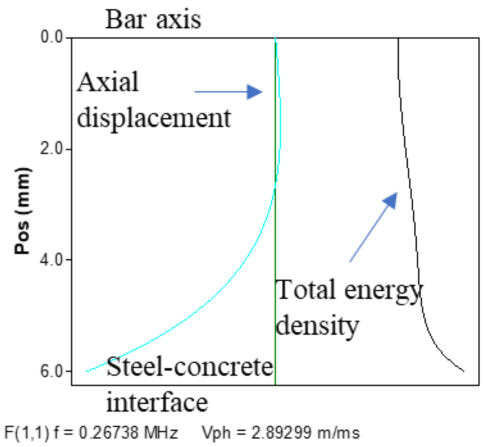

Fig. 4-24 Mode shape of signal in 12 mm steel bar at 270 kHz.

Fig. 4-25 shows the mode shape of the four modes in the time signal at 530 kHz. L (0,2) mode shows a significant amount of axial displacement around both the surface and the core of the bar while the direction of the displacement is opposite to each other. The total energy density varies significantly along the bar radius, but a significant amount of energy concentrates near the core or the bar. F (1,1) mode shows a significant amount of axial displacement and total energy density near the surface, while F (1,2) mode shows a significant amount of total energy density around the surface, but the axial displacement is peaked at 2 mm beneath the surface. In F (1,3) mode, the total energy density peaks around the bar's core and the energy density is negligible near the surface. No noticeable axial displacement is observed at the core and the surface of the bar and the maximum axial displacement occurs in the midway. Hence, it is concluded that F (1,1) mode and F (1,2) mode are sensitive to the bond development at the steel surface, while F (1,3) mode is sensitive to the change in the bar. However, the bar does not change during concrete setting. The change, in this case, is the energy leaked into the surrounding concrete due to the clipping effect of the hardened surrounding material. Based on the mode shape of L (0,2) mode, it looks like this mode is sensitive to both the change at the surface and in the bar. However, the amplitude of this mode is much smaller than the other modes. Hence, the influence of L (0,2) mode

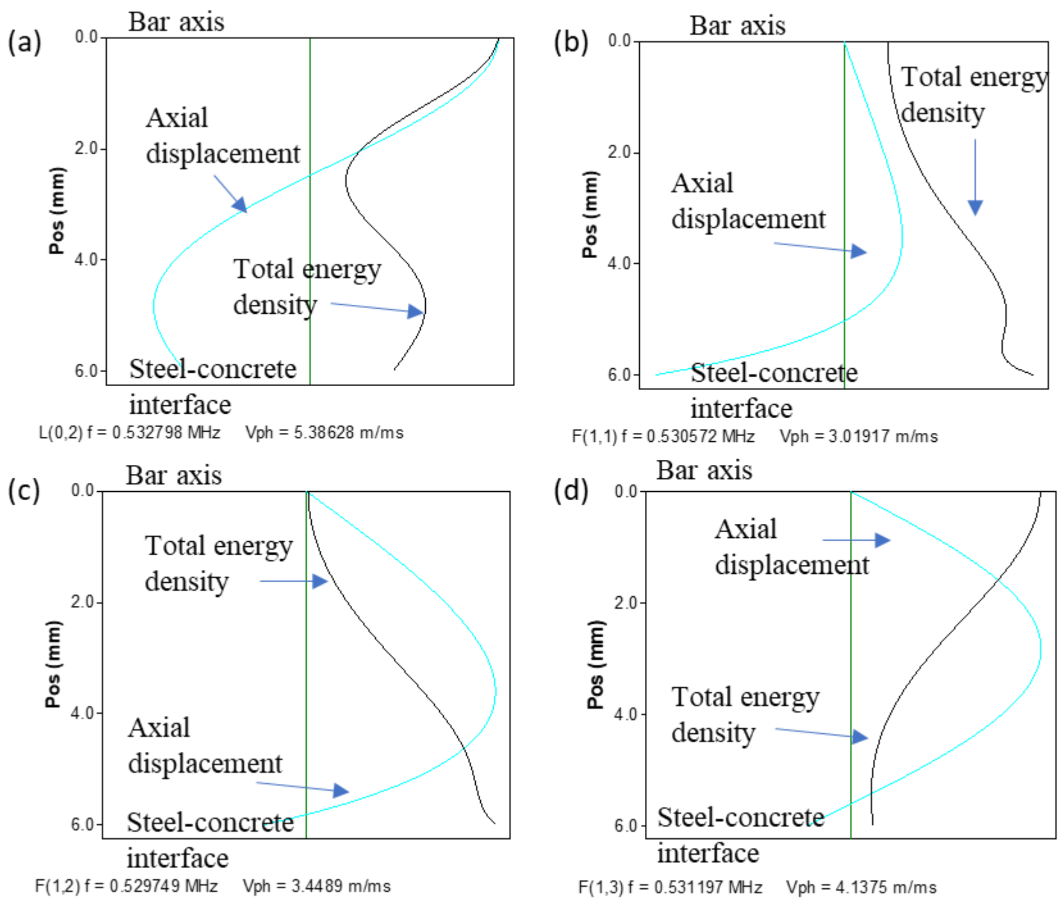

Fig. 4-25Mode shape of signal in 12 mm steel bar at 530 kHz (a) L (0,2) mode, (b) F (1,1) mode, (c) F (1,2) mode and (d) F (1,3) mode.

By analyzing the waveform and the mode shape of the modes in the time signals, it is concluded that the dominating modes in both signals are sensitive to the bond development of the steel-concrete interface. However, the signal at 270 kHz contains one wave packet while the signal at 530 kHz contains three merged wave packets. The waveform of the signal at 270 kHz is much simpler than that at 530 kHz while delivering a similar sensitivity to the bond development. Hence, the signal at 270 kHz is used to monitoring the setting of cement paste.

4.4.2.2. Concrete

The Frequency response of the short bar cast in concrete is similar to that in the bar in concrete with exposed ends, as discussed in Section 4.2.2. Three clear zones can be identified with a peak frequency at 240 kHz, 320 kHz, and 600 kHz. Hence, these frequencies are analyzed to identify the frequency for concrete setting monitoring.

Fig. 4-26 (a) shows the time signal through the bar at 240 kHz in the bar in air condition. Two wave packets can be observed in the time signal, the first one denotes the F (1,1) mode, and the second is the F (1,2) mode. The amplitude of F (1,2) mode is about two times larger than that of F (1,1) mode. Fig. 4-26 (b) and (c) show the mode shape of F (1,1) and F (1,2) mode. Both modes have a significant amount of axial displacement and total energy density at and in the vicinity of the bar surface. Hence, both modes are sensitive to the change at the steel-concrete interface, and they can be used to monitor the bond development during the setting of concrete.

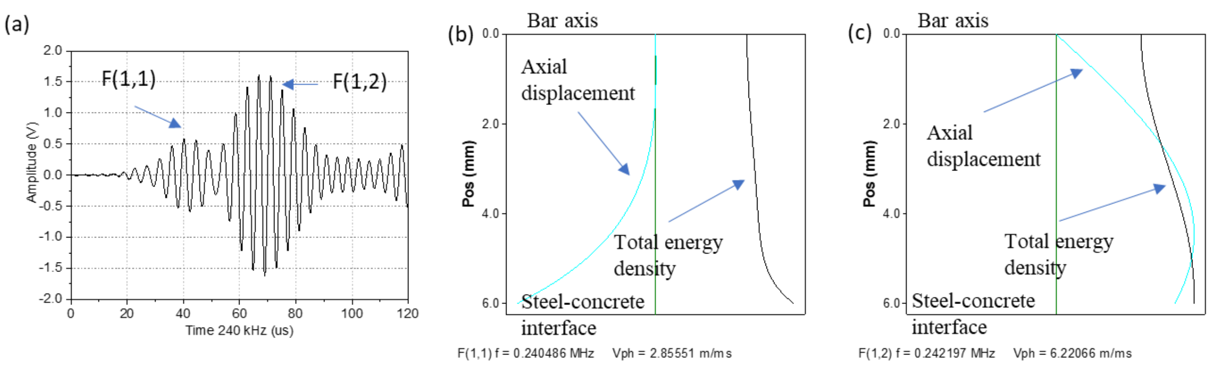

Fig. 4-26 (a) Time signal at 240 kHz, (b) mode shape of F (1,1) at 240 kHz, and (c) mode shape of F (1,2) at 240 kHz

Fig. 4-27 (a) shows the time signal at 320 kHz in the bar in air. There are three wave packets in the time signal. The first wave packet is a mixture of L (0,2) mode and F (1,3) mode. The second wave packet is the F (1,2) mode. The third wave packet is merged with the second wave packet, and the ToF is around 90 us. However, according to the dispersion curves, no wave mode should come at this time. Hence, it is believed that this wave packet is the reflection from the other end of the bar. Fig. 4-27 (b)-(d) show the mode shape of L (0,2), F (1,3) and F (1,2) mode. L (0,2) mode has dominated the amount of axial displacement and total energy density around the surface of the bar. The total energy density of F (1,3) and F (1,2) is distributed along the radius of the bar with a peak at the surface. While the axial displacement for these modes is zero at the core of the bar and peaked at around 2 mm underneath the surface. Hence, F (1,3) and F (1,2) mode is also sensitive to the surface of the bar. Therefore, they can also be used to monitor bond development.

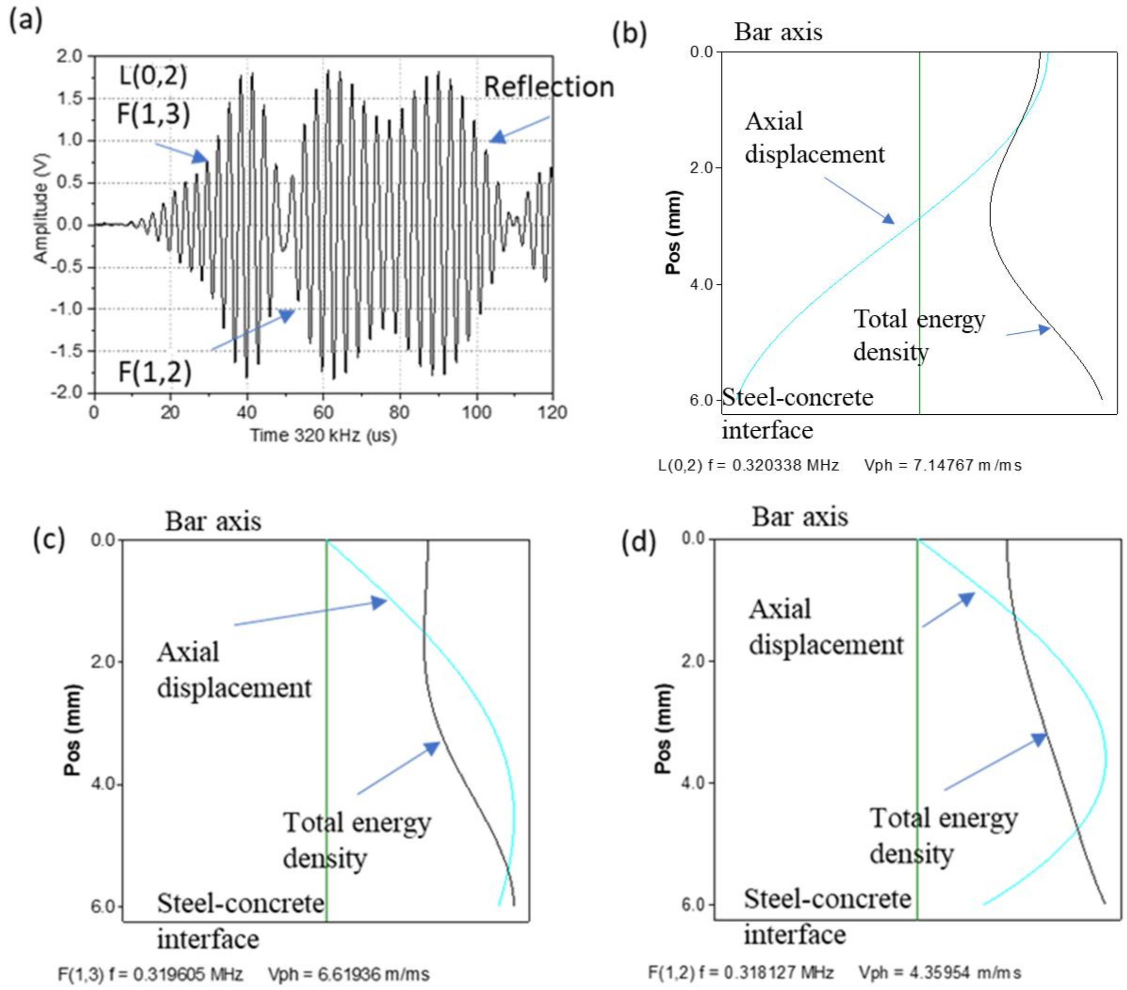

Fig. 4-27 (a) Time signal at 320 kHz, (b) mode shape of L (0,2) at 320 kHz , (c) mode shape of F (1,3) at 320 kHz and (d) mode shape of F (1,2) at 320 kHz

Fig. 4-28 (a) shows the time signal at 530 kHz in the bar in air. There are two wave packets in the time signal: L (0,3) mode followed by L (0,2). The amplitude of these modes is similar. It is recalled that in the time signal in a 400 mm long steel bar, the L (0,3) mode dominates the signal and the L (0,2) is much smaller. This might be caused by the rapid attenuation of L (0,2) mode when traveling in the waveguide while the L (0,3) mode remains strong. Fig. 4-28 (b) and (c) show the mode shape of L (0,3) and L (0,2) mode. L (0,3) mode shows a significant amount of axial displacement and total energy density around the core of the bar, while the amount near the surface is negligible. In L (0,2) mode, the axial displacement and total energy density are mainly concentrated around the core, and a small amount is near the surface. Hence, both modes are core-seeking mode. They can be used to monitor the change in the bar. It is also noted that the L (0,2) mode at 320 kHz is a surface-seeking mode in which the axial displacement and total energy density are concentrated around the bar surface. By increasing the excitation frequency from 320 kHz to 530 kHz, L (0,2) mode shifts from surface-seeking mode to core-seeking mode.

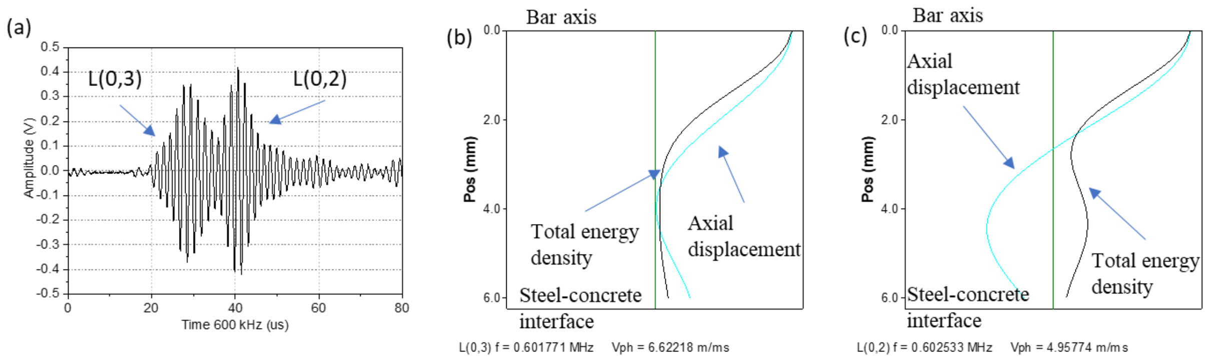

Fig. 4-28 (a) Time signal at 530 kHz, (b) mode shape of L (0,3) at 530 kHz and (c) mode shape of L (0,2) at 530 kHz.

4.4.3. Monitoring cement setting using selected signals.

4.4.3.1. Cement paste

Penetration resistance tests were performed using a spring-type penetrometer according to ASTM C403. The first test was taken after an elapsed time of 3 hours after mixing the cement paste, and the subsequent tests were taken at a 0.5 hours interval. Fig. 4-29 shows the penetration resistance of the cement paste. The test was conducted between 3 and 5 hours after mixing. The initial setting time of the cement paste was measured to be 3.5 hours, and the final setting time was estimated to be around 4.7 hours. The last reading was taken at 5 hours with a penetration resistance of 36.75 MPa. The penetration needle could still penetrate the cement paste after 5 hours. However, the needle could not be fully penetrated in the cement and the depth of the penetration reduced with time, indicating that the setting still occurred even after the final set. No penetration could be made at the 6th hour. Hence it was concluded that the cement paste became solid after 6 hours after mixing.

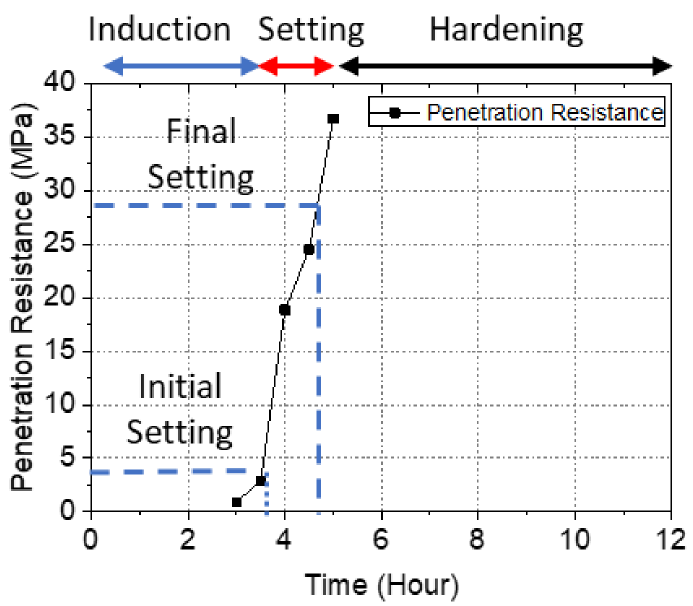

Fig. 4-29 Penetration resistance of the cement paste.

Fig. 4-30 shows the measured temperature in cement paste during the setting period. The measured room temperature was at around 27 °C during the setting period, which was 2°C higher than the test temperature recommended by ATSM C403. The first reading was 27.7°C at the 0.5th hour after cement mixing. The temperature slowly reduced to 27.1°C after 2 hours. Then the temperature increased rapidly from 28.3°C at the 3rd hour to 48.2°C at around the 7.5th hour. From the 8th hour to the 11th hour, the temperature continuously reduced from 48.2°C to 38.8°C. Hence, it was concluded that stage 1 of cement hydration was in the first hour, stage 2 was between the 1st hour to the 3rd hour, stage 3 was between the 3rd hour and the 8th hour, and stage 4 was between the 8th hour to the 11th hour.

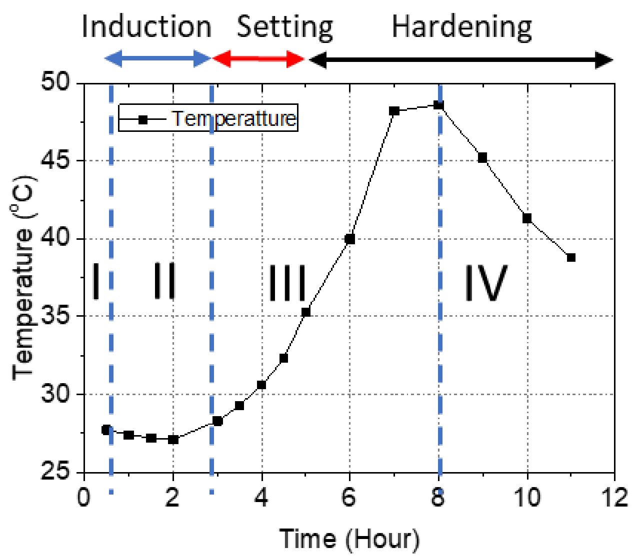

Fig. 4-30 Temperature variation in cement paste with cast-in transducer during cement setting.

Fig. 4-31 shows the ratio of TI of the signal at 270 kHz and 530 kHz during the setting of cement paste. The amplitude of the ratio dropped significantly once the cement paste was poured into the mould. The amplitude reduction of 630 kHz was reduced more than that of 270 kHz, about 12 %. Then the amplitude of the ratio dropped relatively linearly from the 0.5th hour to the 4.5th hour. While the amplitude of 530 kHz dropped exponentially from the 0.5th hour to the 3rd hour, and the amplitude remained steady from the 3rd hour to 4.5th hour. A continuous amplitude increment was observed in both 270 kHz and 530 kHz from the 3rd hour and peaked at the 6th hour. The amplitude continued to drop and became steady after 8 hours. The overall pattern of the amplitude of TI variation in both frequencies was similar, but the amplitude of TI of 270 kHz reduced linearly, and the reduction rate was slower between 0.5th hour to 4.5th hour. Hence it can provide more information about the setting of cement during this period. In addition, the waveform of the signal at 270 kHz is less complex than that of 530 kHz, where the signal at 270 kHz only contains one dominant wave mode, F (1,2), but the signal at 530 kHz contains four wave modes. Hence, the signal at 270 kHz is much easier to analyze, and the result is not affected by the difference in the sensitivity of wave modes to detect the bond development. Therefore, the signal at 270 kHz is used to monitor the setting of cement paste.

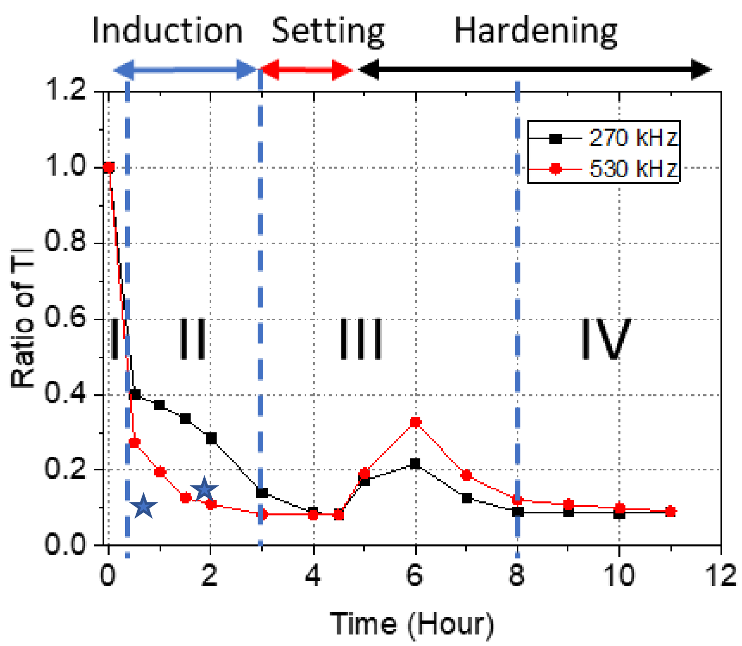

Fig. 4-31 Ratio of TI of guided waves in cement paste.

Stage 1 (0-0.5 hours): the first 0.5 hours is the pre-induction stage. During this stage, the temperature of the cement paste rises rapidly due to the mixing of cement with water. Due to the difficulty of accessing the cement paste during the mixing, no temperature measurement is during this stage. The ultrasonic measure is only taken before and after pouring the mixed cement paste into the mould. The condition of the waveguide changes from the bar in air to the bar embedded in cement paste. Due to the presence of the surrounding cement paste, the attenuation of the guided waves increases dramatically, and signals continuously leak into the surrounding cement paste while traveling in the waveguide. Hence, the amplitude of the received signal reduces significantly, leading to a reduction in TI.

The TI of the signal at 270 kHz dropped by 60% once the cement paste was poured into the mould, indicating the significant attenuation of the guided waves due to the presence of surrounding cement paste. The amplitude profiles of the time signals at 270 kHz in stage 1 are shown in Fig. 4-32. The F (1,2) mode amplitude dropped by 48.7% once the cement paste was poured into the mould. It was also noted that there was a second wave packet that arrived at around 160 us. This was the F (1,2) mode reflected from the excitation side of the bar. After the cement pouring, the amplitude of the reflection reduces significantly. Both the amplitude and the cycle number of the wave packet were reduced.

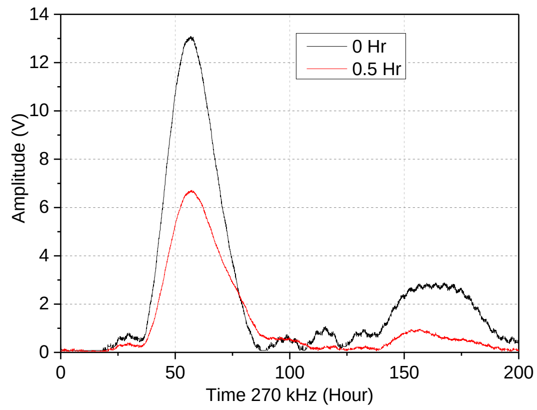

Fig. 4-32 Amplitude profiles of time signals at 270 kHz in bar embedded in cement paste in stage 1.

Stage 2 (0.5-3 hours): The Dormant stage occurs between the 0.5th hour and the 3rd hour according to the temperature measurement and the penetration test. During this stage, the cement paste remained fluid, and the chemical reactions were slow, leading to a relatively steady temperature. Between the 0.5th hour to the 2nd hour, the Temperature slowly reduced to 27.1°C, which was similar to the room temperature. The temperature then increases to 28.3°C at the 3rd hour after cement pouring, indicating the acceleration of the cement hydration. Hence, it was concluded that the acceleration stage occurs after 3 hours of cement mixture.

The TI dropped slowly by 11.5% from 0.5 hours to 2 hours. Then the rate of TI reduction increases with time. The TI dropped by 14.4% from the 2nd hour to the 3rd hour. The pattern of the TI reduction matched well with the variation of the measured temperature. This is because the cement hydration proceeds at an increasing rate, the stiffness of the cement paste increases, leading to an increasing attenuation of the guided wave. Fig. 4-33 shows the amplitude profiles of time signals in stage 2. The amplitude of F (1,2) mode dropped by 12.7% from the 0.5th hour and the 2nd hour and by 18.3% from the 2nd hour to the 3rd hour. It indicated the increasing rate of cement hydration. The cement paste started to stiffen, and the bond between the steel bar and cement pates began to develop. As a result, the attenuation of the guided waves increased with time, and the increasing amount of energy leaked into the surrounding cement paste. This contributed to the increasing rate of TI reduction.

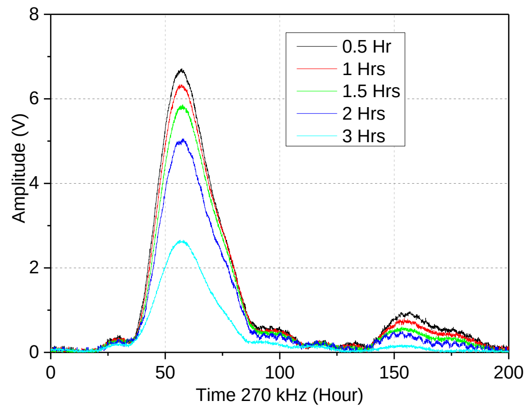

Fig. 4-33 Amplitude profiles of time signals at 270 kHz in bar embedded in cement paste in stage 2.

Stage 3 (3-8 hours): The acceleration stage occurs between the 3rd hour to the 8th hour. The cement hydration occurs rapidly during this stage, indicated by the rapid increment of the temperature. The cement paste continues to stiffen at an increasing rate, the cement paste loses its plasticity with time, and the state of the cement paste transfers from fluid to solid. The initial set and the final set of the cement occur during this stage. The initial set occurs at 3.5 hours after cement mixing, while the final set occurs between the 4th and 5th hour.

The TI of the signal showed a 3-stage variation. First, the TI dropped slowly by 5.8% from the 3rd hour to the 4.5th hour. Then the TI increased by 13.4% from the 4.5th hour to the 6th hour. From the 6th hour to the 8th hour, the TI dropped sharply by 12.6%. Fig. 4-34 shows the amplitude profiles of the time signal during stage 3. The amplitude of F (1,2) mode dropped by 6.9% from the 3rd hour to the 4th hour. Then the amplitude remained steady for the 0.5th hour before it started to rise. A significant amplitude rise, about 21.3%, was observed from the 4.5th hour and peaked at the 6th hour, followed by a continuous drop of about 18.8% until the 8th hour.

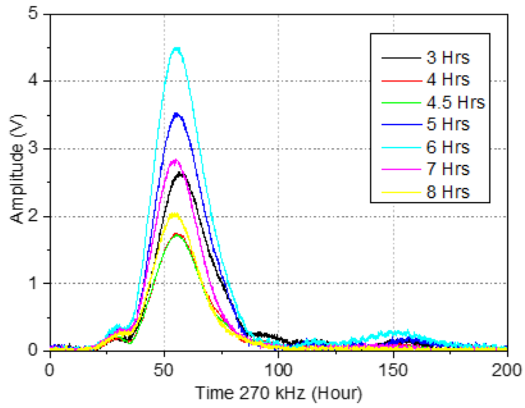

Fig. 4-34 Amplitude profiles of time signals at 270 kHz in bar embedded in cement paste in stage 3.

Stage 4 (8-11 hours): The deceleration stage occurs after the 8^{th} hour of cement mixing. The temperature of the specimen starts to reduce, as shown in Fig. 4-30, which indicates the slowing down of the cement hydration process. The cement paste has become solid state and gained enough stiffness and strength to remove the mold during this stage safely. The TI of the signals at this stage remained steady, at around 8.9%, disregarding the fact that the strength and the stiffness of the cement paste continuously rose during stage 4. Fig. 4-35 shows the amplitude profiles of the time signals in stage 4. It was observed that the signals were almost identical. It confirmed that the signals became steady, and the guided waves were not influenced by the hardening process of the cement paste.

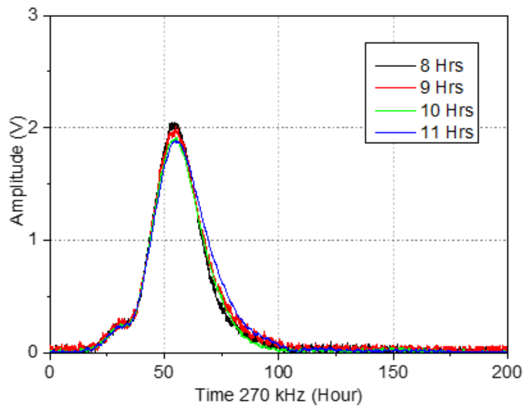

Fig. 4-35 Amplitude profiles of time signals at 270 kHz in bar embedded in cement paste in stage 4.

4.4.1. Monitoring concrete setting using selected signals.

One needle thermometer was cast in the concrete specimen to measure the temperature of the concrete during the setting period. The tip of the needle was located at 150 mm into the concrete to measure the internal temperature. The room temperature was constant at around 22 °C during the setting period. The temperature variation in the concrete during the setting period is shown in Fig. 4-36. The concrete temperature increased slowly and approached the room temperature in the lab in the first 4 hours. From the 4^{th} hour to the 10^{th} hour, the temperature of the concrete increased rapidly, and the rate of the temperature increment increased with time. The temperature of the concrete reached its maximum at 11.5^{th} hour. Then the temperature began to reduce. Based on the measured temperature during the setting period, it was concluded that stage 1 occurred within the 1st hour, stage 2 occurred between the 1^{st} hour and the 4^{th} hour, stage 3 occurred between the 4^{th} hour and the 10^{th} hour, and stage 4 occurred after the 10^{th} hour.

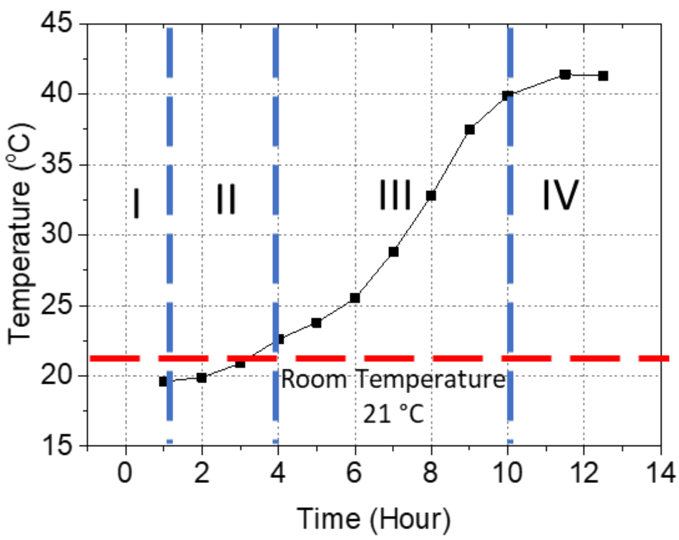

Fig. 4-36 Temperature variation in concrete with cast in transducer during concrete setting

Fig. 4-37 (a) shows the trend of ultrasonic TI of the guided waves at 240 320 and 600 kHz traveling in short plain bar cast in the concrete specimen. The pattern of the TI in bar cast in the concrete specimen is similar to that in bar cast in cement paste. The TI dropped significantly in the 1^{st} hour when fresh concrete was mixed and poured into the mould. The TI of all the frequencies continued to drop from the 1st hour to the 5th hour. The TI of 240 kHz and 320 kHz dropped significantly during this period, while the rate of attenuation of TI was marginal, the TI almost remained steady. A sudden jump in TI was observed at the 6th hour in all frequencies. A rise and fall fluctuation in the TI between the 5th hour and 9th hour was observed in all frequencies. The TI of 240 kHz and 320 kHz peaked at the 7th hour, while the TI of 600 kHz peaked at 600 kHz. Based on the observation in previous sections, it was concluded that the final set occurred in the first half of stage 3, around the time the TI reached the peak. Hence, the final set occurs around the 6th to the 7th hour. The TI continued to drop with time afterward. The TI of 240 kHz became steady after 10 hours of concrete mixing, indicating the concrete had reached the hardening process and gained enough stiffness and strength. The mould could be safely removed after the 10th hour. While the TI of 600 kHz continued to drop at a slow rate as the hardening process proceeded. Hence, it could be sued to monitor the strength gain of concrete during the hardening process.

The trend of the TI of 240 kHz and 320 kHz was similar. It was recalled that both 240 kHz and 320 kHz signals had a significant amount of surface components. Hence, their response to the change steel-concrete interface was similar. The waveform of the signal at 240 kHz is less complex, and it was close to the resonance frequency of the PZT wafer. Therefore, the signal at 240 kHz was used to monitor the concrete setting. The signal at 600 kHz was core seeking mode. The TI continued to drop after the 10th hour. Hence, it was also used to monitor the strength gain during the hardening stage.

Fig. 4-37 (b) shows the trend of ultrasonic TI of the bulk waves that travel through the concrete. No signal was received until the 8th hour. In the first 8 hours of the test, the concrete was in fluid and transition state, from fluid to solid, during the setting period. The bulk waves generated by the PZT wafer were absorbed by the non-hardened concrete paste. At the 8th hour, it was believed that the concrete had passed its final set and began hardening. The concrete has gained enough stiffness and strength so that the bulk wave can be transferred through the concrete body and received by the PZT wafer acting as the signal receiver. Hence the TI continued to rise with time after the 8th hour.

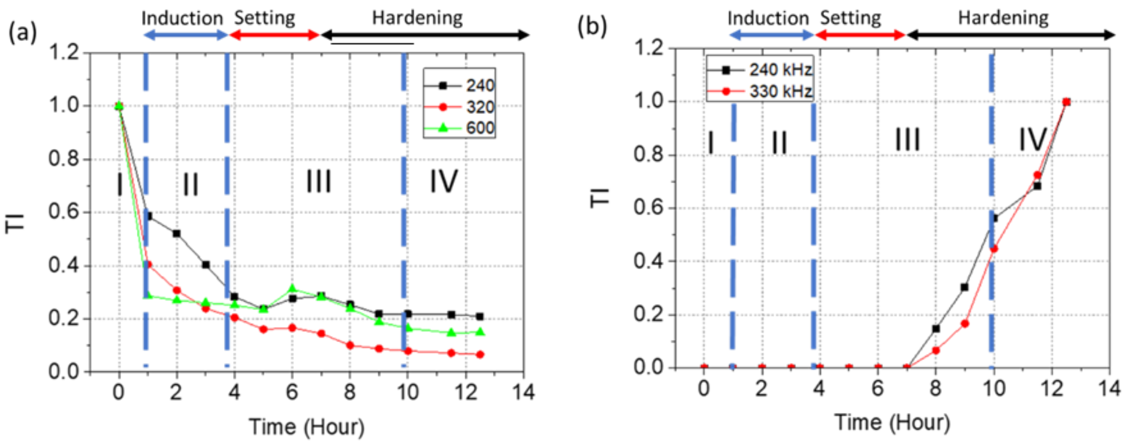

Fig. 4-37 Ratio of TI of (a) guided waves and (b) bulk waves in the concrete specimen.

Stage 1 (0-1 hour): The pre-induction stage occurs during the 1st hour. Due to the difficulty of accessing concrete paste during mixing, the temperature and ultrasonic measurements were only taken before and after pouring the mixed fresh concrete in the mould. No in-between data were taken. The TI of the signal at 240 kHz and 600 kHz dropped by 41.4% and 71.4% in the first hour, respectively. During this stage, the major change lied in the condition of the bar changing from the bar in air to bar embedded in fresh concrete. This significantly increased the attenuation of the guided waves and energy leakage into the surrounding material.

Fig. 4-38 (a) shows the amplitude profiles of the time signal at 240 kHz during stage 1. The amplitude of the F (1,2) mode dropped by 33.4% while the amplitude of F (1,1) mode increased by 39.3 %. There was a noticeable delay in the arrival time of the peaks of both modes. Since the material properties of the waveguide did not change, theoretically, the arrival time of both modes should remain the same. Hence, the delay in arrival time was contributed by the dispersion of the guided waves due to the presence of fresh concrete around the bar. The amplitude profiles of the time signal at 600 kHz are presented in Fig. 4-38 (b). In the bar in air scenario, there were 4 wave packets in the time signal. The first two were the L (0,3) and L (0,2) modes, while the latter two were the reflection of the previous two modes from the other end of the bar. Once the fresh concrete was pouring into the mould, the L (0,3) and L (0,2) amplitude dropped by 32% and 30.5%, respectively. It was also noted that the reflection was completed disappeared. This was because the fresh concrete increased the attenuation of the guided waves and enabled the energy to leak into the surrounding concrete.

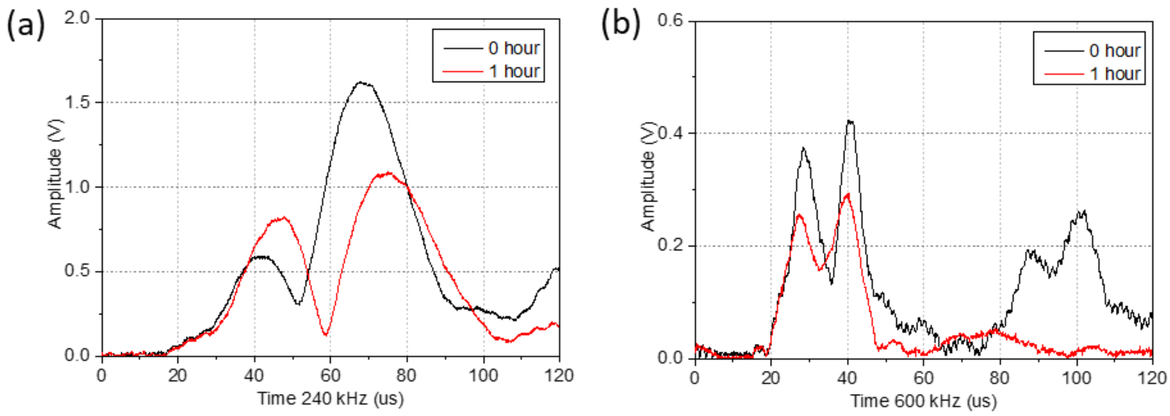

Fig. 4-38 Amplitude profiles of time signals at (a) 240 kHz and (b) 600 kHz in bar embedded in cement paste in stage 1.

Stage 2 (1-4 hours): The Dormant stage occurs between the 1^{st} and 4th hours after pouring concrete. During this stage, the chemical reactions were slow. Hence the temperature increment was slow, and the concrete remained in fluid state. During this stage, the temperature of the specimen grown and approached room temperature. The temperature increased at an increasing rate with time, at an average rate of 1°C/hour. The temperature of the specimen exceeded the room temperature at the 4^{th} hour, and the temperature increasing rate grew afterward. Hence it was concluded that the hydration process reached the acceleration stage after the 4^{th} hour.

The TI of 240 kHz went sharply down by 30.2% during the dormant stage, although the material properties of the surrounding concrete only slightly varied due to the slow chemical reaction. Fig. 4-39 (a) shows the amplitude profiles of time signals at 240 kHz in stage 2. The amplitude of both F (1,1) and F (1,2) mode dropped with time at an increasing rate. At the end of stage 2, the amplitude of F (1,1) and F (1,2) mode dropped by 34.8% and 43.1%, respectively. It was noted that the arrival time of the peaks was moving towards each other, and the amplitude of the merged part, at around 60 us, was increasing with time. This indicated that the guided waves experienced increasing dispersion and attenuation with time during the dormant stage.

The reduction of the TI of 600 kHz was not significant during stage 2. The TI was only reduced by 3.4%. This behavior is significantly different from the TI of 240 kHz. It is already demonstrated in section 4.4.2.2 that the axial displacement and total energy density of signal at 240 kHz are mainly around the surface of the bar while those of signal at 600 kHz are concentrated in the core of the bar. In addition, the main wave modes in the signal at 240 kHz are flexural modes, and the main wave modes in the signal at 600 kHz are longitudinal modes. The signal at 240 kHz continuously travels in between the bar and the surrounding concrete when propagating along the bar. Hence, it is sensitive to the change in the steel-concrete interface. While the signal at 600 kHz mainly travels around the core of the bar and only a small component travels near the surface, it is not significantly influenced by the change in the surrounding material. Fig. 4-39 (b) shows the amplitude profiles of e signals at 240 kHz in stage 2. The peak amplitude of L (0,3) dropped by 3.6% between 1 hour and 2 hours, and then it remained steady. While the peak amplitude of the L (0,2) mode continued to drop by 6.5% with time. However, it was noted that the time signals showed that the majority part of the waveform remained unchanged. This might be because the core components of the signal were not influenced by the slight changes in the surrounding concrete, while the surface components were sensitive to the changes. The core components outstripped the surface components, leading to the marginal reduction in the TI.

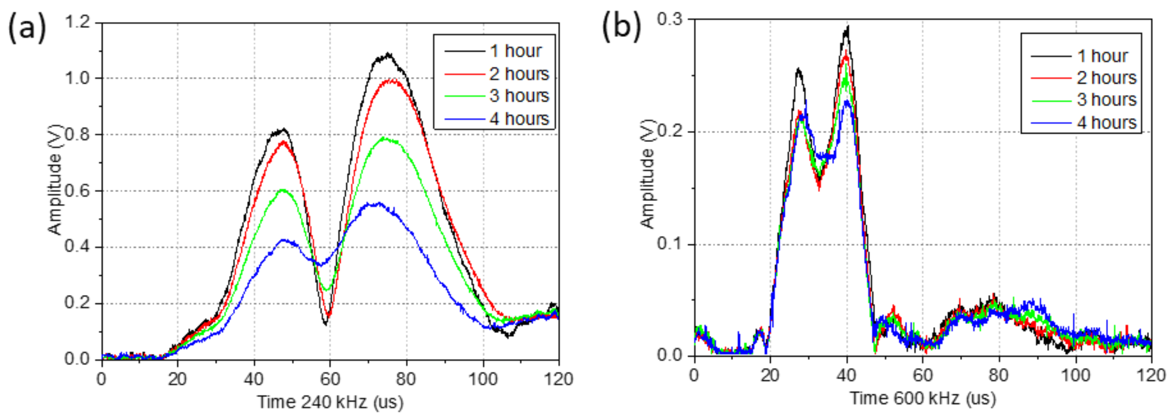

Fig. 4-39 Amplitude profiles of time signals at (a) 240 kHz and (b) 600 kHz in bar embedded in cement paste in stage 2.

Stage 3 (4-10 hours): The acceleration stage occurs between the 4^{th} and 10^{th} hour. The cement hydration occurs rapidly, leading to a continuously stiffening of the fresh concrete. The concrete lost its plasticity and transferred from fluid state to solid state. The temperature continued to rise at a rate of 1.45°C/hour from 4 hours to 6 hours, and the rate increased to about 4°C/hour from 6 hours to 9 hours. Then the temperature increment slowed down. Hence, it was concluded that the initial set occurred after 4 hours, and the final set occurred around 6 hours.

During this stage, the TI of both 240 kHz and 600 kHz showed 3 stage fluctuation. The TI of 240 kHz dropped by 4.7% from 4 hours to 5 hours. Between 5 hours and 7 hours, the TI rose by 4.9%. After 7 hours, the TI dropped again rapidly by 6.8%. Fig. 4-40 (a) shows the time signals at 240 kHz during stage 3. The amplitude of the F (0,1) mode was reduced with time. The amplitude dropped by 27.5% at the end of stage 3. While the trend of the change in the amplitude of F (0,2) mode matched with the trend of the TI. A rise and fall fluctuation in the peak amplitude was observed. Fig. 4-40 (b) shows the time signals at 600 kHz. Between 4 hours and 5 hours, the amplitude of L (0,3) mode remained steady while the L (0,2) mode continued to drop by 1.8%. Then the amplitude of these modes increased by 3.8% and 6.0% respectively from 5 hours to 6 thous. The amplitude dropped again by 8.6% and 9.9% until 10 hours.

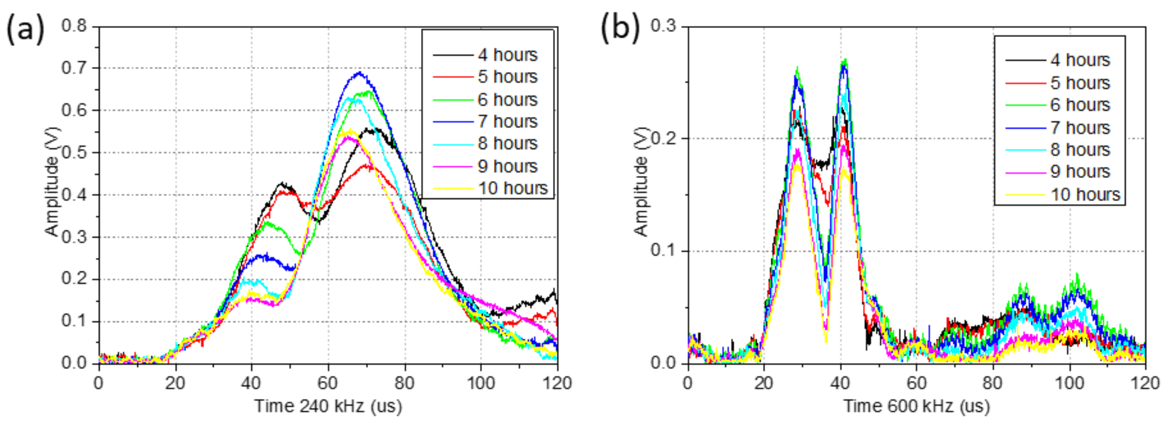

Fig. 4-40 Amplitude profiles of time signals at (a) 240 kHz and (b) 600 kHz in bar embedded in cement paste in stage 3.

The bulk waves through concrete were first detected at the 8th hour. It was believed that the concrete had passed its final set and reached the hardening process. The concrete had gained enough stiffness and strength to pass the bulk wave. A weak wave packet was observed at a ToF of 55us, although the amplitude of the wave packet was comparable with the signal noise (Fig. 4-41 (a)). The amplitude of the wave packet increased with time, and a second wave packet was observed at a ToF of 105us at the 10th hour, indicating the continuous stiffening of the concrete.

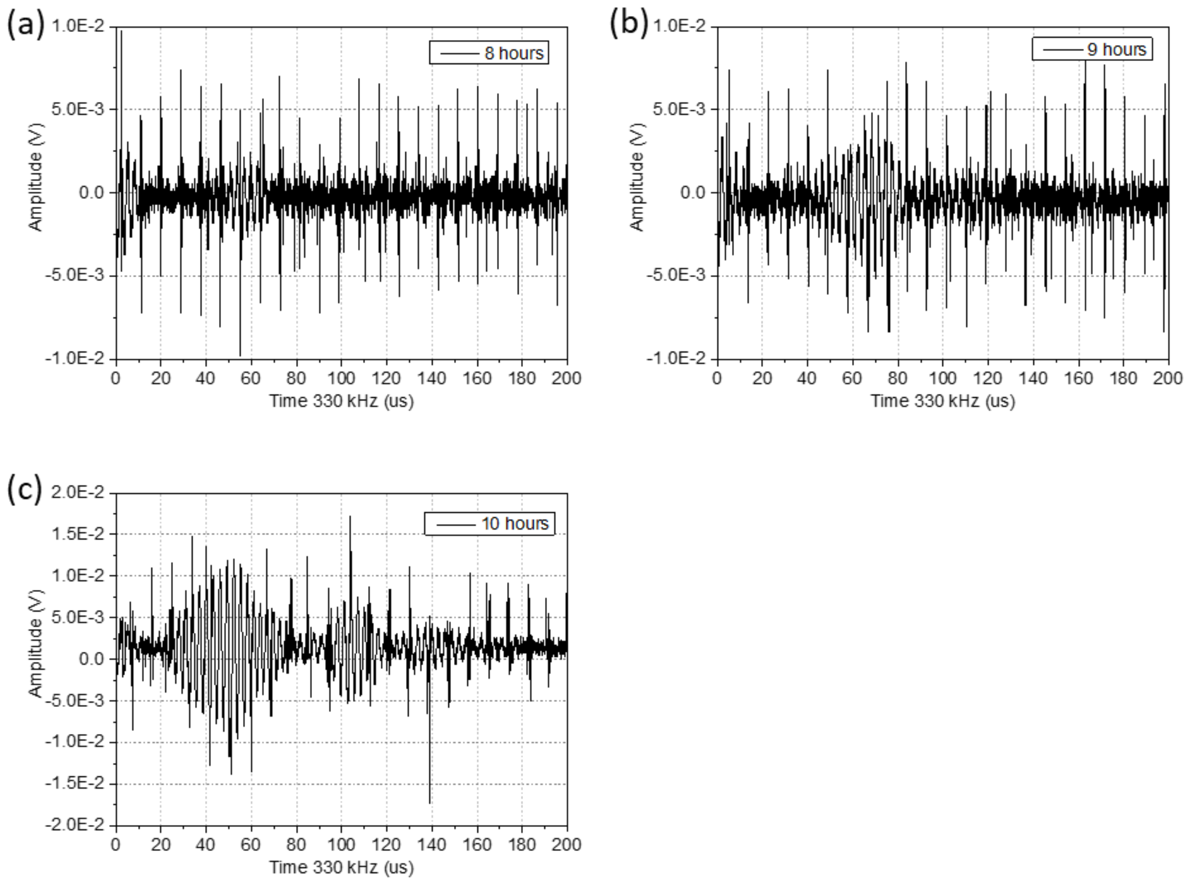

Fig. 4-41 Bulk waves at 330 kHz through concrete after (a) 8 hours, (b) 9 hours, and (c) 10 hours after concrete mixing in stage 3.

Stage 4 (10-12.5 hours): The deceleration stage occurs between 10th and 12.5th hour. The temperature increment slowed down dramatically and reached a plateau. The cement hydration slowed down, but the hardened concrete continued to gain strength with time. The TI of 240 kHz remained steady while the TI of 600 kHz dropped by 1.5%. Fig. 4-42 (a) shows the amplitude profiles of the time signals at 240 kHz in stage 4. The amplitude of the F (1,1) mode increased while the amplitude of the F (1,2) mode dropped with time. It was noted the amplitude increment of F (1,1) mode was similar to the amplitude reduction of F (1,2) mode. These changes canceled each other, resulting in a stabilized TI. As for the time signals at 600 kHz, the amplitude of both modes reduced at a marginal rate with time (Fig. 4-42 (b)). The amplitude of L (0,3) and L (0,2) mode dropped by 1.2% and 1.6%, respectively. During stage 4, the TI variation of both frequencies is marginal, although the concrete continued to gain strength. Hence, it is concluded that the proposed ultrasonic method is not sensitive to the change in the surrounding concrete and cannot monitor the strength gain.

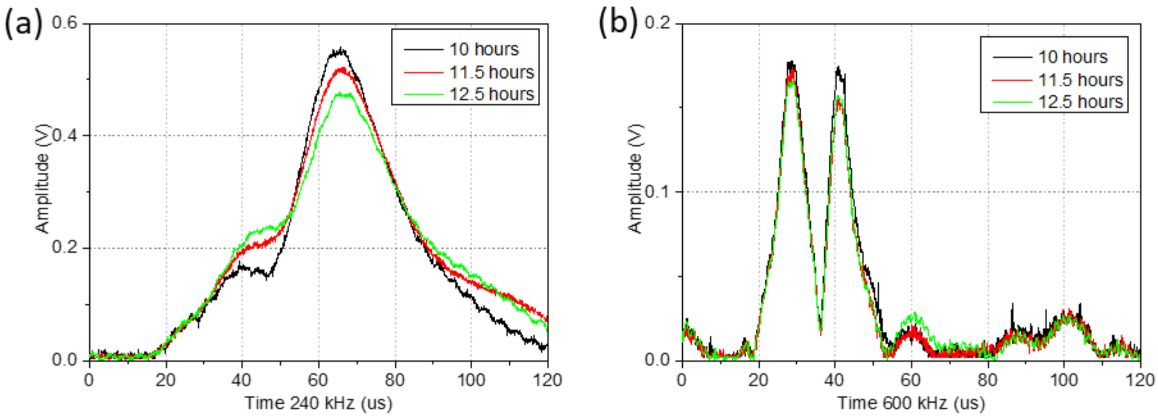

Fig. 4-42 Amplitude profiles of time signals at (a) 240 kHz and (b) 600 kHz in bar embedded in cement paste in stage 4.

Fig. 4-43 shows the time signal of bulk waves during stage 4. The first wave packet increased, and a third wave packet appeared at a ToF of 90us. At the 12.5th hour, the first wave packet was split into two wave packets. It was recalled that the guided waves were sensitive to the concrete setting but became less sensitive to monitor the hardening process. On the other hand, the bulk waves were not detectable before the concrete hardening period and increased rapidly afterward. Hence, the guided waves should be used to monitor the setting of concrete, and the bulk waves could be used to monitoring the hardening of the concrete.

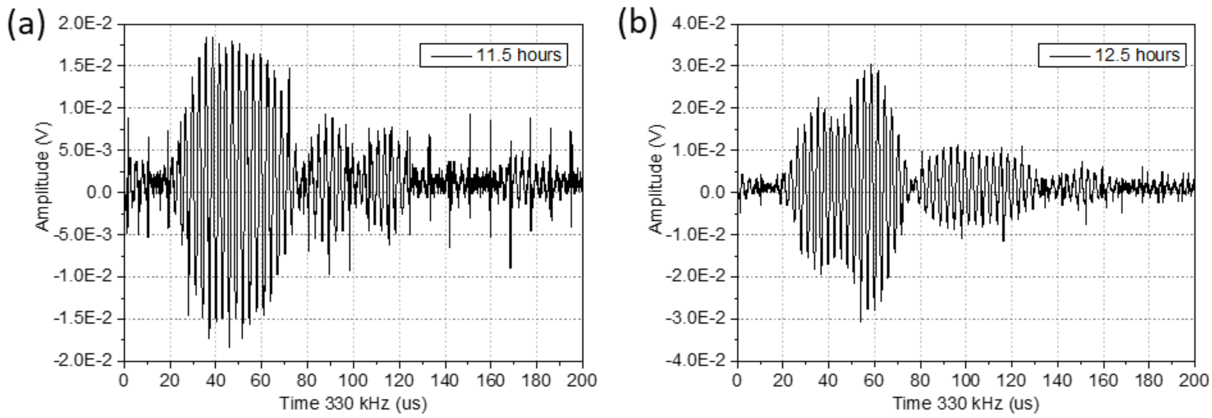

Fig. 4-43 Bulk waves at 330 kHz through concrete after (a)11.5 hours and(b) 12.5 hours after concrete mixing in stage 4.

4.5. Discussion and conclusion

This chapter conducted an experimental evaluation to monitor the concrete hydration using the proposed guided wave method. Both plain bars and deformed bars were employed as the waveguide to monitor the concrete hydration process. In addition, the thick double-sided tape was attached to the bottom part of the bar to simulate the debonding/void owning to the top-bar effect. The trend of TI of plain bar specimen was similar to that of deformed bar specimen. The behavior of TI varied significantly in different stages of concrete hydration.

During cement hydration and concrete setting, the waveguide remained intact, but the condition of the surrounding medium kept changing. Hence, the characteristics of the guided waves were influenced by the changing properties of the surrounding concrete. The dominating wave modes of the signals used to monitor the cement hydration and concrete setting are flexural modes. The out-of-plane motion of the flexural modes allows the leakage of partial energy from the waveguide (steel bar) to the bonded medium (concrete) while propagating in the waveguide. As the properties of concrete, e.g. strength, modulus and hardness, continued to increase with setting, the leakage phenomenon increased, leading to a reduced TI.

Four clear stages were visible, which matched well with the four stages of cement/concrete hydration. In stage 1, the TI dropped sharply when the concrete was poured into the mould. The fresh concrete was directed contact with and wrapped the waveguide. The condition of the waveguide was transferred from the bar in air to the bar embedded in concrete. The vibration of the bar was restricted by the surrounding fresh concrete, comparing to free vibration in air. A significant amount of energy loss occurred, and the attenuation of the guided waves increased significantly. In addition, part of the guided waves continued to leak into the surrounding concrete while propagating. These contributed to the sharp reduction in TI.

In stage 2, the TI of the surface-seeking mode gradually attenuated with time, while the variation in TI of the core-seeking mode was insignificant during the same period. Although the chemical reaction during the dormant stage was slow, the fresh concrete was still gaining stiffness at a slow rate with time. The surface-seeking mode successfully captured this phenomenon.

In stage 3, the TI showed a fall-rise-fall fluctuation. The initial set and final set occurred before and after the valley of the fluctuation. This phenomenon was repeatedly observed in all specimens, plain bars, deformed bars, and short cast-in bars. Unfortunately, the cause of the rise in the TI remains unclear. By referring to literature about cement hydration and concrete setting, several possible causes are proposed but require further investigation. One possible cause is the plastic settlement cracks. Plastic settlement cracks are formed when the concrete is still plastic, and the concrete bleeding continues. Due to the presence of the reinforcing bars, the concrete over the bars is locally restrained from settling while the rest continues to settle, leading to a crack forming over the bar. This results in a local discontinuity between the bar and the surrounding concrete. Energy leakage is locally blocked, and more energy can be retained in the bar, leading to an increased TI. Once the concrete is hardening, the discontinuities no longer increase but the stiffness of the surrounding concrete increases. The attenuation and the energy leakage of the guided waves continue to increase, resulting in a decreasing TI. Another possible cause is the micro-cracks and voids formed around the bars. This also leads to the discontinuities between the bar and concrete.

In stage 4, the TI becomes steady, although the hardened concrete continues to gain stiffness and strength with time. The guided waves are no longer sensitive to detect the effect of the stiffening hardened concrete on the wave propagation. However, this phenomenon can serve as a good indicator to detect hardened concrete. The mould can be safely removed without damage the integrity of the concrete when this phenomenon occurs.

Casted-in short bars are also used as the waveguided to monitor the hydration of cement paste and concrete. Short bars are used to reduce the energy loss due to the attenuation and energy leakage while wave propagating in the bar. The waveguide is designed to be in a twin-bar arrangement with fixed spacing. This allows monitoring the guided waves propagating in the steel bar and detect the bulk wave through the concrete from one bar to the other. The entire system can be seen as a cast-in sensor for cement/concrete hydration monitoring. The TI of guided waves in both cement paste and concrete specimens shows the same trend as previous observation. Four clear stages are visible. A penetration resistance test is also conducted to detect the initial and final set times according to ASTM C403. The results match well with the guided wave results and previous conclusions. The bulk wave was detected only after the concrete is hardened. The TI of bulk waves increases dramatically with time at the later stages of stage 3 and 4. It is observed that the guided waves are not sensitive to monitor the strength gain during this period. By combining guided waves and bulk waves, it is possible to monitor the entire hydration process.

Chapter 5

5. Detection of Top-bar Effect in Reinforced Concrete Using Guided Ultrasonic Waves

Yikuan Wang, Abhijit Mukherjee and Arnaud Castel

The previous chapter reported the application of the proposed guided wave-based method to monitor cement hydration and concrete setting. The 4 stages of hydration were successfully identified by the trend of transmission index (TI). The guided wave method is extended to detect the presence of interfacial defects owning to top bar effect. A linear and a nonlinear damage index is proposed. This chapter includes a published co-authored journal publication in Journal of Structural Engineering entitled "*Detection of Top-Bar Effect in Reinforced Concrete Using Guided Ultrasonic Waves"*. The candidate was responsible for the conception, design of work, acquisition, analysis and interpretation of the guided wave data. The writing of the work was in collaboration with the other authors.

This chapter comprises the following manuscript:

Wang, Y., A. Mukherjee, and A. Castel, *Detection of Top-Bar Effect in Reinforced Concrete Using Guided Ultrasonic Waves*. Journal of Structural Engineering, 2021. **147**(4): p. 04021032.

5.1. Abstract

An ultrasonic shear wave-based non-destructive method is proposed in this paper to detect steel-concrete interface debonding owing to top-bar effect. A concrete wall was cast with horizontal reinforcements at different heights in order to create interfacial defects underneath the top bars. PZT

patches were surface mounted at the ends of the bars to excite and record shear waves. The ultrasonic results showed that the amplitude of the signals increase with the height of the bars. The specimens were cut open after the experiments and top-bar effect was clearly discerned. Its increase with the height of the bar was clearly observed. An increasing difference between the high frequency component and the excitation frequency of the signal was observed between the bottom bar with good bond and the top bars. This feature can be utilised for non-destructively monitoring top-bar effect.

5.2. Introduction

Bond between steel rebar and concrete is paramount for reinforced concrete structures. However, there are several situations where bond has been found to be deficient. In deep beams or wall structures voids below the horizontal rebars have been observed (Jeanty, Mitchell et al. 1988, Chan, Chen et al. 2003, Soylev and François 2003, Castel, Vidal et al. 2006, Nasser, Clément et al. 2010, Zhang, Castel et al. 2011). During curing of concrete, coarse aggregates settle due to gravity, forcing water, air and fine aggregates moving upwards. Part of the water and air is trapped under horizontal reinforcement. As a result, voids are formed underneath the reinforcement in hardened concrete (Söylev and François 2006). This phenomenon is known as the “top bar” effect. Top bar effect can cause a significant reduction in bond strength in deep concrete structures (Mohammed, Otsuki et al. 1999). The influence of the casting position of reinforcing bars on the bond characteristics has been recognized since early 1910s (Jeanty, Mitchell et al. 1988). Pull-out tests to investigate the variation of bond efficiency with the elevation of the rebars in normally vibrated concrete (NVC) indicated that the bond of the top bars were about two-thirds as effective as that of the bottom ones (Arthur 1946). Based on this finding, the top bar effect was first introduced in the American Concrete Institute(ACI) building code in 1951 (Wan, Petrou et al. 2002). ACI 440 defines “top bar” as a horizontally placed reinforcement with more than 12 in (305 mm) of concrete below it and has compensated for the poorer bond strength of top bar by introducing a factor of safety. In 1971, the safety factor was 1.4. In the next decade, Jeanty et al. (1988) conducted another experimental study on full-scale concrete beams and concluded that the top-bar had around 22% lower bond strength. Based on these results, in 1989, the top bar safety factor was reduced from 1.4 to 1.3 in ACI building code, which is still in use. It is noted that the top bar effect is present both in NVC and self-consolidating concrete (SCC) (Soylev and François 2003, Esfahani, Lachemi et al. 2008). In fact, 20% lower bond strength has been reported in case of SCC compared to NVC (Esfahani, Lachemi et al. 2008). Thus, an additional safety factor of 1.3 has been recommended for SCC. Evidently, the approach to cater for the immediate consequence of top bar has been to introduce factors of safety.

The consequence of top bar effect on the long term performance of concrete is earlier occurrence of corrosion (Nasser, Clément et al. 2010, Zhang, Castel et al. 2011). The steel-concrete interface quality influences the rate of chloride-induced corrosion in RC. A higher corrosion rate was found in RC with poor interface quality (Mohammed, Otsuki et al. 1999, Soylev and François 2003, Nasser, Clément et al. 2010, Zhang, Castel et al. 2011). Nasser et al. (2010) assessed the influence of S-C interface condition on the galvanic current in macrocell corrosion of concrete specimens. The macrocell corrosion current density and the mass loss of the rebar with interface debonding was 200% and 56% more than that of control specimens. Zhang et al. (2011) observed a relatively uniform corrosion pattern on the steel surface affected by the top-bar effect, while control specimens showed typical pitting corrosion. Top-bar effect has been observed to accelerate the rate of corrosion. The polarisation resistance (Rp) of specimens with top-bar dropped between 9-17 weeks at chloride content of 0.5-0.8% of mass of cement, whilst in case of control specimen it dropped after 29 weeks at a chloride content of 0.9%. Therefore, an early diagnosis of the presence of top-bar effect and continuous monitoring of the corrosion process is essential for the maintenance and prevention of failure of concrete structures.

Ultrasonic guided waves have been found to be effective in health monitoring for civil infrastructure. It features high sensitivity to various types of defects and capability of continuously monitoring a large area without interfering the functionality and integrity of the examined structure (Lu, Li et al. 2013, Hong, Su et al. 2015, Xu, Yang et al. 2018). The void owing to top-bar effect is formed during the curing process of concrete. The guided wave techniques have been employed to monitor the curing process of concrete (Kong, Hou et al. 2013, Sharma and Mukherjee 2014, Sharma and Mukherjee 2015, Lim, Kwong et al. 2017, Bhalla, Sharma et al. 2018, Lim, Kwong et al. 2018, Lim, Smith et al. 2018). Two or more transducers are either embedded in concrete or surface-mounted to the waveguide to excite the waves and acquire the response. Any variation in the mechanical properties and the geometries of the specimen along the wave path can be captured and characterised. Kong et al. (2013) embedded PZT transducers in concrete to investigate its rate of hydration up to 17 hours after pouring. Three stages of concrete setting, termed the fluid stage, the transition stage and the hardened stage, were identified by analysing the amplitude of the received signals. However, high attenuation of concrete makes it difficult to monitor large structures. Sharma and Mukherjee (2014, 2015) employed the reinforcing bar as a wave guide to alleviate high attenuation of concrete. The mode with maximum surface energy component was employed to monitor the bond development at the steel-concrete interface. The influence of mix design on the setting process was characterised using vibrated and self-consolidating concrete.

As the bond between the steel and concrete develops during the curing process, more energy can leak into the surrounding concrete via the steel-concrete interface. Studies have reported that the amplitude and Time of Flight (ToF) of the received signals are affected by the steel-concrete interface quality (Wu and Chang 2006, Lu, Li et al. 2013, Zima and Rucka 2017, Zima and Rucka 2018, Zima and Kędra 2019). Guided waves in pitch-catch mode was generated by attaching PZT discs to the embedded steel bar (Wu and Chang 2006). A clear increment in the amplitude of the received signal was observed with the length of debonding. In pulse echo mode, the position of the debonding was identified by recording the ToF (Zima and Kędra 2019). Sharma and Mukherjee (2010) employed longitudinal guided waves to detect rebar corrosion simulated as debonding at the rebar-concrete interface. It was reported that the amplitude of the transmitted signal continued to increase with increasing debonding length.

The void created at the bar interface due to top-bar effect can be too small to cause a perceptible change in amplitude of signal. Nonlinear ultrasonics have high sensitivity to small defects or thin cracks. Such cracks open and close during the passage of ultrasonic waves giving rise to higher harmonics (Richardson 1979). Solodov (1994) demonstrated that higher harmonics are generated at the interface when the bond between two solids is not perfect. This is due to the nonlinearity generated by sequential opening and closing of the interface under compression and rarefaction wave cycles. The compressional part of the wave can close the interface and allow transmission, while the tensile part opens the interface and therefore, it cannot be transmitted through it. The transmitted waves result in a localised nonlinearity known as contact acoustic nonlinearity (CAN). The ratios of the peaks of higher harmonic and the excitation frequency has been used to detect and quantify CAN (Solodov, Krohn et al. 2002, Hong, Su et al. 2015). This phenomenon has been extensively employed by researchers for detection of incipient (Guyer and Johnson 2009, Chao, Ming et al. 2013, Hong, Su et al. 2014, Su, Zhou et al. 2014, Wang, Guan et al. 2017, Wang, Wu et al. 2018). Hong et al. (2014) developed a finite element model to investigate second harmonic generation due to the opening and closing of a “seam” crack. Contact elements were employed to model the crack and allow sliding but restrict the mutual penetration of the surfaces. A clear additional wave package was observed in the received signal at the 2nd harmonic frequency range. The model was validated by experiments conducted by the authors to locate a 3mm long fatigue crack in an aluminium plate using PZT patches (Hong, Su et al. 2014, Hong, Su et al. 2015). However, authors are unaware of any study hitherto on application of nonlinear ultrasonics in detection of steel-concrete interface debonding.

This paper is the first attempt of non-destructive detection of steel-concrete interface debonding owning to the top-bar effect. The novelty of this study lies in two areas, (1) guided shear waves for detection of realistic debonding due to top-bar effect as commonly seen in the field and (2) use of nonlinear ultrasonics for indication of presence of top-bar effect. In this study, top-bar effect has been created in the laboratory by a special design of RC samples. Non-destructive detection of top-bar has been attempted for the first time by using guided shear wave propagation in steel reinforcement embedded in concrete. A novel detection system consisting of piezoelectric (PZT) wafers, signals generators and amplifiers has been developed. The creation of top-bar is continuously monitored during the curing process until 290 hours. Both linear and nonlinear features are extracted and analysed. A correlation coefficient is developed between the contact acoustic nonlinearity (CAN) and the top-bar effect.

5.3. Experimental Investigation

5.3.1. Concrete Specimens

Reinforced concrete samples were cast in the laboratory with an aim to create top-bar. A standard composition of concrete, as given in Table. 5-1, was used. The average slump was found to be 54 ± 2 mm. A RC wall of dimension 800 mm × 100 mm × 300 mm, as shown in Fig. 5-1, was cast. The specimen contains 4 steel bars of diameter 12 mm located at 100 mm, 300 mm, 500 mm and 700 mm from the bottom of the specimen. The unobstructed spacing of the bars is 200mm which is commonly seen in the field for reinforced concrete walls. The focus of this study was to investigate how position (height) of the steel bars affect the interfacial bonding, plain bars were used in this investigation to avoid the mechanical bonding formed due to ribbed bar and to minimize the complexity due to internal reflection of waves within ribbed bars. The fresh concrete was equally divided into 4 portions and added into the mould one by one. The mould was vibrated on a vibration table after each portion of fresh concrete was added. The mould was removed after 43 hours and the specimens were wrapped with moist cloth for curing. Water was sprayed daily to maintain the moisture of the cloth for 28 days.

Table. 5-1 Concrete mix component

Mix Component (kg/m^3)	
Coarse aggregate (10mm basalt)	1190.50
Fine aggregate	590.30
OPC (GP cement)	430
Water/binder ratio	0.45

Free water	193.5
Total	2404.3

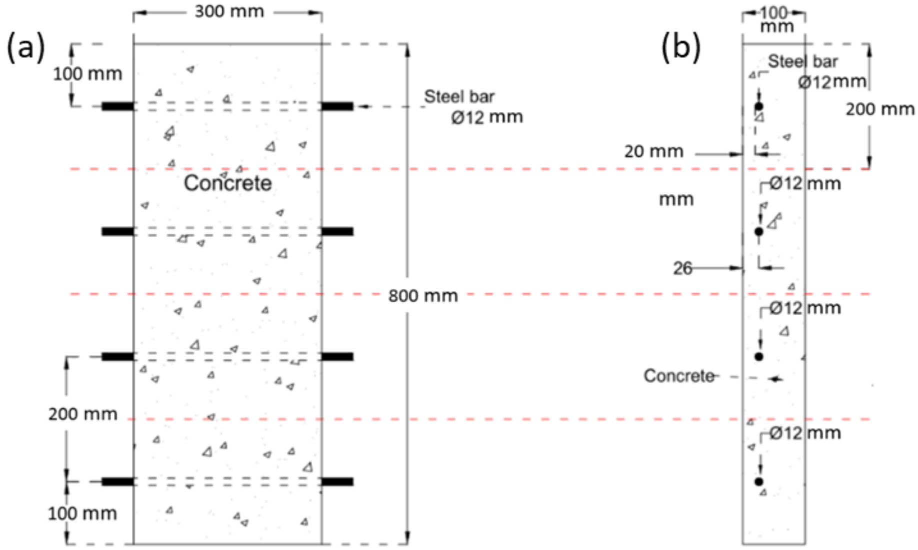

Fig. 5-1 Schematic drawing of specimen (a) Side view and (b) Front view

5.3.2. Non-Destructive Tests

Circular lead zirconate titanate (PZT) wafer manufactured by PI Inc® were mounted to the ends of the steel bars using superglue to act as ultrasonic transducers. Fig. 5-2 illustrates the configuration of the PZT patch. The negative electrode is extended and wrapped around to the same surface as the positive one. The negative electrode side is surface-mounted to the host structure while wires are soldered to the positive electrode side. The polarizing direction is perpendicular to the surface of the patch (in 1-1 direction). When charged, the circular patch deforms in 3-3 direction and hence induces mechanical strain along the edge in 1-1 direction.

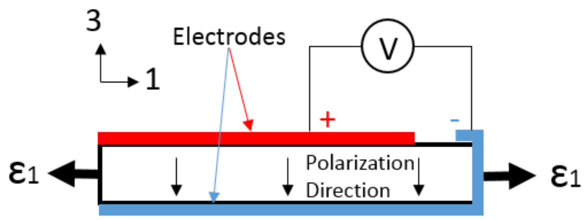

Fig. 5-2. *Side view of PZT wafer operating in 1-3 mode*

The ultrasonic testing system consists of a signal generator (RIGOL DG1032), a Cyprian High Voltage Power Amplifier, PZT discs, oscilloscope (PicoScope2203) and a computer as shown in **Fig. 5-3**. A 20 cycle Hanning-windowed tone burst waveform was created through the signal generator. A signal at a selected excitation frequency and a voltage of 1 $V_{p\text{-}p}$ was generated and got amplified by 200 time to 200 $V_{p\text{-}p}$ by the amplifier. The excitation voltage applied on PZT disc is expressed by:

$$V_{excitation}(t) = A \times V_{generator} \times \sin 2\pi ft \times \left(\frac{1}{2} + \frac{1}{2}\cos(2\pi(\frac{t-t_{max}}{t_{max}}))\right) \tag{5-1}$$

$$t_{max} = n \times \frac{1}{f} \tag{5-2}$$

Where $V_{excitation}$ and $V_{generator}$ is the excitation voltage applied on PZT disc and the output voltage from the signal generator, A is the amplification of signal, f is the central excitation frequency, t is the time domain of the waveform, t_{max} is maximum time of the waveform and n is the number of cycles.

The amplified signal was applied on the PZT on one side of the steel bar and the transmitted signal was captured by the PZT at the other end, and vice versa. The captured signals was then acquired by oscilloscope with a sampling frequency of 10 MHz after averaging 32 samples. The recorded data was analysed with the help of a computer.

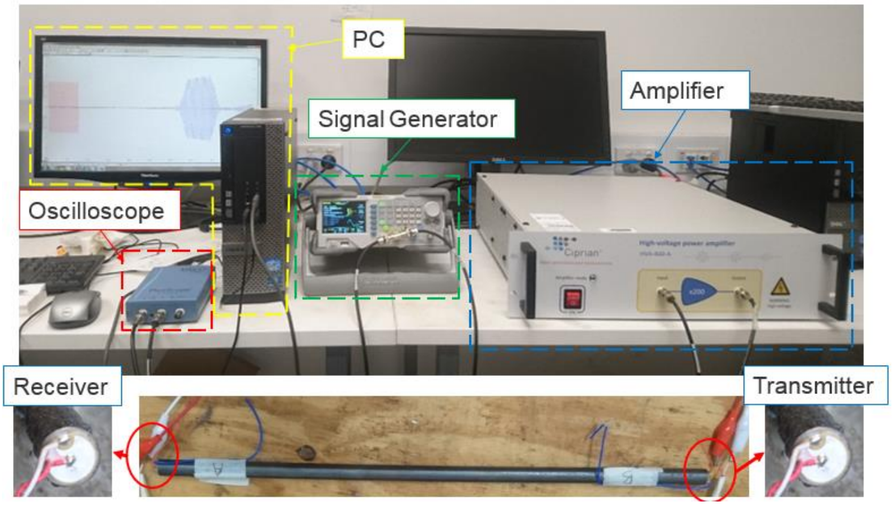

Fig. 5-3. *Experiment instruments and set-up*

Three stages of the specimens, namely bare bar, fresh concrete and hardened concrete were monitored using ultrasonic waves. The signals propagating in steel bar in the mould without pouring concrete were used as the benchmark. Once the benchmark signals were recorded, fresh concrete was poured into the mould to investigate how pouring of concrete influences the wave propagation. The third set of data was taken when the concrete had hardened. The specimens were monitored regularly during the 28 days of curing. The signals stabilised to a uniform pattern and showed no significant variation once the concrete had cured for 100 hours.

5.3.3. Excitation Frequency

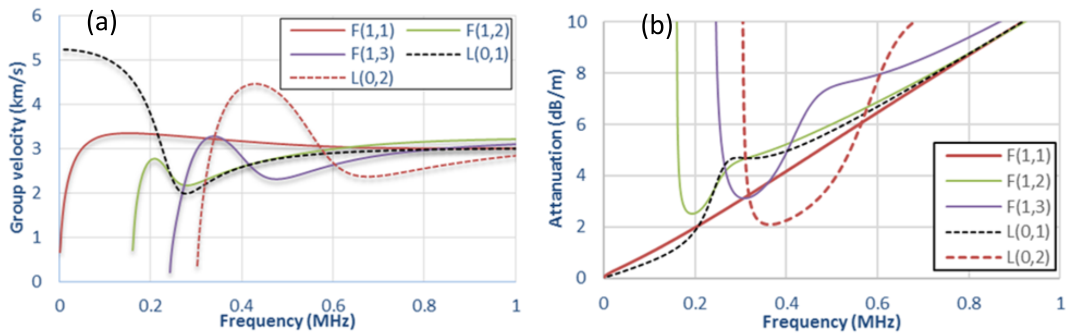

Fig. 5-4. *Dispersion curves for waves travelling in steel bar (12mm) (a) Group velocity (km/s) and (b) attenuation (dB/m)*

The best excitation frequency and the corresponding modes can be selected through the solution of the wave equations for all the frequencies and observing their attenuations. However, the solution is available for simple wave guides only (Su, Ye et al. 2006). In this case, a 12 mm diameter bar in concrete is modelled using a commercial available software DISPERSE (Pavlakovic, Lowe et al. 1997). The group velocities and attenuation of different modes that fall within the frequency range of interest are plotted in Fig. 5-4. The curves are labelled as per the type of mode: Longitudinal (L) and flexural (F). A dual index system, as the numerals in the parentheses, helps to track the modes. The former refers to the circumferential mode of the mode, which indicated the integer number of wavelengths around the circumferential of the bar. The later refers to the order of the modes of the vibration. The PZT discs are surface-mounted to the ends of the steel bar and the main vibration direction of PZT disc is parallel to its plane direction, hence shear waves are generated and captured. The 1st order flexural mode, F (1,1), constantly exists in the excited signals and the group velocity remains steady at the selected frequency range. Weak longitudinal waves can also be generated due to the deformation of the PZT. The 1st and 2nd longitudinal mode of circumferential mode 0, (L (0,1) and L (0,2)), start to be generated after 100 kHz and 300 kHz respectively. A preliminary test has been conducted on the steel bar and RC to determine the excitation frequency. The experiment was performed over a frequency range of 100 kHz to 500 kHz per step of 50 kHz. It was found that 400 kHz was the most suitable excitation frequency that can generate both strong fundamental and high frequency components. The L (0, 2) mode is the fastest propagating mode and exhibits an attenuation of 2dB/m. The rest of the generated modes exhibits a relatively high attenuation of 4-6 dB/m. It is expected to receive a weak longitudinal wave mode L (0, 2) which comes first (4400m/s), followed by a strong shear wave mode F (1, 1) (3300m/s). The group velocities of wave modes L (0, 1), F (1, 2) and F (1, 3) are similar (2500m/s). A merged wave packet, consisting of L (0, 1), F (1, 2) and F (1, 3), is expected, following the shear wave mode F (1, 1).

5.4. Damage Index (DI)

The wave energy is one of the most straightforward linear features of ultrasonic waves. In a reinforced concrete structure, the material properties change due to concrete setting and the interface quality between steel and concrete can significantly influence the magnitude of the scattered guided wave energy (Sharma and Mukherjee 2010). A linear damage index is developed to evaluate the deviation in the wave energy of captured ultrasonic signal with regard to its benchmark (bar in air), as

$$DI_{linear}(i) = \frac{A_1(i)}{A_1(0)} \quad (5\text{-}3)$$

$$A_1 = \sum_{f_0-\frac{B}{2}}^{f_0+\frac{B}{2}} A(f) \quad (5\text{-}4)$$

$$\mathrm{A(f) = FFT(f(x))} \quad (5\text{-}5)$$

where $A_1(i)$ is the wave energy of the signals around the excitation frequency at time i. f_0 is the excitation frequency. B is the bandwidth of the signal. FFT stands for Fast Fourier Transform. A(f) and F(x) is the signal in frequency and time domain. Due to the formation of interface debonding, less amount of wave energy leak into the surrounding concrete, more wave energy can be captured, resulting in a greater DI_{linear}.

Nonlinear damage index is also developed using the nonlinear features extracted from the ultrasonic signals. For ultrasonic waves traveling in a medium, the nonlinearity, originates from material, geometric and instrumental nonlinearity, may exist even in its intact state. To minimize the effects of these sources of nonlinearity and to emphasize CAN, an amplitude ratio of high frequency component to excitation frequency component is employed. The nonlinear damage index is established as the correlation between the amplitude ratio of current state and that of its intact state, as:

$$DI_{nonlinear}(i) = \frac{A_2(i)/A_1(i)}{A_2(0)/A_1(0)} \quad (5\text{-}6)$$

$$A_2 = \sum_{2f_0-\frac{B}{2}}^{2f_0+\frac{B}{2}} A(f) \quad (5\text{-}7)$$

where $A_2(i)$ is the wave energy of the signals around $2f_0$ at time i. In case of wave traveling in bar embedded in concrete with good interface quality, the high frequency component experiences strong attenuation, resulting in a smaller $DI_{nonlinear}$. For wave traveling in bar embedded in concrete with interface debonding, CAN may get generated, resulting in a greater $DI_{nonlinear}$.

5.5. Experimental Results

5.5.1. Ultrasonic Testing

Fig. 5-5 illustrates the wave propagation in bar of RC. In RC with good S-C interface bond, as shown in Fig. 5-5 (a), the amplitude of signal traveling in bar drops due to signal attenuation along the bonded S-C interface and energy leaking into the surrounding concrete. Reflection of waves at the two ends of the embedded bar also results in amplitude reduction. For signal travelling in bar subjected to top-bar effect, as shown in Fig. 5-5 (b), the portion traveling at the top half of the bar experiences attenuation and energy leakage similar to that in a RC with good bond. While the portion that propagating at the bottom half of the bar travels through a bonded-debonded-bonded S-C interface. The attenuation at the debonding zone is low and no energy leaks into the concrete via the debonded interface. Reflections can occur at the two ends of the embedded bar and the two ends of the debonding zone.

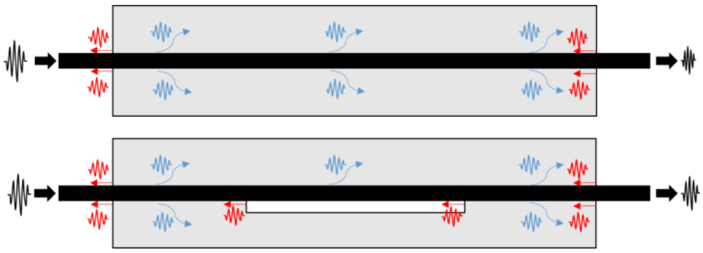

Fig. 5-5. *Wave propagation in rebar in RC with (a) good S-C interface bond and (b) subjected t to top-bar effect*

Fig. 5-6 shows the received transmission signals in the bottom bar (A1) at 100 mm and the top bar (A4) at 700 mm in the mould at different time of specimen preparation. The wave modes in the signals are identified and the peak-to-peak amplitude are calculated. For signals before pouring concrete, there are 3 wave modes are identified, which are L (0, 2), F (1, 1) and F (1, 2) in both the bottom and the top bar. When concrete is poured into the mould, the amplitude of F (1, 1) and F (1, 2) drops dramatically but the amplitude of L (0, 2) remains similar. As the fresh concrete is poured, a steel concrete interface is created, which leads to the leakage of energy into the surrounding concrete and thus results in a reduction in the amplitude of signals, especially for shear waves. The concrete gets hardened after 15 hours, the strength of concrete is improved and hence further reduction in signal amplitude is observed in both bottom and top bar. It is also observed that the L (0, 2) mode is eliminated from the signal received in bottom bar but remains in the signal in top bar. The bond between steel bar and surrounding concrete provides resistance of vibration in steel bar in the direction perpendicular to the surface of bar and along the bar direction. Hence, the L (0, 2) get attenuated while propagating in the steel in RC with good bond. For signal propagating in RC with interface debonding, the portion of L (0, 2) mode that traveling in the top half of the bar experience strong attenuation due to the S-C interface, whilst the portion that traveling in the bottom half remains in the bar and transmit to the other end of the bar. Thus, it is reasonable to assume that the signal traveling in the bar embedded in RC with interface debonding is superposition of the signals traveling in bare bar (bottom half) and in the bar embedded RC with good interface bond (top half). Hence the characteristics of the received signals are dominated by the portion of signal that travels in the bottom part of the steel bar.

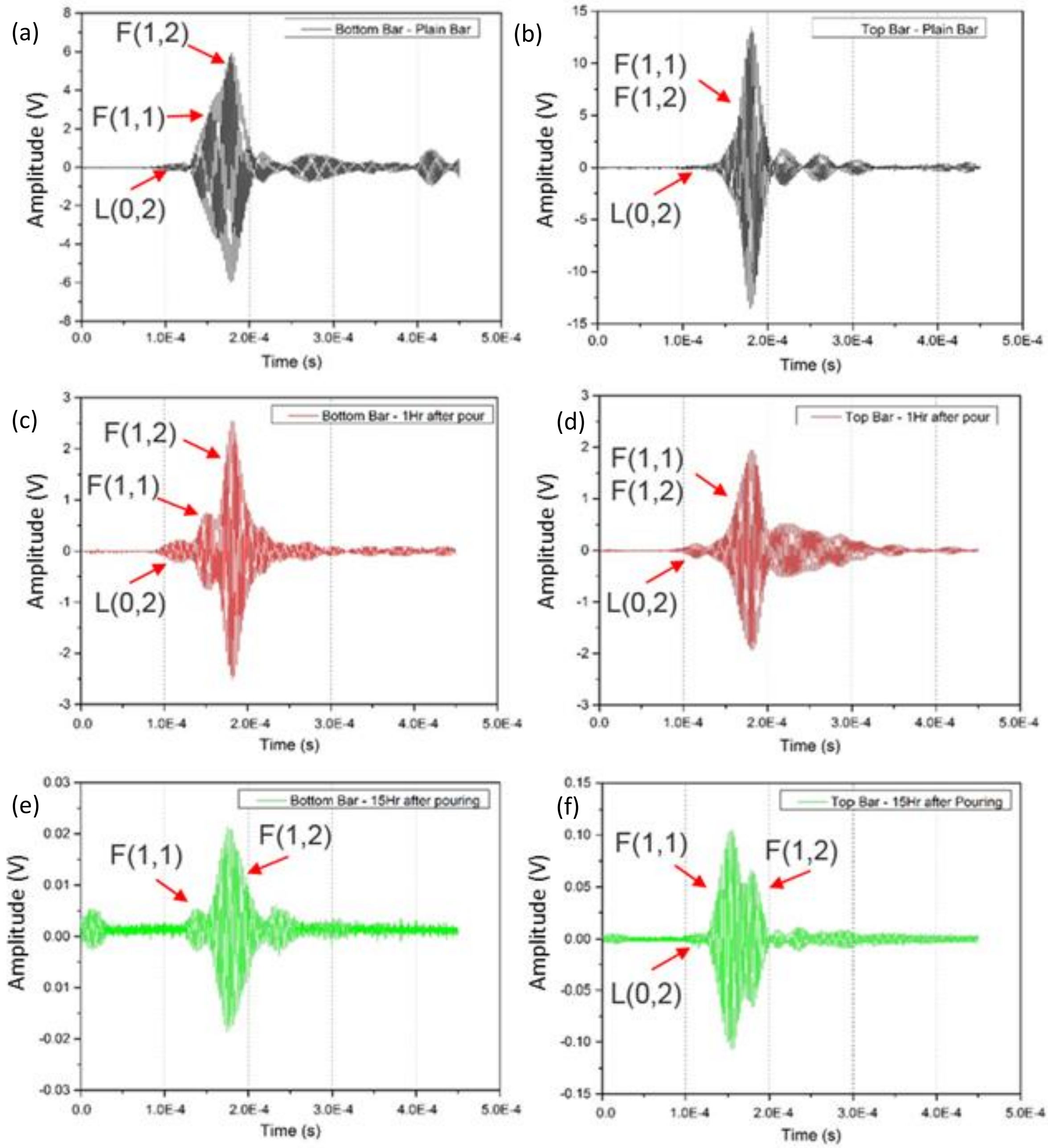

Fig. 5-6. *Received signals in time domain in bottom bar (A1 at 100mm) (a) before pouring concrete (c) 1 hour after pouring (e) 15 hours after pouring and in top bar (A4 at 700mm) (b) before pouring concrete (d) 1 hour after pouring (f) 15 hours after pouring*

The linear damage index DI_{linear} indicating the relationship between the amplitude of received signals over time and the amplitude of the signal in benchmark (bare bar) is employed to investigate the energy loss of the signal over time. The DI_{linear} of signals received in bar A1 (100mm), A2 (300mm), A3 (500mm) and A4 (700mm) up to 290 hours are plotted and compared in Fig. 5-7. When fresh concrete is poured into the mould (1 hour), the amplitude of the signals drops by 40 % to 90%. It is noted that the amplitude in the bottom bar A1 reduces the least. Once the concrete get hardened at 15th hour, the amplitude in all bars drops significantly and the amplitude of signal in the bottom bar A1 drops the most by about 99.7%. Since then, the DI_{linear} for signals in all bars remains steady until 66th hour when the mould is removed. A noticeable increment in the DI_{linear} is observed in all bars but the bar A2. This is because when the mould is removed, the energy that use to leak into the mould via the steel-timber interface is retained in the steel bar and hence the amplitude increases. The holes in the mould at the location of bar A2 are loose, so no energy is expected to leak into the mould and hence the amplitude of signal travelling in bar A2 is not influenced by the mould. The DI_{linear} of signals again becomes steady with higher rate once the mould is removed. The DI_{linear} of signal in the bottom bar, where good S-C interface is expected, is the lowest among all the bars at about 2.1%. The DI_{linear} in all other bars where top-bar effect is expected varies between 4.4% and 9.8%.

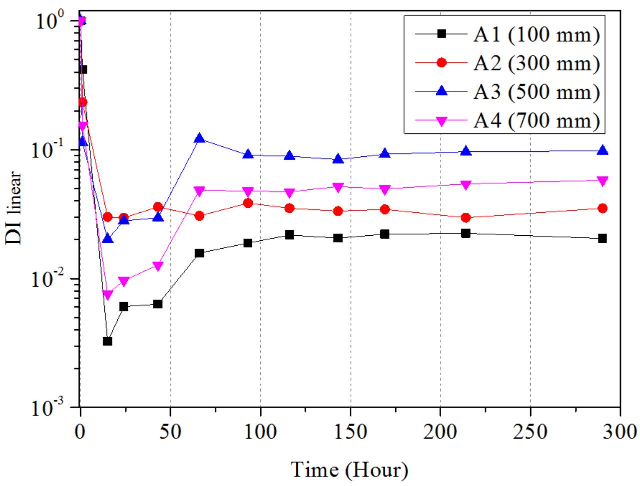

Fig. 5-7. *The linear damage index DI_{linear} of signals at different time after pouring concrete*

5.5.2. Destructive Tests

After 28 days, the concrete wall specimen were sawn into four specimen, each one of these contained one steel bar with a concrete cover of 20 mm. Then, four slices of about 70 mm thickness was sawn to observe the interface quality using a video-microscope with a magnification of 100 times. Fig. 5-8 illustrates the photos of S-C interface located at a height of 100 mm, 300 mm, 500 mm and 700 mm from the bottom of the specimen. The specimen, with a steel bar located at a height of 100 mm, exhibit a perfect bonding. Interfacial debonding is observed in the bottom surface (regarding to casting direction) of the horizontal bars located at heights of 300mm, 500 mm and 700 mm. It is observed that the size of the debonding varies along the steel bar, accurate estimation of the area of the interfacial debonding would be challenging. In general, the width of the interfacial defect at 500 mm is slightly larger than that at 700mm. However, the length of the debonding is measured to be around 70mm at 300mm height, 130 mm at 500 mm height and 200 mm at 700 mm height. None of these debonding (at 300mm, 500 mm and 700 mm) are throughout the length of the bar. As a result, significant reflection of signals are expected at the two ends of the specimens.

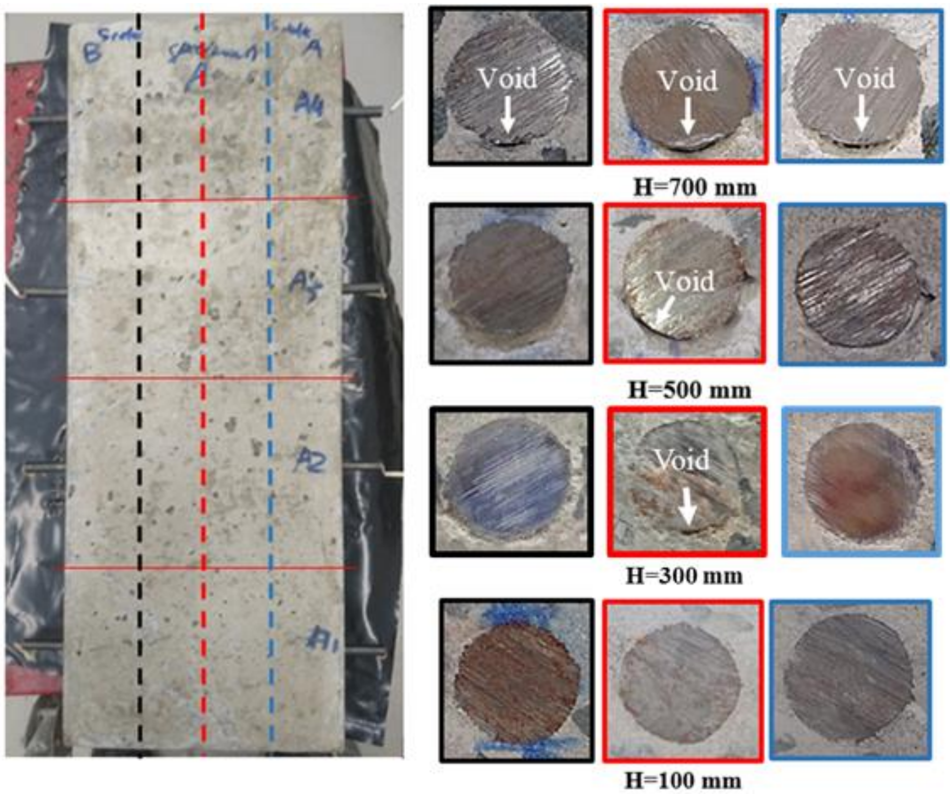

Fig. 5-8. *Bars at 100 mm, 300 mm, 500 mm and 700 mm height from bottom; top-bar is observed in bars at higher levels*

5.5.3. High Frequency Components

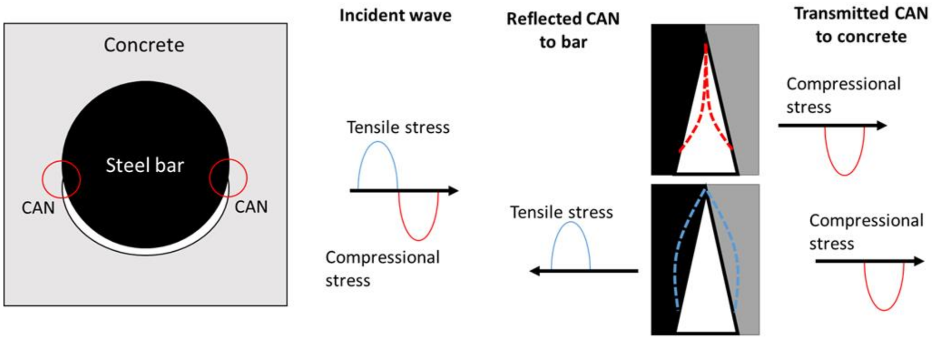

Fig. 5-9. *Schematic diagram illustrating CAN at steel-concrete interface debonding*

It is already demonstrated in Fig. 5-8 that top bar effect generates very thin gaps between concrete and steel which are likely to generate CAN when inspected with ultrasonic waves. Fig. 5-9 shows a schematic of generation of scan in the case of top bar, especially at the crack tips. When ultrasonic waves strike the interface, the compressive part closes the debonding and transmits into the surrounding concrete. While the tensile part further opens the debonding and reflects back to the bar. CAN generated using the transmitted compressive part of the ultrasonic wave through the defect has been extensively applied to characterise small-scale defects (Chao, Ming et al. 2013, Hong, Su et al. 2014, Wang, Wu et al. 2018). This is the first application of CAN using the rebar as the wave guide. It combines the advantages of low attenuation of guided waves and high sensitivity of CAN to thin cracks.

The frequency profiles of the signals received in bar A1-A4 are shown in Fig. 5-10. At first, the bar in air is investigated. Clear peaks can be observed due to the excitation frequency component (EFC) at 400 kHz and at the double of that frequency, a high frequency component (HFC) at 800 kHz in all bars in air. It is well known that HFC can be due to the geometric and material nonlinearities of the specimen, as well as the instrument nonlinearity (IN) generated by the ultrasonic system. As the bar in air is unlikely to have material or geometric nonlinearities, the HFC can be contributed to IN. The experiment has been repeated immediately after pouring of concrete and at regular intervals after that. Immediately after concrete is poured into the mould, the amplitude of both EFC and HFC reduced considerably. This is due to leakage of energy from the bar into concrete. As the concrete hardened, more and more energy leaked from the bar into concrete. Therefore, the EFC peak went down further. At 66 hours, there has been a marginal increase in the peak. This is due to the removal of formwork at that time. After that, the peak remains steady, which means that concrete has hardened enough and no more leakage is taking place.

Unlike EFC, the trend in HFC varied with the position of the bar. HFC in all the bars was very similar when in air. They were also similar 1 hour after pouring of concrete. That indicates that there is no significant debonding at the SC interface until 1 hour after pouring of concrete. But the differences are clear at 15 hours. In bar A1, the HFC peak went sharply down with progression hardening of concrete. In the 15 hours, HFC was not discernible at all and it remains so for the entire period of the experiment. It may be concluded that no CAN is generated in case of A1 and therefore, no debonding due to top-bar effect is detected. This observation is validated by the destructive test conducted at the end of the experiment. Fig. 5-8 shows that no debonding was observed in A1. However, in all other bars, although the HFC peak attenuated considerably after pouring of concrete, it was clearly visible all though the period of the experiment. This observation suggested that there is a possibility of CAN in bars A2, A3 and A4. However, the possibility of IN must be eliminated. IN is presented to the same extent in A1 as well, but no HFC is observed in A1. Therefore, it can be concluded that the attenuation of the signal due to concrete has brought HFC down below the measurement level. Thus HFC observed in the bars A2, A3 and A4 is due to CAN. Our ultrasonic tests have detected debonding due to the top-bar effect in bars A2, A3 and A4. This observation is validated through destructive tests at the end of the experiment (see Fig. 5-8). Thus, HFC is a very useful indicator for detecting and monitoring top-bar effect. It can be seen that the formation of top-bar after pouring of concrete could be clearly detected with the proposed method.

.

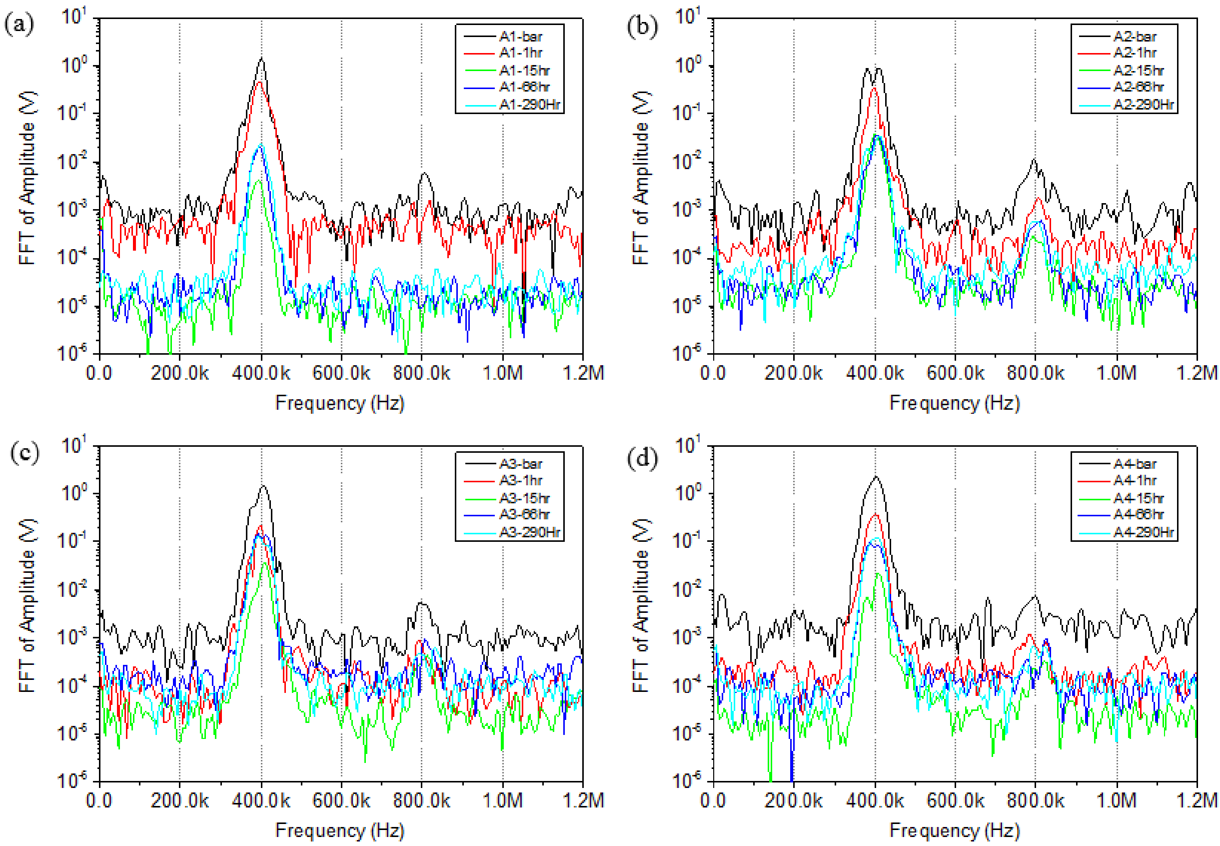

Fig. 5-10*. Frequency profile of received signals at different time after pouring concrete in (a) bar A1 at 100mm and (b) bar A2 at 300mm (c) bar A3 at 500mm and (d) bar A4 at 700mm*

In the previous discussion we have seen that EFC and HFC vary differently in presence and absence of top-bar. The nonlinear damage index $DI_{nonlinear}$ has been explored as a source for easy classification for top-bar. The amplitude of HFC and EFC are calculated by adding up the total amplitude around 800 kHz ± 50 kHz and 400 kHz ±100 kHz respectively. The ratio of bar in air is consider as the benchmark. Fig. 5-11 shows the $DI_{nonlinear}$ in different bars with time after concrete pouring. It is noted that in the bottom bar A1, where good S-C interface bond is expected, the $DI_{nonlinear}$ is close to 0 once the concrete is hardened. No CAN is generated and no system nonlinearity is detected due to strong attenuation at the S-C interface. In all other bars, the $DI_{nonlinear}$ is much higher than A1. Thus this method can clearly classify bars with top-bar from the bar without. After the concrete is poured, the $DI_{nonlinear}$ shot up dramatically in A3 and A4 indicating formation of top-bar. The increase was relatively moderate in case of A2. It may be recalled that A2 was at a lower level than A3 and A4. Thus, it is likely that top-bar formation is delayed in this bar. The $DI_{nonlinear}$ came down sharply for A3 and A4 and became steady well above the benchmark for the rest of the experiment. In case of A2, on the other hand, the ratio increases steadily during the first 50 hours and became steady at the same level of A3 and A4. All three bars had a $DI_{nonlinear}$ well above that of A1, indicating clearly the top-bar effect. It is likely that top-bar had generated more quickly in the bars at higher elevation than A2, which was at 300mm.

As all the $DI_{nonlinear}$ for bars with top-bar varied within a narrow range, it is not clear how the $DI_{nonlinear}$ varies with the extent of top-bar. It may be recalled that the present experiment did not especially design top-bar with a varying extent. It merely cast bars using a standard methodology and top-bar was obtained when concrete of a certain minimum depth was available below the bars. Thus, another set of experiment with a precise control is being planned to explore the ability of the present non-destructive technique in calibrating the extent of the top-bar effect.

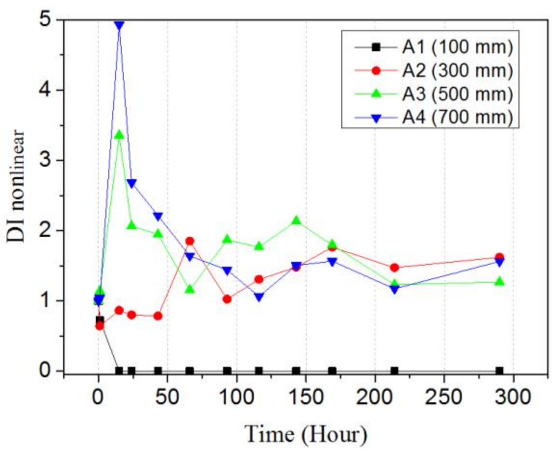

Fig. 5-11. *The nonlinear damage index $DI_{nonlinear}$ of the received signals in steel bars at different height over time*

5.6. Conclusion

This paper proposes a non-destructive technique for monitoring top-bar effect in concrete. Such a technique has been developed for the first time. It uses ultrasonic guided waves to detect possible debonding at the steel-concrete interface due to the creation of top-bar. Reinforced concrete wall samples have been cast with bars placed at different elevations with an aim to creation of possible top-bar. Piezo patches attached to the ends of the bars and excited through a signal generator and amplifier circuit. The samples have been investigated from casting until the concrete has hardened enough so that there is no significant change in the signals. The signal transmitted through the bar is recorded and analysed for discerning the change in their signatures. At the end of the experiment, the samples were cut open to look for visible evidences of top-bar. Contact acoustic nonlinearity generated due to interaction of the debonded surfaces has been utilised for non-destructive detection of top-bar. Following major conclusions can be made from this investigation:

- Top-bar effect was present in the bars at elevation of 300 mm and above.
- Guided ultrasonic waves are capable of non-destructive detection of top-bar.
- The signal travelling in the embedded top-bar is a superposition of signals for bar in air and that in the embedded bar with good interface.
- The energy-based linear damage index DI_{linear} can be employed to classify the bars with top-bar effect with respect to the DI_{linear} of the bar without. A greater DI_{linear} is expected in the bar with larger interface debonding.
- High frequency component of the signal is a very useful indicator of top-bar. The bars with top-bar effect can be clearly classified from the bars without. The proposed $DI_{nonlinear}$ can be used as a reference-free method to detect top-bar. In the hardened concrete specimen, the $DI_{nonlinear}$ is greater than 1 in the bars with top-bar effect. Whilst the $DI_{nonlinear}$ is equal to 0 in the bottom bar with good interface.
- Boundary reflection from the mould has significant effect on the signal strength. It is suggested that the bars should not tightly contact with the holes on the mould.

Although this investigation clearly demonstrates the ability of the present nonlinear ultrasonic technique to detect top bar, there are a few issues that may affect the results. The design vertically aligns all of the reinforcement. Thus, the unobstructed free distance below any individual bar is at a maximum of 200 mm. The vibration duration of the concrete is not uniform for the four layers. This may have affected the bond quality. As the debonding underneath the bar is only due to top-bar effect in the present study, the location and the size of the debonding cannot be controlled and hence is impossible to accurately measure. Quantifying the size of the debonding using the signal strength and the proposed damage indices still remains a challenging task. The proposed nonlinear method shows a promising potential of being a reference-free indicator of top-bar effect. However, a referencing bar (e.g. bar without debonding and bars with various size of debonding) is required to establish a correlation between the features of ultrasonic signals and the sizes of debonding, hence quantifying the size. Numerical and experimental parametric studies are proposed to correlate the damage indices with the size of the debonding by controlling the size of the debonding underneath the bars.

Reference

Arthur, P. C. (1946). Comparative Bond Efficiency of Deformed Concrete reinforcing Bars. Journal of Research of the National Bureau of Standards, 37(RP 1755), 399-407. doi:10.14359/8754

Baolin Wan, M. F. P. K. A. H., & Aly, A. H. (2002). Top Bar Effects in Prestressed Concrete Piles. ACI structural journal, 99(2), 208-214. doi:10.14359/11546

Bhalla, N., Sharma, S., Sharma, S., & Siddique, R. (2018). Monitoring early-age setting of silica fume concrete using wave propagation techniques. Construction and Building Materials, 162, 802-815. doi:https://doi.org/10.1016/j.conbuildmat.2017.12.032

Castel, A., Vidal, T., & Viriyametanont, K. (2006). Effect of Reinforcing Bar Orientation and Location on Bond with Self-Consolidating Concrete. ACI structural journal, 103(4), 559-567. doi:10.14359/16432

Chan, Y.-W., Chen, Y.-S., Chen, & Liu, Y.-S. (2003). Development of Bond Strength of Reinforcement Steel in Self-Consolidating Concrete ACI structural journal, 100(4), 490-498.

Chao, Z., Ming, H., Zhongqing, S., Qiang, W., & Li, C. (2013). Evaluation of fatigue cracks using nonlinearities of acousto-ultrasonic waves acquired by an active sensor network. Smart Materials and Structures, 22(1), 015018.

Guyer, R. A., & Johnson, P. A. (2009). Nonlinear Elasticity and Nondestructive Evaluation and Imaging. In Nonlinear Mesoscopic Elasticity (pp. 323-367). Weinheim: WILEY-VCH Verlag GmbH & Co. KGaA.

Hong, M., Su, Z., Lu, Y., Sohn, H., & Qing, X. (2015). Locating fatigue damage using temporal signal features of nonlinear Lamb waves. Mechanical Systems and Signal Processing, 60-61, 182-197. doi:https://doi.org/10.1016/j.ymssp.2015.01.020

Hong, M., Su, Z., Wang, Q., Cheng, L., & Qing, X. (2014). Modeling nonlinearities of ultrasonic waves for fatigue damage characterization: Theory, simulation, and experimental validation. Ultrasonics, 54(3), 770-778. doi:https://doi.org/10.1016/j.ultras.2013.09.023

Jeanty, P. R., Mitchell, D., & Mirza, M. S. (1988). Investigation of "Top Bar" Effects in Beams. Structural Journal, 85(3). doi:10.14359/2613

Kong, Q., Hou, S., Ji, Q., Mo, Y. L., & Song, G. (2013). Very early age concrete hydration characterization monitoring using piezoceramic based smart aggregates. Smart Materials and Structures, 22(8), 085025. doi:10.1088/0964-1726/22/8/085025

Lim, Y. Y., Kwong, K. Z., Liew, W. Y. H., Padilla, R. V., & Soh, C. K. (2018). Parametric study and modeling of PZT based wave propagation technique related to practical issues in monitoring of concrete curing. Construction and Building Materials, 176, 519-530. doi:https://doi.org/10.1016/j.conbuildmat.2018.05.074

Lim, Y. Y., Kwong, K. Z., Liew, W. Y. H., & Soh, C. K. (2017). Practical issues related to the application of piezoelectric based wave propagation technique in monitoring of concrete curing. Construction and Building Materials, 152, 506-519. doi:https://doi.org/10.1016/j.conbuildmat.2017.06.163

Lim, Y. Y., Smith, S. T., & Soh, C. K. (2018). Wave propagation based monitoring of concrete curing using piezoelectric materials: Review and path forward. NDT & E International, 99, 50-63. doi:https://doi.org/10.1016/j.ndteint.2018.06.002

Lu, Y., Li, J., Ye, L., & Wang, D. (2013a). Guided waves for damage detection in rebar-reinforced concrete beams. Construction and Building Materials, 47, 370-378. doi:https://doi.org/10.1016/j.conbuildmat.2013.05.016

Lu, Y., Li, J., Ye, L., & Wang, D. (2013b). Guided waves for damage detection in rebar-reinforced concrete beams. Construction and Building Materials, 47(Supplement C), 370-378. doi:https://doi.org/10.1016/j.conbuildmat.2013.05.016

Nasser, A., Clément, A., Laurens, S., & Castel, A. (2010). Influence of steel–concrete interface condition on galvanic corrosion currents in carbonated concrete. Corrosion Science, 52(9), 2878-2890. doi:https://doi.org/10.1016/j.corsci.2010.04.037

Pavlakovic, B., Lowe, M., Alleyne, D., & Cawley, P. (1997). Disperse: A General Purpose Program for Creating Dispersion Curves. In D. O. Thompson & D. E. Chimenti (Eds.), Review of Progress in Quantitative Nondestructive Evaluation: Volume 16A (pp. 185-192). Boston, MA: Springer US.

Reza Esfahani, M., Lachemi, M., & Reza Kianoush, M. (2008). Top-bar effect of steel bars in self-consolidating concrete (SCC). Cement and Concrete Composites, 30(1), 52-60. doi:https://doi.org/10.1016/j.cemconcomp.2007.05.012

Richardson, J. M. (1979). Harmonic generation at an unbonded interface—I. Planar interface between semi-infinite elastic media. International Journal of Engineering Science, 17(1), 73-85. doi:https://doi.org/10.1016/0020-7225(79)90008-9

Sharma, S., & Mukherjee, A. (2010). Longitudinal Guided Waves for Monitoring Chloride Corrosion in Reinforcing Bars in Concrete. Structural Health Monitoring, 9(6), 555-567. doi:10.1177/1475921710365415

harma, S., & Mukherjee, A. (2014). Ultrasonic guided waves for monitoring the setting process of concretes with varying workabilities. Construction and Building Materials, 72, 358-366. doi:10.1016/j.conbuildmat.2014.09.018

Sharma, S., & Mukherjee, A. (2015). Monitoring freshly poured concrete using ultrasonic waves guided through reinforcing bars. Cement and Concrete Composites, 55, 337-347. doi:10.1016/j.cemconcomp.2014.09.011

Solodov, I. Y. (1994). Nonlinear NDE using contact acoustic nonlinearity (CAN). Proceedings of the IEEE Ultrasonics Symposium, 2, 1279-1283.

Solodov, I. Y., Krohn, N., & Busse, G. (2002). CAN: an example of nonclassical acoustic nonlinearity in solids. Ultrasonics, 40(1), 621-625. doi:https://doi.org/10.1016/S0041-624X(02)00186-5

Soylev, T. A., & François, R. (2003). Quality of steel–concrete interface and corrosion of reinforcing steel. Cement and Concrete Research, 33(9), 1407-1415. doi:https://doi.org/10.1016/S0008-8846(03)00087-5

Söylev, T. A., & François, R. (2006). Effects of Bar-Placement Conditions on Steel-Concrete Bond. Materials and Structures, 39(2), 211-220. doi:10.1617/s11527-005-9030-7

Su, Z., Ye, L., & Lu, Y. (2006). Guided Lamb waves for identification of damage in composite structures: A review. Journal of Sound and Vibration, 295(3), 753-780. doi:10.1016/j.jsv.2006.01.020

Su, Z., Zhou, C., Hong, M., Cheng, L., Wang, Q., & Qing, X. (2014). Acousto-ultrasonics-based fatigue damage characterization: Linear versus nonlinear signal features. Mechanical Systems and Signal Processing, 45(1), 225-239. doi:https://doi.org/10.1016/j.ymssp.2013.10.017

Tarek Uddin, N. O., & Makoto, H. (1999). Corrosion of Steel Bars with Respect to Orientation in Concrete. ACI Materials Journal, 96(2), 154-159. doi:10.14359/439

Wang, R., Wu, Q., Yu, F., Okabe, Y., & Xiong, K. (2018). Nonlinear ultrasonic detection for evaluating fatigue crack in metal plate. Structural Health Monitoring, 1475921718784451. doi:10.1177/1475921718784451

Wang, Y., Guan, R., & Lu, Y. (2017). Nonlinear Lamb waves for fatigue damage identification in FRP-reinforced steel plates. Ultrasonics, 80, 87-95. doi:https://doi.org/10.1016/j.ultras.2017.05.004

Wu, F., & Chang, F.-K. (2006). Debond Detection using Embedded Piezoelectric Elements for Reinforced Concrete Structures - Part II: Analysis and Algorithm. Structural Health Monitoring, 5(1), 17-28. doi:10.1177/1475921706057979

Xu, C.-b., Yang, Z.-b., Chen, X.-f., Tian, S.-h., & Xie, Y. (2018). A guided wave dispersion compensation method based on compressed sensing. Mechanical Systems and Signal Processing, 103, 89-104. doi:https://doi.org/10.1016/j.ymssp.2017.09.043

Zhang, R., Castel, A., & François, R. (2011). Influence of steel-concrete interface defects owing to the top-bar effect on the chloride-induced corrosion of reinforcement. Magazine of Concrete Research, 63(10), 773-781. doi:10.1680/macr.2011.63.10.773

Zima, B., & Kędra, R. (2019). Reference-free determination of debonding length in reinforced concrete beams using guided wave propagation. Construction and Building Materials, 207, 291-303. doi:https://doi.org/10.1016/j.conbuildmat.2019.02.143

Zima, B., & Rucka, M. (2017). Non-destructive inspection of ground anchors using guided wave propagation. International Journal of Rock Mechanics and Mining Sciences, 94, 90-102. doi:https://doi.org/10.1016/j.ijrmms.2017.03.005

Zima, B., & Rucka, M. (2018). Guided ultrasonic waves for detection of debonding in bars partially embedded in grout. Construction and Building Materials, 168, 124-142. doi:https://doi.org/10.1016/j.conbuildmat.2018.02.107

Chapter 6

6. Monitoring corrosion in reinforced concrete with interfacial debonding owning to top-bar effect using guided waves.

6.1. Introduction

From the discussion in literature reviews of top-bar effects, it is clear that the corrosion process in concrete with top-bar defects is fundamentally different from those without interfacial voids. Discerning the presence of top-bar defects is paramount. In the previous chapter, a guided wave-based nondestructive method is proposed and successfully detects the presence of the top-bar defects in reinforced concrete. In this chapter, the proposed method is extended to monitor corrosion of reinforced concrete with and without top-bar defects to find the pathway for nondestructive estimation of the state of corrosion and the residual capacity. The specimens are subjected to accelerated corrosion and simultaneously monitored with the presented guided wave-based technique. Guided waves are first employed to investigate bar corrosion alone to explore the influence of bar deterioration on the propagation of guided waves. Then the method is extended to corrosion of bars embedded in concrete. The specimens are corroded to two milestones, termed surface stain and visible surface cracking. The results of ultrasonic signals are analyzed and mapped onto the well-defined corrosion process of reinforced concrete. The results in reinforced concrete with and without top-bar defects are compared and discussed. Eventually, the specimens are cut in half, and the bars are extracted to visually inspect the steel-concrete interface and the deterioration of the bars.

6.2. Monitoring corrosion in reinforced concrete using guided waves : guided waves propagating in the plain bar.

The specimens are subjected to anodic current to accelerate the corrosion. The corrosion of reinforced concretes is continuously monitored in two stages, termed surface stain and surface cracking. The received signals in RC with and without interface debonding owning to the top-bar effect are compared, and the differences are discussed. The specimens are then subjected to several destructive tests to evaluate the interface condition and the residue mechanical properties of the corroded steel bars.

Surface stain and concrete cracking are typical indicators of concrete corrosion by visual inspection. To study the corrosion process of reinforced concrete, the experiments are categorized into three stages: intact, surface stain, and concrete cracking. The details of specimens used in this study are summarised in Table. 6-1. Two parameters were varied: the elevation of the reinforcing bar and the stage of the corrosion process. The elevation of the bars is denoted by letters B and T, where B is the bottom bar located at an elevation of 100 mm, T is the top bar located above 300 mm from the concrete bottom. The stage of corrosion is denoted by letters I, S, and C, where I stands for Intact, S stands for the surface stain on concrete cover, and C stands for the concrete cracking.

Table. 6-1 Details of specimens

Specimen	Event	Elevation of bar	Top-bar defect
BI	Intact	100 mm	NA
BS	Surface Stain	100 mm	NA
BC	Concrete Cracking	100 mm	NA
TI	Intact	≥ 300 mm	
TS	Surface Stain	300 mm	low
TC	Concrete Cracking	700 mm	High

6.2.1. Experiment Results

6.2.1.1. Bar in air

The ultrasonic characteristics of the waveguide have been established by conducting ultrasonic tests on the bar before pouring concrete. A frequency sweep has been conducted from 200 kHz to 600 kHz at an interval of 20 kHz to determine the best excitation frequency ω. The dispersion curve for a 12 mm steel plain bar is presented in Fig. 6-1. It is noted that only two wave modes, L(0,1) and F(1,1), exist in the signal at 200 kHz. As the excitation frequency increases, more wave modes are generated. The newly generated modes have the highest velocity, while the existing modes convergent to a constant velocity. The attenuation of the modes is around 2 dB/m at 200 kHz and 4 dB/m to 8 dB/m at 600 kHz. The attenuation of all the modes in the plain bar is low within the selected frequency range. Hence, a high amplitude of transmitted signals is expected.

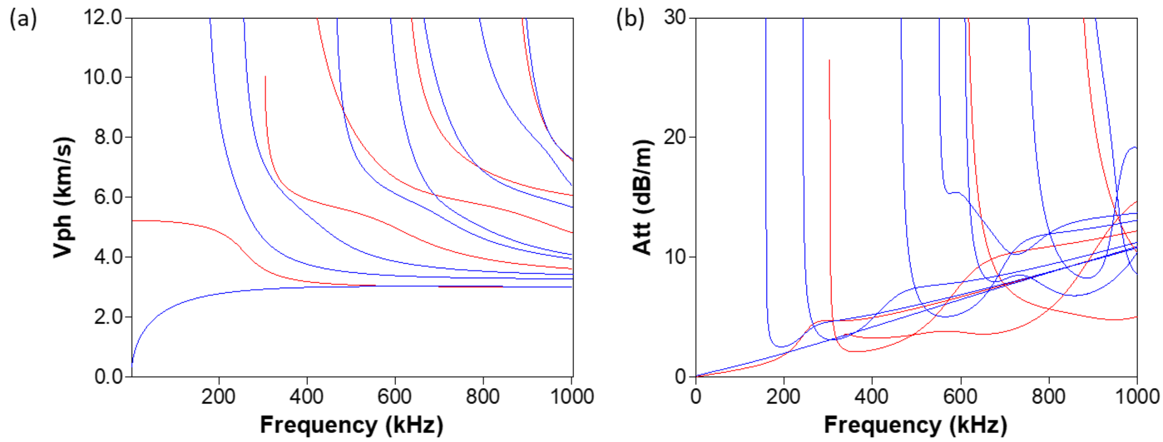

Fig. 6-1 Dispersion curves for 12 mm diameter steel plain bar (a) phase velocity and (b) attenuation.

The typical TI variation from 200 kHz to 600 kHz of the transmitted signal received in the bar in air is shown in Fig. 6-2. The TI varies significantly with different excitation frequencies. Three distinct zones can be clearly identified, which are 200 kHz to 280 kHz (zone 1), 280 kHz to 450 kHz (zone 2), and 450 kHz to 600 kHz (zone 3). Zone 1 is peaked at 250 kHz. It is recalled that the resonance frequency of the PZT wafer is between 230 kHz to 260 kHz. Hence, this peak corresponds to the resonance amplitude of the PZT wafer. However, the TI of the received signal is not solely dependent on the resonance amplitude of the wafer. Other features such as the geometry of the waveguide, the attenuation of the wave mode, and mode shape can also influence the amplitude of the TI. Hence, the peak amplitude over the entire frequency range is at 350 kHz in zone 2. The variation of the amplitude in zone 2 is the largest. The amplitude increases about eight times from 280 kHz to 350 kHz. In zone 3, the peak amplitude is at 500 kHz. The variation of the amplitude of the TI in zone 2 is much smaller than that in zone 3.

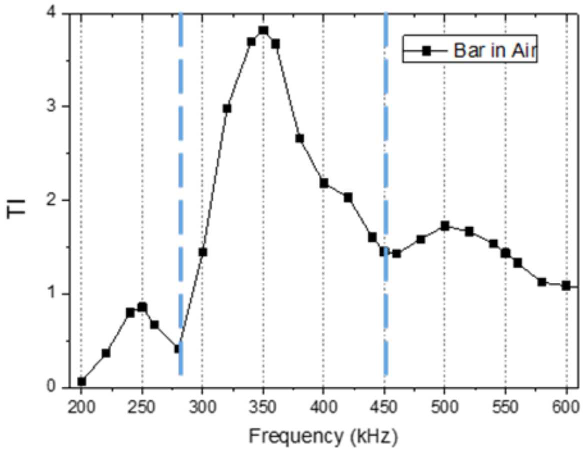

Fig. 6-2 Typical TI of Transmitted signal in Bar in air.

Fig. 6-3 shows a typical excitation signal and received signal in a bar in air at a central frequency of 350 kHz. The effective frequency range is 300 kHz to 350 kHz with a central excitation frequency, ω, of 350kHz, and the bandwidth of excitation signal, B, is 100 kHz as shown in Fig. 3-23 (b). Hence, the amplitude of the FFT of the received signal from 300 kHz to 350 kHz is summed up to obtain the TI, as shown in Fig. 3-23 (d).

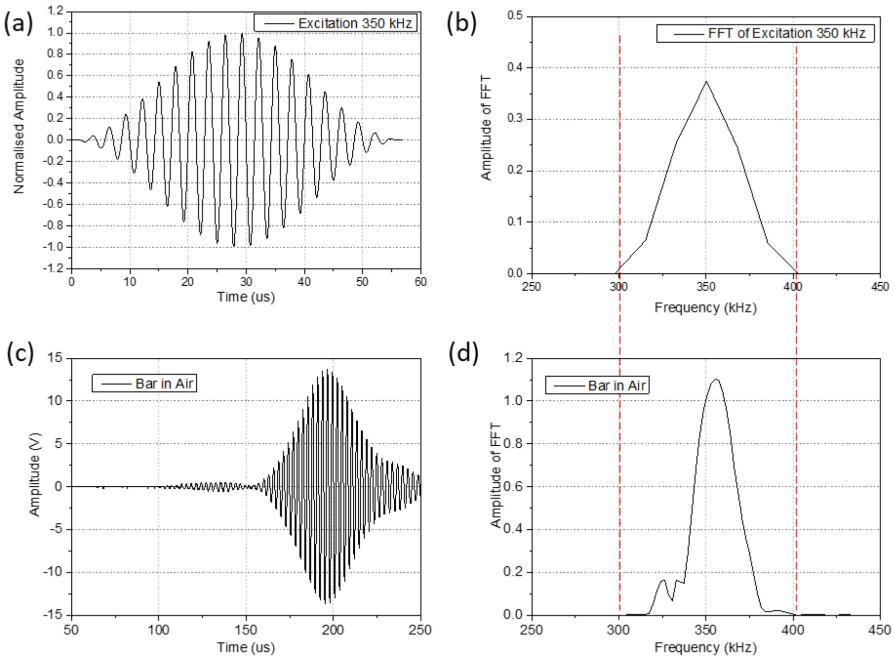

Fig. 6-3 (a) Excitation signal in the time-domain at 350 kHz, (b) Excitation signal at frequency domain, (c)a typical received time signal in the bar in air, and (d) received signal at frequency domain.

6.2.1.2. *Fresh concrete*

6.2.1.2.1. *Stage 0: Fresh concrete*

After 28 days, the concrete slab was sawn into four smaller specimens. Each small specimen contains a reinforcing bar with a minimum concrete cover of 20 mm. For corrosion experiments, one set of specimens, sawn from the same concrete slab, were subjected to anodic current. The other set of specimens were further sawn to observe the interfacial quality using a video microscope with a magnification of 100 times. Fig. 6-4 shows the photos of the S-C interface located at the height of 100 mm, 300 mm, 500 mm, and 700 mm from the bottom of the concrete slab. With a steel bar located at a height of 100 mm, the bottom specimen exhibits a perfect bond. While interfacial debonding is observed in the bottom surface (regarding casting direction) of other horizontal bars. It is noted that the depth and width of the debonding vary along the same bar. Accurate estimation of debonding size would be challenging. The observation at one section of the specimen is only used to estimate the tendency of the size of the debonding against the height. A similar phenomenon has been observed by other researchers (Zhang, Castel et al. 2011)(Zhang, Castel et al. 2011) In general, the size of the debonding increases with the height of the bar. The width of debonding at 500 mm is slightly larger than that at 700 mm. However, the debonding length is measured to be around 130 mm at 500 mm height and 200 mm at 700 mm height.

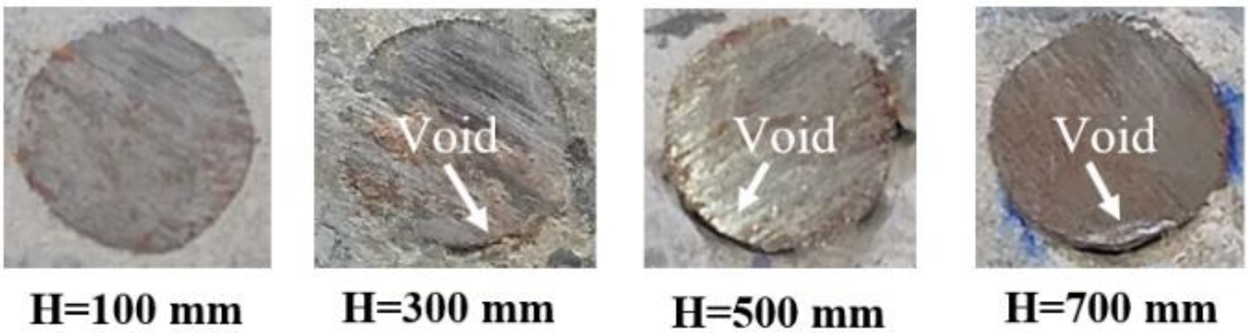

Fig. 6-4 Bars at 100mm, 500mm and 700mm height from the bottom; top-bar is observed in bars at higher levels

Fig. 6-5 shows the dispersion curves for 1 12 mm steel plain bar embedded in concrete with infinite thickness. It is immediately observed that some modes are incomplete, and F (1,1) mode is missing from the curves. Reinforced concrete is a multiple-layered system with different material properties. The complicity of such a system increases the instability of the calculation and the generation of the dispersion curves. Other than this, the phase velocity curve for the 12 mm diameter steel plain bar embedded in concrete is similar to that for the 12 mm diameter plain bar, indicating that the bond around the bar does not significantly influence the velocity of the guided wave. The significant difference between a plain bar and an embedded bar lies in the attenuation. The attenuation of the signal in an embedded bar is around 180 dB/m at 200 kHz and 250 dB/m to 430 dB/m at 600 kHz, which is 90 times and 54 times more than these in a plain bar. It is also noted that the attenuation rate for F (1,2) mode increases dramatically between 300 kHz to 400 kHz. The attenuation is about 680 dB/m, while the value is 5 dB/m in a plain bar system.

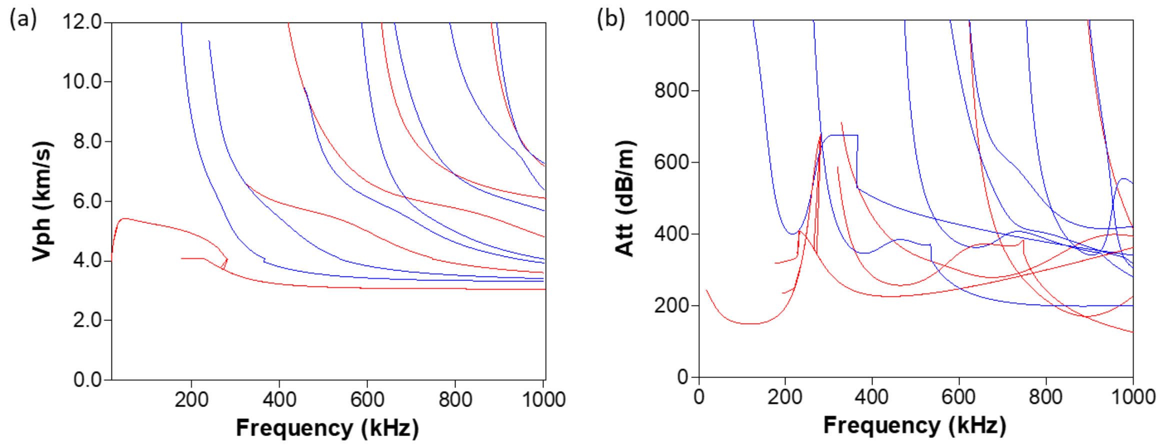

Fig. 6-5 Dispersion curves for 12 mm diameter steel plain bar embedded in concrete (a) phase velocity and (b) attenuation.

Fig. 6-6 shows the transmitted energy in embedded bars at different elevations using frequency sweep. The pattern of the amplitude-frequency distribution varies significantly in bars at different elevations. However, the three zones can be clearly identified. In the bar at an elevation of 100 mm, where the steel-concrete interface is perfectly bonded, the maximum amplitude of the TI lies in zone 1. As the evaluation of the bar increases, the amplitude of zone 2 and zone 3 increases. In the bar at an elevation of 300 mm, the peak amplitude of the three zones is similar. As the elevation of the bar increases to 700 mm, the pattern of the amplitude-frequency distribution is similar to that in the bar in air with a peak amplitude at 350 kHz. It is recalled that an interfacial void is formed underneath the bar at 300 mm and above and the size of the void increases with the elevation of the bar. The embedded bar is getting similar to the bar in air as the void increase with the bar elevation. As a result, the amplitude-frequency distribution of the signal in the embedded bars is getting closer to that in the bar in air with the increasing bar elevation. The amplitude of the TI in zone 1 remains strong in all scenarios, while the amplitude in zone 2 varies significantly with the elevation of the bar. Hence, the signals excited using the frequencies in zone 2 are sensitive to the bond variation at the steel-concrete interface, and the maximum change happens around 350 kHz.

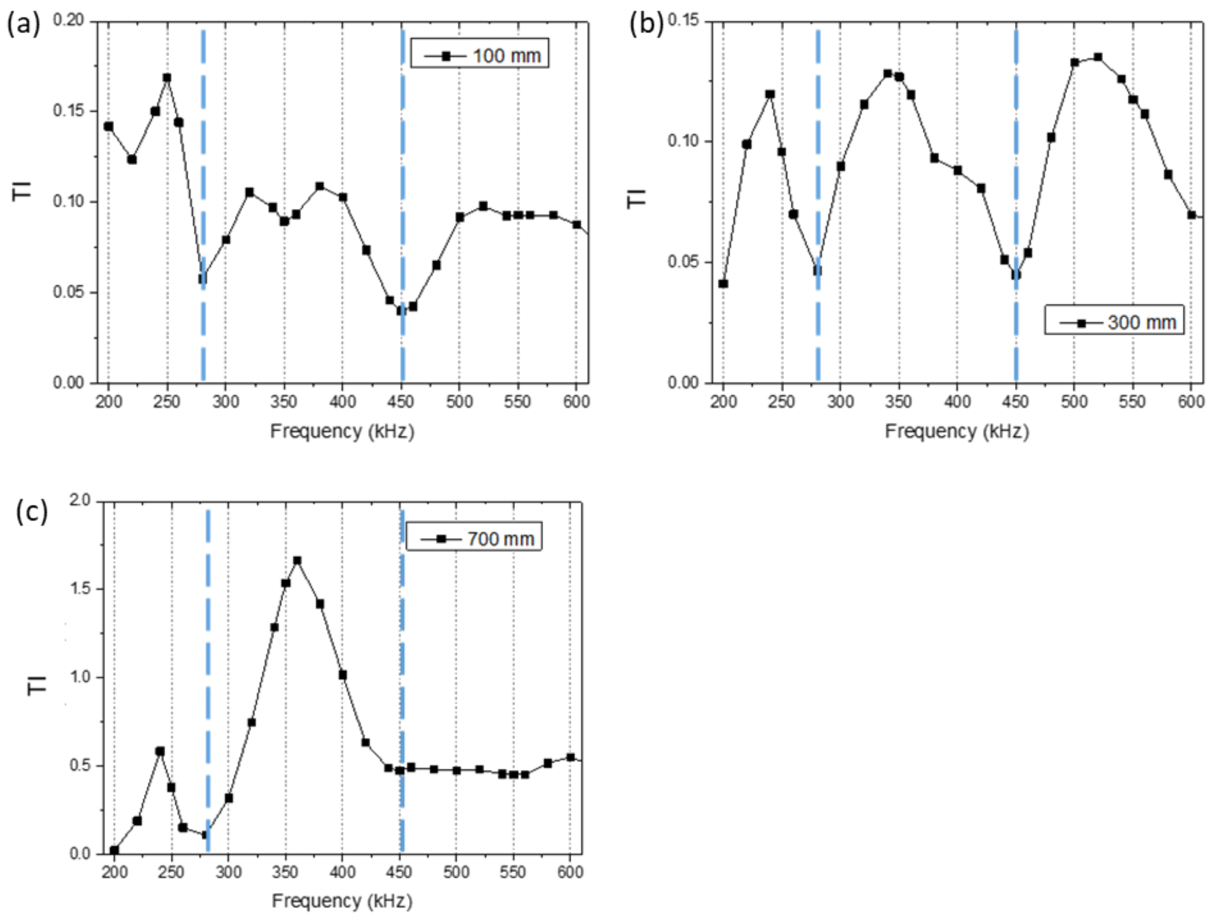

Fig. 6-6 TI of Transmitted signal in intact specimens at an elevation of (a) 100 mm, (b) 300 mm, and (c) 700 mm

Fig. 6-7 shows a typical received signal at 350 kHz. By referring to the dispersion curves of a 12 mm diameter round steel bar, the two wave packets are identified as the F (1,1) mode and the F (1,2) mode. The mode shape of F (1,1) and F (1,2) are shown in Fig. 6-7 (b) and (c), respectively. Both modes show significant axial displacement and energy density at and near the surface of the bar. Hence, it is sensitive to the variation in the steel-concrete interface. In addition, the signal excited at 350 kHz delivered high signal strength in all specimens. Therefore, signal excited at 350 kHz was used to evaluate the corrosion process.

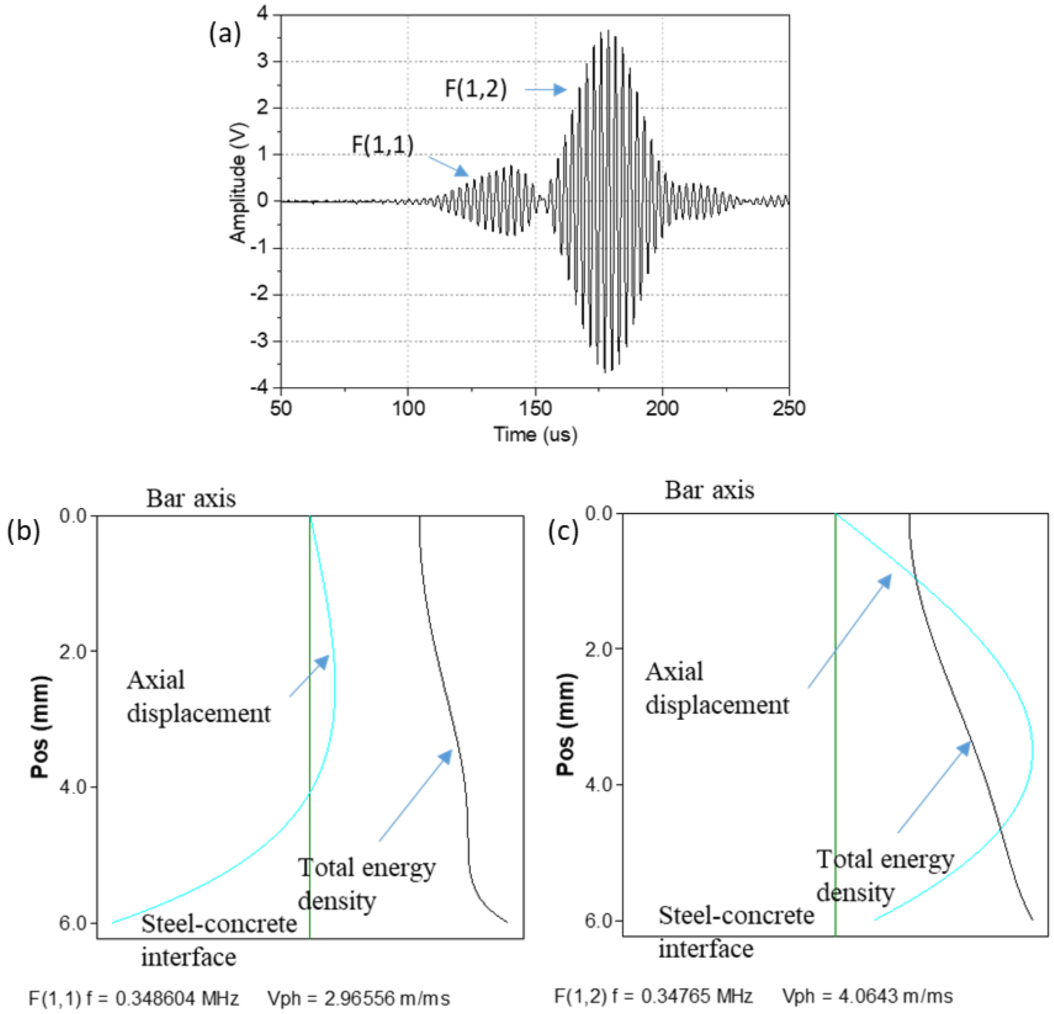

Fig. 6-7 Typical received signal in an embedded bar (a) in time domain, (b) mode shape of F (1,1), and (c) mode shape of F (1,2).

6.2.1.3. Exposure to corrosion

Two sets of RC specimens, each contains one specimen with a good S-C bond (bottom bar) and one with S-C interface debonding owning to top-bar effect (top bar), have been subject to accelerated corrosion using anodic current. All specimens are monitored through the steel bar using a sweeping-frequency guided wave. The patterns of the TI of different frequencies were similar in the same specimen but varied with different specimens. Visual inspection is the most frequently used method to monitor concrete corrosion in the field. Rust stain and corrosion-induced cracking are the most commonly used indicators to identify the corrosion stage of a concrete structure. Hence, the corrosion experiment targets two concrete corrosion stages, namely surface stain, and concrete cracking. One set of specimens, containing one bottom bar specimen and one top bar specimen at 300 mm, is corroded until the rust stain appears on the concrete cover while the other set, containing one bottom bar specimen and one top bar specimen at 700 mm, is tested until the complete cracking of concrete cover.

6.2.1.3.1. Bar alone

A plain bar is corroded at a constant current of 0.03A to evaluate the influence of corrosion on the guided waves. The bottom half of the middle 200 mm of the bar was submerged in NaCl solution and subjected to an anodic current to induce corrosion in the bar with a top-bar defect. The top half of the bars remained unaffected. Fig. 6-8 shows the condition of the bottom half of the corroded bars at different points of mass loss. Initially, the bar had a dark grey appearance because of the mill scale formed on the surface of the bar. The grey mill scale disappeared gradually and a lighter grey with increasing corrosion. Shallow surface corrosion was observed up to a mass loss of 0.79%, and no pits were observed. As the corrosion proceeded further, pits started to form on the corroding surface. Two long and deep slots are observed at the end of the experiment, with a mass loss of 2.93%.

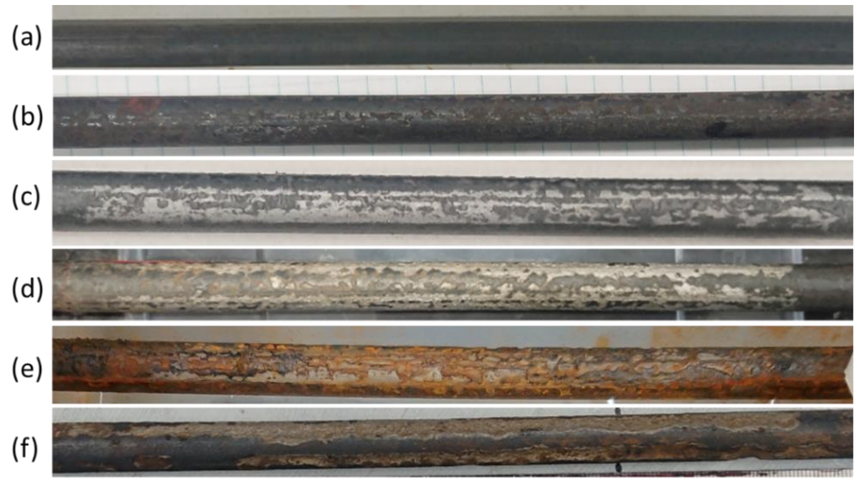

Fig. 6-8 Visual inspection of the condition of the bar in air specimen with a mass loss of (a) 0%, (b) 0.28%, (c) 0.54%, (d) 0.79%, (e) 1.62% and (f) 2.93%.

Fig. 6-9 shows the trend of ultrasonic TI in the bar in air specimen. Two stages were visible. The TI increased by about 33% in stage 1, with a mass loss of up to 0.79%. Then the TI dropped monotonically with the further loss of mass (Stage 2). In stage 1, the mass loss is insignificant, and the loss of the material is uniformly spread on the corroding surface, and no pits are formed. In stage 2, pits start to form on the surface of the bar leading to an increasing wave scattering and attenuation of the TI. Hence, the TI continues to drop with the increasing size of pits.

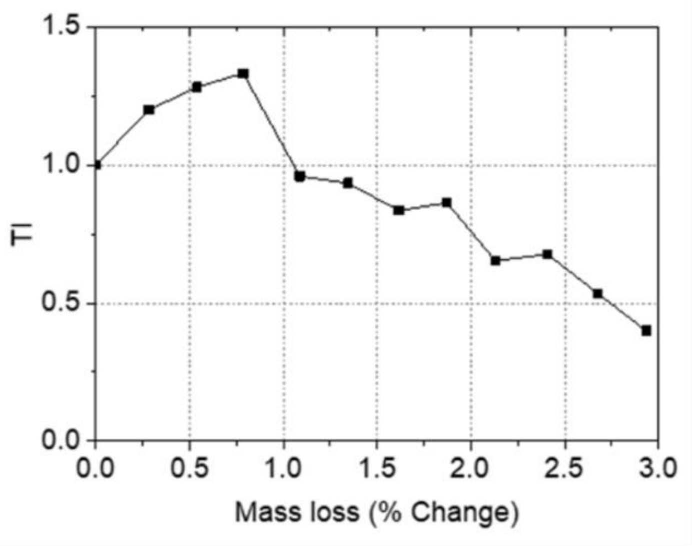

Fig. 6-9 TI of transmitted signal at 350 kHz of the bar in air.

6.2.1.3.2. Stage 1: Surface stain

6.2.1.3.2.1. Visual inspection

In specimen BS, the rust stain appeared on the concrete surface until 190 hours of accelerated corrosion (Fig. 6-10 a). The current remained 0.03A at a constant voltage of 5 V. The extracted bar showed localized pits formation only in the middle of the bar where the rust stain appeared. Only shallow and insignificant pits were observed on the surface facing the dripping side, and the other side of the bar was intact. There was no significant loss of material. The specimen was sawn along the bar to observe the S-C interfaces.

Fig. 6-10 Visual inspections of the condition of concrete beams and bars at the end of corrosion: (a) rust stain on the surface of specimen BS (b) pits and irregularities on the surface of the extracted bar facing the dripping side, and (c) intact surface on the other side.

The steel-concrete interface was presented in Fig. 6-11 (a). Rust was observed over the entire interface facing the dripping side, and no significant rust was observed on the other side. A dark brown zone was observed as circled in the figure, indicated aggressive corrosion occurred in this area. It was diagnosed that the bond between the steel bar and the concrete was partially damaged due to demoulding. The discontinuity between the bar and the concrete left a gap for NaCl solution to accumulate and induce corrosion. The dark brown zone indicated the initial debonding at the interface. The specimen was further sawn through the surface stain to inspect the crack propagation. The cross-section of the specimen that cut through the surface stain is shown in Fig. 6-11 (b). Cracks were observed on the right side of the cross-section, and no sign of crack was observed on the left side. The location of the crack initiation was identified. Two cracks, marked by red and green arrows, were initiated from that location. The crack marked as the green arrow propagated about 3 mm the stopped. The other crack propagated horizontally to the nearest aggregate and then propagated through the cement-aggregate interface along the path of the crack. The total length of the crack was about 21 mm.

(a)

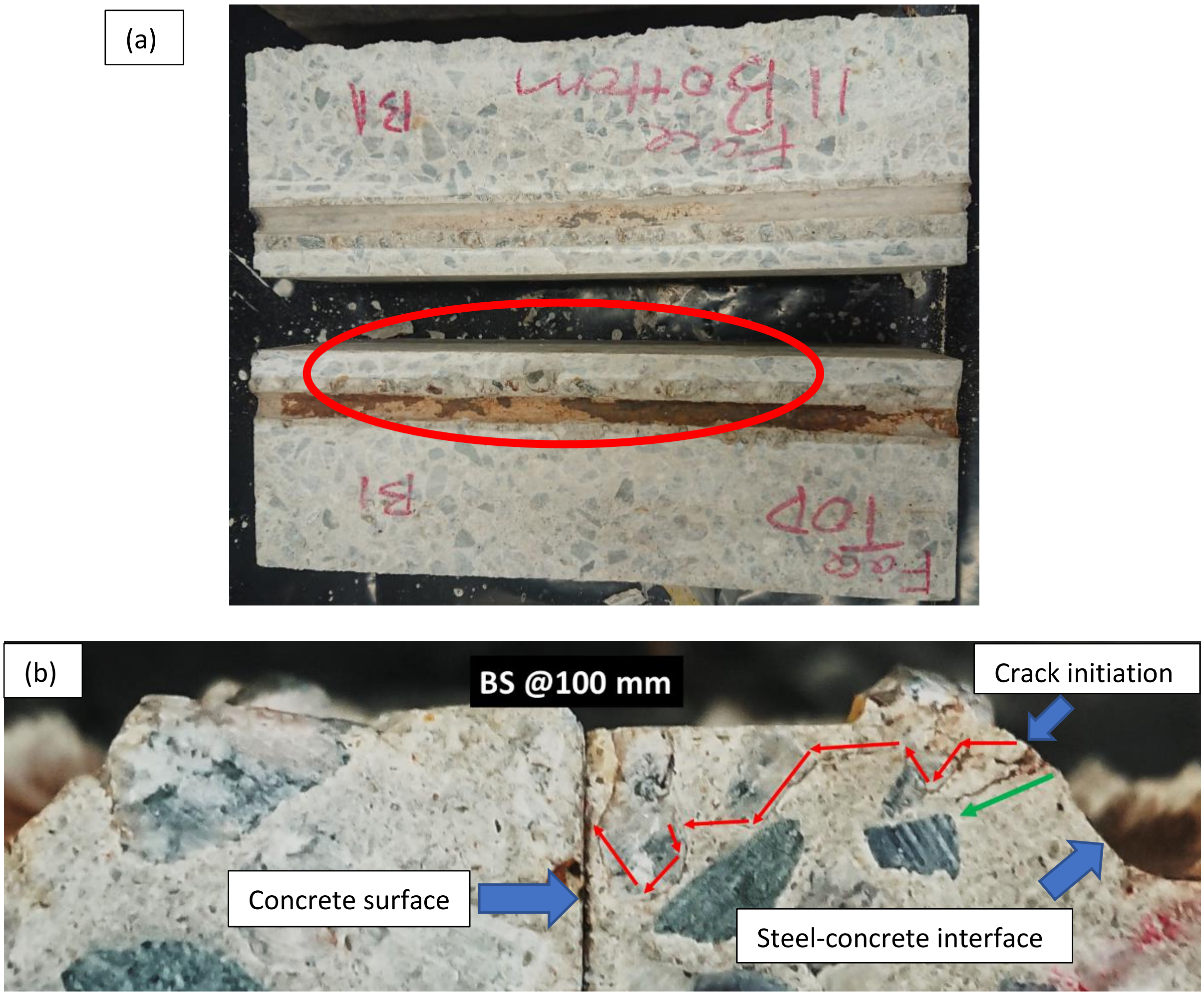

Fig. 6-11 steel-concrete interface and cross-section view through the stain in specimen BS (a) S-C interface and (b) cracking from S-C interface to concrete surface.

The rust stain appeared on the surface in specimen TS until 246.5 hours (Fig. 6-12 a). The current started at 0.02 A and increased to 0.03 A at 146 hours. Then it remained 0.03A at a constant voltage of 5 V since then. The extracted bar showed widespread and significant pits and irregularities over the surface of the entire embedded part of the bar facing the dripping side. The material loss was irregular, but the material lost the most from the middle bottom part of the bar where the debonding owning to top-bar effect was expected to form. No sign of corrosion was observed on the surface on the other side.

Fig. 6-12 Visual inspections of the condition of concrete beams and bar at the end of the corrosion periods: (a) rust stain on the surface of specimen TS (b) pits and irregularities on the surface of the extracted bar facing the dripping side and (c) intact surface on the other side.

Figure Fig. 6-13 (a-d) shows the condition of specimen TS after 0, 169, 228.5, and 246.5 hours of accelerated corrosion. The time was selected based on the appearance of the visual sign of corrosion on the surface of the concrete specimen. No sign of corrosion was observed in the first 150 hours of corrosion. After 165 hours of exposure to chloride-induced corrosion, reddish-brown liquid rust oozed out from the right end of the specimen, indicating the first visual sign of the occurrence of corrosion of the steel bar. The liquid rust continued to ooze out only from the right end until 228.5 hours, when liquid rust was observed at the left end of the specimen. The rust stain appeared on the concrete cover after 246.5 hrs of corrosion.

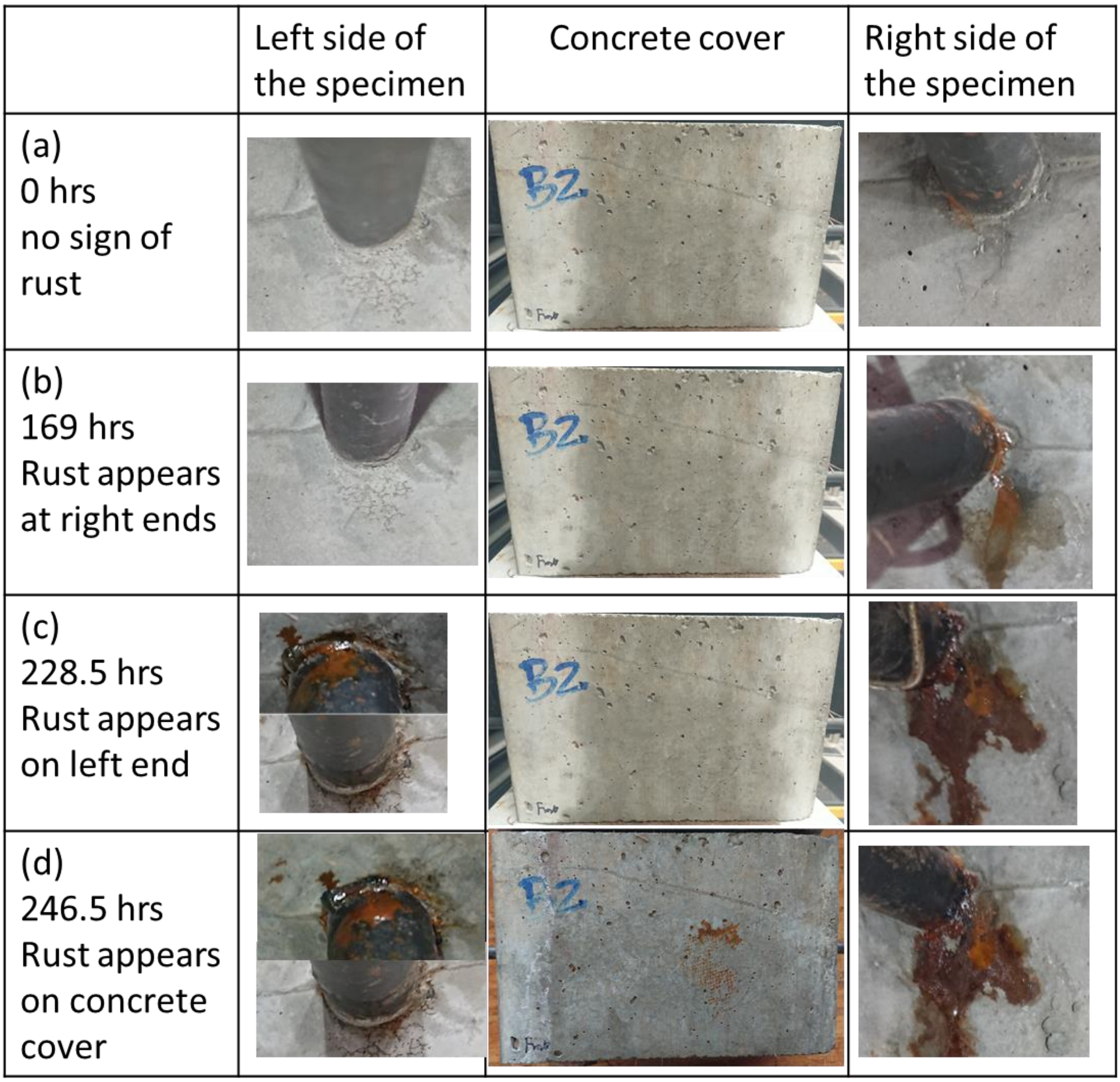

Fig. 6-13 Visual inspections of specimen TS after 0, 169, 228.5, and 246.5 hours of accelerated corrosion.

A significant amount of rust stain was observed over the entire S-C interface facing the dripping side as shown in Fig. 6-14 (a), indicating the bar corrosion within the gap owning to top-bar effect. Rust was also observed in the vicinity area, revealing the intrusion of rust into pores. Localized rust stain was observed on the other side of the interface. The cross-section of the specimen that cut through the surface stain is shown in Fig. 6-14 (b). Cracks were observed on both surfaces of the cross-section and the locations of the crack initiation were identified. The crack on the left surface first propagated through an aggregate next to the location of the crack initiation. Then the crack propagated towards the aggregate near the concrete surface through cement. Once the crack reached the aggregate, it propagated through the cement-aggregate interface and reached the surface of the concrete cover. The total length of this crack was about 30 mm. While the crack on the right side propagated through the cement-aggregate interface from the crack initiation to the surface of the concrete cover. The total length of this crack was about 48 mm.

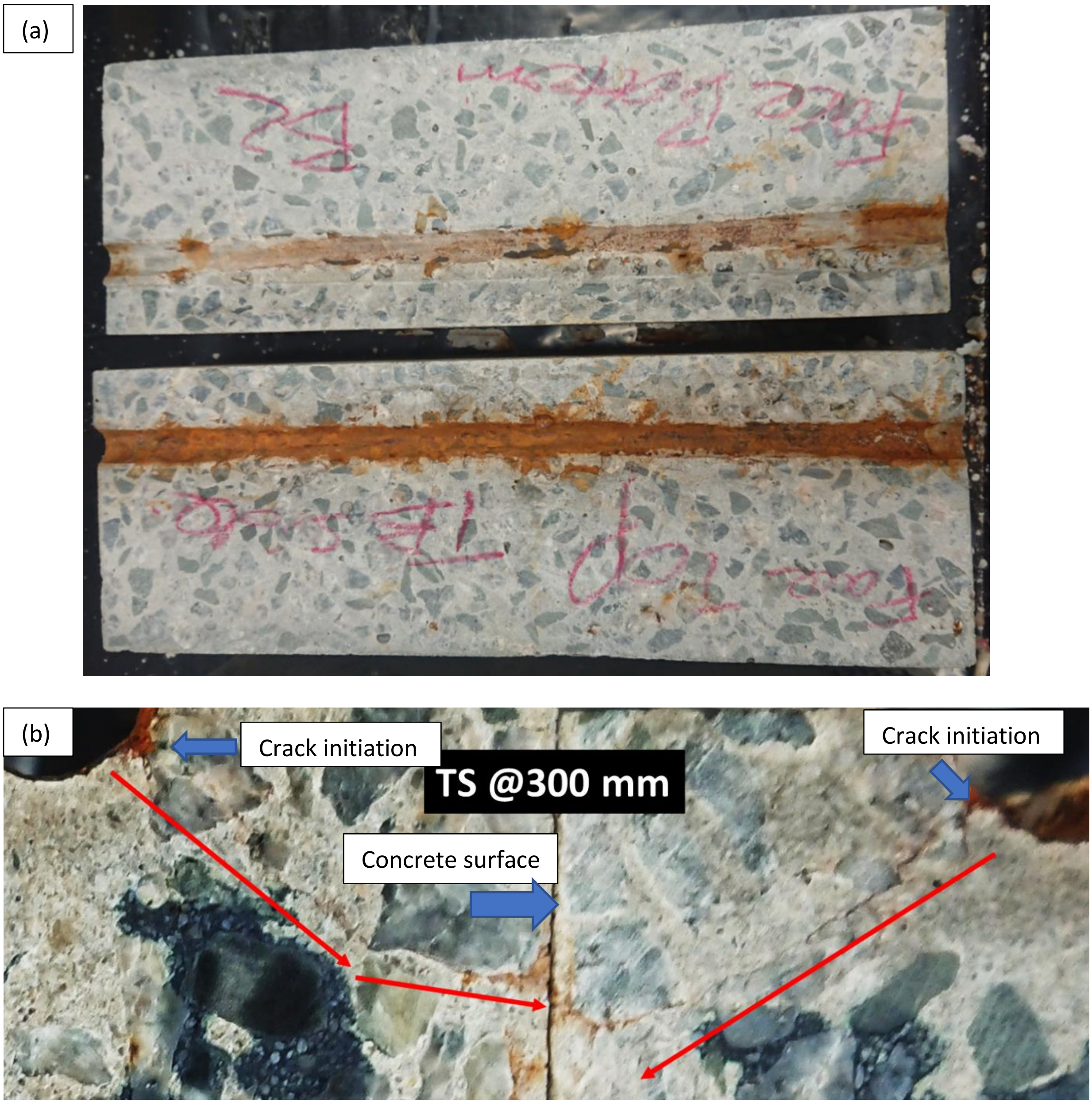

Fig. 6-14 (a) steel-concrete interface of specimen TS and (b) crack at the cross-section

By comparing the visual inspection results of the two specimens, it is noted that the size of the rust stain on specimen TS widely spread over a large area around the location of the bar, while the rust stain on specimen BS is small and only concentrated at one point. It is possibly due to the different patterns of corrosion occurring in the two specimens. The bar extracted from specimen BS shows localized corrosion, while the bar in specimen TS shows generalized corrosion over the entire area of the bar where the top-bar is expected. In specimen BS, localized corrosion occurs at one point, and the corrosion-induced crack initial from there. Subsequently, the rust fills in the crack that further expends the crack until the crack reaches the surface of the concrete cover. Since the corrosion is localized, the expensive pressure induced by the rust is only focusing on one point. The width of the crack is expected to be narrow, which matches with the destructive test result in figure Fig. 6-11 (b). The crack was only observed at one side of the cross-section, while in specimen TS, cracks were observed on both sides of the cross-section, as shown in Fig. 6-14 (b). The expensive pressure applied over a larger area and the crack might initiate at one point but expended over a larger area, resulting in the wider crack.

6.2.1.3.2.2. Monitoring with guided wave

Fig. 6-15 shows the trend of TI of the received signal in specimen BS using guided wave at 350 kHz. The specimen was corroded until the rust stain appeared on the concrete cover.

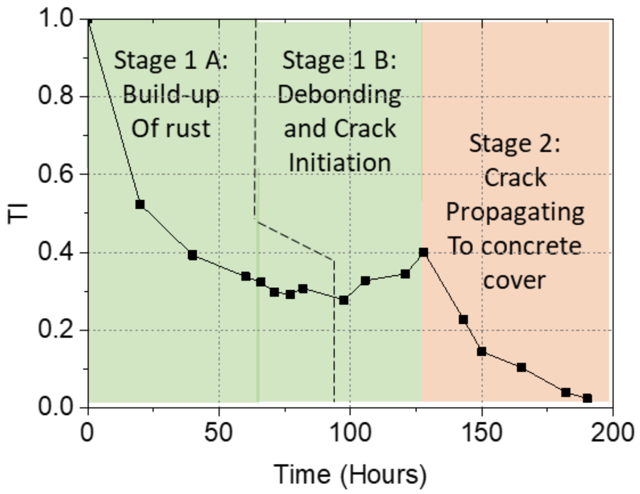

Fig. 6-15 TI of transmitted signal at 350 kHz of specimen BS

Stage 1 A: The rust is building up around the bar during this stage. The corrosion products were generated around the bar and filled the voids in the vicinity. Hence no visual signal could be observed to identify the occurrence of stage 1 A. However, as for the ultrasonic results, the TI of the received signal initially reduced about 47.7 % in the first 20 hours and then continued to drop about 24.6 % until 100 hours of corrosion before it started to rise, as shown in Fig. 6-15.

Fig. 6-16 shows the envelope of the time signal at 350 kHz in specimen BS during stage 1 A. The amplitude of the F (1,1) mode and the F (1,2) mode dropped significantly in the first 60 hours of corrosion, about 48.2 % and 75.6 %, respectively. Then the reduction of the amplitude of both modes slowed down at about 1% per 20 hours. It was noted that the wave packet of the F (1,2) mode was slightly separated into two wave packets at 40 hours. Further separation was observed after 60 hours, and the shape of the wave packets remained consistent until the end of stage 1 A.

The continuous reduction of TI indicated the occurrence of stage 1A. The generated rust first filled the porous voids around the bar. At this stage, no compressive pressure should be generated at the interface. Hence, the contact between steel bar and concrete remained steady. As the rust was further generated, compressive pressure on the surrounding concrete was generated, leading to a tight contact between the bar and the concrete. The pressure increased with the corrosion and further increased the contact at the interface. More waves could leak into the surrounding concrete, and fewer waves could be transmitted, resulting in a reduced TI. Theoretically, at the beginning of stage 1 A, the change in the contact between the steel bar and the surrounding concrete was insignificant. The TI of the signals should remain steady. However, it was observed that in the first 60 hours, the TI dropped significantly. This was because the bond between the steel bar and the concrete was partially damaged when the specimen was removed from the mould. By comparing the amplitude of the signal before demoulding and other intact specimens, a significant increment in the amplitude of the received signal was observed once the specimen was demoulded. As a result of the partial debonding, the rust filled the debonding zone and instantly increased the contact between the steel bar and the surrounding concrete, leading to a sharp reduction in the TI.

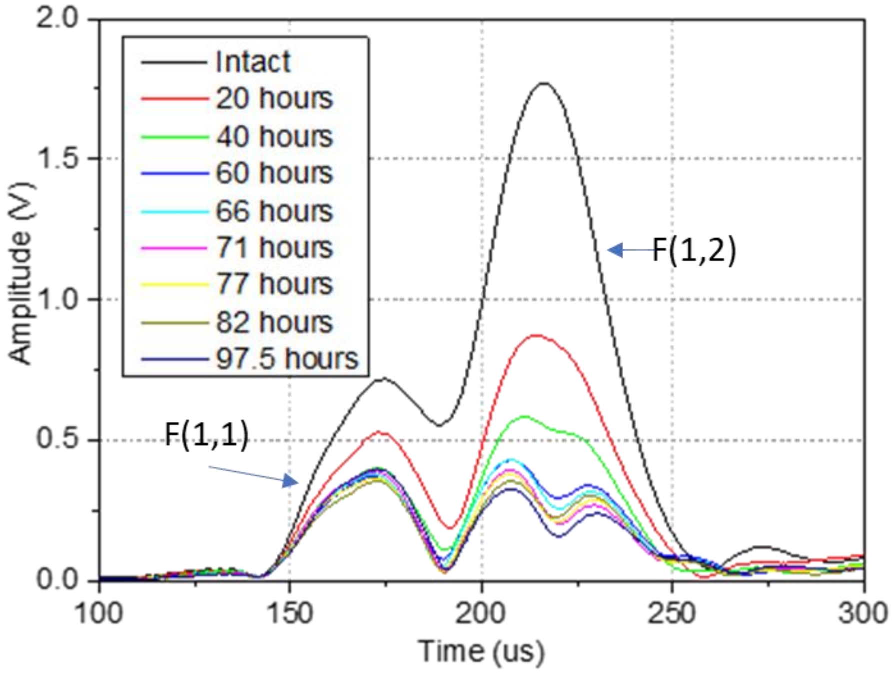

Fig. 6-16 The envelope of the time signal during stage 1 A.

Stage 1 B: During stage 1 B, delamination at the steel-concrete interface occurs, and the corrosion-induced crack is initiated at the end of the stage. The TI of the signals increased about 12.3 % from 97.5 hours to 128 hours of corrosion. The time signals at 350 kHz during stage 1 B are presented in Fig. 6-17. From 97.5 hours to 105.5 hours, the amplitude of the F (1,1) mode decreased while the F (1,2) mode increased, which resulted in an overall TI increment of 5.0 %. Then both modes increased with corrosion until 128 hours. It was noted that the second peak of the F (1,2) mode slowly merged to the first peak.

The increment of TI indicated the occurrence of stage 1 B. The exceeded rust at the interface induced the delamination at the interface. This reduced the contact between the steel bar and the surrounding concrete, leading to an increment in the TI as more waves being retained in the bar. The delamination also allowed the accumulation of more rust, which further increased the compressive pressure. When the rust-induced compressive pressure exceeded the bearing capacity of the surrounding concrete, the crack started in the concrete cover. The crack initiation released the compressive strength on the concrete, leading to an increment in the TI.

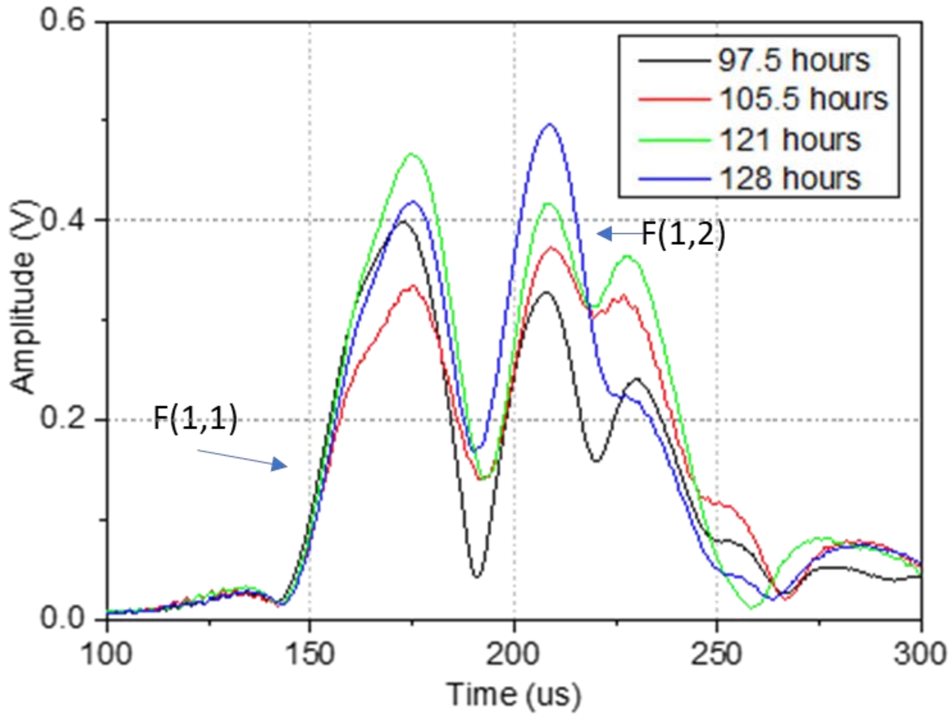

Fig. 6-17 The envelope of signals at 350 kHz during stage 1 B.

Stage 2: The crack propagates from the bar towards the surface of the concrete during this stage. The TI of the signals continuously dropped by 37.6 % throughout the entire duration. The time signal during stage 2 is presented in Fig. 6-18. The amplitude of the F (1,1) mode dropped sharply by 87.9 % from 128 hours to 182 hours, and then the amplitude remained steady until the surface stain was observed. While the first peak of the F (1,2) mode dropped sharply with time, and the two peaks merged with time. The two peaks completely merged from 165 hours until the end of the exposure period.

The change in the trend of the TI indicated the occurrence of the initiation of the crack propagation, and the continuous reduction in the TI indicated the crack propagation towards the surface of the concrete. During the crack propagation process, the rust continuously filled in the cracks, which further expend the crack until it reached the surface of the concrete. The crack allowed easy access of NaCl solution to reach the steel bar. Rapid chemical reactions occurred at the vicinity of the cracks, leading to a localized bar deterioration. Hence, the attenuation of the guided waves increased as the geometry of the bar getting complex due to the deterioration. As a result, the TI continued to drop over time.

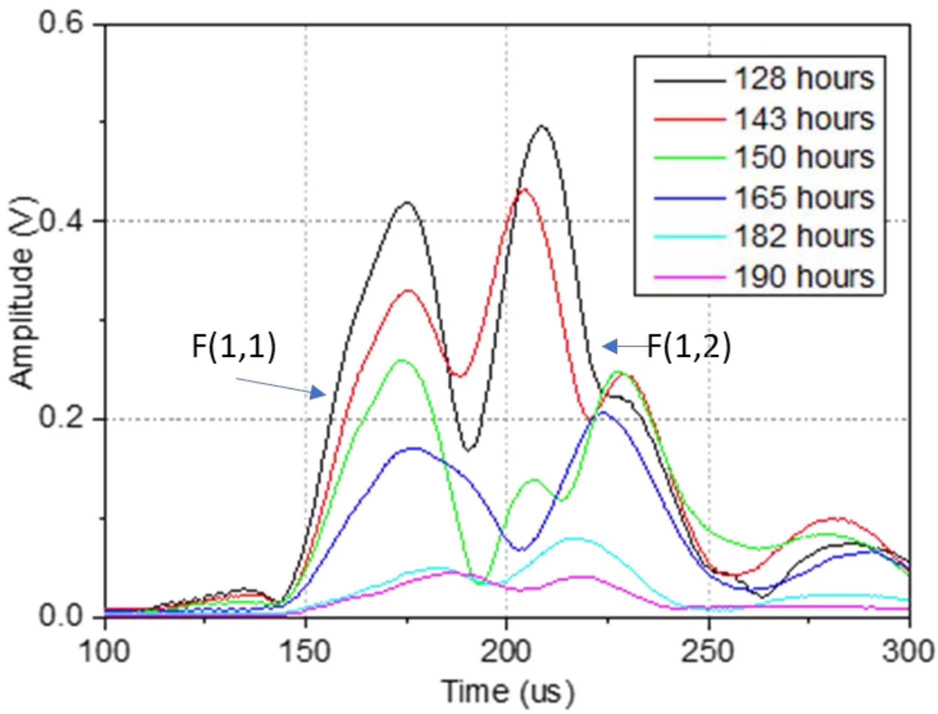

Fig. 6-18 the envelope of the signal at 350 kHz during stage 2.

Fig. 6-19 shows the maximum amplitude of F (1,1) mode and F (1,2) mode in the received signal at 350 kHz. The amplitude of both F (1,1) mode and F (1,2) mode dropped sharply in the first hours. It was recalled that the specimen BS was partially debonded. The rusts generated at the interface in the first 60 hours significantly increased the contact between the bar and the concrete. More energy leaked into the surrounding concrete, and therefore, the amplitude of the two modes dropped with time. The effect of the bond on the guided wave in a good bond specimen was claimed. The amplitude of the F (1,1) mode became steady, and the amplitude of the F (1,2) mode dropped at a slow rate from 60 hours to 100 hours of corrosion. This is the expected signal fluctuation in a controlled specimen during the initial stage of the corrosion. The rust filled in the porous voids around the bar, and the expensive pressure began to build up. The increment in the contact between the bar and the concrete was mainly contributed by the filled void. Hence, the amplitude reduction was not significant. As the expensive pressure further increased, debonding occurred at the steel-concrete interface, resulting in the increment in the signal amplitude from 105.5 hours to 128 hours. The amplitude of both F (1,1) mode and F (1,2) mode dropped over time until the rust stain appeared on the concrete cover.

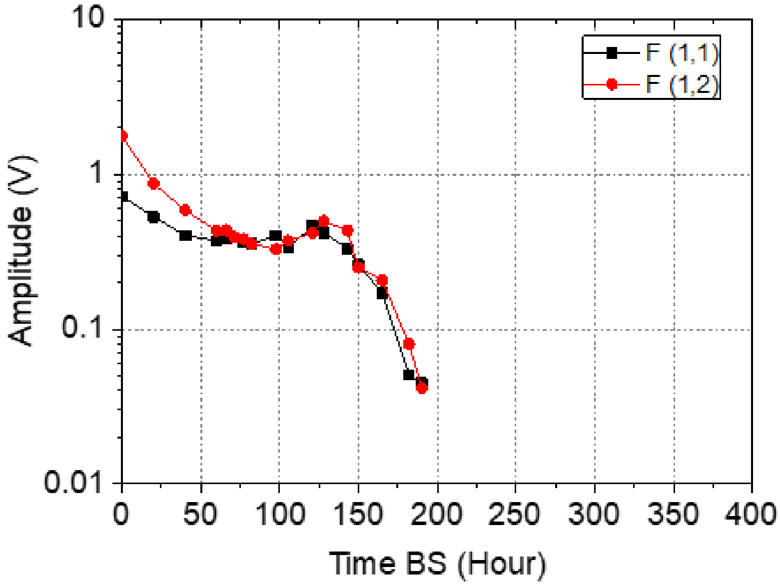

Fig. 6-19 Maximum amplitude of F (1,1) and F(1,2) mode in specimen BS.

Fig. 6-20 shows the trend of TI of the received signal in specimen TS using guided wave at 350 kHz. The specimen was corroded until the rust stain appeared on the concrete cover. The TI first dropped about 7 % in 6 hours and remained steady until 22 hours. Then it continued to decrease throughout the entire period of the experiment. In contrast to the trend of the TI in specimen BS, no distinguish stages could be observed in specimen TS. In the first 22 hours, the loss of material was slight, the deterioration of the bar was negligible. The attenuation of the signal due to the bar deterioration was insignificant. In addition, the rust was accommodated by the void. No compressive pressure was buildup at the S-C interface. Therefore no noticeable change in TI was observed. It was noticed that the increment rate of TI after 90 hours was slower than that before. Due to the presence of voids underneath the bar, NaCl solution was directly contacted with the bottom surface of the bar. Once anodic current was applied through the specimen, rust would be generated immediately after the breakdown of the passive protective layer. The condition of this part of the bar was equivalent to a bare steel bar submerged in NaCl solution. In this case, the deterioration of the bar occurred before the delamination of the S-C interface, which resulted in the continuous reduction of TI.

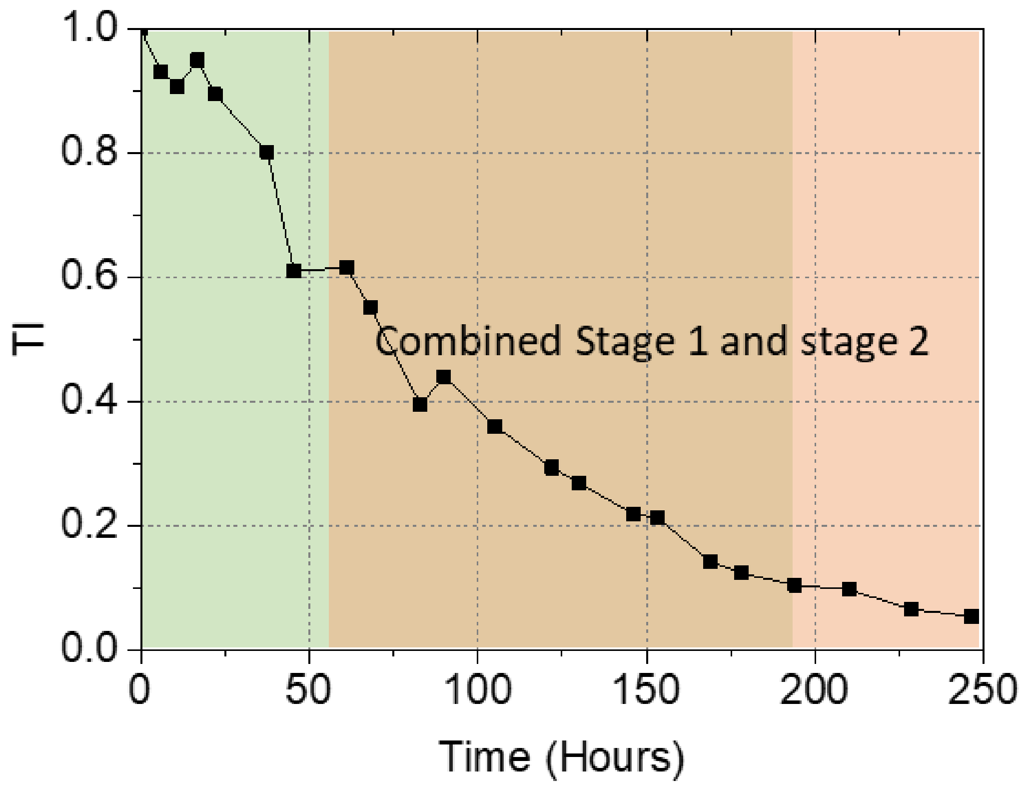

Fig. 6-20 TI of transmitted signal at 350 kHz of specimen TS

The envelope of the time signals was presented in Fig. 6-21. The F (1,1) mode and the F (1,2) mode were merged, but the two peaks could be clearly identified. The time signals were almost identical in the first 22 hours, and then the amplitude of the signals reduced with time. It was noted that the amplitude of the F (1,2) mode dropped at a faster rate than that of the F (1,1) mode.

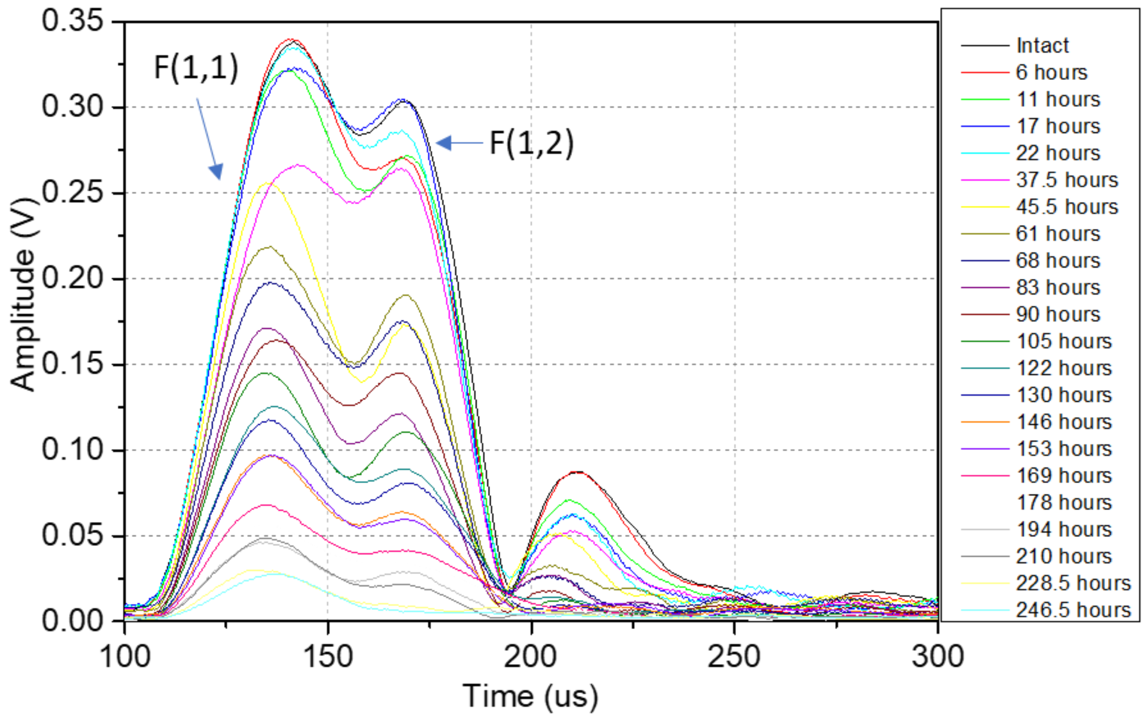

Fig. 6-21 The envelope of time signal at 350 kHz in Specimen TS

Fig. 6-22 shows the peak amplitude of the F (1,1) mode and the F (1,2) mode of the signal in specimen TS. In the first 22 hours, the amplitude of the F (1,1) mode remained steady while the F (1,2) mode slightly dropped, indicating the occurrence of the bar corrosion. The location of the corrosion was believed to be within the top-bar zone. The amplitude of the F (1,1) mode and the F (1,2) mode continuously dropped with time until the end of the corrosion period. It was noted that the amplitude of the F (1,2) mode shown an up and down fluctuation between 22 hours and 90 hours. This is because the bar corrosion and the interface debonding simultaneously affect the guided waves. It is recalled that the axial displacement and the energy density of the F (1,2) mode are in the vicinity of the bar surface. Hence, the F (1,2) mode is sensitive to the steel-concrete interface and the bar deterioration on the bar surface. Bar corrosion reduced the amplitude of the guided wave while interface debonding increased it, resulting in the up and down fluctuation in the amplitude. It was also noted that, from 90 hours, the reduction rate of the F (1,2) mode was much faster than that of the F (1,1) mode. The F (1,2) mode was more sensitive to corrosion in specimens with the top-bar effect as it monitored both bar deterioration at the surface and the change in the steel-concrete interface.

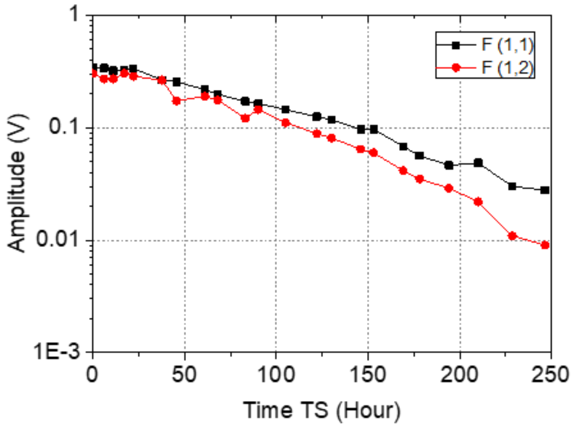

Fig. 6-22 The peak amplitude of F (1,1) and F (1,2) mode in specimen TS.

6.2.1.3.3. Stage 2: Concrete cracking

6.2.1.3.3.1. Visual inspection

In stage 2, specimen BC and TC undergoing accelerated corrosion showed the formation of the horizontal crack along the bar as shown in Fig. 6-23 and Fig. 6-26. Liquid rust oozed out from the middle part and at both ends of the concrete specimen during the accelerated corrosion process.

In specimen BC, the liquid rust first oozed out from both ends of the specimen at 171 hours. The rust stain appeared on the concrete cover after 213 hours of accelerated corrosion. With the increment in the rust volume, the crack initiated at the rust stain and progressed along the bar. Brown liquid rust continuously oozed out from the concrete cover, but no clear crack was observed until 290 hours. The concrete cover was completely split within 350 Hours. As shown in Fig. 6-23 (c), two significant pits were observed near the location of surface stain from the extracted bar, indicating the occurrence of the localized corrosion.

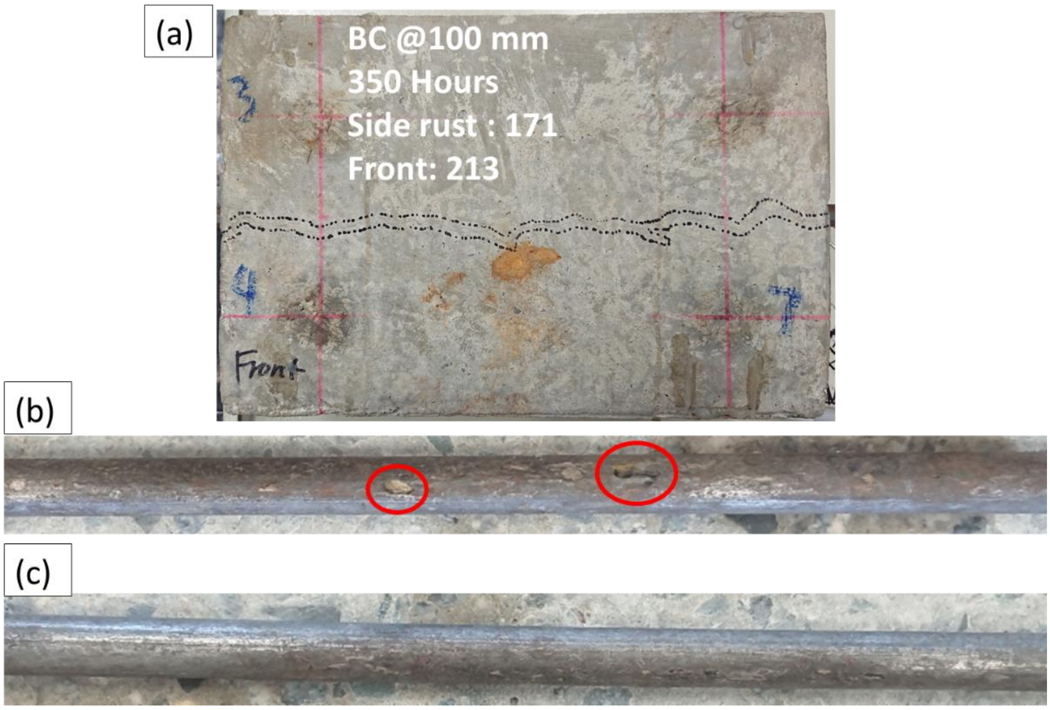

Fig. 6-23 Test 2: Visual inspection of the condition of concrete beams and bars: (a) rust stain and crack on the surface of specimen BC (b) pits and irregularities on the surface of the extracted bar facing the dripping side and (c) intact surface on the other side.

Fig. 6-24 shows the condition of specimen BC after 0-, 171-, 213- and 350 hours of accelerated corrosion. No sign of corrosion was observed in the first 151 hours of corrosion. At 171 hours of corrosion, reddish-brown liquid rust was observed underneath the bar at both ends of the specimen, as shown in Fig. 6-24 (b). Since then, liquid rust continued to ooze out from the ends of the specimen, and no other sign of corrosion was observed until 213 hours. Two rust stains, marked as stain 1 and stain 2, appeared on the concrete cover. The locations of the stains matched well with the locations of the pits on the extracted bar. Both rust stains grew with time, and stain 2 grown more aggressively. It is known that the crack has already grown to the concrete cover once the rust stain appears on the surface. However, a visible hairline crack was first observed at 310 hours of corrosion. This was because the crack was too thin to be identified, and the liquid rust could also mask the crack. The liquid rust continued to ooze out from the crack, further widened the thickness, and increased the length of the crack. Simultaneously, more liquid rust oozed out from the increased crack leading to a widespread surface stain, as shown in Fig. 6-24 (e). The crack grew from the middle of the concrete cover and expanded towards both ends, leaving a complete split of the concrete cover and widespread rust stains on the concrete cover after 350 hours of accelerated corrosion.

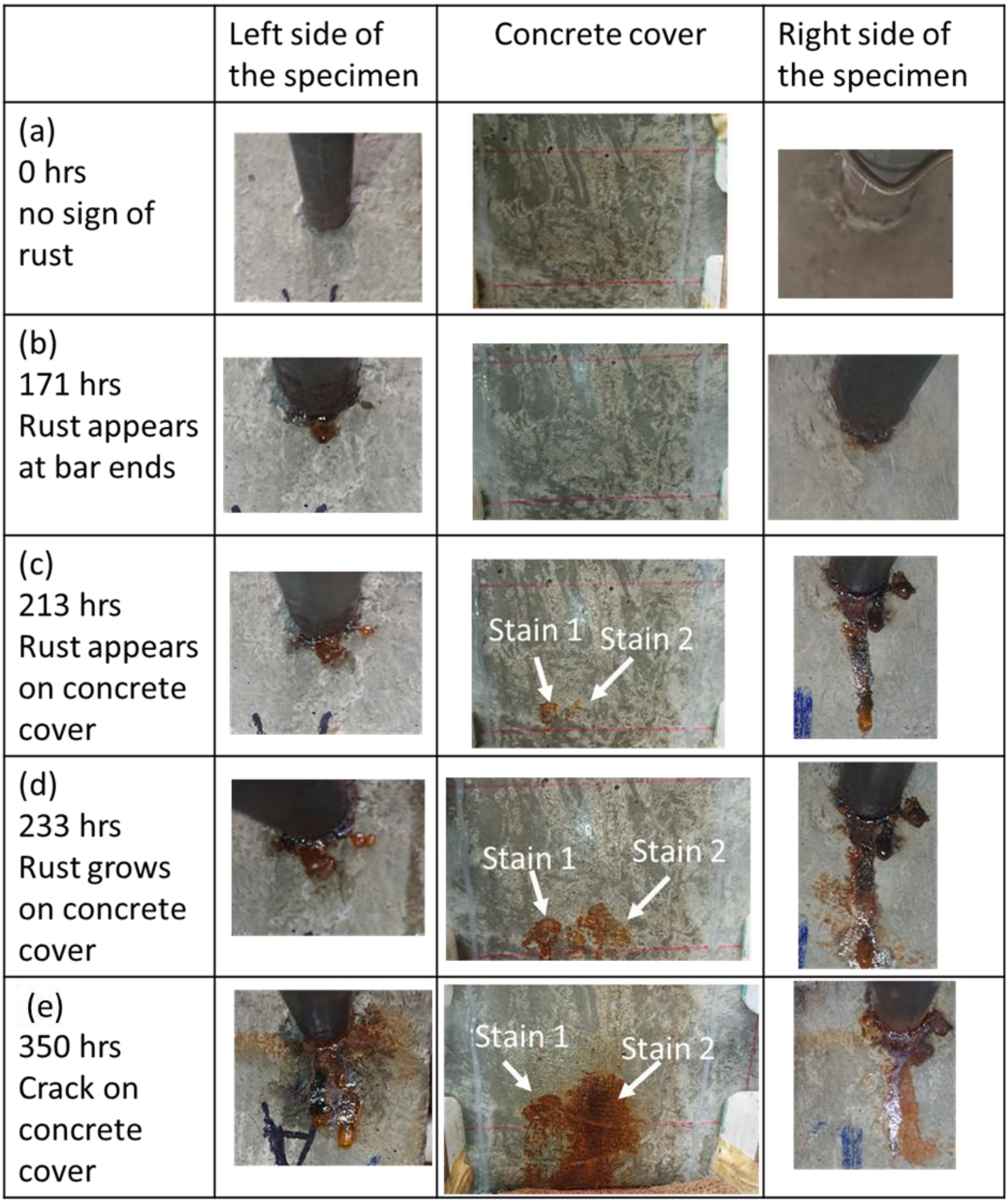

Fig. 6-24 Visual inspections of specimen BC after 0, 171, 213, 233, and 350 hours of accelerated corrosion

The specimen was sawn through the stains to observe the condition of the steel-concrete interface, as shown in Fig. 6-25. (a). The rust mainly appeared at the middle 100 mm of the interface. Aggregates at the location of the surface stains were color by the rust, indicating the intrusion of liquid rust into the concrete cover through the cracks. The rest part of the interface was clear. No rust stain can be observed, indicating no corrosion occurred at these places.

The specimen was further sawn to exam the cracking from the steel-concrete interface to the concrete cover, the cross-section through stain 1 and stain 2 were shown in Fig. 6-25 (b). Cracks were observed on both surfaces of the cross-sections. Two cracks were developed from the steel-concrete interface on all the surfaces, one propagated to the concrete cover and the other propagated towards the other side. The crack length through stain 1 was 30 mm, and the length of the crack through stain 2 was 48 mm. The crack opening at stain 1 was larger than that at stain 2, and residual rust was observed in the crack in stain 2. This is because the corrosion near the location stain 2 is more aggressive. The rust widened the crack and increased its length. Subsequently, it further increases the flow of the liquid rust, leaving a widened crack through on the cross-section and the widespread stain on the concrete cover.

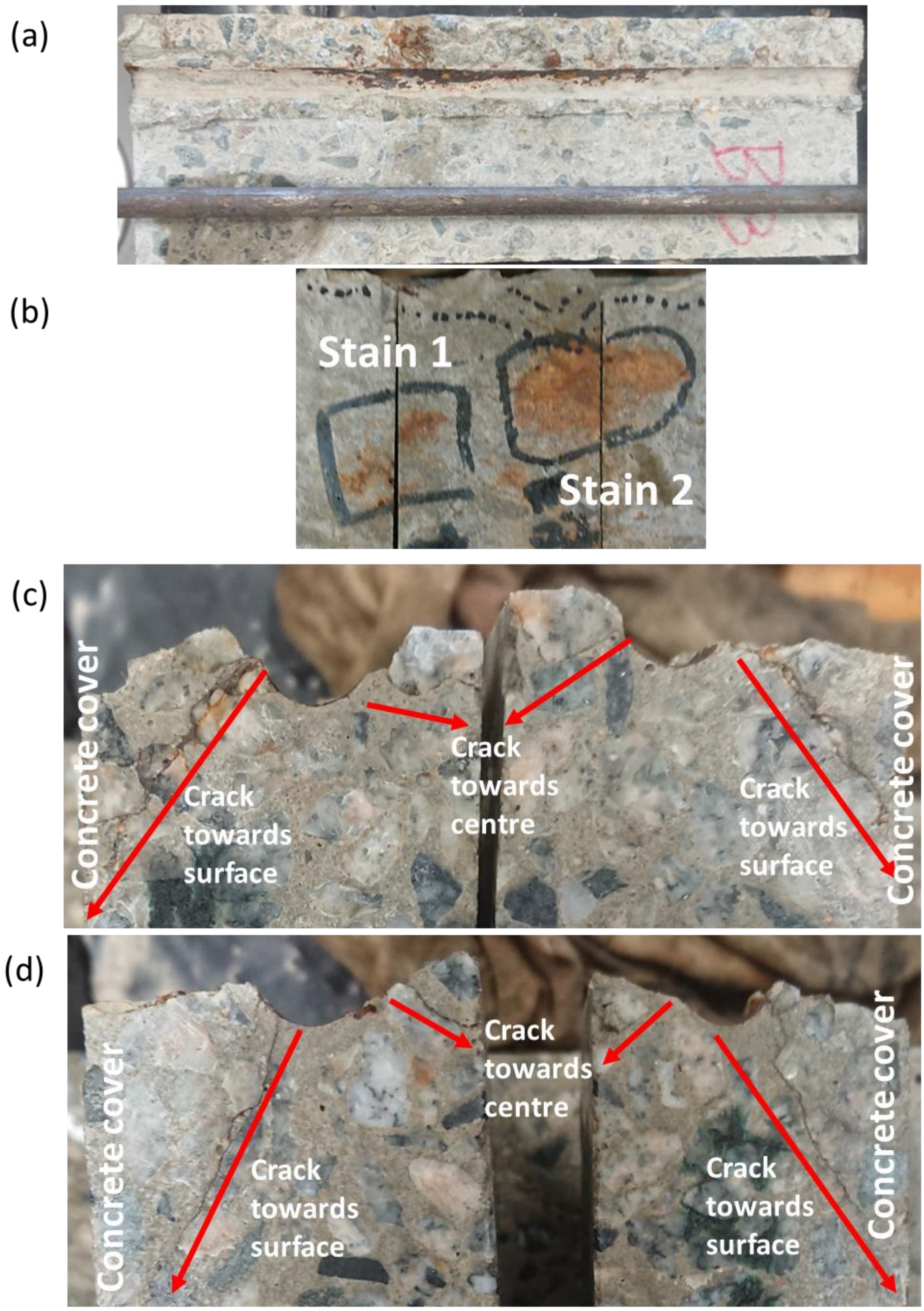

Fig. 6-25 steel-concrete interface and the cross-section through stain 1 and stain 2 in specimen BC (a) S-C interface, (b) stains on concrete cover, (c) cross-section through stain 1 and (d) cross-section through stain 2.

In specimen TC, a rust stain appeared on the concrete cover and at the end of the specimen at 60 hours. The liquid rust continued to leak from the ends throughout the entire duration of the test. The stain on the concrete cover remained unchanged until 180 hours, and then it began to increase. The surface crack initiated and progressed along the direction of the bar until the concrete cover was split at 340 hours. The extracted bar was shown widespread uniform corrosion and significant pits over the entire bottom part of the bar. There was a significant loss of material, as confirmed by visual inspection and mass loss. The top part of the bar was mainly intact.

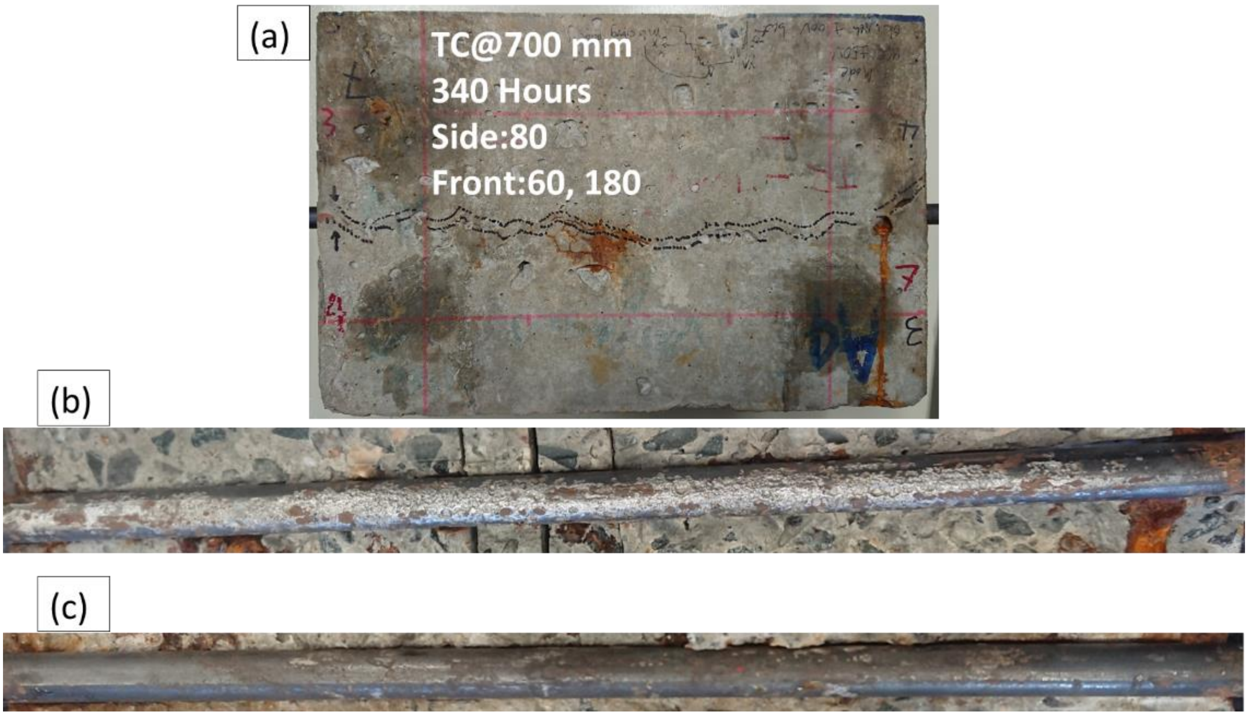

Fig. 6-26 Test 2: Visual inspection of the condition of concrete beams and bars: (a) rust stain and crack on the surface of specimen TC (b) pits and irregularities on the surface of the extracted bar facing the dripping side, and (c) intact surface on the other side.

Fig. 6-27 shows the visual inspection result of specimen TC after 0, 40, 60, 80, 180, and 340 hours of accelerated corrosion. Watermarks appeared underneath the bar at both ends of the specimen. This might be because the NaCl solution cumulated in the void owning to the top-bar effect, and the solution leaked through the weak and short bond at both ends of the specimen, leaving the watermarks underneath the bar. A light brown rust mark was observed underneath the bar at the left end of the specimen after 60 hours of corrosion, indicating the occurrence of the corrosion visually. The rust stain appeared on the surface of the concrete cover after 60 hours of corrosion, and the liquid rust leaked from the right end of the specimen after 80 hours. Subsequentially, the liquid rust continued to ooze out from the ends, but the rust stain of the concrete cover remained unchanged until 180 hours. Since then, the rust stain on the concrete cover started to grow until the concrete cover was completely split after 340 hours of corrosion.

In contrast to specimen BC, the liquid rust mainly oozed out from the ends of specimen TC. Only a small rust stain was left on the concrete cover even when the concrete cover was split. It was recalled that generalized corrosion was observed almost on the entire bottom part of the bar embedded in concrete. This part of the bar was believed to be disconnected from the concrete and void owing to the top-bar effect formed within this zone. Hence, the bond only existed at the ends of the specimen, and the bond was short. Liquid rust could easily penetrate through the bond and created debonding at the ends. It was easier for the liquid rust to ooze out through the broken bond than breaking through the concrete cover. Hence, in specimen TC, the liquid rust mainly oozed out from the sides through the broken bond instead of leaking from the concrete cover, leaving a relatively small and localized rust stain.

	Left side of the specimen	Concrete cover	Right side of the specimen
(a) 0 hours No sign of Rust			
(b) 40 Hours Water mark under bar			
(c) 60 Hours Rust appears at left end and on concrete cover			
(d) 80 Hours Rust appears at right end		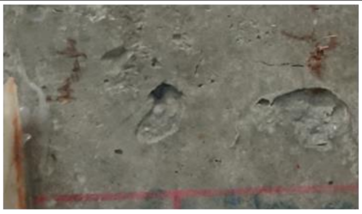	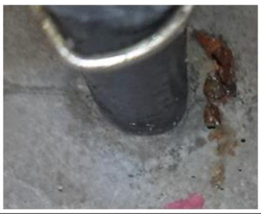
(e) 180 hours Rust on concrete cover expends			
(f) 340 hours Crack on concrete cover			

Fig. 6-27 Visual inspections of specimen BC after 0, 40, 60, 80, 180, and 340 hours of accelerated corrosion

The steel-concrete interface is shown in Fig. 6-28 (a). The image below shows the interface subjected to the void owning to the top-bar effect and facing the dripping of NaCl solution. Rust stains were observed over the entire interface. Two distinct colors were observed at the interface, a dark reddish-brown stain was observed in the middle 200 mm interface, and a reddish-brown stain was observed at both ends. It was believed that the dark reddish-brown zone was the void zone where corrosion first occurred and liquid rust cumulated. The interface within the void zone was immersed in the liquid rust since the beginning of the accelerated corrosion. Hence, the interface was severely colored, leaving a dark reddish-brown stain. The top image shows the interface that bonded to the top part of the steel bar. Rust stains were observed only at some locations over the interface, but these stains were mainly at the sides of the interface. These stains might be caused by the intrusion of liquid rust from the void.

Fig. 6-28 (c) shows the cross-section of the specimen through the rust stain (Fig. 6-28 (b)) on the concrete cover. Cracks from the steel-concrete interface to the surface of the concrete cover appeared on both sides of the cross-section. The length of the cracks was about 25 mm. It was also noted that the residual rust was observed in the cracks and the area in the vicinity of the concrete cover, about 5 mm in thickness. The opening of the crack was smaller than that in specimen BC, even though the severity of the bar corrosion was much higher in specimen TC. This is because the liquid rust is mainly leaked from the ends of the specimen TC, while the rust is mainly leaked from the concrete cover of specimen BC. The limited flow of liquid rust towards the concrete cover reduced the widening of the crack and limited the spread of the surface stain.

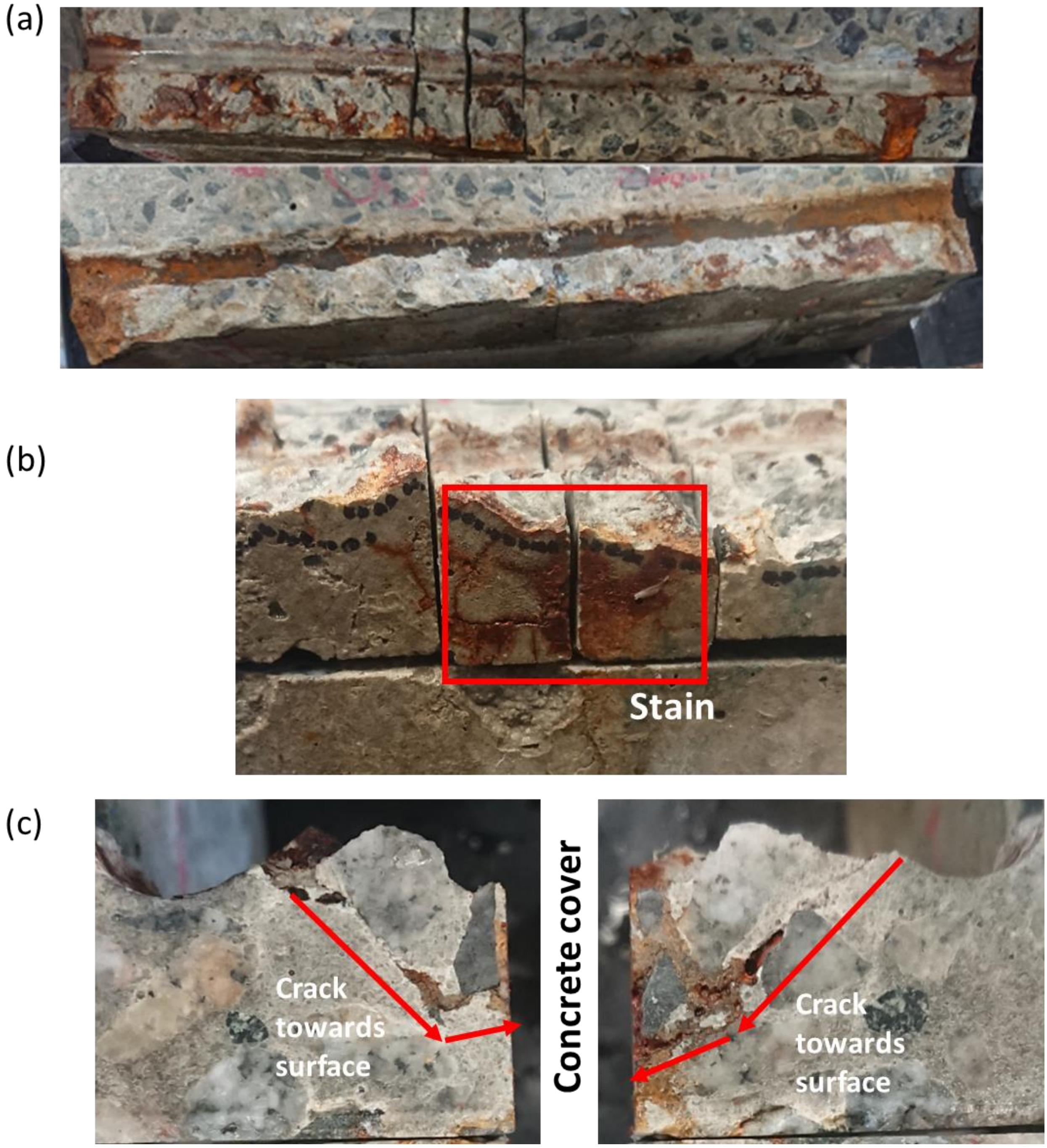

Fig. 6-28 steel-concrete interface and the cross-section through stain in specimen TC (a) S-C interface, (b) stain on concrete cover, and (c) cross-section view through the stain.

6.2.1.3.3.2. Guided wave monitoring

Fig. 6-29 shows the TI of transmitted signal in BC until complete cracking of concrete cover. The TI of the signal shows a clear 3- stage variation. Stage 1 A indicates the building up of rust around the bar, represented by the continuous reduction of the TI in the first 82 hours. A sudden increment in the TI was observed at the end of stage 1 A, indicating the crack initiation at the steel-concrete interface, this is known as stage 1 B. In stage 2, the crack propagates towards the concrete cover and finally leaves a rust stain on the surface of the concrete cover. The TI continuously reduces during stage 2. During stage 3, the crack propagates horizontally on the concrete cover until the cover is completely split. The TI first reduces with time. Then it starts to rise from 290 hours of accelerated corrosion.

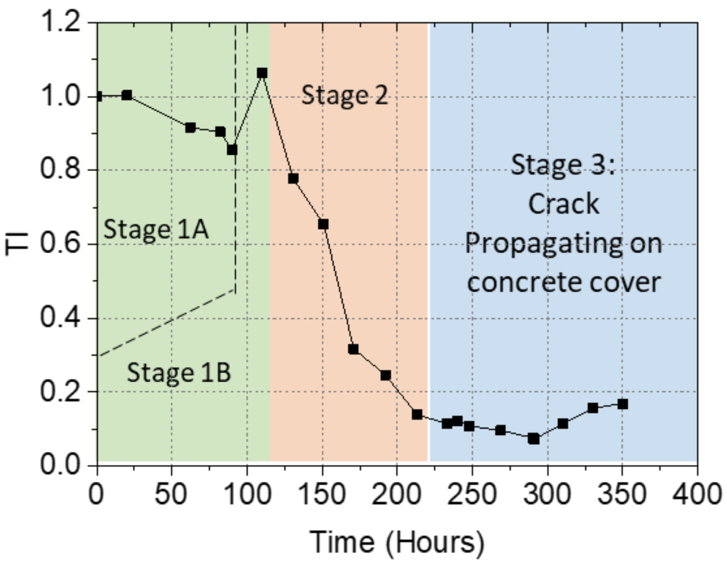

Fig. 6-29 Normalized TI of the transmitted signal at 350 kHz of specimen BC

Stage 1 A: The rust is building up around the bar during this stage. The rust was generated around the bar during this stage and filled the void in the vicinity area. In this case, the contact between the steel and the concrete was increased. Since these all happened at the steel-concrete interface inside the concrete, no visual signal could be observed from the surface of the specimen. Ultrasonic results, on the other hand, successfully capture the change at the interface. In the first 20 hours, the TI was almost identical, indicating the corrosion of the bar was not initiate yet, or the corrosion was negligible. Then the TI continued to drop from 20 hours to 82 hours of accelerated corrosion, by 14.4%.

Fig. 6-30 shows the envelope of the time signals during stage 1 A. It was noted that the 20 cycle F (1,1) mode wave packet was separated into two wave packets with around 12 cycles. This might be caused by the overlap of the transmitting signal and the reflection at the bar in air to the embedded bar boundary. However, the arrival and end time for these two wave packets matched well with those in a single 20-cycle F (1,1) mode wave packet. After 20 hours of accelerated corrosion, the first peak of the F (1,1) mode remained steady, and the second peak dropped significantly while the F (1,2) increased slightly. These variations in the time signal did not result in a noticeable change in the TI of the signal. As the corrosion continued, the amplitude of the first peak remained steady, but both the second peak of F (1,1) mode and the F (1,2) mode dropped with time, resulting in a continuous reduction in the TI.

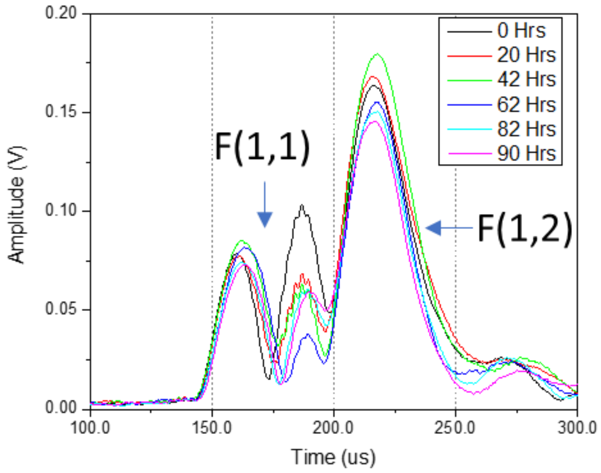

Fig. 6-30 The envelope of the time signal during stage 1 A.

Stage 1 B: A sudden rise in the TI occurs during stage 1 B, indicating the crack initiation at the steel-concrete interface due to the building up of the expensive pressure exceeding the bearing capacity of the surrounding concrete. The envelope of the time signals during stage 1 B is presented in Fig. 6-31. The second peak of the F (1,1) wave packet continued to reduce and merged with the first peak of F (1,1) mode and F (1,2) mode after 110 hours of accelerated corrosion. While the first peak of the F (1,1) packet and F (1,2) packet increased with time. This was because the expensive pressure applied on the surrounding concrete was temporarily released by the crack initiation, leading to a reduction in the contact between the steel bar and surrounding concrete. Fewer waves leaked into the surrounding concrete, and more got retained in the bar and transmitted to the receiver, resulting in a sudden increment in the TI by 20.7 %. It was noted that the TI at 110 hours was larger than the TI with no corrosion. This indicated that the debonding occurred at the steel-concrete interface. The influence of the debonding was masked by the contact increment due to the expensive pressure, resulting in an overall increment in the TI. When the pressure was released, the influence of the debonding at the interface dominated the characteristics of the guided waves, leading to the increased TI.

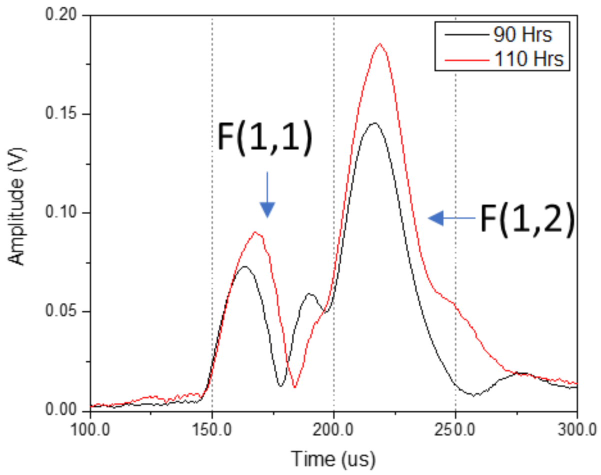

Fig. 6-31 The envelope of the time signal during stage 1 B.

Stage 2: During this stage, the crack propagates from the steel-concrete interface towards the concrete cover. The variation of the TI due to corrosion was shown a bilinear trend. The TI first dropped sharply by 74.5 % from 110 hours to 171 hours, then the reduction rate of TI slowed down from 171 hours to 213 hours, and the TI dropped by 17.8 % during this period. It was recalled from Fig. 6-24 (b) that liquid rust was oozed out from the ends of the specimen. The leakage of liquid rust at the ends of the specimen released the compressive pressure generated by the rust, which reduced the energy leakage into the surrounding concrete. However, due to the continuous corrosion, the compressive pressure was constantly generated, and the bar deterioration occurred, resulting in an overall reduction in the TI with a reduced reduction rate. Fig. 6-32 shows the envelope of the time signals during stage 2. During this stage, both the amplitude of the F (1,1) mode and the F (1,2) mode dropped with time. The amplitude of the mode F (1,1) dropped by 0.056 V from 110 hours to 171 hours and further dropped by 0.015 V from 171 hours to 213 hours. While the amplitude of the F (1,2) mode dropped by 0.13 V and 0.033 V during these two time periods, respectively. It was noted that the amplitude of the F (1,2) mode was almost double that of the F (1,1) mode at 110 hours, and the amplitude of these two modes was almost identical after 213 hours of corrosion. Hence, it was concluded that the F (1,2) mode was more sensitive to the change in the waveguide during stage 2.

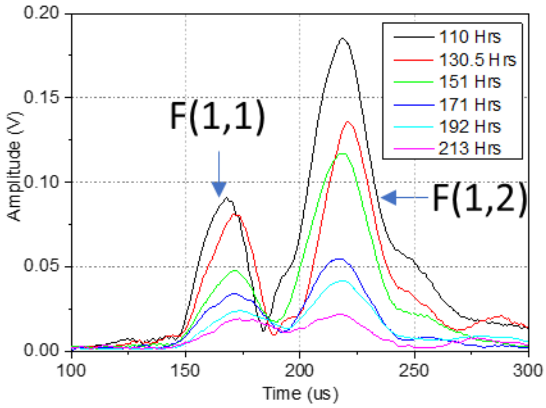

Fig. 6-32 The envelope of the time signal during stage 2.

Stage 3: The crack propagates horizontally on the surface of the concrete cover until the complete slip of the concrete cover. The TI shows a bilinear trend during this stage. The TI dropped linearly by 6.2 % from 213 hours to 290 hours of corrosion. it was noted that the reduction rate at this stage was much lower than that in stage 2. Then, the TI rose about 9.3 % from 290 hours to 350 hours when the concrete cover was split.

Fig. 6-33 (a) shows the envelope of the time signals from 213 hours to 290 hours. The amplitude of the F (1,1) mode showed a rise and fall fluctuation within this period, but the change was insignificant. While the amplitude of the F (1,2) mode first dropped about 0.0056 V from 213 hours to 233 hours and a temporary rise of 0.0025 V from 233 hours to 240 hours. The amplitude continued to drop by 0.0083 V until 290 hours. The dominating mode shifted from F (1,2) mode to F (1,1) mode with time.

Fig. 6-33 (b) shows the envelope of the time signals from 290 hours to 350 hours. Both F (1,1) mode and F (1,2) mode increased with time and the increment in F (1,2) mode was more dramatic compared to the increment in F (1,1) mode. The amplitude of the F (1,1) mode increased by 0.0034 V from 290 hours to 330 hours, then the amplitude remained steady. The amplitude of F (1,2) mode increases by 0.0184 V from 290 hours to 350 hours. During this period, the F (1,2) mode was increasingly dominating the received signal with time.

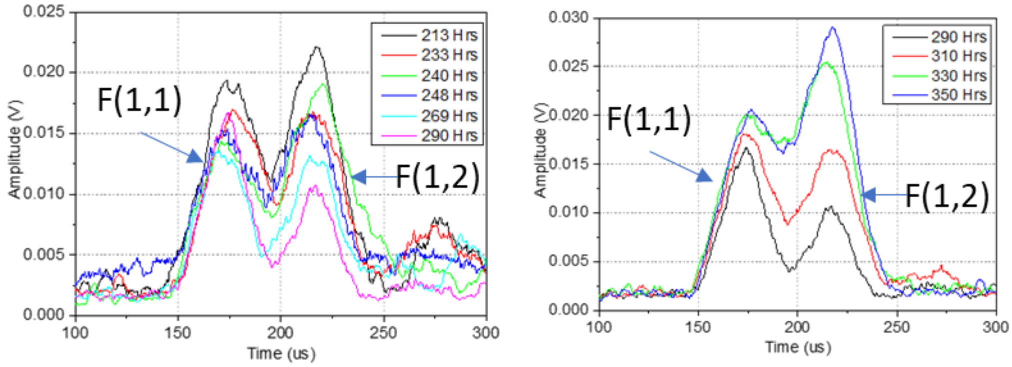

Fig. 6-33 The envelope of the time signal during stage 3 (a) 231 hours to 290 hours and (b) 290 hours to 350 hours.

The trend of the TI of specimen BC before the appearance of surface stain in the bottom bar specimen was similar to that in specimen BS. Initially, the corrosion products increased the compressive pressure, resulting in energy leakage into the surrounding concrete. It was likely that the corrosion-induced cracking was initiated between 90 and 110 hours. The compressive pressure was released as the corrosion product entered the cracking, reducing energy leakage. It was noted that the TI at 110 hours was larger than the benchmark. This might be due to the initiation of corrosion-induced cracking, resulting in local debonding. Less energy was leaked into the concrete in the debonding zone, and more energy was retained in the bar. Hence the TI was higher than the benchmark. The chloride ions presented in the cracking directly contacted and reacted with the bar, resulting in deterioration of the bar through the local material loss. After this, the cracking initiated from the surface stain and propagated horizontally along the bar direction. The crack propagation speed was slow at the initial stage, and the speed increased with time of corrosion. Hence, at the initial stage of concrete cracking, the energy reduction of signal due to bar deterioration overwhelmed the energy increment due to S-C debonding. As the cracking got larger, longer S-C debonding was expected, the influence of debonding on received signal overwhelmed that of bar deterioration, resulting in a rising TI.

In specimen TC, the TI went sharply down by 90% with concrete corrosion in the first 60 hours, and then it dropped slowly at a steady rate until the concrete cover was completed split. At the end of the corrosion process, the TI was reduced by 99%. The TI reduction for both TS and TC was about 90%

when the surface stain appeared. For specimens at higher elevations, the TI reduction rate was much higher than that in lower elevation. For the same anodic potential, it took 246.5 hours to generate the surface stain for specimen TS, while it only took 60 hours for specimen TC. It was already demonstrated in Fig. 6-4 that the size of the void underneath the bar at the height of 700 mm is much larger than that at the height of 300 mm. It was expected that a larger area of the bar was directly contacted with NaCl solution. Hence the corrosion rate in the specimen at a higher elevation was higher, resulting in faster material loss. The rapid deterioration of the bar led to a faster reduction of the TI due to more substantial attenuation of the transmitted signal.

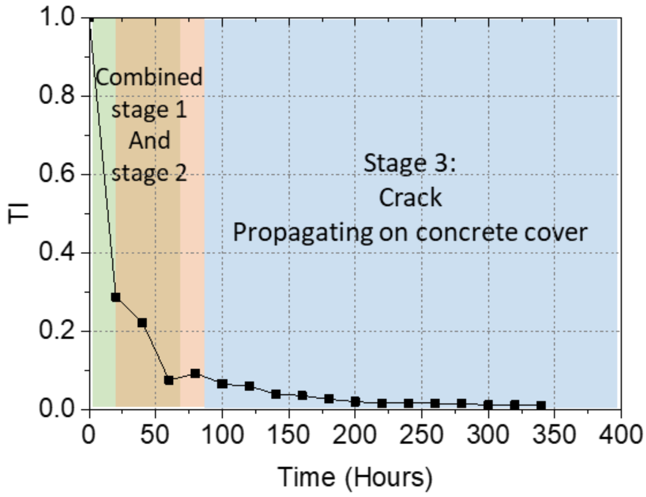

Fig. 6-34 Normalized TI of the transmitted signal at 350 kHz of specimen TC.

Combined Stage 1 and 2: For a top-bar specimen, the amplitude of TI drops linearly. Stage 1 and stage 2 of the corrosion process are merged, and no clear differentiation can be made by analyzing the ultrasonic results and the visual inspection of the specimen. Fig. 6-35 shows the envelope of the time signal during 0 hours to 60 hours. Before the accelerated corrosion, the amplitude of the F (1,2) mode was about eight times that of the F (1,1) mode. After 20 hours of accelerated corrosion, the amplitude of the F (1,2) mode dropped from 4.04 V to 1.15 V. The amplitude of the F (1,1) mode only dropped slightly, from 0.62 V to 0.55 V, but a noticeable time shift of 12 us was observed at the peak of the envelopes. The amplitude of both modes continued to reduce with time, while an increasing time delay was observed at the peak of the envelopes. The amplitude of the two modes was similar, 0.25 V for F (1,1) mode and 0.23 V for F (1,2) mode, after 60 hours of accelerated corrosion when the stain appeared on the surface of the concrete cover.

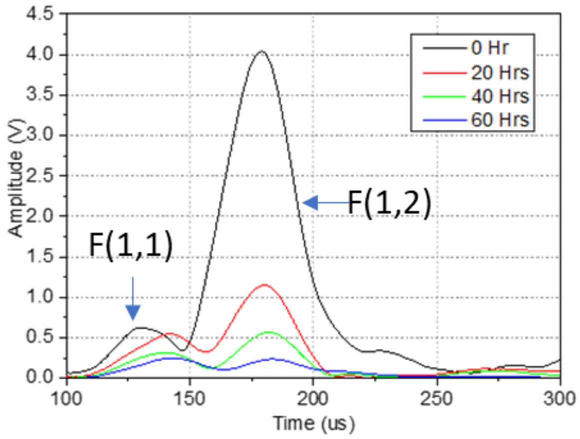

Fig. 6-35 The envelope of the time signal during stages 1 and 2.

Stage 3: The crack propagates horizontally on the concrete cover during this stage. The TI temporarily increased from 60 hours to 80 hours before the continuous reduction of TI. Fig. 6-36 (a) shows the envelope of the time signals from 60 hours to 80 hours. It was observed that the amplitude of the F (1,1) dropped slightly while the amplitude of the F (1,2) mode increased from 0.23 V to 0.34 V. It was recalled that liquid rust oozed out from both ends of the bar, indicating a through bar length debonding of the steel bar. The debonding reduced the contact between the bar and the surrounding concrete, less energy leaked into the concrete, and more energy was retained in the bar, leading to a temporary increment in the amplitude of the signal.

The amplitude of the modes continuously drooped from 80 hours to 180 hours, as shown in Fig. 6-36 (b). The amplitude of the F (1,1) mode dropped from 0.23 V to 0.11 V and the arrival time of the peak shifted from 142us to 152 us. While the amplitude of the F (1,2) mode dropped from 0.34 V to 0.03 V and the arrival time of the peak remained constant. The two modes were merged and formed a single wave package after 180 hours of corrosion, and the amplitude of the merged wave packet dropped from 0.11 V to 0.07 V at 220 hours. The merged wave packet was separated into two at 240 hours.

The amplitude of both modes continuously dropped from 240 hours to 300 hours, and then the amplitude remained steady until the end of the corrosion process. This might be because, at the end of stage 3, the increasing size of the crack reduced the contact between the bar and the concrete and increased the amplitude of the received signal. However, the accelerated corrosion continued to deteriorate the bar, leading to a continuous reduction in the amplitude. The co-occurrence of the crack-induced debonding and the bar deterioration resulted in steady signals, even the accelerated corrosion was more aggressive at the end of stage 3.

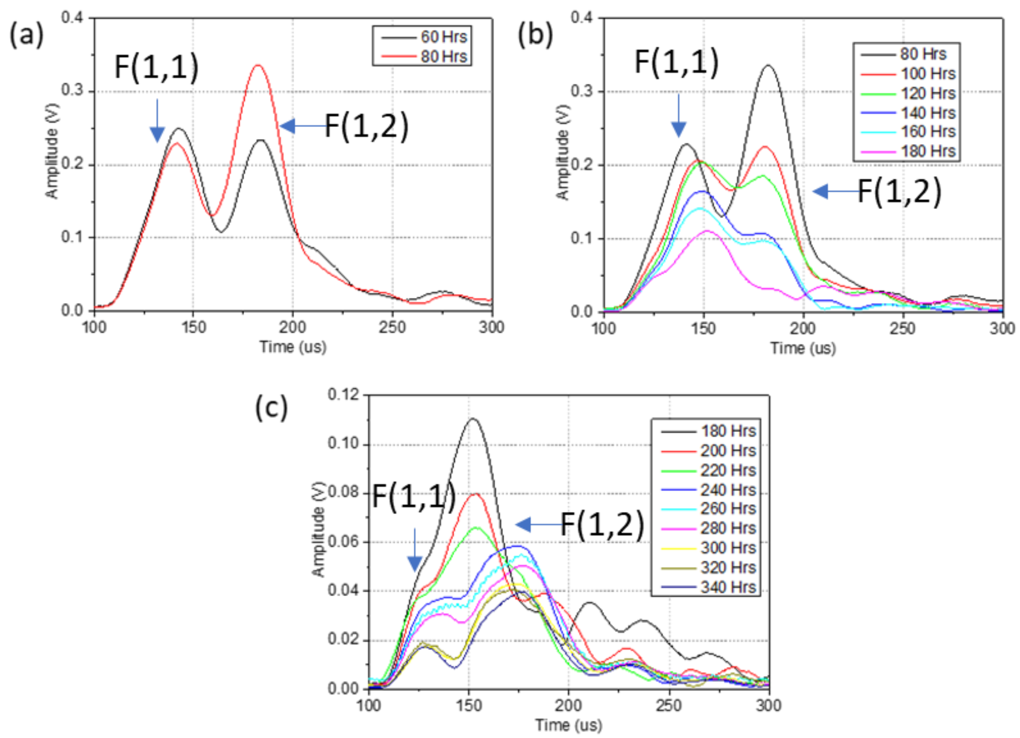

Fig. 6-36 The envelope of the time signal during stage 3 (a) from 60 to 80 hours, (b) from 80 to 180 hours and (c) from 180 to 340 hours.

6.2.1.3.4. Discussion

The TI of the received signal in control specimens shown a clear 3 stage corrosion process. In stage 1, the TI first decreased due to the increment in compressive pressure. The compressive pressure continued to increase until it went beyond the bearing capacity of the surrounding concrete, leading to the initiation of cracking. An increased TI was observed. The crack initiation was clearly identified by the change in the pattern of TI. In stage 2, as the cracking continued to propagate from the bar toward the surface of the concrete cover, the TI reduced sharply due to the buildup of pressure at the S-C interface and the deterioration of the steel bar. In stage 3, the crack propagated horizontally along the bar. At this stage, the TI was influenced by the deterioration of the bar and the debonding of the S-C interface due to cracking. At the beginning of this stage, the crack propagation rate was slow, the TI increment due to debonding was moderate. The TI was mainly influenced by the deterioration of the bar. Hence, the TI reduced slowly. While the crack propagation rate increased, the TI increment due to debonding overwhelmed the TI reduction due to bar deterioration, resulting in an overall increment in the TI.

However, in the top-bar specimen, due to the presence of the void, the bar started to corrode immediately once an anodic current was applied. A significant amount of rust could be generated before the development of compressive pressure to initiate cracking. Deterioration of the bar occurred before the corrosion-induced deterioration of the S-C interface. Hence, the TI of the top-bar specimen only showed a 2-stage corrosion process as stage 1, and stage 2 were merged. First, the TI went sharply down until the appearance of the surface stain. Then the TI reduced slowly as the crack propagates horizontally along the bar.

It was also noted that the reduction rate of TI in both bottom bar and top bar specimens became slower in stage 3 after the formation of surface stain. At this stage, the crack propagated along the bar direction of the concrete cover. The signal strength increased due to the debonding of the S-C interface. In the meantime, the signal strength was reduced due to bar deterioration. The combined effect of bar deterioration and S-C interface debonding resulted in the slower reduction rate of the TI. Thus, it was concluded that the corrosion process of the bottom bar specimen with a good S-C bond was first influenced by the bond delamination and then affected by the deterioration of the bar, which led to pit formation and local material loss, result in surface stain and cracking. As for the top bar specimen, visual examination of the concrete interface revealed the delamination of the bar.

However, this phenomenon was not observed from the ultrasonic results. Hence it was believed that the deterioration of the bar dominated the corrosion process of the top-bar specimen.

6.2.1.3.5. Destructive test

The bars were extracted from the concrete and subjected to destructive tests once the corrosion tests were completed. Tensile test and mass loss measurement of the bars were conducted to establish the residual mechanical properties of the corroded bars. The bars were cleaned with a wire brush and acetone to remove the attached rust and mortar. All the cleaned bars were weighted using an electronic scare with the precision of 0.1 g and tested for tensile strength using Shimazu AGS-X 300 kN UTM.

Table 6-2 indicates the properties of the extracted bars. The mass loss of BS and BC was 0.22% and 0.56%, respectively. While the mass loss for TS and TC was 4.19% and 4.79%. It was recalled that the total corrosion period of TS was about 25% longer than that of BC and the corrosion period of both BC and TC were almost identical. However, the mass loss of top bars was 19 and 8.5 times larger than that of bottom bars. It was reasonable to conclude that the severity of corrosion of top bars, before the appearance of surface stain, was much higher than that in bottom bars even when the surface crack appeared on the controlled specimens.

Table. 6-2 Residual properties of the extracted bars

Specimen	Mass loss g (%)	Nominal Yield Stress (MPa)	Nominal Ultimate strength (MPa)	Strain (%)
Intact bar	0	360	505.85	0.420
BS	0.6 (0.22%)	360 (0%)	496.83 (1.78%)	0.395 (5.95%)
BC	1.5 (0.56%)	360 (0%)	495.83 (1.98%)	0.298 (29.05%)
TS	11.2 (4.19%)	336 (6.67%)	489.82 (3.17%)	0.230 (45.24%)
TC	12.8 (4.79%)	328 (8.89%)	476.43 (5.82%)	0.199 (52.62%)

The stress-strain curves of the referencing intact bar and the corroded bars are shown in Fig. 6-37. Due to the difficulty of accurately measuring the cross-section area, the residual strength was calculated based on the original cross-section area. The stiffness of all bars was similar. The nominal yield stress of corroded bottom bars was similar to the intact one, while the nominal yield stress of top bars was reduced by 6.67% and 8.89% for test 1 and test 2, respectively. The nominal ultimate strength reduced gradually with the increasing corrosion degree of steel bars. In general, the ultimate strength reduction of top bars was much more than that of the bottom bars. The maximum strength loss was 5.82% at a mass loss of 4.79%. It was noticed that the ultimate strength reduction of BC was only 11% more than BS, even though the mass loss of BC was 2.5 times of BC. While the ultimate strength reduction of TC was 1.8 times that of TS, the mass loss of TC was 14% more than TS.

Unlike the moderate reduction of strength, the ductility reduction due to corrosion was significant. The strain reduction for BS and BC was 5.95% and 29.05%. The strain reduction for TS and TC was 45.24% and 52.62%, which were much higher than the bottom bars. The residual strength of the bars was mainly dependent on the minimum residual cross-section area, while the residual ductility was dominated by the non-uniform distribution of cross-section along the bar. It was recalled that only micro pits were observed in BS, but two large elliptical pits and widespread micro pits were identified in BC. These pits contributed to the significant strain reduction of BC even though the mass loss for both bars was moderate. Both general and pitting corrosion was observed at the bottom part of the top bars. The entire bottom part of the embedded bar was severely deteriorated, resulting in a more irregular residual section, leading to a more significant reduction of ductility.

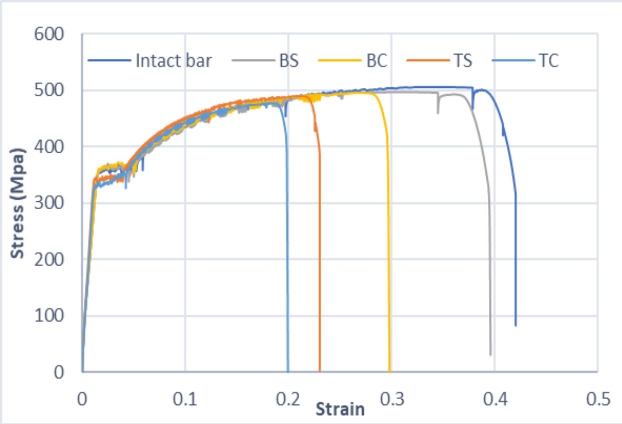

Fig. 6-37 Stress-strain curves

The fracture morphology of the extracted steel bars and a referencing intact steel bar was shown in Fig. 6-38. The referencing bar showed a typical necking phenomenon. The fracture of BS was similar to that of the intact bar. It was recalled that the mass loss of BS was only 0.22%, the effect of such marginal mass loss on the ductility was negligible. As the corrosion degree increased, it was clearly observed that the necking phenomenon gradually reduced, the fracture shifted to a more brittle behavior, which indicated the reduction of the ductility of steel bars. In TC, which lost the most mass due to corrosion, an apparent 45-degree shear failure was observed.

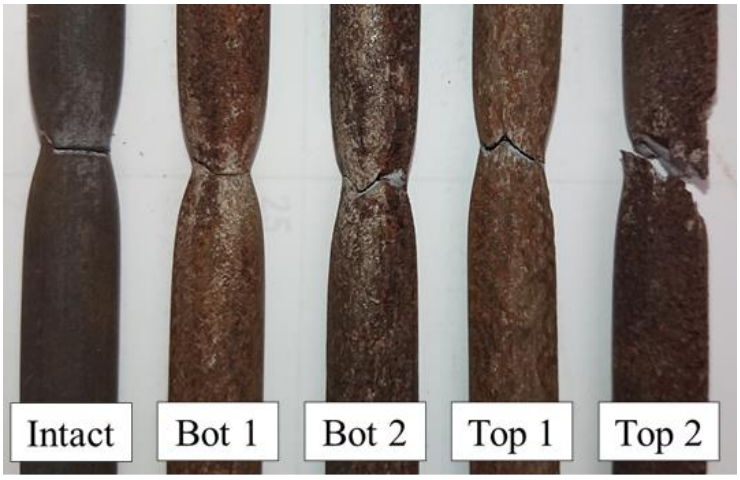

Fig. 6-38 The fracture morphology of the extracted steel bars

6.3. Conclusion

This chapter presented an investigation of corrosion of reinforced concrete with and without top-bar defects using the proposed ultrasonic technique. Two reinforced concrete wall samples have been cast vertically with bars placed at different heights aiming to create top-bar effect. Piezo patches were mounted to the ends of the bars and exited using a signal generator and amplifier. Some samples were cut open to inspect the steel-concrete interface visually and to identify the top-bar defects. The other samples have been subjected to accelerated corrosion using anodic current and investigated with ultrasonic guided waves for the entire duration of corrosion exposure. The signal transmitted through the bars has been collected and analyzed for discerning the change in their signatures. At the end of the experiment, the samples were subjected to various destructive tests to evaluate the residual mechanical properties of the bars.

Following major conclusions can be made from this investigation:

- Void formation due to top-bar defect was observed underneath the bars at an elevation of 300 mm and above. The size of the void increases with the elevation of the bar.
- The control specimens have shown clear pitting corrosion. The top-bar specimens have shown corrosion distributed over the bottom surface of the bar, while no clear sign of corrosion was observed on the top surface.
- Guided ultrasonic waves are capable of nondestructive monitoring and distinguishing corrosion of reinforced concrete with and without top-bar defects.
- Control specimens showed a clear three-stage pattern, which matched the three-stage corrosion-induced cracking model and visual observation. The pressure buildup, crack initiation, crack propagating toward concrete cover and crack propagating on the concrete cover could be clearly identified.
- The top-bar specimens, on the other hand, showed a two-stage pattern. Due to the presence of voids at the interface, significant bar deterioration occurred before the pressure buildup and crack initiation. Hence stage 1 and stage 2 of the controlled specimen were combined in case of top-bar specimens.
- Before the appearance of surface stain, the TI of the controlled specimen was influenced by the S-C interface condition and bar deterioration, while the TI of the top-bar specimen was dominated by bar deterioration.
- After the appearance of surface stain, the TI of both control and top-bar specimens was influenced by a combined effect of S-C interface condition and bar deterioration.
- The degree and rate of corrosion were found to increase with the elevation of the bar. At higher elevations, the top-bar defect causes more widespread voids leading to faster corrosion.

The pattern of ultrasonic results of the reinforced specimens with and without top-bar defect shows a significant difference. The pattern of TI in controlled specimens matches well with the theoretical states of corrosion in reinforced concrete. While the pattern of TI in top-bar specimens continuously drops with minor fluctuation until the rust stain appears on the surface of the concrete cover. This pattern is similar to stage 1 of corrosion in the controlled specimens. If the presence of the top-bar defects is unknown, solely relying on the ultrasonic signals may lead to misestimation of the severity of the corrosion in the concrete. The finds have indeed highlighted the importance of discerning the presence of top-bar before monitoring the corrosion.

Although this investigation clearly demonstrates the ability of the proposed method to monitor corrosion of RC and identify the differences in the corrosion pattern of RC with and without the top-bar effect, several areas would need further investigation. An improved ultrasonic technique would be necessary to clearly identify the pressure buildup and crack initiation in top-bar specimens. Additional measurements, such as ultrasonic scanning, are suggested to improve the evaluation at these stages. Moreover, the accelerated corrosion results need validation through long-term natural environment exposure.

Reference

Zhang, R., A. Castel and R. François (2011). "Influence of steel-concrete interface defects owing to the top-bar effect on the chloride-induced corrosion of reinforcement." Magazine of Concrete Research 63(10): 773-781.

Chapter 7

7. Monitoring corrosion of reinforced concrete using combined ultrasonic and electrochemical techniques: from bar in air to bar exposed to air.

7.1. Introduction

In the previous chapters, surface-mounted PZT wafers are employed to monitor the setting, detect the presence of the top-bar, and monitor concrete corrosion. PZT wafers are cheap, light, robust against environmental degradation, and easy to install. It can also be permanently bonded to the steel reinforcement and embedded on reinforced concrete. It has been demonstrated that PZT based system is capable of lifecycle monitoring of reinforced concrete. One of the main drawbacks of PZT wafers is that the excitation energy of the signal is low. Although a signal amplifier can amplify the excitation amplitude of the signal, the use of high voltage may reduce its service life, even damage the wafers.

Contact transducers, on the other hand, can excite a strong signal without damaging the transducer. Through careful selection of excitation frequencies, specific longitudinal wave modes can be excited. In this experiment, 24 mm round bars are employed to better fit the contact transducers' size. Two wave modes, L (0,1) mode at 100 kHz and L (0,7) mode at 1 MHz, are employed to evaluate the change in the steel-concrete interface and the change in the bar itself, based on their mode shape. L (0,1) mode at 100 kHz is termed the surface-seeking mode as its axial displacement and total energy density is concentrated near the bar's surface. L (0,7) mode at 1 MHz is termed the core-seeking mode as its axial displacement, and total energy density are concentrated at the center of the bar. A reinforced concrete column is cast vertically, aiming to create the top-bar effect naturally. Two bars are embedded, one locates at an elevation of 100 mm, and the other one locates at an elevation of 500 mm. The setting of the reinforced concrete column specimen is monitored using these two modes. Then the concrete column is sawed to smaller specimens and subjected to accelerated corrosion. Four techniques are employed simultaneously to monitor the corrosion process: half-cell potential, linear polarization resistance, ultrasonic guided waves, and ultrasonic scanning. The former two techniques have been extensively employed both by technicians in the field and researchers to monitor the corrosion process of reinforced concrete in the laboratory. Ultrasonic guided waves are employed to evaluate the deterioration of the bond at the steel-concrete interface and the bars. SAFT-based ultrasonic scanning is employed to detect the initiation of corrosion-induced cracking and monitor its propagation by reconstructing the image of the cross-section of the specimens. All four techniques are first analyzed individually and compared. Then a combined algorithm that combines all these techniques is proposed to provide more comprehensive monitoring of the corrosion process of the reinforced concrete.

7.2. Monitoring setting of reinforced concrete using longitudinal guided waves.

Lab-based experiments have been conducted to validate the proposed methodology for concrete setting monitoring using contact transducers. A concrete column specimen is cast vertically to create debonding owning to the top-bar effect following the procedure in section 3.2. Two round steel bars, 24 mm in diameter and 500 mm in length, are placed at an elevation of 100 mm and 500 mm above the bottom of the mould. The bar located at the elevation of 100 mm is termed the bottom bar while the bar located at 500 mm is termed the top bar. According to the observations from previous experiments, it is believed that the bottom bar is perfectly bonded with the surrounding concrete while a debonding owning to top-bar effect is formed underneath the top bar.

The excitation frequency of the signal is controlled by the central frequency of the contact transducer. The excitation frequency is selected following the procedure in section 3.4.2. In this experiment, one pair of ULTRAN GC100-D25-10 transducer and one pair of Olympus V303 1.0MHZ/0.5'' transducers are used. ULTRAN GC200-D25 transducers have a central frequency of 200 kHz and an active diameter of 25 mm. Olympus V303 1.0MHZ/0.5'' transducers have a central frequency of 1 MHz and an active diameter of 0.5 inches (12.7 mm). JSR DPR300 Pulser/Receiver is used to control the output voltage and amplify the received signals. To maximize the strength of the pulsing and received signal, the output voltage is set to be 475 V with damping of 44 hms. The bandpass filter is set to be 0 MHz to 5

MHz. The gain of the receiver allows us to amplify the received signal. However, if the gain is set too high, the transducer may get saturated, leading to underestimated peak-peak voltage. Hence, the gain is manually adjusted with specimens to get the maximum voltage of the received signals without saturated the transducers. In the bars used in this experiment, the gain is set to be 25 dB.

7.2.1. Bar in air

Fig. 7-1 (a) shows the pulse transmission signals in the bar in air at L (0,1) mode at 100 kHz. The signals contain two groups of wave packets. The first is the direct transmission with a peak-peak voltage of 8 V and a ToF of about 104 us. It consists of two distinct windows of the signal. The first one has a shorter window length, but the peak-peak voltage is higher, at 8 V. The latter has a longer window length, but the peak-peak voltage is lower, at 4 V. The second one denotes the reflection from the other side of the bar. The peak-peak voltage is about 4 V, and ToF is about 361 us. The frequency profiles of these signals are presented in Fig. 7-1 (c). The bandwidth of the signal is about 200 kHz, from 0 kHz to 200 kHz. The main component of the frequency profiles lies between 50 kHz and 100 kHz and peaked at 60 kHz, although the central frequency of the transducer is 100 kHz. A second frequency at a central frequency of 450 kHz is observed in the frequency profile. This frequency is believed to be the instrument nonlinearity generated by the ultrasonic system.

Fig. 7-1 (b) shows the pulse transmission signals in the bar in air at L (0,1) mode at 100 kHz. These signals also contain two groups of wave packets which are the direct transmission and the reflection. The direct transmission arrives at 100 us and contains 13 wave packets with a peak-peak voltage of about 8 V. While the reflection arrives at 325 us with a peak-peak voltage of about 2 V. The voltage of the reflection of L (0,7) is about 50% of that of L (0,1) mode, indicating the higher attenuation of L (0,7) mode. Fig. 7-1 (d) shows the frequency profiles of the L (0,7) mode in the bar in air scenario. The bandwidth of the signal is about 1.4 MHz, from 0.2 MHz to 1.6 MHz, with a peak frequency at 1MHz. The amplitude of the FFT gradually reduces with the frequency that is further from the central frequency.

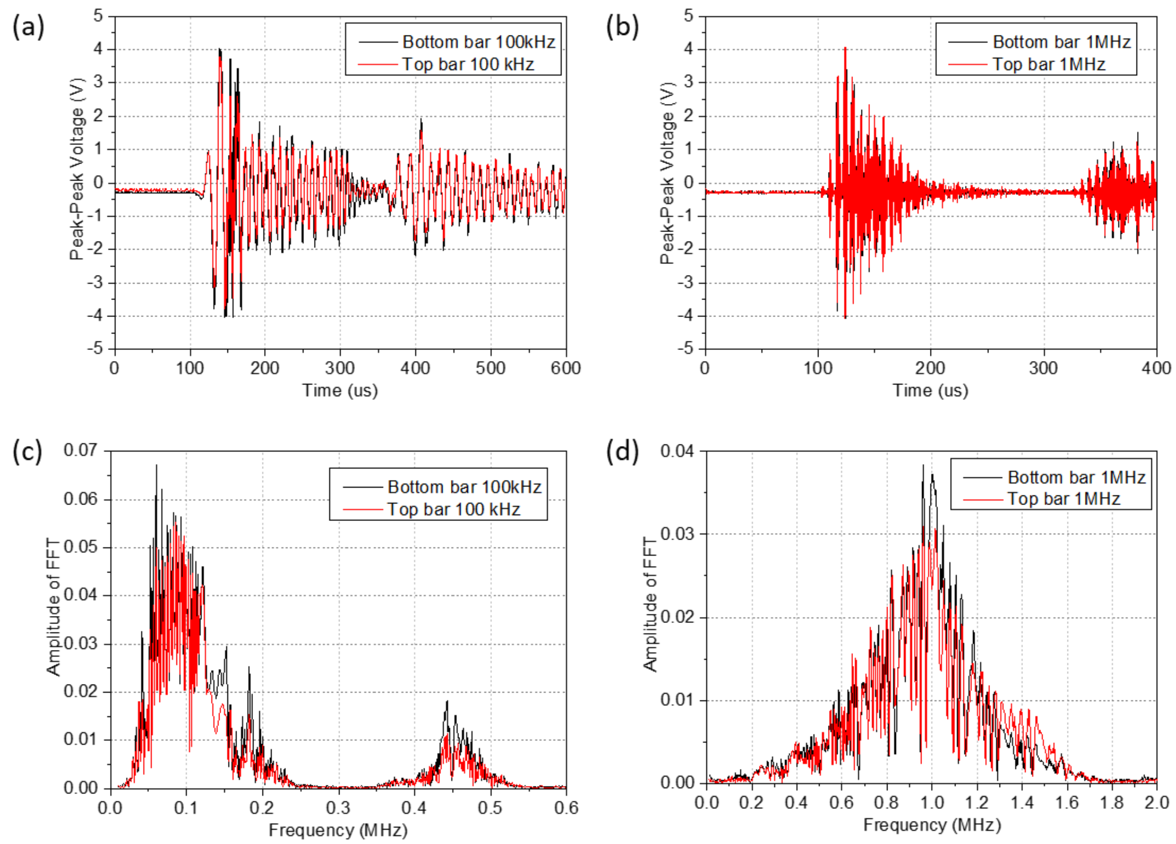

Fig. 7-1 Pulse transmission signals in bar in air scenario using (a) L (0,1) mode at 100 kHz and (b) L (0,7) mode at 1 MHz; The frequency profiles of the (c) L (0,1) mode at 100 kHz and (d) L (0,7) mode at 1 MHz.

The signals of L (0,7) mode at 1 MHz in both bars are almost identical, while the L (0,1) mode signals at 100 kHz show good similarity. Unlike the signal excited by PZT wafers with varies significantly with bars, the signals excited by contact transducers in different bars of the exact dimensions are consistent. It is recalled that the size of the 100 kHz transducer is 25 mm in diameter and the mode shape of the L (0,1) at 100 kHz shows the axial displacement and total energy density is concentrated at the surface. The match between the active area of the transducer and the exciting area on the bar ends does affect the excitation and capture of the signals. The difference in the signals of L (0,1) mode is contributed by the mismatch of the transducers and the bar. While the 1 MHz transducer has a diameter of 12.7 mm and the axial displacement and total energy density of L (0,7) mode at 1 MHz is concentrated at the center of the bar. This ensures a 100% match between the active area of the transducer and the bar ends. The signal mainly travels in the core of the bar. Hence it can be fully received by the receiver.

7.2.2. Bar embedded in freshly poured concrete

7.2.2.1. Monitoring concrete setting by temperature measurement

The phenomenon of the setting of concrete is observed by temperature measurement. As used in Chapter 5, a needle-type thermometer is cast in the concrete specimen to measure the temperature at the center of the concrete during the concrete setting. The temperature of the concrete specimen and the circumstance during the setting period is plotted in Fig. 7-2. The room temperature was maintained at around 20.5 °C. The first record was taken at 0.5 hours after pouring concrete into the mould. The temperature of the concrete was lower than the room temperature. Then the temperature increased slowly between the 0.5th hour and the 2.5th hour. The temperature increased at an increasing rate between the 2.5th hour and the 9th hour. The temperature increment slowed down between the 9th hour and the 10th hour. Beyond the 10th hour, the temperature of the concrete reached a plateau and remained steady until the end of the experiment. Hence, it is concluded that stage 1 of the cement hydration occurs in the first 0.5 hours, stage 2 occurs between the 0.5th hour and the 2.5th hour, stage 3 occurs between the 2.5th hour and the 9th hour and stage 4 occurs after the 10th hour. It is known that the initial set and final set occur at the early stage of stage 3. However, the exact time for the initial set and final cannot be detected by temperature alone, and conventional methods such as needle penetration and penetration resistance test cannot provide accurate measurement due to the presence of the coarse aggregates in the concrete. Based on the observation from previous tests, the initial set occurs soon after the hydration process entering stage 3, and the setting process lasts for about 2 hours. Hence, it is concluded that the initial set occurs at about 3.5 hours and the final set occurs at 5.5 hours.

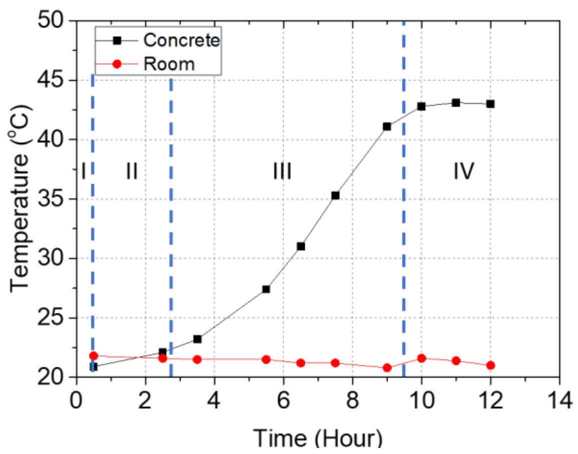

Fig. 7-2 Temperature variation during the concrete setting period

7.2.2.2. Monitoring concrete setting using ultrasonic pulse transmission.

Ultrasonic pulse signals were recorded used the selected modes. Since the voltage of the excited and received signal was highly dependent on the pressure applied on the transducer when taking the record, each record was averaged by 100 samples, and the process was repeated three times. The signal with the highest voltage was used as the final signal. The first pulse signals are capture within the first 30 mins after pouring concrete into the mould, and then subsequent signals are recorded at regular intervals to monitor the setting and early hardening process of the concrete.

Fig. 7-3 and Fig. 7-4 show the pulse signal in the bottom bar and top bar recorded at different times after pouring concrete in the mould using L (0,1) at 100 kHz, respectively. The peak-peak voltage of the signal in the top-bar remained steady with a slight variation in the first 2.5 hours. While the peak-peak voltage of the signal in the bottom bar first reduced to 6 V and then increased back to 8 V. It was mentioned that the voltage of the signal highly depended on the allied pressure. The fluctuation in the signal in the bottom bar might cause by the poor control of the applied pressure. In general, the peak-peak voltage of the signals in both bars remained steady in the first 2.5 hours, the voltage reduced at a fast rate with time. It was also noted that the second window of the transmission signals in both bars reduced dramatically once the concrete was poured into the mould. The reflection was completely disappeared after 5.5 hours.

Fig. 7-5 and Fig. 7-6 show the pulse signal in the bottom bar and top bar recorded at different times after pouring concrete in the mould using L (0,7) at 1 MHz, respectively. The peak-peak voltage of the signals in both bars remained at 8 V in the first 2.5 hours, then the voltage reduced at a slower rate than L (0,1) mode with time. The number of wave packets of the transmission signal remained steady in the first 2.5 hours. Then it reduced gradually with time. At the end of the experiment, the number of wave packets was reduced by 7. The window length is noticeably shortened with time.

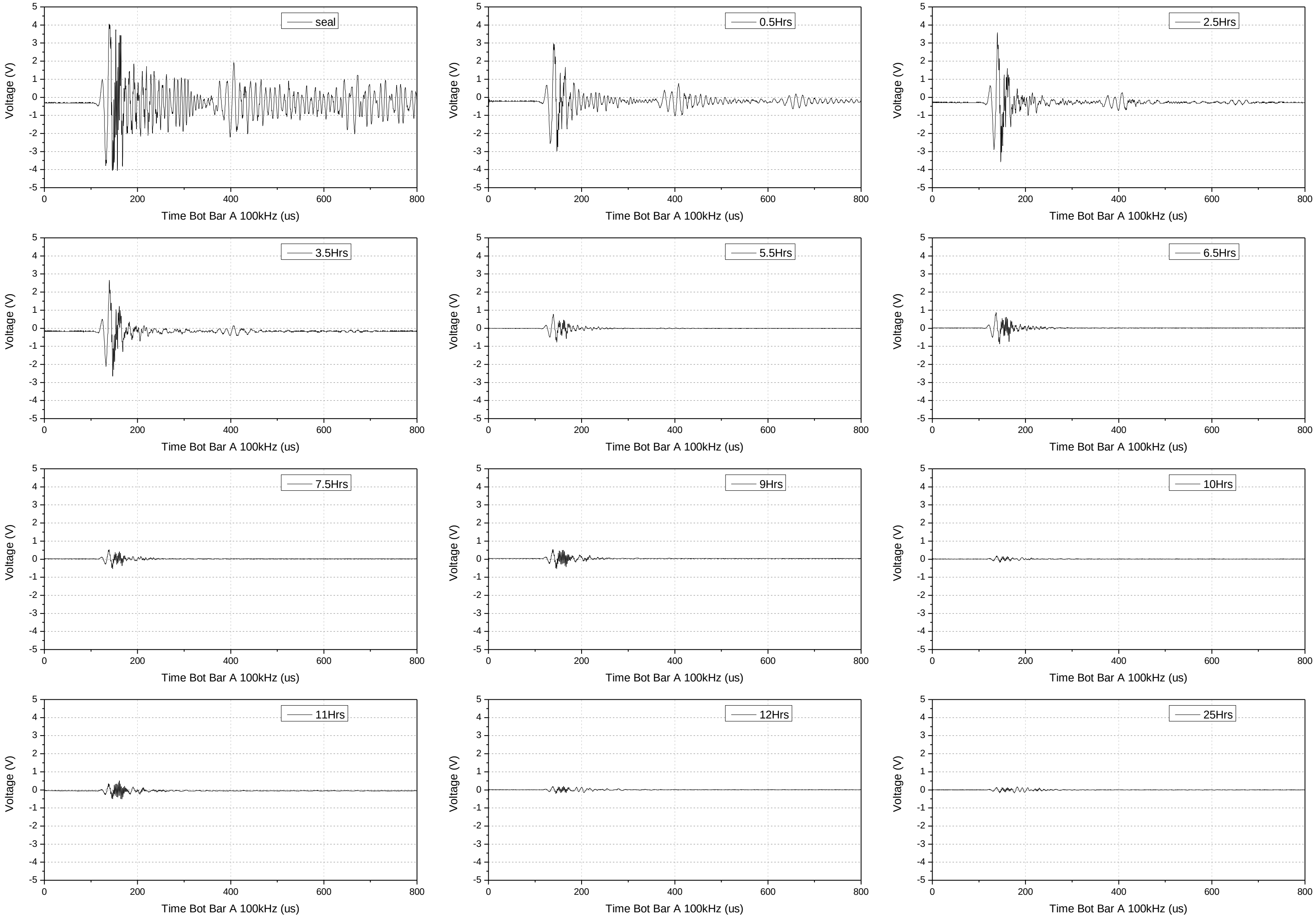

Fig. 7-3 Time signals in the bottom bar at different times after pouring concrete using L (0,1) mode at 100 kHz.

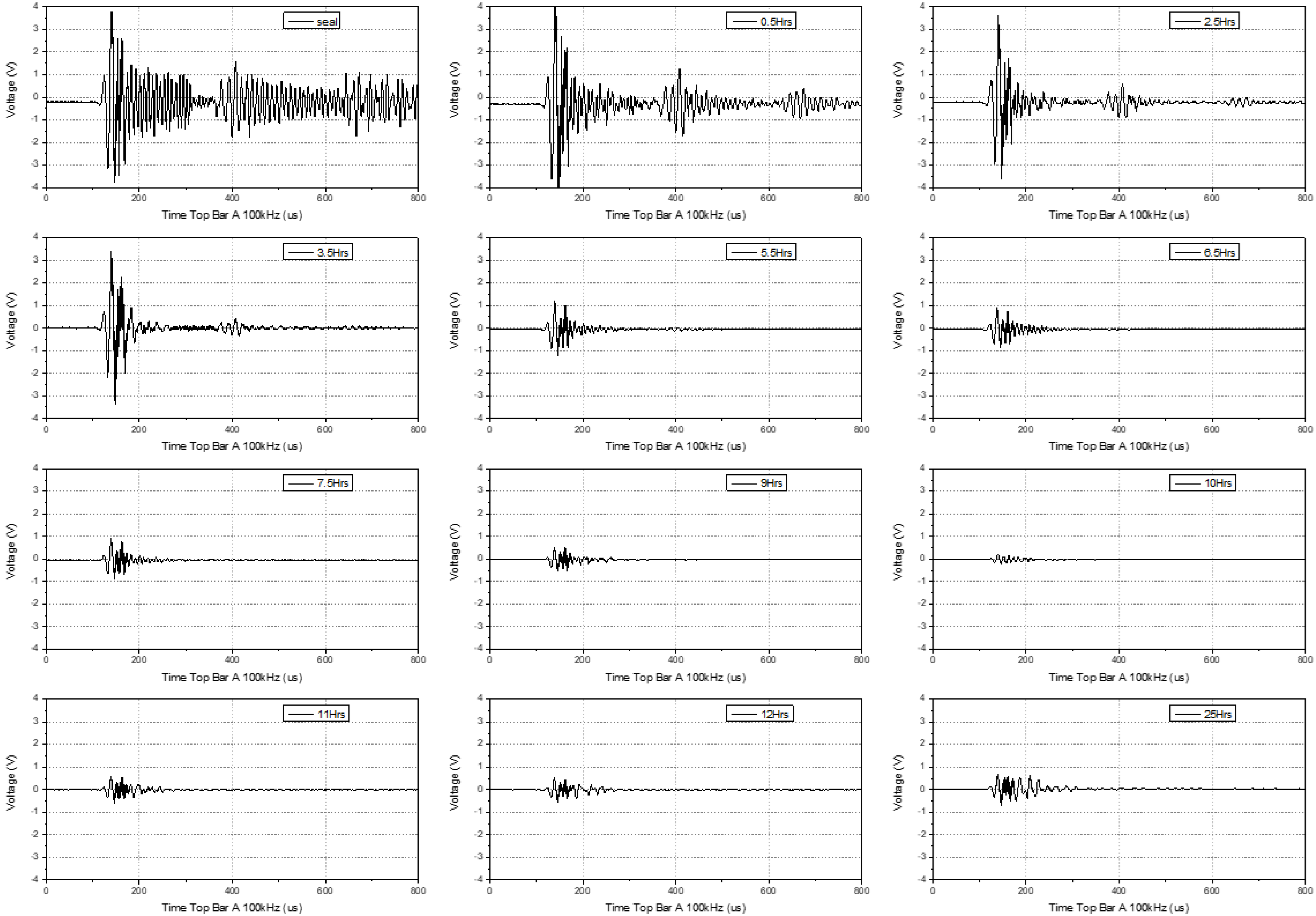

Fig. 7-4 Time signals in the top bar at different times after pouring concrete using L (0,1) mode at 100 kHz.

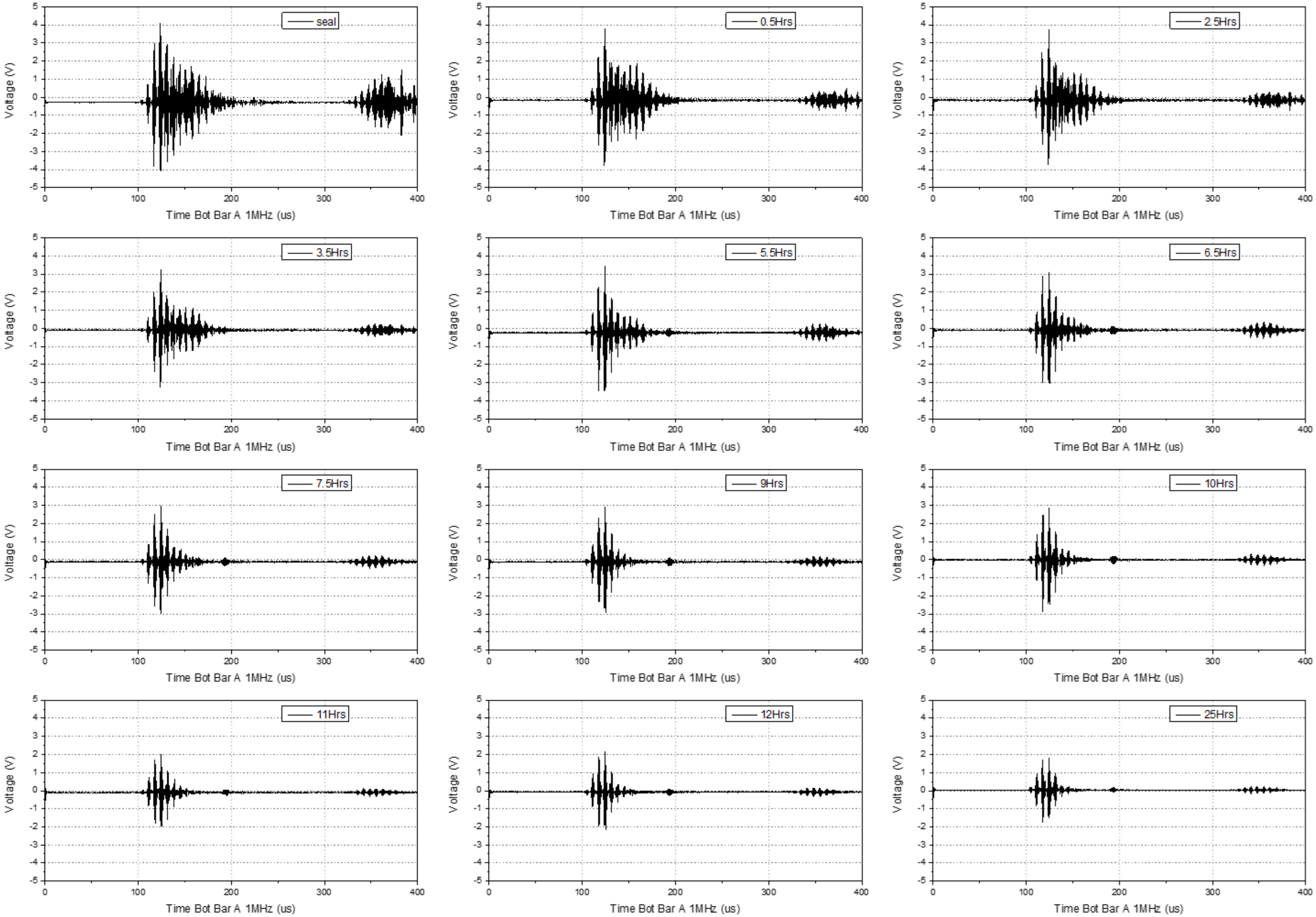

Fig. 7-5 Time signals in the bottom bar at different times after pouring concrete using L (0,7) mode at 1 MHz.

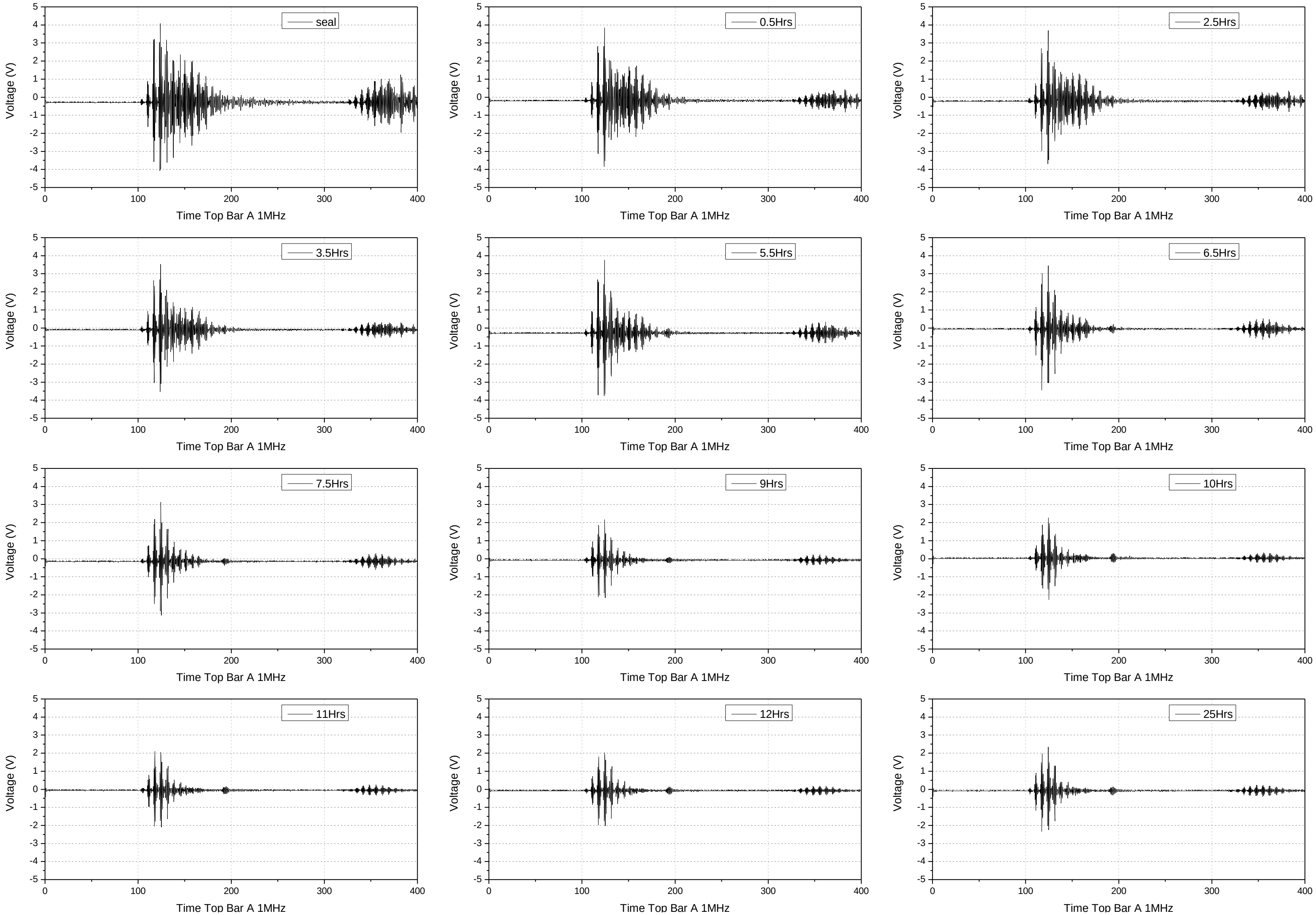

Fig. 7-6 Time signals in the top bar at different times after pouring concrete using L (0,7) mode at 1 MHz.

The peak-peak voltage of the signal is one of the most straightforward characteristics of the guided waves. It has been repeatedly used to monitor concrete setting and concrete corrosion (Zhang, Castel et al. 2011, Sharma and Mukherjee 2015). The peak-peak voltage of the signals at different times after concrete pouring is calculated. Fig. 7-7 (a) shows the peak-peak voltage of signal using L (0,1) mode at 100 kHz with the increasing concrete setting time. The trend of the TI in both bars was similar. Four stages variation in the voltage was visible. In the first 2.5 hours (stage 1), the peak-peak voltage almost remained steady with a negligible reduction. Between 2.5 hours and 6 hours (stage 2), the voltage dropped dramatically from 8 V at 2.5 hours to less than 2 V at the 6th hour. Then the rate attenuation rate of the voltage reduced, and the voltage of the signal gradually reduced at a slower rate from the 6th hour to the 10th hour (stage 3). Between the 10th hour and the 11th hour, the voltage of signals in both bars rose. Beyond the 11th hour, the voltage of signals in the top bar remained steady while the voltage of the signal in the bottom bar first dropped at the 12th hour then became steady.

Fig. 7-7 (b) shows the peak-peak voltage of the signal excited by L (0,7) mode at 1 MHz. A slight voltage drop of about 0.5 V was observed in both bars once the concrete was poured into the mould at the 0.5th hour. Two stages variation was observed in the bottom bar. The voltage of signals in the bottom bar gradually reduced slowly from the 0.5th hour to the 10th hour. Between the 10th hour and the 11th hour, a sudden voltage drop was observed. Beyond the 11th hour, the peak-peak voltage remained steady. In the top bar, three stages variation was visible. The voltage of the signal remained steady from the 0.5th hour to the 5.5th hour. The voltage reduced significantly by 3.2 V from the 5.5th hour to the 10th hour. Then it remained steady until the end of the experiment.

It is noted that the residual voltage of the signal in the top bar is higher than that in the bottom bar throughout the setting period, although the excitation voltages in the bar in air were almost identical. It is expected that a debonding owning to top-bar effect formed underneath the top bar. The debonding leads to a reduction in the energy leakage from the bar to the surrounding concrete. More energy can be retained in the bar and be received by the signal receiver, resulting in a higher voltage of the signals. An interesting observation lies in the Voltage trend of L (0,7) mode. The bottom bar shows two stages variation, while the top bar shows three stages. The voltage of the signal in the bottom bar reduces at a steady rate until the 10th hour. While in the top bar, the voltage of the signals only drops between the 5.5th hour and the 9th hour at a fast rate. The residual voltage of the signal in the top bar is temporarily lower than that in the bottom between the 9th and 10th hour.

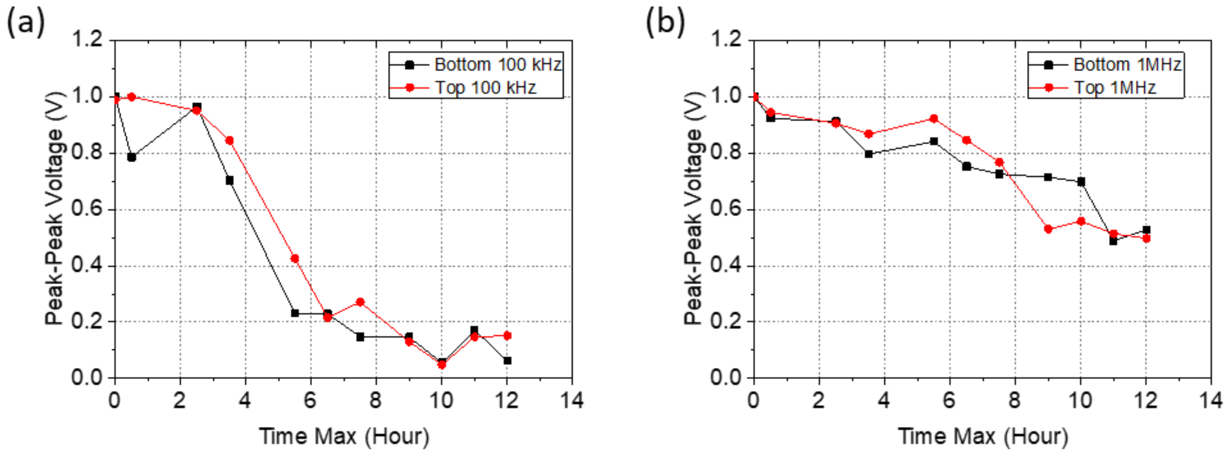

Fig. 7-7 The peak-peak voltage of signals in the bottom bar and top bar using (a) L (0,1) mode at 100 kHz and (b) L (0,7) mode at 1 MHz.

The setting of the concrete specimen significantly influences two characteristics of the transmission signals. One is the reduction of the peak-peak voltage with the aging of the concrete setting. The other one is the reduction of the number of wave packets throughout the entire setting process. It is recalled that the number of the wave packets in L (0,1) mode reduces significantly right after pouring concrete in the mould. While the number of wave packets in L (0,7) mode remained steady in the first 2.5 hours, the number continued to drop with time. However, the peak-peak voltage of the L (0,1) mode and L (0,7) mode remained steady in the first 2.5 hours. It has been revealed in Chapter 5 that the slight stiffness of the fresh concrete due to slow chemical reactions before the initial set of concrete can significantly influence the characteristics of the guided wave, especially during the pre-induction stage where the condition of the bar changes from the bar in air to bar embedded in fresh concrete. The attenuation of the modes increases dramatically. However, this phenomenon is not observed by analyzing the peak-peak voltage of the signals before the initial set. It is clear that analyzing the peak-peak voltage alone leads to missing information during the early stage of the concrete setting, particularly the reduction in the packet number is not considered. Therefore, in addition to the peak-peak voltage measurement, the transmission index (TI) proposed in Section 3.5.2 is employed to monitor the concrete setting. The TI indicates the total residual energy of the transmitted waves with respect to the total energy of the waves in the bar in air. It consists of both the voltage of the wave and the number of wave packets, therefore providing more comprehensive information about the change in the guided waves due to concrete setting.

Fig. 7-8 (a) shows the TI of L (0,1) mode at 100 kHz in the bottom bar and top bar. At 0.5 hours after pouring concrete, the TI of the bottom bar and top bar dropped by 65% and 30%, respectively. The change in the condition of the bar, from the bar in air to the embedded bar, was successfully identified by the TI reduction. It was recalled that the peak-peak voltage of the signal in the bottom bar dropped significantly at the 0.5th hour then increased to the value of bar in air at the 2.5th hour. This might be caused by the poor contact between the transducer and the bar, leading to an overestimated TI reduction. Between the 0.5th hour and the 5.5th hour, the TI in both bars reduced monotonically with time. The residual TI in the bottom and top bars was 5% and 10% at the 5th hour. Then the TI remained steady from the 5th hour to the 10th hour. A slight rose was observed in both bars between 10 hours and 11 hours. Then the TI reached a plateau. At the end of the setting process, the TI of the bottom bar and top bar reduced by 97.6% and 93.7%, respectively. It is noted that the TI in the top bar is larger than that in the bottom bar throughout the entire setting process. It is recalled that the L (0,1) mode at 100 kHz is a surface-seeking mode. The signal attenuation caused the TI reduction due to the bond development with time. A smaller TI reduction indicates a poorer development of bonds at the steel-concrete interface. Hence, it is concluded that the debonding owning to the top-bar effect is formed underneath the top bar.

Fig. 7-8 (b) shows the TI of L (0,7) mode at 1 MHz in the bottom bar and top bar. The TI in the bottom bar and top bar dropped by 70% and 76% in the first 0.5 hours, indicating the pouring concrete in the mould. Then the TI dropped slowly from 0.5 hours to 3.5 hours. A plateau was observed in both bars between 3.5 hours and 5.5 hours. The TI in the top bar dropped significantly from 5.5 hours to 9 hours and then remained steady until the end of the process. While the TI in the bottom bar continuously dropped at a slower rate from 5.5 hours to 9 hours. The TI remained steady between 9 hours and 10 hours. A sudden drop of TI by 10% occurred between 10 hours and 11 hours. Then the TI remained steady again. In general, the TI in the top bar is larger than that in the bottom bar. The TI in the top bar dropped more rapidly between 5.5 hours and 10 hours. The difference in TI reduced with time from 5.5 hours to 7.5 hours, and the TI in the top bar was temporarily lower than that in the bottom bar between 9 hours and 10 hours. At the end of the setting process, the TI in the bottom bar and the top bar dropped by 75% and 72%, respectively.

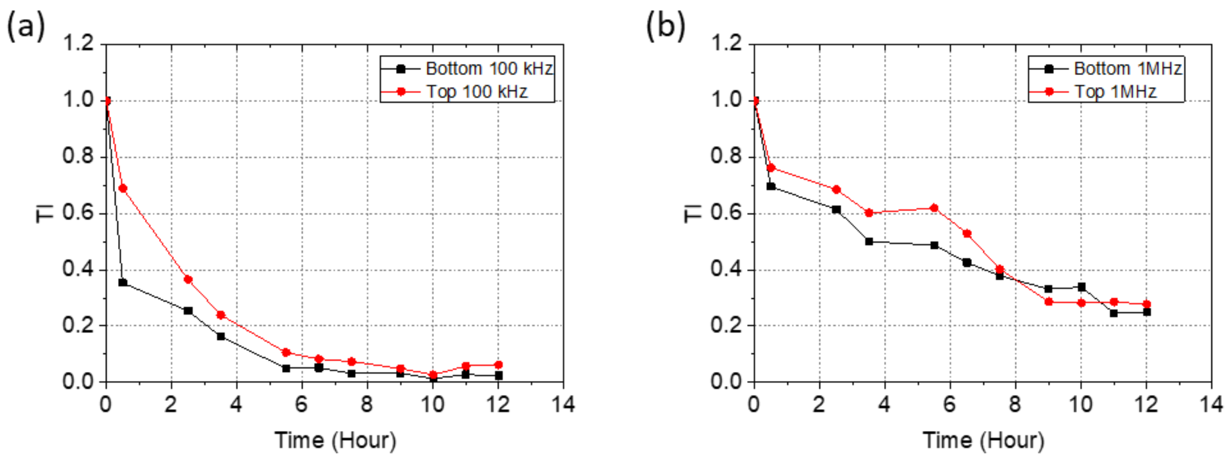

Fig. 7-8 TI of (a) L (0,1) mode at 100 kHz and (b) L (0,7) mode at 1 MHz in the bottom bar and top bar.

The peak-peak voltage can serve as a good indicator of different stages of the hydration process. However, the voltage remains steady during early hydration, particularly the stage 1 and 2, making it insensitive to monitor the development of the bond between the bar and the surrounding concrete, although the bond development is slow. On the other hand, the TI of the signals drops significantly with time until the concrete reaches its final set. The early stages of the hydration process cannot be differentiated clearly. By employing both characteristics of the signals, the stages of the hydration process can be clearly identified by the peak-peak voltage of the signals, while the bond development during each stage can be monitored using the proposed TI.

Stage 1 Pre-induction stage (0-0.5 hour): In the first 0.5 hours after pouring concrete, the peak-peak voltage of L (0,1) mode remains steady while the peak-peak voltage of L (0,7) mode drops slightly by

8%. However, the reduction in the TI is significant during this stage, L (0,1) reduces by 30%, and L (0,7) drops by 24%. This indicates the pouring of concrete in the mould and the initial contact between the steel bar and the surrounding liquid concrete. The surrounding material changes from air to fluid concrete, the attenuation of the guided wave increases significantly, although the bond between the steel and the surrounding concrete is not yet formed.

Stage 2 Dormant stage (0.5-2.5 hours): The chemical reactions occur slowly during this stage, leading to the slow development of the bond between the bar and the surrounding concrete. The peak-peak voltage of both modes remains steady during this period. The TI of the L (0,1) mode drops significantly by 32%, while the TI of the L (0,7) mode drops by 10%. Although the bond development is slow, the attenuation of the L (0,1) mode increases rapidly, leading to a sharp reduction in the TI of the L (0,1) mode. The reduction in the TI of L (0,7) mode, on the other hand, is mild. It is recalled that the L (0,1) mode is the surface seeking mode while the L (0,7) mode is the core seeking mode. Hence, the L (0,1) mode is more sensitive to the change in the bond than that of the L (0,7) mode.

Stage 3 Acceleration stage (2.5-10 hours): The chemical reactions occur rapidly during his stage, leading to a gradual development of the bar and the concrete bond. The initial and final set of the concrete occurs at the 2.5th and 5.5th hours. The concrete gradually losses its plasticity and transfers from liquid state to solid state during this period. The peak-peak voltage and the TI of the L (0,1) mode drop rapidly between the 2.5th hour and the 5.5th hour, indicating the rapid bond development during the setting period. While the voltage and the TI of the L (0,7) mode first dropped then remained steady. The process passes the final set, and the initial hardening occurs after the 5.5th hour. The reduction in the voltage and the TI of the L (0,1) mode slows down. The bond between the bar and the surrounding concrete is formed, and the bond strength continues to develop over time. The L (0,1) mode is less sensitive to the development of the strength of the bond than the development of the stiffness of the bond. In contrast, the voltage and the TI of the L (0,7) mode drops rapidly. This indicates the continuous gain of stiffness and strength of the solid concrete. As the stiffness and the strength of the concrete increase, more energy leaks into the surrounding concrete from the bar, leading to a reduction in the TI of the L (0,7) mode.

Stage 4 Deceleration stage (10 -12 hours): The chemical reactions slow down during this stage, indicated by the slowing down of the temperature increment. The change in the peak-peak voltage and the TI of both modes are insignificant, confirming that the concrete is hardened. The guided waves are no longer sensitive to the change in the bond and the surrounding concrete, although the concrete's stiffness and strength continue to gain with time.

7.3. Monitoring corrosion of reinforced concrete

7.3.1. Inducing accelerated corrosion

The concrete column specimen is sawn to small specimens after 28 days of curing. The dimension of the specimen is 200 mm X 200 mm X 400 mm. Each specimen contains a round steel bar located at the center of the specimen. The specimens are first merged in 3.5 % NaCl solution for two days to saturate the specimens. Then they are subjected to accelerated corrosion using impressed current. A cotton sheet is wrapped around the mid-one-third of the concrete specimen to keep the specimen moisture. A stainless steel wire mesh is wrapped above the cotton sheet and used as the cathode by connecting it to the negative terminal of the power supply. The steel bar is used as the anode by connecting it to the positive terminal of the power supply. The electric current was impressed between the steel bar and the wire mesh at a controlled voltage. Fig. 7-9 shows the impressed voltage and the induced current during the entire corrosion process. The impressed voltage was set to 5 Vpp in the first 500 hours of corrosion. The initial induced current was 0.02 A and 0.03 A in the top bar and bottom bar specimens. The amplitude of the voltage and the current remained steady for 160 hours. Then the impressed voltage was temporarily increased to 5.5 Vpp. The current in the top bar specimen was then increased to and maintained at 0.03 A, the same as the current in the bottom bar. However, the current in the bottom bar specimen remained at 0.03 A for about 20 hours, then it reduced to 0.02 A although the voltage was increased to 5.5 Vpp. The current in both specimens remained steady for 122 hours at an impressed voltage of 5.5 Vpp. The voltage was reduced back to 5 Vpp at 342 hours.

The current in the top bar dropped to 0.02 A while the bottom bar remained at 0.02 A. One possible reason for the current drop in the bottom bar specimen is that the corrosion initiates and creates a local debonding, reducing the ionic current flow. Hence, the measured current is dropped although the impressed voltage is increased. The impressed voltage was increased to 10 Vpp between 490 hours and 1880 hours to accelerate the corrosion of the concrete. The induced current was doubled and remained at 0.04 A for the entire duration. Beyond 1900 hours, the impressed voltage was increased to 15 Vpp to further accelerate the corrosion of the concrete. The induced current was increased to 0.06 A for about 80 hours, then the current fluctuated between 0.06 A and 0.08 A, indicating the aggressive progression of corrosion.

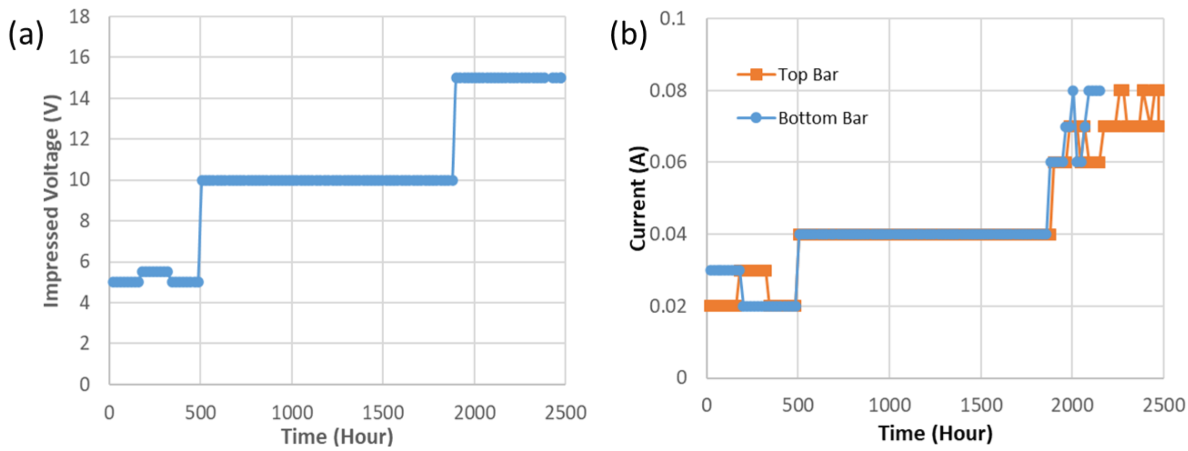

Fig. 7-9 (a) Impressed voltage and (b) induced current for accelerated corrosion.

Since the impressed voltage was increased two times during the experiment to accelerate the corrosion process and the induced current in the specimens varied with specimen and time, analyzing and comparing the experiment results in terms of time of corrosion exposure would not accurately reflect the corrosion process. As shown in Fig. 7-10, the cumulative electric energy was employed to replace the time of corrosion exposure.

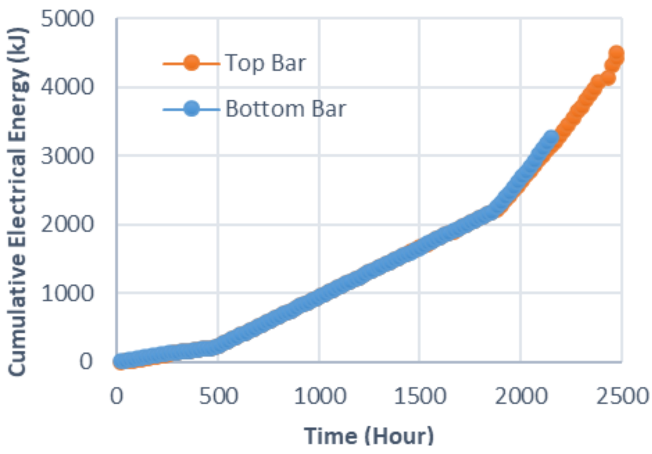

Fig. 7-10 Cumulative electric energy with increasing corrosion exposure.

7.3.2. Electrochemical investigation

7.3.2.1. Half-cell potential (HCP)

Half-cell potential measurements were taking on the specimens daily with the increasing corrosion exposure. Half-cell potential provides the probability of the occurrence of corrosion activity at the time of measurement. Typical values of half-cell potential for the probability of corrosion are giving in Table. 7-1 (Sharma and Mukherjee 2013).

Table. 7-1 Corrosion probability from potential measurement according to ASTM C876 (ASTM 1999)

Potential (mV/CSE)	Probability of steel corrosion activity
>-200	Less than 10%
-200 - -350	Uncertain
<-350	More than 90%

Fig. 7-11 presents the half-cell potential measured during the corrosion exposure in terms of the impressed energy. For the bottom bar specimen, the potential was positive in the first 75 kJ of exposure. A positive value of half-cell potential usually refers to a dry concrete (0 - +200mV) according to RILEM TC-154. This may indicate that the specimen is not fully saturated, and the NaCl solution is not yet reaching the steel bar at the measurement location. The potential continued to decrease with impressed energy. The potential fluctuated between -100 mV and -200 mV from 86 kJ to 154 kJ of impressed energy. The potentials first reached and remained below -200 mV after 154 kJ of impressed energy. This may indicate the initiation of the corrosion, although the probability of the corrosion is 10%. Then the potential fluctuated between -200 mV and -350 mV from 154 kJ to 2184 kJ of impressed energy. A potential increment, from -300 mV to -200 mV, occurred between 1000 kJ and 1300 kJ. The potential first reached below -350 mV after 2257 kJ of impressed energy. The potential started reducing rapidly with exposure after this point. This indicates the aggressive progression of corrosion occurring in the bottom bar. shortly after this, liquid rust was oozed out from the side of the specimen and a through-thickness crack appeared on the specimen after 3273 kJ of impressed energy.

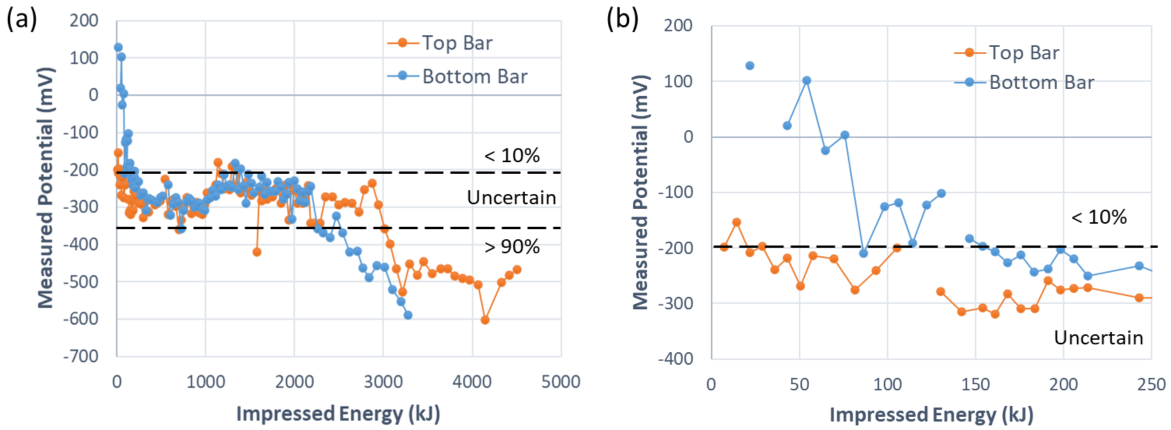

Fig. 7-11 (a) Half Cell Potential measurements with increasing corrosion exposure and (b) zoom in at 0-250 kJ (0-500 Hours)

In the top bar specimen, the potential was already at -200 mV after 7.2 kJ pf impressed corrosion, indicating the corrosion initiation occurred right after the impressed current was applied. This phenomenon was repeatedly observed in the specimens with top-bar effect in previous experiments. In case of the top bar, NaCl solution directly reaches the bottom surface of the bar due to the presence of voids underneath the bar. The passive layer on the steel bar likely breaks once the impressed current is applied, and the corrosion initiates soon after the layer is broken. The potential remained between -200 mV and -350 mV until 3000 kJ of impressed energy. During this period, the probability of corrosion activity remained uncertain. Potential below -350 mV was first recorded at 3000 kJ, and the potential dropped sharply to -537 mV at 3214 kJ. A sudden jump was observed between 3214 kJ and 3295 kJ, then the potential dropped at a slower rate from -450 mV to -500 mV, indicating the aggressive progression of corrosion.

The potential of the top bar specimen was already below -200 mV in the first record, while it takes 154 kJ of impressed energy for the potential of the bottom bar specimen to drop below -200 mV. Although the probability of the reinforcing bar corrosion occurring is only 10%, the top bar specimen shows a much earlier sign of reinforcing bar corrosion initiation than the bottom bar. This matches with the conclusion made in the previous experiments that the top-bar effect advances the corrosion of reinforcing bars. However, it takes 743 kJ more of the impressed energy for the potential of the top bar specimen to drop below – 350 mV than that of the bottom bar specimen. By the time liquid rust is observed at the side of the bottom bar specimen, no visual signal is observed in the top bar, and the potential of the top bar specimen remained between -200 mV and -350 mV. The probability of reinforcing bar corrosion in the top bar specimen remained uncertain based on the HCP measurement. However, it is known that the severity of the bar in the top bar specimen is worse than that in the bottom bar specimen due to the presence of the debonding owning to the top bar effect. Hence, the probability of the bar corrosion in the top bar specimen may be underestimated solely relay on the HCP measurement.

7.3.2.2. Linear polarization resistance (LPR)

The corrosion current density (i_{corr}) can actively provide the corrosion rate at the time of the measurement. However, it cannot provide the corrosion severity and the corrosion state of the reinforcing bar. Table. 7-2 presents the typical values of i_{corr} for corrosion rate classification (ASTM 1999). In general, the situation of the bar corrosion rapidly transferred from inactive (low i_{corr}) to a significant level of corrosion rate (high i_{corr}), indicating the depassivation of the reinforcing bar and the initiation of the corrosion (Andrade and Alonso 2004).

Table. 7-2 Typical values of corrosion current density, $i_{corr,}$ related to the rate of corrosion activity.

Corrosion current density i_{corr} (μA/cm^2)	Corrosion Level	Corrosion description
≤ 0.1	Negligible	Corrosion rate is negligible and the steel is in passive state
0.1 – 0.5	Low	Low rate of corrosion
0.5 - 1	Moderate	Corrosion has been initiated and is proceeding at a moderate rate
> 1	Hight	High rate of corrosion

In this experiment, the LPR scan, in a range of 200 mV and –1000mV of corrosion potential, was performed using EZstat Pro Potentiostat. The scanning rate was set to be 1mV/s. The corrosion current density, i_{corr}, was measured daily after the specimen was discharged from the power supply and rested for at least 2 hours. Fig. 7-12 presents the measured i_{corr} value in both specimens with increasing corrosion exposure. The i_{corr} of both specimens was already above 0.2 uA/cm^2 after the first day of accelerated corrosion. This is because the chloride content in the specimens is high even before the experiment as the specimens are saturated with NaCl solution. According to Table. 7-2, the corrosion of the steel bar in both specimens is initiated, but the corrosion rate is low.

For the bottom bar specimen, the i_{corr} value initiated at 0.21 and continuously increased with increasing exposure to corrosion in the first 1000 kJ of impressed energy. The i_{corr} value first passed 0.5 after about 200 kJ and reached one after 961 kJ of energy. This confirmed the depassivation of the steel bar, and the corrosion has initiated. Theoretically, this i_{corr} value means the corrosion rate of the steel bar is high. However, the i_{corr} value began to reduce afterward. The i_{corr} value continued to drop to 0.45 between 961 kJ and 1484 kJ of impressed energy, and then the i_{corr} value fluctuated around 0.5 between 1484 kJ and 2257 kJ. According to Table. 7-2, the corrosion rate of the steel bar transferred to and remained moderate. Between 2257 kJ and 2541 kJ, the i_{corr} value increased to 0.92, followed by a sudden jump at 2705 kJ. Beyond 2705 kJ, the i_{corr} value sharply rose with increasing corrosion exposure and peaked at about two after 3195 kJ of impressed energy.

For the top bar specimen, the i_{corr} value initiated at 0.23, which was slightly higher than that of the bottom bar specimen. The i_{corr} value first increased to 0.31 then reduced to 0.21 between 28.8 kJ and 57.6 kJ. Between 57.6 kJ and 93.2 kJ, the i_{corr} value remained steady around 0.2 with a slight reduction trend. The i_{corr} value sharply rose between 93.2 kJ and 394 kJ, then the i_{corr} value increased at a slower rate with noticeable fluctuation from 394 kHz and peaked at 0.84 after 961 kHz of impressed energy. The i_{corr} value started to drop afterward, as in the bottom bar specimen. The i_{corr} value dropped from 0.84 to 0.35 between 961 kJ and 1785 kJ. Then the i_{corr} value remained steady around 0.4 until 2943 kJ. The corrosion rate of the specimen remained low. A sharp and continuous rose in the i_{corr} value occurred between 3943 kJ and 4501 kJ, indicating the continuous increase of the corrosion rate. The corrosion rate remained high after 3549 kJ of impressed energy, indicating the occurrence of aggressive corrosion.

The trend of the i_{corr} value is similar in both specimens. The i_{corr} value first increased with increasing corrosion exposure in the first 1000 kJ of impressed energy. Then the i_{corr} value of the bottom bar and top bar specimen dropped to 0.5 and 0.4, respectively. The i_{corr} value of the bottom bar remained at around 0.5 for about 773 kJ before it started to rise. While the i_{corr} value of the top bar remained at 0.4 for about 1157 kJ and then continuously rose until the end of the experiment.

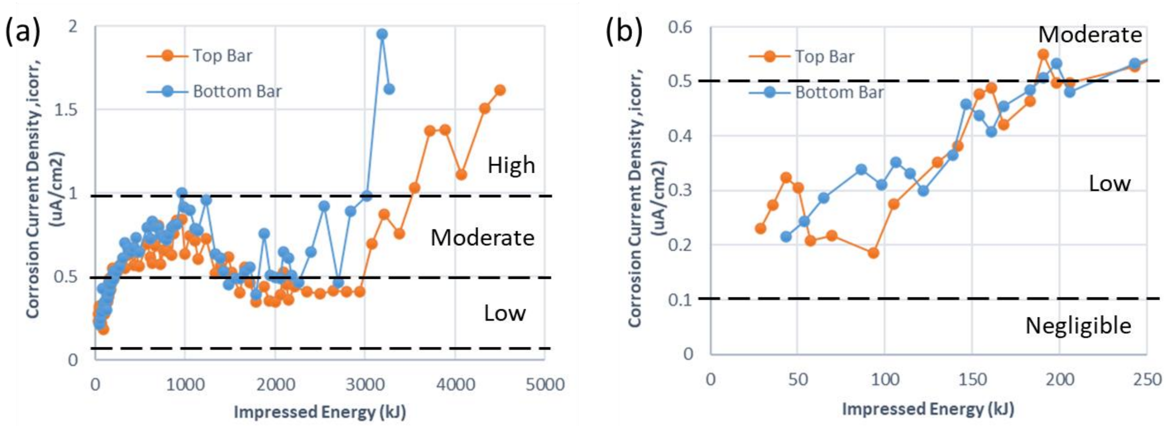

Fig. 7-12 (a) Corrosion current density measurements with increasing corrosion exposure and (b) zoom-in between 0 kJ and 250 kJ.

7.3.3. Ultrasonic investigation

7.3.3.1. Guided waves

7.3.3.1.1. Bar in air

7.3.3.1.1.1. Mass Loss

Based on the observation of prior experiments in section 5, it has been concluded that the TI reduction with the increasing corrosion of an embedded bar is resulting from the co-effect of debonding at the steel-concrete interface and the bar deterioration. Hence, before conducting corrosion experiments in the reinforced concrete specimens, a bare bar corrosion experiment has been conducted to examine the effect of the corrosion-induced bar deterioration on the characteristics of the surfaces-seeking mode, L (0,1) and the core-seeking mode, L (0,7). In this experiment, the TI variation due to debonding is not included. To simulate the corrosion in the top bar specimen, only the bottom part of the steel bar is immersed in the NaCl solution and subjected to accelerated corrosion. The impressed current is 0.02 A (0.02g/hour) in the first 480 hours of accelerated corrosion to study the corrosion initiation and early stage of corrosion. Then the current is set to be 0.04 A (0.04g/hour) to further accelerate the corrosion. Fig. 7-13 shows the measured and calculated mass loss of the steel bar with increasing corrosion exposure in terms of the impressed energy. The measured mass loss of the bar matches well with the calculated mass loss.

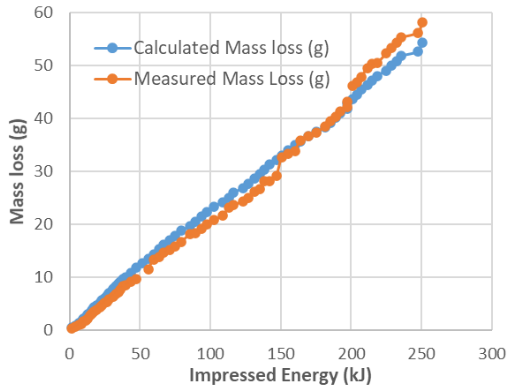

Fig. 7-13 Measured and calculated mass loss (g).

7.3.3.1.1.2. Visual Inspection

Fig. 7-14 presents the condition of the steel with increasing exposure. The corrosion only occurs on the bottom surface of the bar, and the top surface remained intact throughout the entire experiment. Therefore only the photos of the bottom surface are presented. On day 1, the impressed energy is calculated as 1.6 kJ. Two noticeable but shallow slots, along with some pits, were observed on the bottom surface. The slots were becoming larger and deeper with increasing corrosion exposure. The silver colour of the bar was first observed after 8.2 kJ of impressed energy. As circled in Fig. 8-14, three large and deep pits appeared on the bar after 31.2 kJ. Subsequently, the pits grew larger and deeper and becoming generalized corrosion with increasing corrosion. Severe corrosion was observed at the end of the experiment after 250.5 kJ of impressed corrosion. The depth of the corrosion was about one-fourth of the bar diameter.

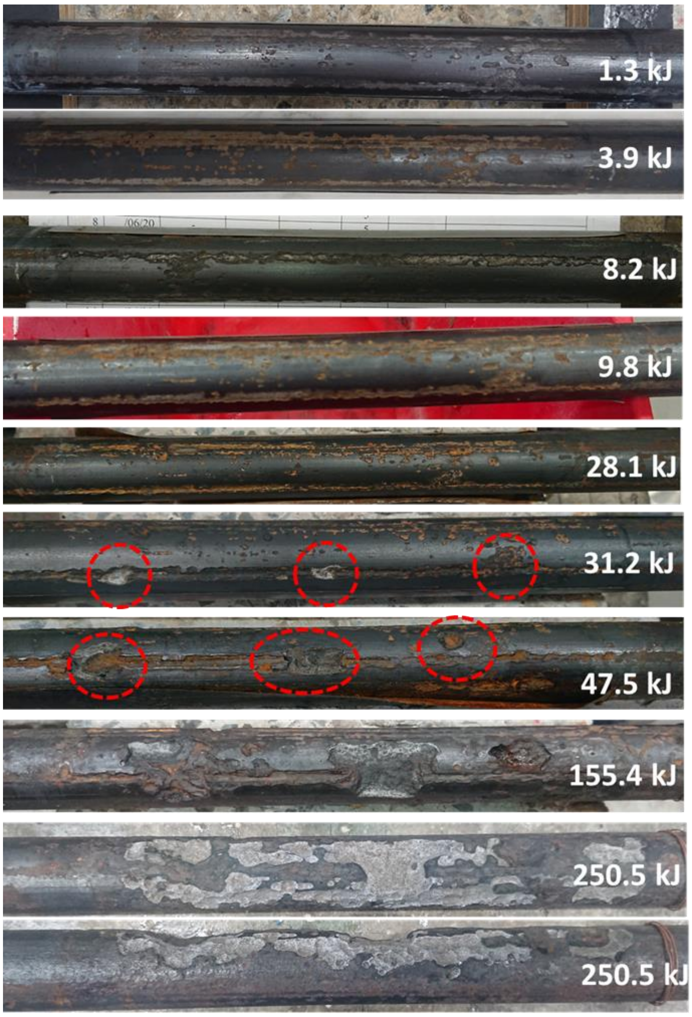

Fig. 7-14 Condition of steel bar with increasing corrosion exposure.

7.3.3.1.1.3. Ultrasonic Results

Fig. 7-15 shows the pulse transmission signals with the increasing exposure using L (0,1) mode at 100 kHz. Before corrosion, there were two wave packets in the time signal. The first wave packet had a peak-peak voltage of 7 V, and the ToF of the peak was 100 us. The second wave packet had a peak-peak voltage of 4 V, and the ToF of the peak was 200 us. The signal remained steady in the first 9.8 kJ of energy, although noticeable slots were observed on the bar. With increasing exposure to corrosion, the voltage of the first wave packet remained steady while the voltage of the second peak reduced with corrosion. It was also noted that the sidebands in the first wave packet reduced with corrosion exposure, indicating the attenuation of the higher frequency component in the time signal.

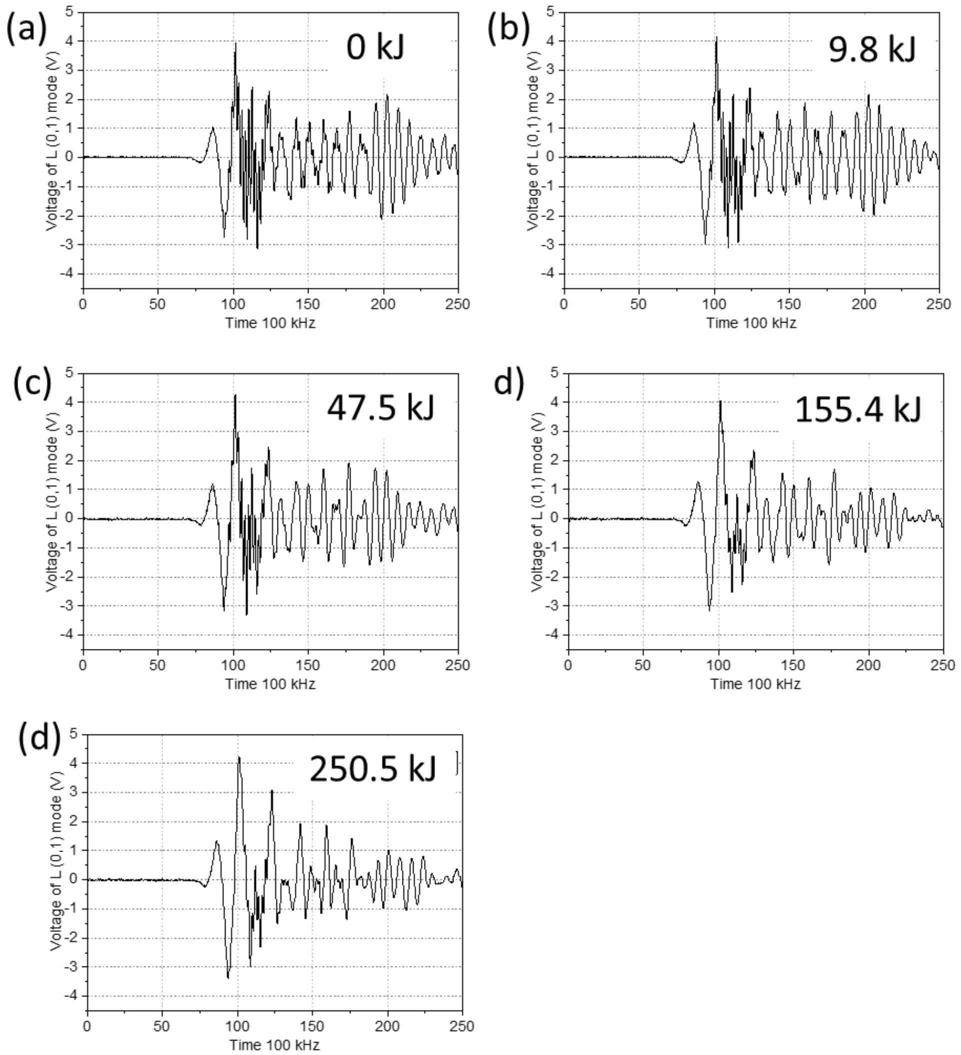

Fig. 7-15 Pulse transmission signals with increasing corrosion exposure using L (0,1) mode: (a) 0 kJ, (b) 9.8 kJ, (c) 47.5 kJ, (d) 155.4 kJ and (d) 250.5 kJ.

Fig. 7-16 shows the pulse transmission signals with the increasing exposure using L (0,7) mode at 1 MHz. Before the corrosion, the peak-peak voltage of the signal was about 8 V, and the signal contained seven wave packets. In the first 9.8 kJ of impressed energy, the signals remained steady. Subsequently, the peak-peak voltage and the number of wave packets of the time signal reduced with increasing corrosion exposure. The peak-peak voltage of the signal was reduced to 2.7 V, and the number of the wave packets was reduced to 5 at the end of the experiment.

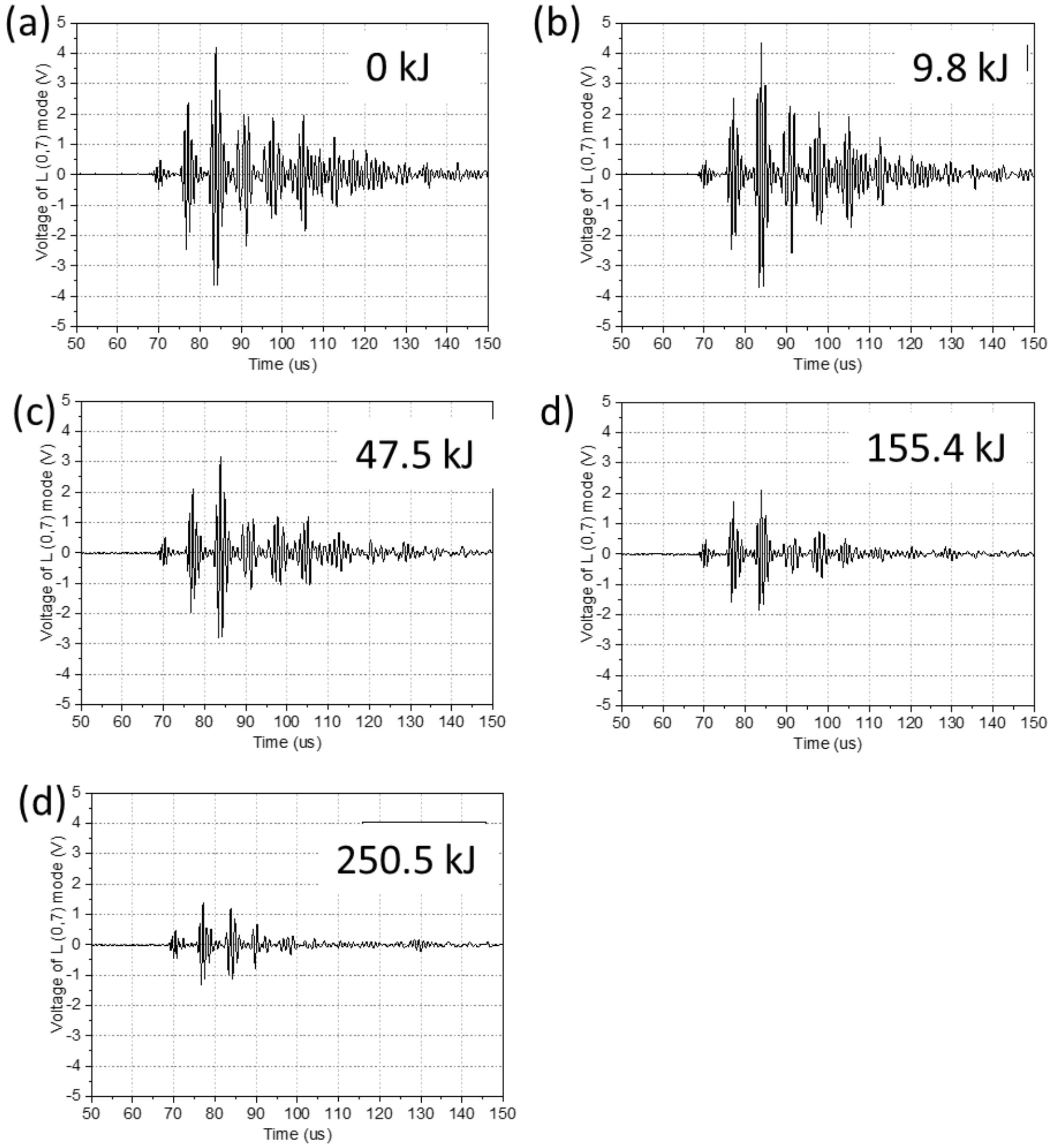

Fig. 7-16 Pulse transmission signals with increasing corrosion exposure using L (0,7) mode: (a) 0 kJ, (b) 9.8 kJ, (c) 47.5 kJ, (d) 155.4 kJ and (d) 250.5 kJ.

Fig. 7-17 presents the TI of L (0,1) mode and L (0,7) mode with increasing corrosion exposure. For the L (0,1) mode, the TI first dropped by 0.1 in the first 6.6 kJ of impressed energy. Then the TI gradually increased to 1.05 between 6.6 kJ and 21 kJ. Then the TI remained steady at a value of around 1.05 until 126.8 kJ of impressed energy. A sudden drop in the TI of about 0.2 occurred between 126.8 kJ and 134.9 kJ. Then the TI remained steady until the end of the experiment. Bumps were observed between 155 kJ and 181 kJ and between 185 kJ and 218 kJ. The results showed that the attenuation of the surface seeking mode, L (0,1), did not vary with the increasing bar deterioration due to corrosion. No significant change in the TI of the L (0,1) mode occurred even the mass loss of the bar was 3.8% of the total mass of the bar, and deep damages were observed. Hence, it was concluded that the variation in the TI of the L (0,1) mode was mainly contributed by the variation in the bond at the steel-concrete interface.

For the core-seeking mode, L (0,7), the TI dropped by 0.1 in the first 3.9 kJ then the TI gradually increased back to 1 between 3.9 kJ and 11.4 kJ. The total mass loss was 1.9 g (0.12%). The TI sharply dropped by 60% between 11.4 kJ and 71 kJ. Significant fluctuation, about 20%, in the amplitude of TI was observed during this period. A sudden TI rose was observed between 71 kJ and 79.5 kJ. Then the TI remained steady for about 10 kJ before a continuous fall of the TI. The TI value dropped to 0.2 at the end of the experiment. It is recalled that noticeable corrosion damage appears on the surface of the bar even after 1.9 kJ of impressed energy. However, the TI only started to drop after 13 kJ of impressed energy with a mass loss of 2.2 g (0.14%). It indicated that the core-seeking mode was not sensitive to corrosion initiation, but it could be used to detect the early corrosion of the bar. The results also confirmed that the core-seeking mode, L (0,7) was sensitive to the bar deterioration due to corrosion. Hence it could be used to monitor the corrosion-induced bar deterioration.

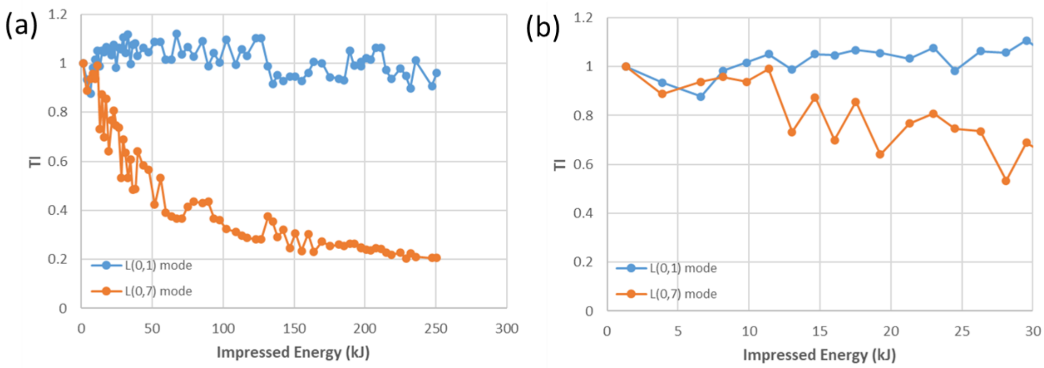

Fig. 7-17 (a) TI of L (0,1) mode and L (0,7) mode with increasing corrosion exposure and (b) zoom-in between 0 kJ and 30 kJ.

It was noticed that the sidebands of the L (0,1) mode reduce with increasing corrosion, indicating the attenuation of the higher frequency component of the signals, although the TI of the signal remained steady. Hence, the frequency profiles, as shown in Fig. 7-18, are also analyzed. There are two clear peaks in the frequency profiles, one ranges from 0 MHz to 0.1 MHz named as the low frequency component (LFC), and another one ranges from 0.1 MHz to 0.2 MHz, named the high frequency component (HFC). At first, both the LFC and HFC increased slightly with corrosion, as shown in Fig. 7-18 (a) and (b). with further increment in the corrosion exposure, the LFC increased while the HFC decreased. It indicates an energy shift from the HFC to LFC with increasing corrosion.

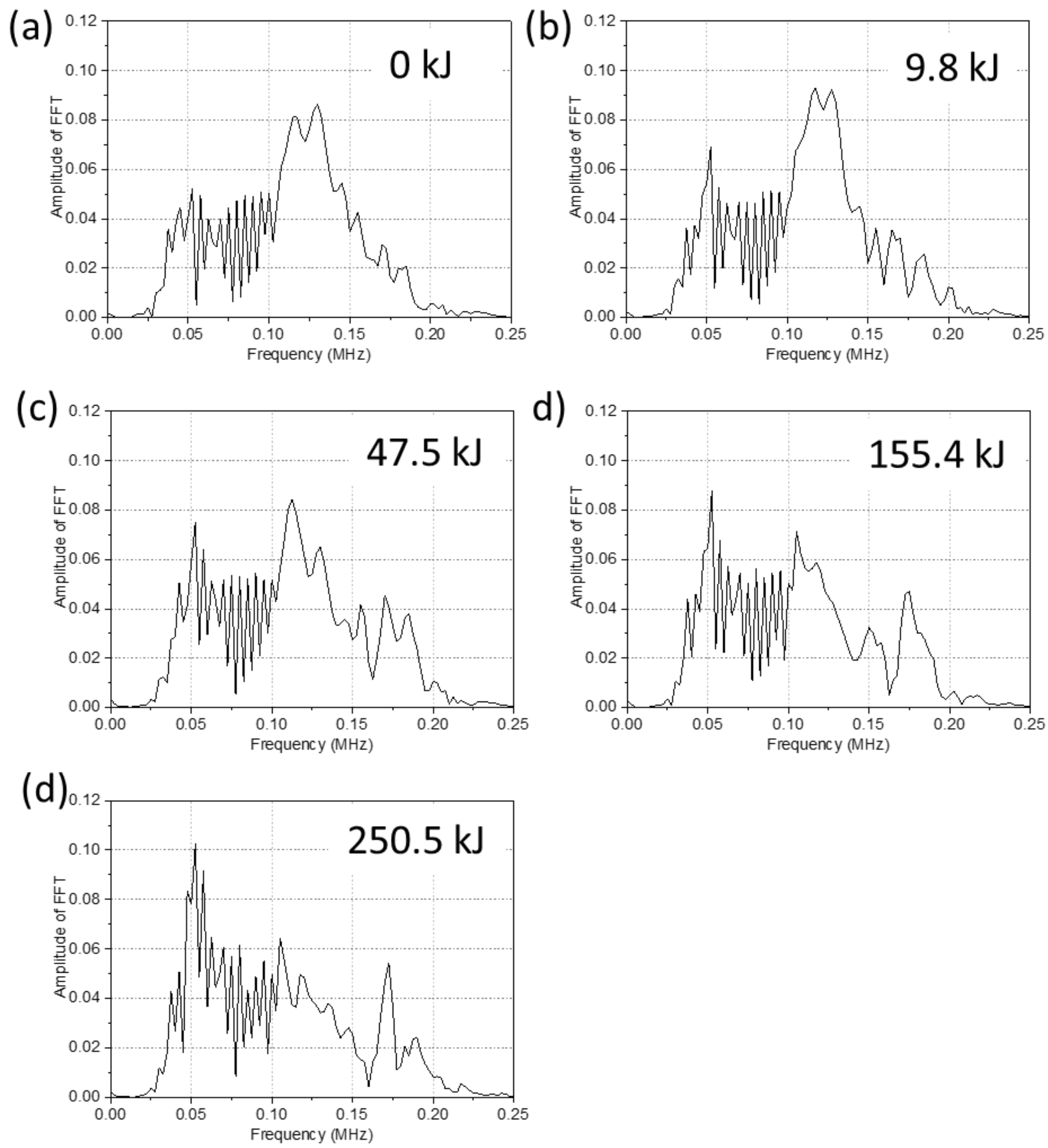

Fig. 7-18 Frequency profiles of the signals with increasing corrosion exposure using L (0,1) mode: (a) 0 kJ, (b) 9.8 kJ, (c) 47.5 kJ, (d) 155.4 kJ and (d) 250.5 kJ.

To analyze the energy shift from HFC to LFC, TI of LFC and HFC are calculated, and the normalized ratio of TI of LFC to the TI of HFC is employed to evaluate the energy shift. The ratio before the corrosion is considered as the benchmark. Fig. 7-19 shows the normalized ratio with increasing corrosion exposure. The ratio increased linearly with increasing corrosion exposure, indicating the energy shift from the HFC to the LFC. The ratio was more than doubled at the end of the experiment although the TI of the signals was almost identical. Hence, it was concluded that the energy of the L (0,1) mode did not attenuate but was being shifted from HFC to LFC with the increasing corrosion-induced bar deterioration. Therefore, the energy shift in the frequency component of L (0,1) mode can be a good indicator to monitor the bar deterioration.

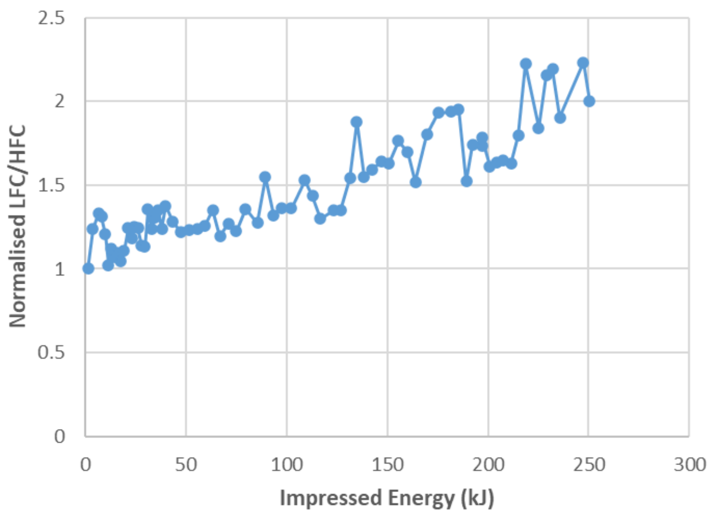

Fig. 7-19 Normalised LFC/HFC with increasing corrosion exposure.

Fig. 7-20 shows the frequency profiles of L (0,7) mode with increasing corrosion exposure. Similarly, the frequency profile remained steady in the first 9.8 kJ. Then the signal attenuated sharply with increasing corrosion. No energy shift between frequencies was observed in the L (0,7) mode like in the L (0,1) mode. Hence, for L (0,7) mode, the energy attenuation can be used to monitor the bar deterioration due to corrosion.

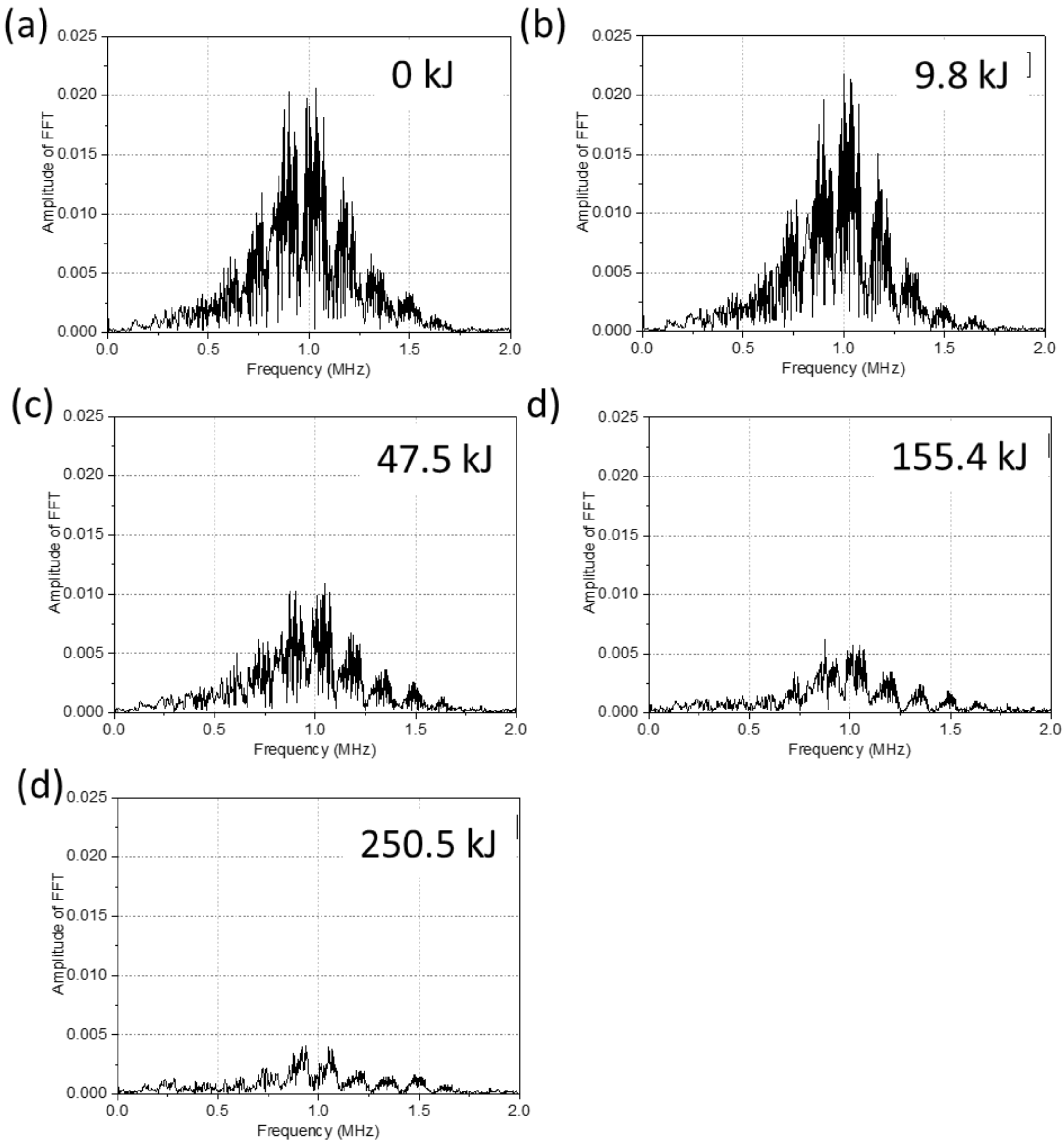

Fig. 7-20 Frequency profiles of the signals with increasing corrosion exposure using L (0,7) mode: (a) 0 kJ, (b) 9.8 kJ, (c) 47.5 kJ, (d) 155.4 kJ and (d) 250.5 kJ.

7.3.3.1.2. Embedded bar in concrete

7.3.3.1.2.1. Visual Inspection

Bottom bar

The bar (anode) was located at the center of the specimen. The specimen was wrapped by a cotton sheet and wire mesh which was used as the cathode. Hence, the crack might grow in any direction and appear on any surface of the specimen. Fig. 7-21 shows the visual inspection result of the bottom bar specimen after 2020, 2040, 2060, and 2100 hours of accelerated corrosion. The visual sign of concrete corrosion was first observed after 2020 hours of corrosion. Reddish-brown liquid rust was observed at the steel-concrete interface at the left end of the bar. The rust appeared at the half circumference of the bar, and no sign of rust was observed at the other half. This part of the bar was facing the dripping of the NaCl solution. Hence, chloride ions continued to penetrate through the pores in the concrete and reach this part of the bar. It may have a higher chance of corrosion. The rust continued to ooze out from the left side, and a hairline crack appeared at 2040 hours, denoted by the red line in Fig. 7-21 (b). The crack grew wider and longer at 2060 hours. The right end of the specimen remained intact during this period. By 2010 hours, the concrete cover was completed cracked. The crack appeared on the surface that coincident with the dripping side. A crack from the reinforcing bar to the concrete cover was observed at both ends of the bar.

Visual sign	
(a) 2020 Hours/3016 kJ Rust appears at bar end	
(b) 2040 Hours/3105kJ Hairline crack appears at bar end	
(c) 2060 Hours/3196 kJ Crack grows from bar end	
(d) 2100 Hours/ 3273 kJ Crack on concrete cover	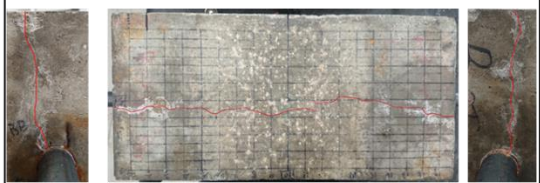

Fig. 7-21 Visual inspections of Bottom bar Specimen after (a) 2020, (b) 2040, (c) 2060, and (d) 2100 hours of accelerated corrosion.

The specimen was sawn into two parts to inspect the condition of the steel-concrete interface and the extracted bar. Rust stain was widespread over the steel-concrete interface of the bottom bar specimen (Fig. 7-22 (a) and (b)), indicating the fully debonding of the bar from the concrete. An Orange rust stain was observed on the side facing the dripping/ crack surface, indicating aggressive corrosion within that region. A small crack was also observed in the middle part of the interface. The direction of the crack was perpendicular to the crack that appeared on the surface of the concrete. This indicated that the cracking was initiated at multiple locations. The cracking that appeared on the surface was only the most aggressive one. Fig. 7-22 (c) shows the surface of the bar that facing the dripping/ cracking side. Widespread pits and generalized corrosion were observed along the bar. The mill coating of the bar was removed in the middle of the bar, exposing the silver part of the bar, as shown in Fig. 7-22 (c). While in the counterpart of the bar, the bar was almost intact, with only shallow pits on the mill coating. This might be caused by the local corrosion within the voids distributed over the steel-concrete interface.

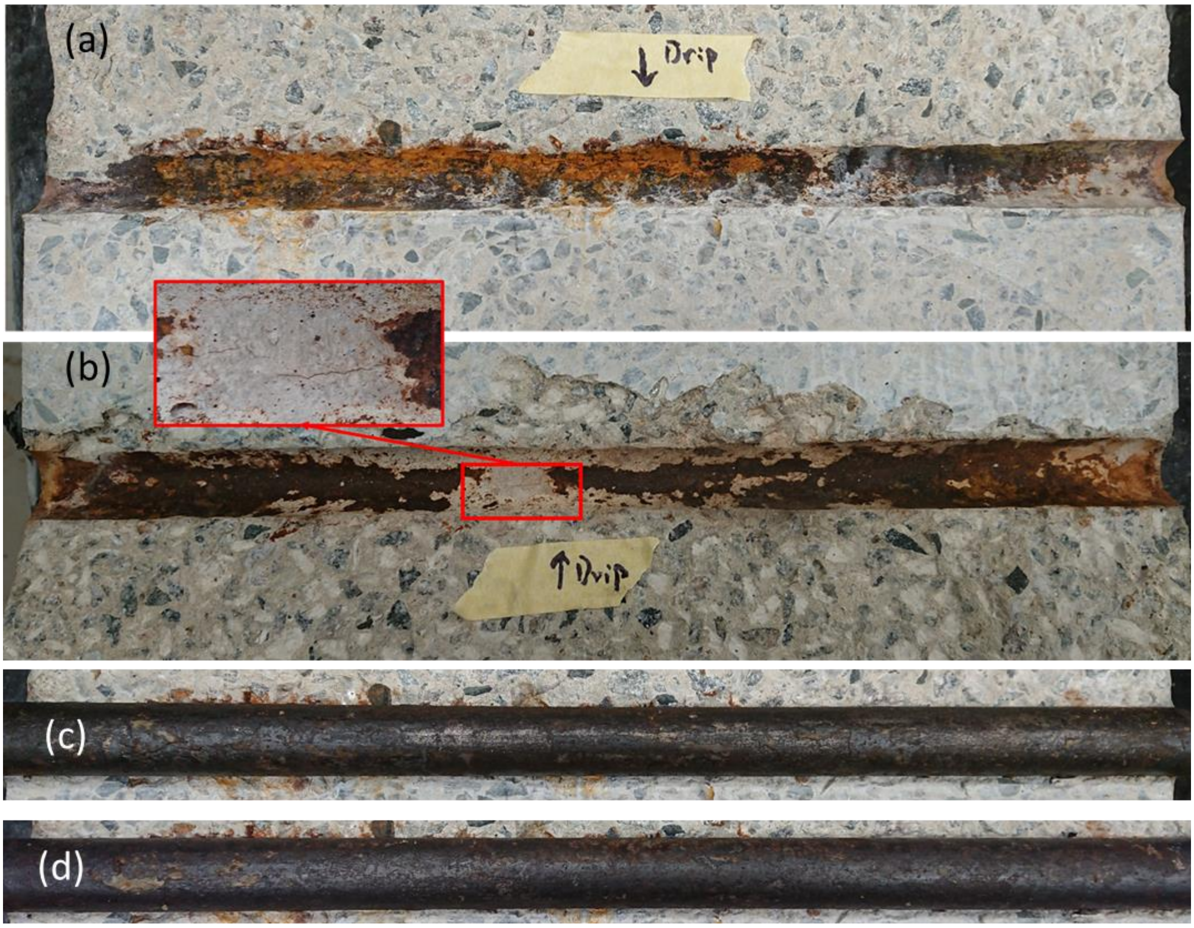

Fig. 7-22 Visual inspections of the condition of (a) and (b) steel-concrete interface and (c) the surface of the extracted bar facing the crack and (d) the surface that counter the crack.

Fig. 7-23 shows the visual inspection of the top bar specimen during the experiment. No sign of corrosion was observed in the first 1860 hours of accelerated corrosion. Liquid rust was first observed at 1880 hours. The rust oozed out from the steel-concrete interface at the left end of the bar. It was noted that the side of the bar where the rust oozed out was believed to have debonding owning to the top-bar effect, and it was perpendicular to the dripping direction. This might indicate that the corrosion initiated and proceeded within the debonding. In addition, the bond at the debonding side was weak, leading to the early rust leakage. At 2040 hours, the rust appeared at the right end of the specimen. Liquid rust has continued to ooze out from the ends of the specimen since then, unlike the crack growing pattern in the bottom bar. In the top bar specimen, the crack grew from the center of the specimen towards the ends. A hairline crack, 130 mm in length, appeared on the concrete cover at 2360 hours. It was noted that this surface of the concrete was facing the top part of the bar where the bond was intact. At 2380 hours, the surface of the concrete cover was completed cracked, while the crack grew from the surface towards the bar at both ends. The crack at the left end was longer than that at the right end. At 2400 hours, the crack at the length end reached the bar, indicating the completed crack of the concrete cover.

Visual sign	
(a) 1880 Hours/2429 kJ Rust appears underneath bar at left side of specimen	
(b) 2040 Hours/3012kJ Rust appears underneath bar at right side of specimen	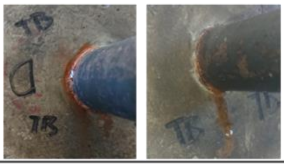
(c) 2360 Hours/4326 kJ Crack appears on concrete cover	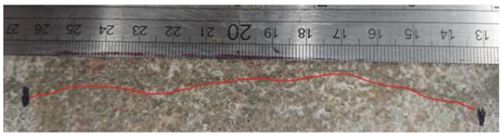
(d) 2380 Hours/ 4419 kJ Through length crack on surface of concrete cover	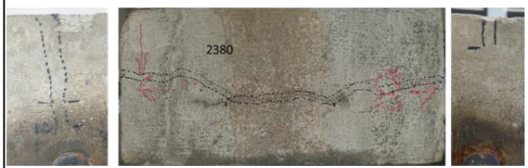
(e) 2400 Hours/ 4502 kJ Completed crack of concrete cover	

Fig. 7-23 Visual inspections of Topbar Specimen after (a) 1880, (b) 2040, (c) 2360, (d) 2380, and € 2400 hours of accelerated corrosion.

The condition of the steel-concrete interface in the top bar specimen was presented in Fig. 7-24 (a) and (b). The NaCl solution was dripping from the in-plane direction. The crack appeared on the surface, which countered the void owning to the top bar. Reddish rust stain was observed on the void side and the crack side of the interface, while part of the interface in the in-plane direction shown no rust stain. Hence, it was concluded that the corrosion was mainly in the void side and the crack side, and the bar was not fully debonded from the concrete at the end of the experiment. The extracted bar has shown a generalized corrosion pattern on the surfaces of the bar that coincident with the void and the crack. The corrosion was more severe on the void side than that on the crack side. However, the crack appeared on the side that countered the void side. This was because the void could accommodate the rust and thus release the rust-induced pressure, postponing the crack initiation. While on the counter side of the bar, once the corrosion was initiated, expensive pressure could quickly build up and lead to the crack initiation and propagation.

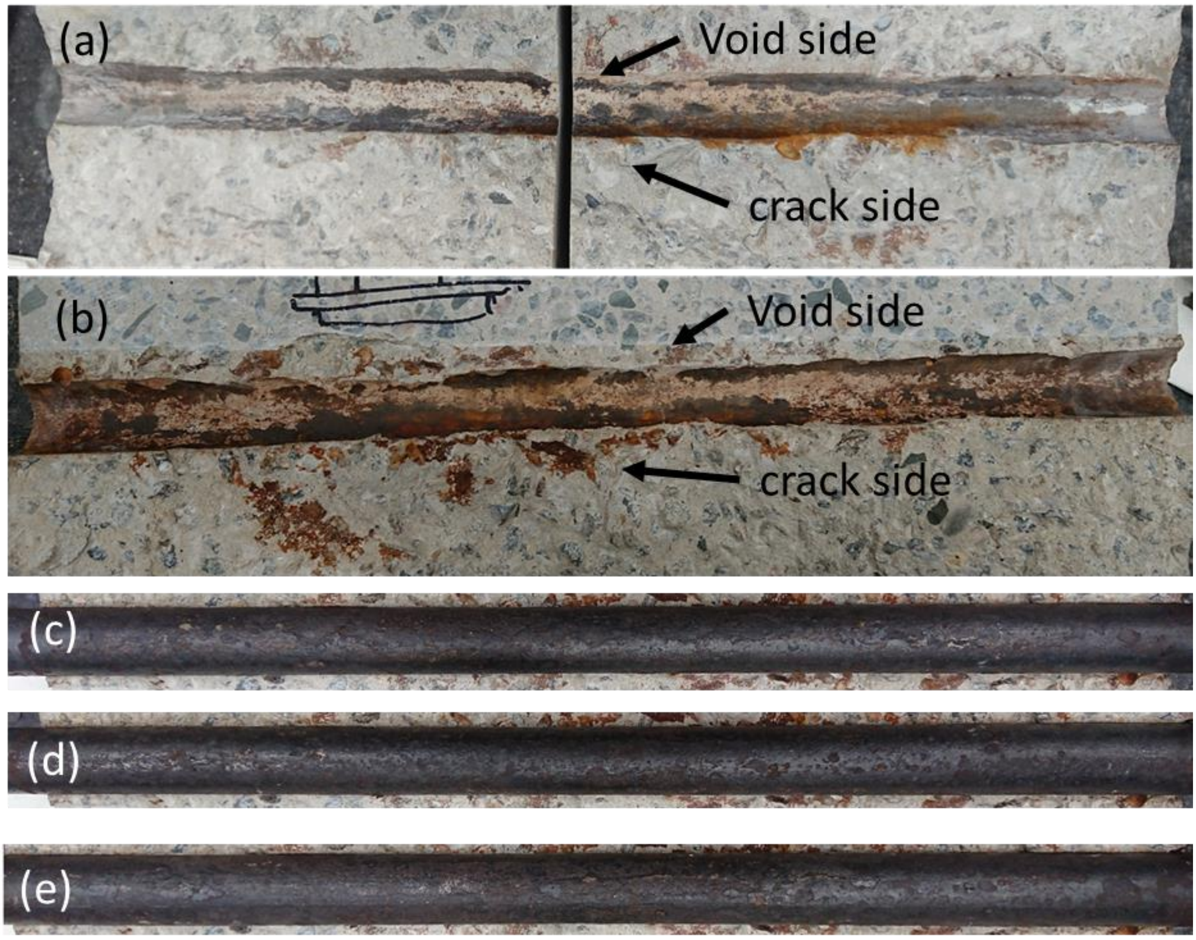

Fig. 7-24 Visual inspection of (a) and (b) the steel-concrete interfaces and (c) crack side, (d) dripping side, and (e) void side of the extracted bar in top bar specimen.

7.3.3.1.2.2. Ultrasonic results

Fig. 7-25 shows the trend of ultrasonic TI in the bottom bar specimen. The TI showed large variations in the amplitude. It is recalled that the energy of the signal, both at the excitation and the reception, is highly dependent on the contact pressure at the transducer-steel bar interface as well as the contact area between the transducer and the cross-section of the bar. The large variation in the TI between two records might be caused by the manual record error. Hence, the overall pattern of the TI within a certain window length, instead of analyzing individual data, is employed to analyze the corrosion. Five clear stages were visible. Stage 1 lasted about 200 kJ. The TI of the L (0,1) mode remained steady around 1.1. This increment in the TI might be caused by the underestimated benchmark TI. While the TI of the L (0,7) mode shown significant fluctuation between 0.6 and 1 during this stage. Although the TI showed big fluctuation, it was noted that the TI could always rose back to 1 periodically. Hence, the fluctuation in the TI of the L (0,7) mode was mainly caused by the uncertainty of the manual record. Therefore, it was concluded that the TI of both modes remained unchanged in the first 200 kJ.

A sudden rise in the TI of L (0,1) mode was observed around 200 kJ (stage 2). The TI increased to 1.2 and remained steady between 200 kJ and 1000 kJ. While the TI of the L (0,7) mode shown a slightly increasing trend. The TI varied with the increasing impressed energy, but the value of the TI was above 1 and peaked at 1.3 at the end of stage 2. The increment in TI during stage 2 indicates the corrosion initiation, followed by local debonding and increment in the interfacial debonding. As a result, the energy leakage from the bar to the surrounding concrete reduces, leading to an increasing TI. However, the corrosion rate during this stage is moderate, referring to the LPR measurement. The corrosion-induced debonding at the interface is not significant. Hence, the increment in the TI is not significant with the increasing corrosion.

Stage 3 occurred between 1000 kJ and 2150 kJ of impressed energy. The TI of the L (0,1) continued to increase with the impressed energy while the TI of the L (0,7) mode gradually reduced. The continuous increment in the TI of the L (0,1) mode indicates the gradual loss of bond between the steel bar and the concrete due to the corrosion on the surface of the bar. The bar is further separated from the concrete by the layer of rust, and less energy of the pulse signal leaks into the surrounding concrete. This leads to an increment in the TI. However, the TI of the L (0,7) shows a gradual reduction during this stage. This matches with the initial stage of the TI of the L (0,7) mode in the bar in air corrosion. Hence, it is concluded that the mill scale on the bar is gradually removed due to corrosion and causes the formation of rust at the steel-concrete interface. This leads to the debonding at the interface, resulting in the increment in the TI of the L (0,1) mode, while the removal of the mill coating leads to a slight reduction in the TI of the L (0,7) mode.

Between 2150 kJ and 2923 kJ (stage 4), the TI of the L (0,1) mode continued to drop, and the TI of the L (0,7) dropped sharply. This indicates the formation of the pits, leading to the deterioration of the bar. The L (0,7) mode is distorted and scattered by the irregularity of the waveguide, resulting in a reduction in the TI of the L (0,7) mode. Although the irregular surface of the bar leads to the scattering of the L (0,1) mode that reduces the energy of the transmitted signal, the TI of the L (0,1) continues to rise during this stage. It is because the steel-concrete interface continues to debond with the increasing corrosion. The energy leakage from the bar to the concrete is reduced. Hence, the TI of the L (0,1) mode is affected by both scattering (reduction in TI) and debonding (increment in TI), among which the debonding is dominating the TI during this stage.

Beyond 2923 kJ (stage 5), both the L (0,1) mode and the L (0,7) mode dropped sharply with increasing corrosion exposure. It is recalled that liquid rust is observed at around 3000 kJ of impressed energy at both ends of the specimen, indicating the full debond between the steel bar and the concrete. As the corrosion exposure proceeded, the generated rust products accumulated at the steel-concrete interface, increasing contact between the bar and the concrete. More energy can leak from the bar to the surrounding concrete, resulting in reduced energy of the transmitted signal. From now on, the signal scattering due to the irregularity of the bar and the energy leakage is dominating the energy of the pulse signal, resulting in a sharp reduction in the TI.

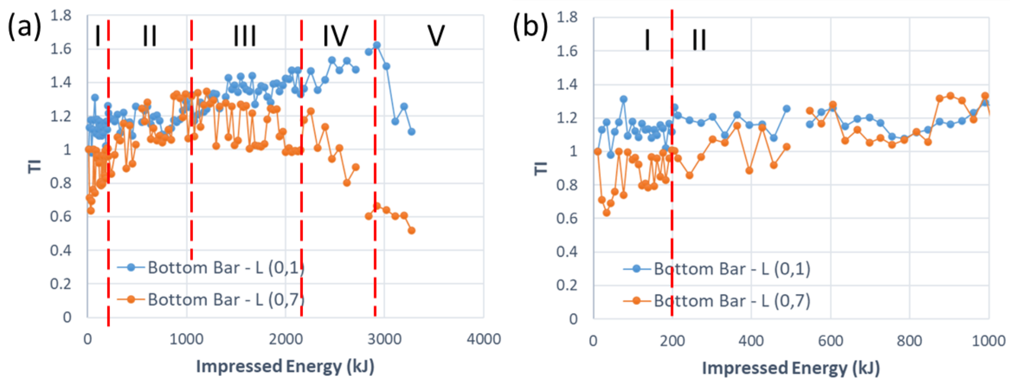

Fig. 7-25 (a) TI of the transmitted pulse signal of bottom bar specimen and (b) zoom-in the first 1000 kJ of impressed energy.

Fig. 7-26 shows the trend of ultrasonic TI in the top bar specimen. Five stages were also visible in the TI, but the trend of the TI in the first four stages was significantly different from those in the bottom bar specimen. Stage 1 lasted for about 14.4 kJ of impressed energy. The TI of the L (0,1) mode remained steady during this period, while the TI of the L (0,7) mode dropped by 0.25. It is believed that void owning to the top-bar effect is formed underneath the bar. The NaCl solution can be stored in the void owning to the top-bar effect and directly in contact with the unbonded part of the bar. Once the current is applied to the specimen, the corrosion of the bar should initiate instantly. Hence, it is believed that this reduction in the TI of the L (0,7) mode is caused by the removal of the mill scale from the unbonded part of the bar, which matches with the observation during the initial stage of the corrosion of the bar in air. The rust can go to the interfacial void and does not generate the interfacial pressure as in the bottom bar specimen. Thus, the contact between the bar and the surrounding concrete remained unchanged, leading to a steady TI of the L (0,1) mode.

In stage 2 (between 14.4 kJ and 81.3 kJ), the TI of both modes increased. A sudden rise in the TI of the L (0,1) mode was observed at 21.6 kJ. Then the TI remained steady at 1.2. While the TI of the L (0,7) mode increased gradually from 0.75 to 1.15 between 14.4 kJ and 81.3 kJ. This indicates the debonding at the steel-concrete interface. The bar was partially separated from the concrete by the generated layer of rust, which impedes the leakage of the energy of the pulse signal from the bar to the surrounding concrete. More energy was retained in the bar and transmitted through the bar, leading to the increment in the TI.

Stage 3 occurred between 81.3 kJ and 755.1 kJ. During this stage, the TI of both modes gradually dropped with the increasing corrosion exposure. The TI of the L (0,1) mode dropped by 0.3, and the TI of the L (0,1) mode dropped by 0.4. It is already concluded that the corrosion occurs within the void in the first two stages, as more impressed energy was applied, the bar was further corroded. The generated rust filled the interfacial void, and the excess rust started to generate interfacial pressure on the concrete. This increased the contact between the bar and the concrete. Hence more energy leaked into the surrounding concrete from the bar, resulting in the reduced TI of the L (0,1) mode.

While the TI of the L (0,7) mode was affected by both energy leakage and signal scattering due to bar deterioration, the reduction in the TI was more aggressive than that in the L (0,1) mode and the TI in the bar in air scenario.

Between 755.1 kJ and 3078.5 kJ (stage 4), the TI of the L (0,7) mode first increased between 755.1 kJ and 874.7 kJ and then gradually fell until the end of this stage. It was noted that the TI of the L (0,1) mode was steady, around 0.8 for 8 records before the sudden rise. It was believed that this rise was caused by the formation of cracking near the interface that separated the bar from the concrete. The TI of the L (0,1) mode gradually rose from 0.9 to 1 during this period, confirming the conclusion. Subsequently, the TI of the L (0,7) mode showed a reduction trend, indicating the continuous bar deterioration due to corrosion. Some sudden rises after continuous reduction in the TI were also observed. However, the fluctuation in the TI was about the same magnitude. Analyzing the guided wave alone could not be confirmed whether this phenomenon was caused by the formation of crack or just the measurement uncertainty. In contrast, The TI of the L (0,1) mode remained steady with a small fluctuation around 1 although the impressed energy increased. The corrosion-induced cracking (confirmed by SAFT imaging) at the steel concrete was observed. The trend of the TI was similar to the TI of the L (0,1) mode in the bar in air scenario, where the TI remained steady even severe bar deterioration was observed. Hence, it was believed that the corrosion of the bar mainly occurred at the void side during this stage. The corrosion at the bonded part of the bar was insignificantly that did not influence the energy transmission in the bar.

At stage 5, The TI of both modes sharply reduced with increasing impressed energy. The Trend of the TI of the L (0,1) mode began with a gradual increment. It was recalled that liquid rust oozed out from both ends of the specimen during this period, indicating the formation of a through-thickness debonding at the void side of the bar. With the increasing corrosion, the debonding gradually formed around the circumference of the bar until the bar was entirely separated from the concrete. The debonding impeded the energy leakage from the bar to the surrounding concrete, leading to a temporary increment in the TI. However, as the corrosion proceeded with increasing impressed energy, the contact between the bar and the concrete increased again due to the excess rust accumulated within the debonded steel-concrete interface. In the meantime, the corrosion of the bar led to irregularity on the surface of the bar, increasing the scattering of the transmitted signal in the bar. The combined effects of the signal scattering and the energy leakage resulted in the sharp reduction in the TI of the L (0,1) mode. A gradual increment between 3549 kJ and 3892 kJ was also noted after a continuous drop in the TI. This might be caused by the formation of the cracking at the bonded side of the bar that released the contact pressure between the bar and the concrete. Once the crack was filled with the rust, the contact pressure was generated again, leading to the increased energy leakage. Thus, the TI was reduced again. While the TI of the L (0,7) continuously dropped with the impressed energy, indicating the increasing bar deterioration and the development of contact pressure at the steel-concrete interface. The TI reduction rate of the L (0,7) in stage 5 was much higher than that in stage 4 where the void side of the bar was corroding. This was because, in stage 5, both the void side and the bonded side of the bar were corroding. The deterioration of the bonded side of the bar and the development of the contact pressure at the interface further reduced the energy of the transmitted signal in the bar, leading to a more aggressive attenuation of the TI.

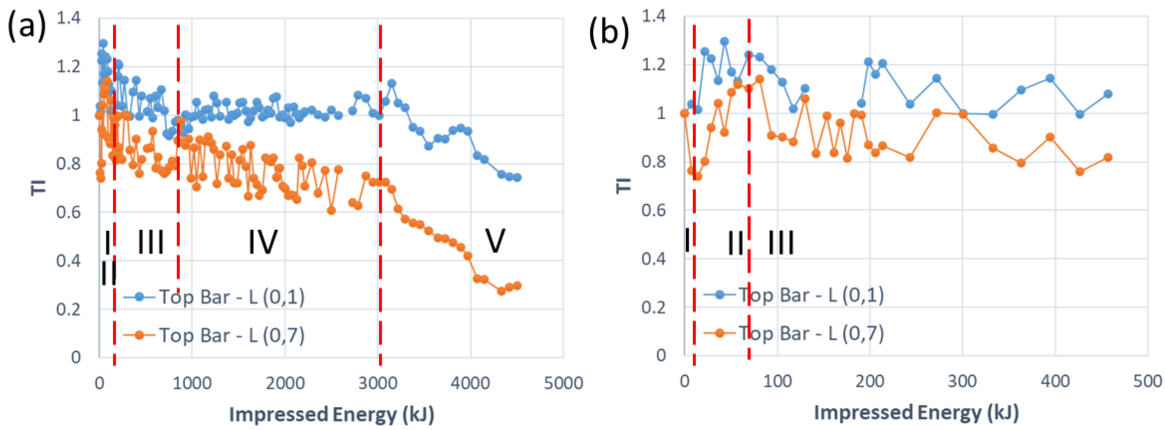

Fig. 7-26 (a) TI of the transmitted pulse signal of top bar specimen and (b) zoom-in the first 1000 kJ of impressed energy.

7.3.3.2. Ultrasonic imaging using synthetic aperture focusing technique (SAFT)

The schematic drawing of the scanning approach is shown in Fig. 7-27 (a). The scanning was taken on the surface (X-Y plane) of the specimen opposite to the dripping side. A pair of 200 kHz transducers were tied together and moving along marked lines (as shown in Fig. 7-27 (b)) in X-axis at a 10 mm interval. The scanning was taken along sections Y6, Y8, Y10, Y12, and Y14 where the wet cotton cloth wrapped the concrete, and the anodic current was applied. Each section consisted of 15 inspection points. The scanning was taken from the bottom of the specimen to the top (casting direction). Hence, in the top bar specimen, the scanning wave was first encountered with the void and then with the bar. The image reconstruction was carried out in X-Z direction to illustrate the location of the bar and the crack propagation owing to concrete corrosion.

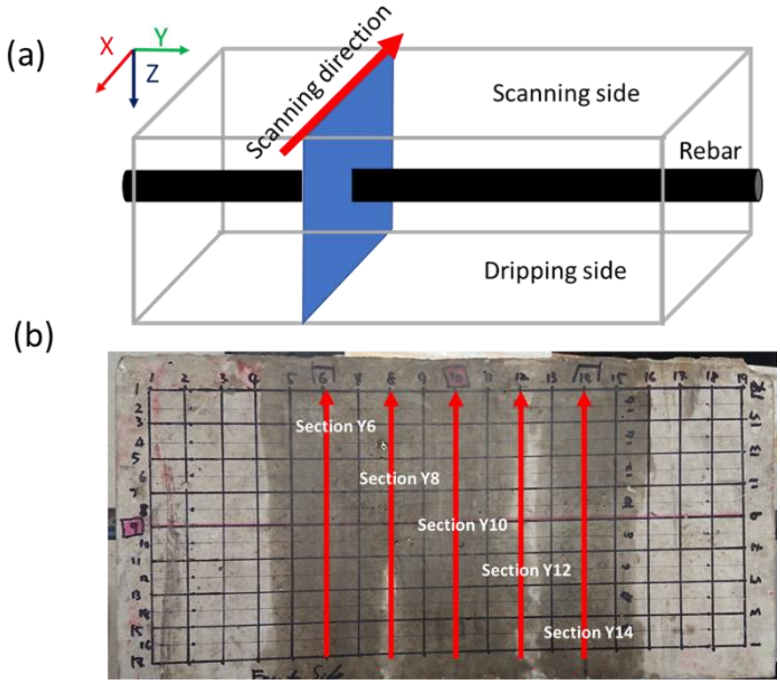

Fig. 7-27 (a) Schematic drawing of scanning approach and (b) marked lines on the specimen.

The SAFT images along the x-z plane at various sections in the bottom bar specimen are presented in Fig. 7-28. The images in the x-z plane revealed the cross-section of the specimen, depicting the rebar's location and the crack propagation from the rebar to the surface of the specimen. Five critical scenarios during the corrosion process were selected to analyze the crack initiation and propagation in the concrete. The detailed SAFT images were provided in the appendix. The SAFT images before impressing energy were used as the benchmark for comparison purposes. Observation of cracks 1 and 2 indicated the scenarios when the crack was first detected at both sides of the bar. The images before stage 5 where the TI sharp fall was also presented. The last column presented the image of the cross-section at the end of the specimen.

The rebar was clearly visible in all the cross-sections in the benchmark images, denoted by the red-blue-red pallet marked by the black circle. It was noted that the location of the pallet was not at the center of the cross-section, although the rebar was located at the center of the specimen. The pallet is located at the slightly upper left of the actual location of the bar. This was because the waves get reflected from the upper steel-concrete interface, and more data point was taken at the left side of the concrete due to the limited size of the specimen and the limitations of the tie together setup of the transducers. Thus, the pallets indicated the location of the upper left side of the rebar, not the center of the rebar. Strong colour pallets were also observed at the bottom of the images. These pallets were the reflection of the waves from the bottom boundaries of the specimen. A gap between the pallets was also observed, and the gap's location matched with the bar's location. This was because the waves were blocked and reflected by the rebar, thus resulting in the gap.

The crack 1, denoted by the red circles, detected between 363 kJ and 1206 kJ of impressed energy at various sections. The first crack 1 was observed at Section 12 after 363 kJ of impressed energy. The location of the crack was on the lower left side of the rebar. It should be acknowledged that the waves only reflected from a crack that grows to a certain length and width. In general, the waves can detect the crack of a length that is equal to or larger than half of the wavelength. Hence, it was believed that the crack had been initiated before it was detected by SAFT imaging. The last crack 1 was generated at section 6 after 1206 kJ of impressed energy. The crack was located at the lower right side of the rebar. The location of the crack appeared on either side of the rebar. A crack propagation pattern from the location of the rebar initiation towards both sides of the crack was not observed. This indicated that local corrosion could initiate at different sections at different amounts of impressed energy. Crack

2, located at the opposite side of crack 1, was detected between 668 kJ and 2542 kJ. The first crack 2, located at the lower right side of the rebar, was detected at section 8 after 668 kJ of impressed energy. While the last crack 2 was detected at section 6 after 2542 kJ. It is noted that crack 2 in some sections occurs earlier than crack 1 in other sections. This further confirms the occurrence of local corrosion in the bottom bar specimen and the crack initiation at different sections separately. At the beginning of stage 5, the pallets become larger and clearer, indicating the propagation of the cracks from the rebar towards the surface of the concrete. The pallets denote the rebar also become longer and connect with the pallets that denote the crack. This indicates fully debonding at the upper steel-concrete interface. At the end of the experiment, clear colour pallets were observed at the right side of the specimen in all sections. Although the crack was visually observed on the right surface of the concrete, the SAFT images only shown a crack within the specimen, about 40 mm from the right surface. This was caused by a lack of data points at the side of the specimen, especially at the two sides of the cross-section. The focus could not be formed, leading to the underestimated length of the crack. However, it was noted that the pallets that denoted the boundary reflections from the bottom surface were disappeared. This indicated a full-length crack of the specimen. All the waves were reflected by the crack and hence could not reach and be reflected by the bottom surface.

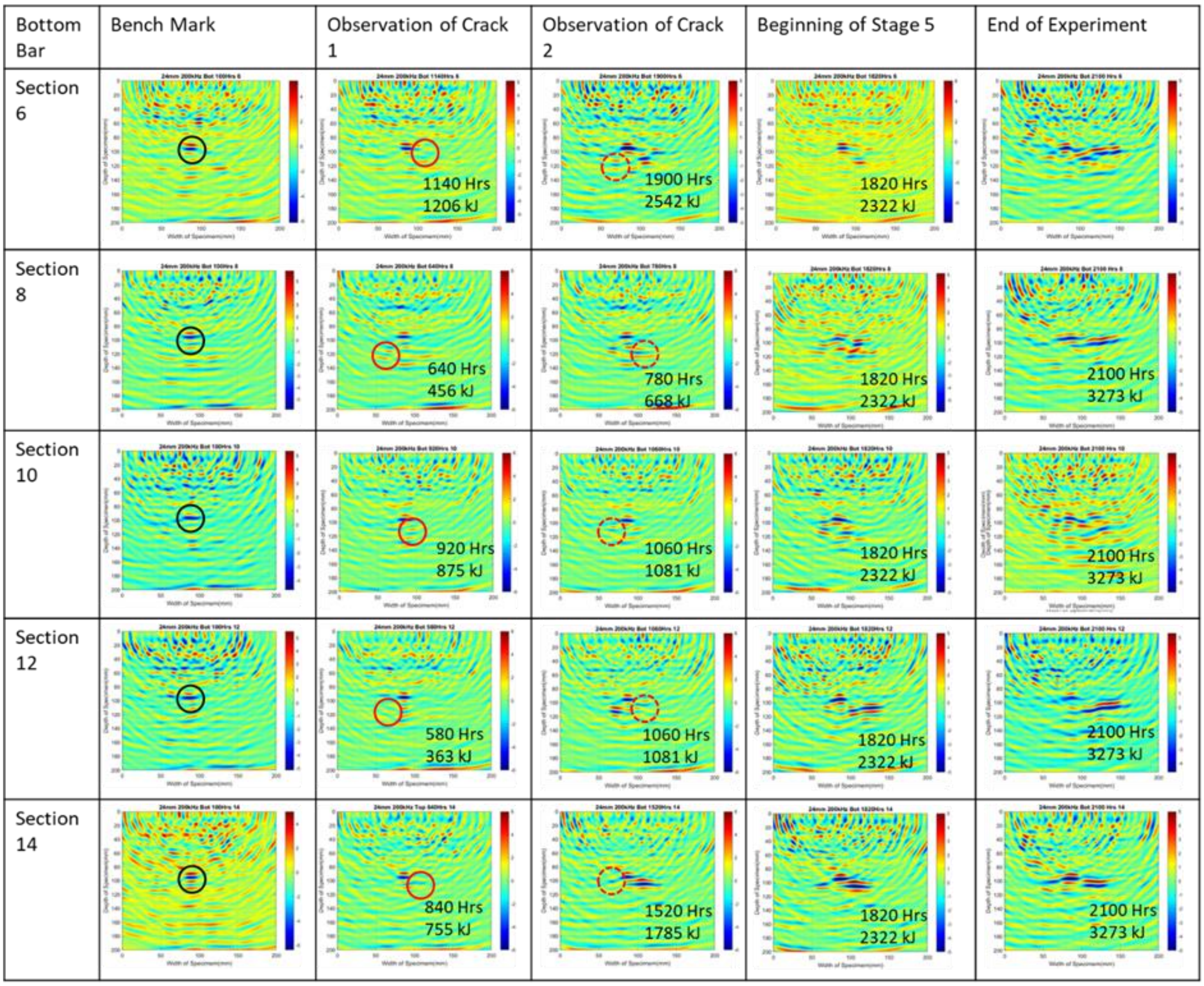

Fig. 7-28 SAFT images in the x-z plane at various sections in the bottom bar specimen.

The SAFT images along the x-z plan in the top bar specimen are presented in Fig. 7-29. The scanning direction was from the bottom of the specimen to the top (in casting direction). Hence, in the reconstructed image, the void was located on the left side of the rebar. In the benchmark images, the location of the rebar was clearly identified in all sections by the colour pallet marked by the black circle. However, in section 14, colour pallets of the same magnitude as the rebar were also observed in the vicinity of the rebar. This may be caused by the strong reflection from the large aggregate/aggregates, which could mask the corrosion-induced crack formed at the same location, leading to inaccurate detection of crack at this section.

The corrosion-induced crack was first detected in section 8 after 668 kJ of impressed energy. A light colour pallet was observed on the left side of the rebar at the same depth, indicating the initiation of the corrosion-induced crack. It was recalled that the void was also located on the left side of the rebar. Hence, the crack was believed to be generated by the expansive pressure induced by the excess rust in the void. Then the crack propagated to section 6 after 755 kJ. After 875 kJ of impressed energy, the crack propagated to section 10, and the second crack in section 6 appeared on the right side of the rebar. Subsequently, the crack on the right side of the rebar propagated from section 6 to section 12 between 875 kJ and 1320 kJ.

The SAFT image in section 14 was complex. Two clear colour pallets were visible on both sides of the bar. However, due to the presence of the pallets on the right side of the rebar in the benchmark image, it was difficult to conclude whether this pallet was a crack or not. At the beginning of stage 5, the length of the pallets increased slightly, but the pallets' color became darker. The darker colour indicates stronger waves being reflected from the location of the pallet. It was concluded that the crack mainly grew in width to further open the crack between 1484 kJ and 2060 kJ, resulting in the increasing reflection of the waves. At the end of the experiment, clear pallets were observed on both sides of the rebar in all sections. The length of the pallets was much longer than that at the beginning of stage 5, indicating the growth of the crack in length. Hence, it was concluded that the crack rapidly propagated from the rebar towards the surface of the concrete during stage 5. It was also noted that the cracks grew on both sides of the rebar, and the length of the cracks was similar, although the crack was only visually observed on the right surface of the concrete. While in the bottom bar specimen, the crack mainly grew on the right side of the rebar, and the growth of the crack on the left side of the rebar was marginal. The corrosion in the bottom bar specimen could induce complete cracking in the concrete cover, but the corrosion in the top bar specimen might lead to a complete split of the entire specimen. Hence, it was concluded that the top bar effect could cause more severe corrosion damage to the integrity of the structure, although the visual sign of the specimens was identical.

Fig. 7-29 SAFT images in the x-z plane at various sections in the top bar specimen.

To validate the accuracy of the reconstructed cross-section using SAFT imaging, a scanning near the cracked surface in the y-z plane was conducted to image the crack on the cracked surface. The reconstructed SAFT image was then compared to the actual crack that was visually observed. The actual crack on the surface of the bottom bar specimen and the reconstructed surface using SAFT imaging are presented in Fig. 7-30. The reconstructed crack matched well with the actual crack. A discontinuity in the crack at (230, 100) was successfully reconstructed by the SAFT imaging, indicating the precision of the SAFT imaging. However, only the top crack was reconstructed, while the bottom crack was not visible. This was because the top crack masked the bottom crack. The waves only reflected from the top one and did not interact with the bottom crack. This revealed the limitation of the SAFT imaging. It could only reconstruct the first encountered crack and was unable to detect any crack below. In addition, the crack at the two sides of the cross-section was also not reconstructed due to the lack of data points.

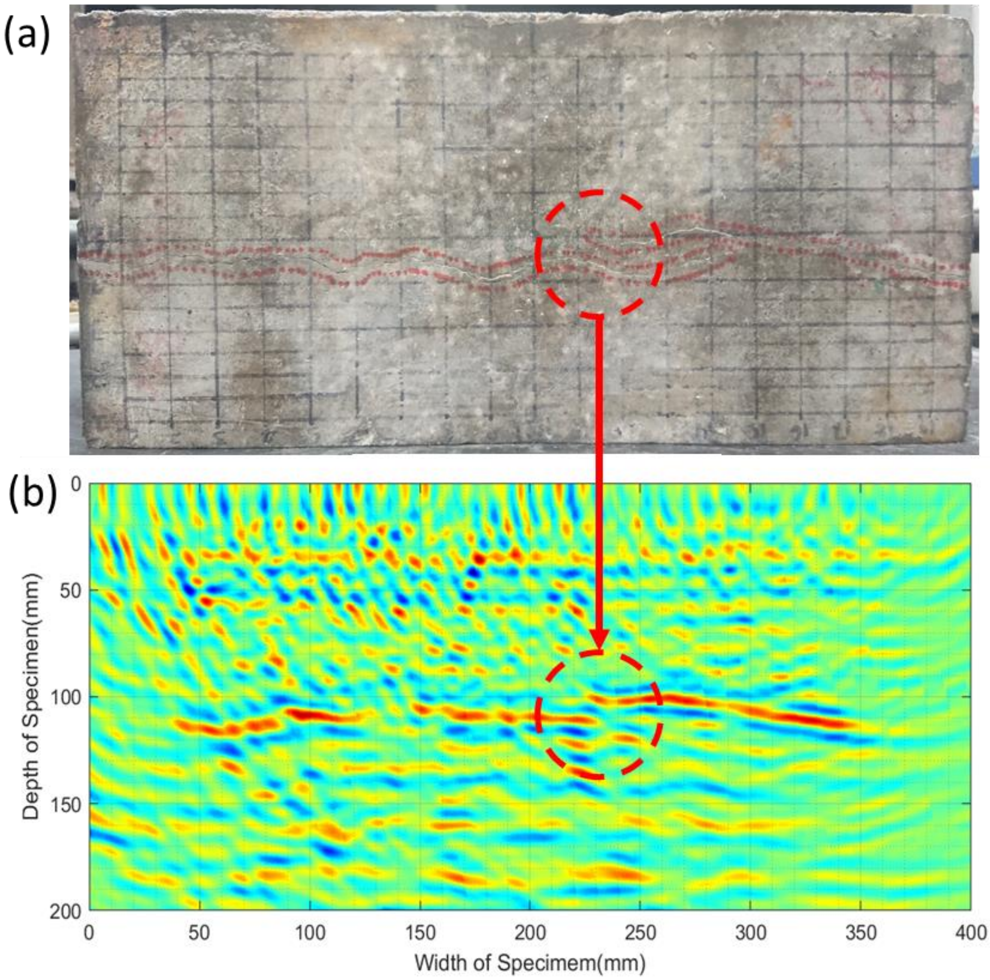

Fig. 7-30 SAFT image along the y-z plane in bottom bar specimen at the end of the experiment.

7.3.4. Concrete corrosion monitoring using combined techniques.

Four NDT techniques, HCP, LPR, ultrasonic guided waves, and SAFT imaging, have been employed in this experiment to monitor the accelerated corrosion of the reinforced concrete. From the results (Fig. 7-11), it is clear that the HCP indicates the probability of the corrosion in the concrete through the reduction in the half cell potential with the increasing exposure to corrosion. However, HCP can only provide two critical scenarios of corrosion in concrete, less than 10% and more than 90% probability of corrosion. The probability of the corrosion in between, which occupies the majority period of the corrosion process, cannot be identified. Furthermore, HCP cannot provide quantitative information about the progression of the corrosion, e.g., deterioration of the bar, location, and propagation of the corrosion-induced cracks. Similarly, LPR results (Fig. 7-12) can clearly indicate the corrosion rate at the time of recording through the change in the corrosion current density. It provides information about the rate of corrosion but not quantitative information about the progression of the corrosion.

Ultrasonic guided waves propagating through the reinforcing bar are capable of monitoring the bar deterioration and the change in the bond at the steel-concrete interface using the core-seeking L (0,7) mode and the surface-seeking L (0,1) mode. In addition, the trend of TI of the guided waves successfully differentiates between the corrosion in reinforced concrete with a good bond (bottom bar) and interfacial void owning to top-bar effect (top bar). However, the guided waves can only provide information about the deterioration of the reinforcing bar and the change of the bond at the steel-concrete interface. The locations and the propagation of the corrosion-induced crakes cannot be detected by guided waves in the reinforcing bar alone. In contrast, the SAFT imaging can visualize the location and the propagation of the corrosion-induced cracks and detect the location of the reinforcing bar in the concrete. Hence, by combining all the four NDT techniques, more comprehensive information about the corrosion process of the reinforced concrete can be obtained.

Fig. 7-31 shows the schematic diagram of the corrosion monitoring results using the combined NDT techniques in the bottom bar specimen.

In stage 1, LPR results indicate that the corrosion rate of the specimen is low. The guided wave results remain steady during this period. At the end of stage 1, a sudden jump in the guided wave results is observed. The TI of L (0,1) mode increases from 1.1 to 1.2. Meanwhile, HCP indicates a 10% probability of corrosion. This indicates the breakdown of the passive layer around the bar and the corrosion initiation in the specimen. The SAFE images of all the selected sections only show the colour pallet that represents the reinforcing bar. Hence, it is believed that no corrosion-induced crack is generated during this stage.

In stage 2, HCP is no longer capable of detecting the probability of corrosion, but the corrosion rate becomes moderate according to LPR measurement. The bar starts to corrode at an increasing rate. Local corrosion occurs and produces rust that separates the bar from the surrounding concrete. In this case, the TI of L (0,7) mode increases with the increasing corrosion. However, the TI of L (0,1) mode remains steady at 1.2. This may be because the local debonding is too small to affect the overall bond between the bar and the concrete. The corrosion-induced crack is first detected by SAFT imaging at impressed corrosion energy of 363 kJ. It has been discussed previously that the corrosion-induced crack may occur much easier due to the limitation of the detectability of SAFT. Between 200 kJ and 363 kJ, it is observed that the TI of L (0,7) mode first reduces then continuously increases. This may be because the generated rust first fills the voids around the bar, and the excess rust starts to generate expansive pressure on the surrounding concrete. This increases the contact between the bar and the concrete, leading to the temporary reduction in the TI due to energy leakage. Once the expansive pressure overcomes the bearing capacity of the concrete, it induces crack in the steel-concrete interface, leading to a temporary release of pressure and a discontinuity of the contact, resulting in an increment in the TI. Hence, it is more likely that the crack initiates in section 12 between 242 kJ and 271 kJ. The cracks are continuously generated with increasing exposure to corrosion.

The second crack is detected in section 8 after 456 kJ of impressed energy. The in-between section, section 10, remains intact until 875 kJ, which is the 4th crack that is being detected. At the end of stage 2, cracks are detected in sections 8-14. The location and the length of the crack vary significantly with sections. Hence, it is believed that the crack only occurs locally. Crack that along bar direction is not formed.

In stage 3, HCP results remain uncertain, and the corrosion rate is moderate. Due to the presence of the crack, the NaCl solution can accumulate in the crack and thus provides enough reactant to corrode the bar. Theoretically, the corrosion becomes more aggressive, and the rate of corrosion increases. However, LPR is not capable of providing precise information about the corrosion rate. The guided waves, on the other hand, show a clear monotonic trend with the increasing corrosion. The continuously increased TI of the surface-seeking L (0,1) mode indicates the debonding at the steel-concrete interface. While the TI of the core-seeking L (0,7) mode shows a gradual reduction trend, which matches the initial stage of the bar corrosion results. This indicates the gradual removal of the mill scale from the bar. The surface of the bar becomes irregular due to the formation of pits, and thus the waveguide is disturbed. Scattering of the waves occurs at the rough surface leading to the reduction in the TI of the L (0,7) mode. Theoretically, the scattering from the pits should also negatively influence the L (0,1) mode and cause a reduction in the TI. However, it is believed that the corrosion of the bar is not severe during this stage. The L (0,1) mode is less sensitive to detect such small irregularity on the surface than the L (0,7) mode. In addition, debonding at the steel-concrete interface occurs during this stage, which prevents waves from leaking to the surrounding concrete. More energy is retained in the bar leading to the increment in the TI.

The SAFT imaging results show that the cracks grow rapidly during stage 3. The cracks are detected at both sides of the bar. The colour pallets that denote the cracks become longer in length and darker in colour. This indicates the propagation of the crack towards the concrete cover. The rusts fill in the cracks that extend the crack as well as further open the crack. The crack becomes longer and wider, which allows more NaCl solutions to accumulate in the crack and thus accelerate the corrosion of the bar. The increased crack can reflect more waves to the top surface and thus increases the energy of the received signal, leading to longer and darker colour pallets.

Guided wave alone or SAFE imaging alone can only provide a monotonic result. The guided wave results indicate the debonding of the steel-concrete interface and the removal of the mill scale at the surface of the bar. However, guided wave results alone lead to an underestimated severity of the concrete integrity. The SAFT images reveal that the cracks grow aggressively during this stage. Hence, to obtain an accurate estimate of the corrosion of the concrete, it is essential to generate and analyze both guided wave results and SAFE images. By analyzing the results of the combined techniques, it is concluded that the corrosion mainly occurs at the surface of the bar and generates rusts that lead to severe corrosion-induced cracking. The mill scale is gradually removed and thus generates rusts at the steel-concrete interface, separating the bar from the surrounding concrete. The bar deterioration is not significant, but the generated rusts filled in and extended the cracks. The cracks separate the bar from the concrete and provide space for reactions to occur that lead to local corrosion and further produce rusts.

In stage 4, HCP indicates a 90% probability of corrosion while the corrosion rate remains moderate. The TI of the L (0,1) mode continues to increase, but the TI of the L (0,7) mode falls sharply. The pits continuously form on the surface of the bar leading to a more irregular surface. The waveguide is further disturbed, more waves scatter from the pits, leading to the continuous falling of the L (0,7) mode. The produced rusts, on the other hand, debond the steel-concrete interface. The bar keeps separating from the surrounding concrete, impeding the waves from leaking. More energy gets retained in the bar leading to the continuous increment in the TI of the L (0,1) mode. The cracks grow rapidly during this stage. The SAFT images illustrate the propagation of the cracks at different sections. The cracks grow in both length and width, denoted by the longer size of the pallets and the barker of the colour. In some sections, the pallet denotes the bar becomes longer and is connected to the pallet denotes crack. This indicates the delamination between the bar and the concrete due to the opening of the crack. Hence, it is concluded that the separation of the bar from the concrete is contributed by the debonding due to local corrosion and the delamination of the debonded steel-concrete interface due to crack opening. The delamination also allows rust and NaCl solution to accumulate in between the steel and the concrete. Corrosion occurs over the debonded surface of the bar, leading to generalized corrosion.

In stage 5, the LPR results indicate a high rate of corrosion in the concrete. The TI of the L (0,1) mode falls sharply. It is recalled that the liquid rust is observed at the side of the specimen underneath the bar at around 3000 kJ. Hence, it is believed that the steel-concrete interface is completely debonded at this point. Subsequently, the pits began to dominate the TI of the L (0,1) mode as the debonding of the interface no longer increased. The rough surface causes strong scattering of the guided waves, leading to strong attenuation of the TI. The SAFT images clearly illustrate the propagation of the cracks. However, it fails to detect cracks close to the surface of the concrete due to the lack of data points near the surface.

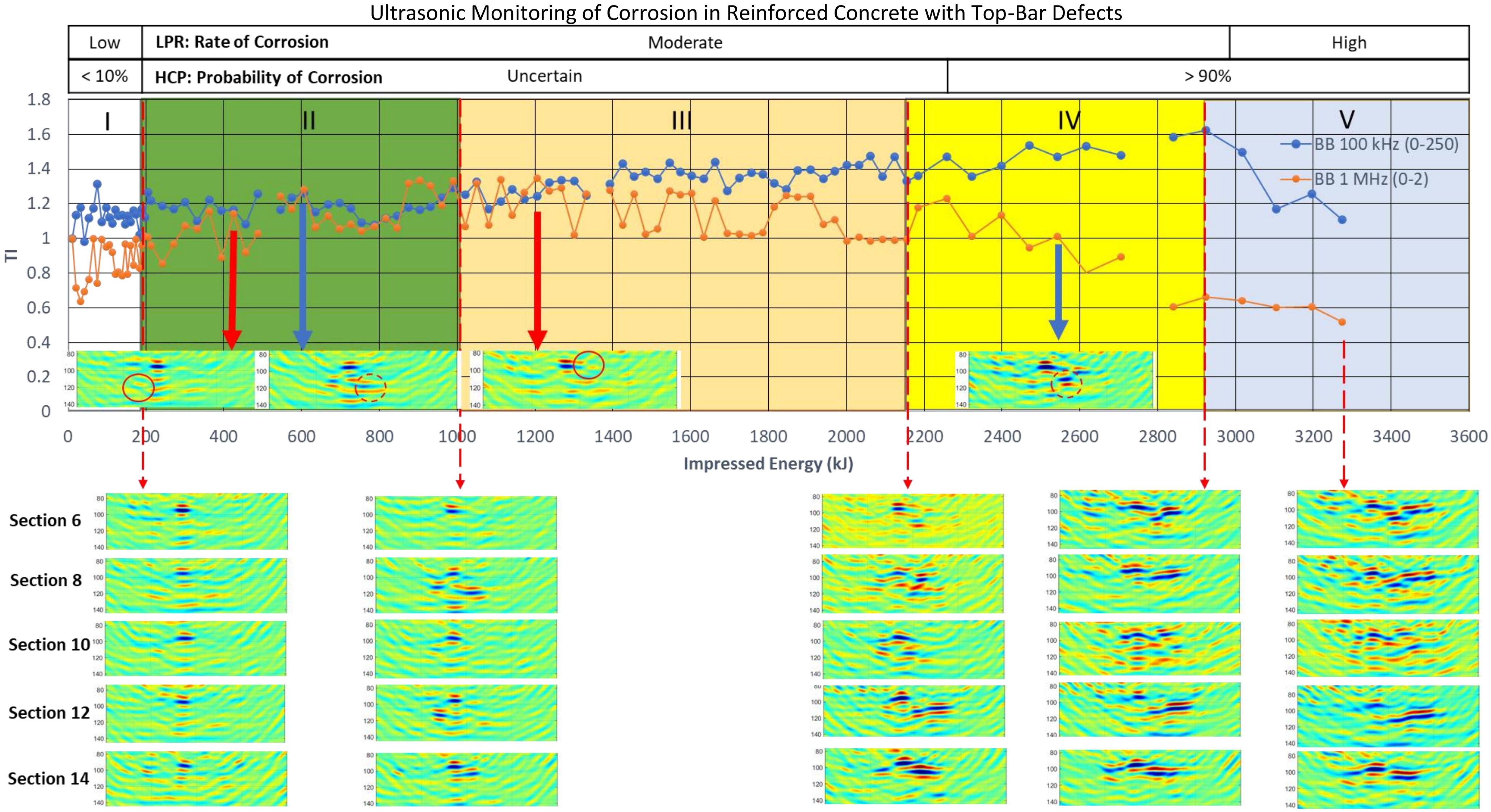

Fig. 7-31 Schematic diagrams of corrosion monitoring using combined NDT techniques: Bottom bar specimen.

Fig. 7-32 shows the schematic diagram of the corrosion monitoring results using the combined NDT techniques in the top bar specimen.

In stage 1, the HCP results indicate a possibility of 10 % in the first few days of exposure to corrosion, and the corrosion rate is low. This indicates much earlier corrosion in the top bar specimen than in the bottom bar specimen. In an accelerated corrosion scenario, the mill scale on the bar at the void side began to be removed once the impressed current was applied, leading to the corrosion initiation. This results in the reduction in the TI of the L (0,1) mode. The generated rusts can accumulate in the void and thus do not generate expansive pressure on the surrounding concrete. Hence, debond and cracks are not expected during this stage. The SAFT images illustrate the location of the bar. No cracks are detected at all sections.

In stage 2, HCP results are no longer capable of identifying the possibility of corrosion in the concrete. The corrosion rate remains low. Both the L (0,1) mode and the L (0,7) mode gradually increases. This may be caused by the local debonding at the top surface of the bar. This prevents the leakage of waves into the concrete, leading to a temporary increment in the TI. The SAFT results remain steady. Hence, it is believed that crack is not initiated yet.

In stage 3, the possibility of corrosion remains uncertain, but the corrosion rate increases from low to moderate, indicating more aggressive corrosion of the specimen. The TI of both modes gradually drops during this stage. This may be because the rusts filled in the void owning to the top-bar effect. This increases the contact between the bar and the concrete, which does not exist in the pristine state. The waves initially impeded by the void from leaking to the concrete can leak to the surrounding concrete through the rust in the void. Meanwhile, generalized corrosion alongside local pits formed on the surface of the void side of the bar. This leads to the scattering of the L (0,1) mode from the irregular surface. As a result, the TI of the L (0,7) mode decreases. The SAFT imaging illustrates the initiation of the crack after 668 kJ in section 8. The crack is located on the void side of the bar. This confirms that the void is filled with rusts, expansive pressure builds up, and the contact between the bar and the concrete increases within the void zone. At the end of stage 2, the SAFT images change slightly compared to those in stage 2. No other cracks can be clearly identified.

In stage 4, the TI of the L (0,7) gradually drops, indicating the continuous occurrence of the generalized corrosion on the surface of the bar. In contrast, the TI of the L (0,1) mode remains steady with slight fluctuation. By looking at the guided wave results alone, it seems like there is no change in the steel-concrete interface. However, the SAFT images reveal the initiation and propagation of cracks on both sides of the bar in all sections. This indicates the generation of the debonding and delamination at the steel-concrete interface. This should increase the TI of the L (0,1) mode due to the prevention of energy leakage into the surrounding concrete. However, it remains steady. One possible reason is that the TI of L (0,1) mode is dominated by both debonding and deterioration of bar during this stage. The debonding increases the TI while the deterioration leads to scattering from the surface irregularity, thus reduces the TI of the L (0,1) mode. The co-effect of the debonding and bar deterioration results in a steady TI. Therefore, it is concluded that analyzing the guided waves results alone may give a false estimation of the corrosion, especially in stage 4. The SAFT images that illustrate the cracks are essential for an accurate estimate of the corrosion process. Cracks are observed on both sides of the bar. The cracks on the counter void side grow more aggressively. This is because the steel-concrete interface at this side is fully bonded. The corrosion initiation is slower than the void side, but it can quickly build up the expansive pressure to induce the cracks once the rusts are generated. Much less amount of rust is required to fill in and extend the cracks.

In stage 5, the possibility of corrosion is above 90 %, and the corrosion rate is high. Aggressive corrosion of the concrete is expected. The TI of both L (0,1) mode and L (0.7) mode drops sharply. Liquid rusts are observed at both ends of the specimen after 3000 kJ of impressed energy, indicating the complete debonding at the steel-concrete interface. Hence, the scattering of the waves from the pits is dominating the TI of the waves. The surface irregularity of the bar increases with corrosion exposure. This leads to a stronger scattering that reduces the TI. The SAFE images reveal that the crack first extends in the counter void side of the specimen. The cracks at this side grow rapidly with the increasing corrosion exposure. Once the crack appears on the concrete cover, the growth of the crack on the counter void side slows down.

In contrast, the cracks at the void side start to grow rapidly. At the end of the experiment, the concrete cover on the counter void side is completely split, while the concrete cover on the void side looks intact. However, the SAFT images indicate severe cracks at the void side of the specimen. A conventional method such as visual observation and a single technique such as guided waves alone may underestimate the severity of the corrosion damage. The proposed combined technique can successfully monitor the bar deterioration, the debonding and the propagation of the cracks, which can provide a more accurate estimation of the corrosion, especially in specimens with top bar defects.

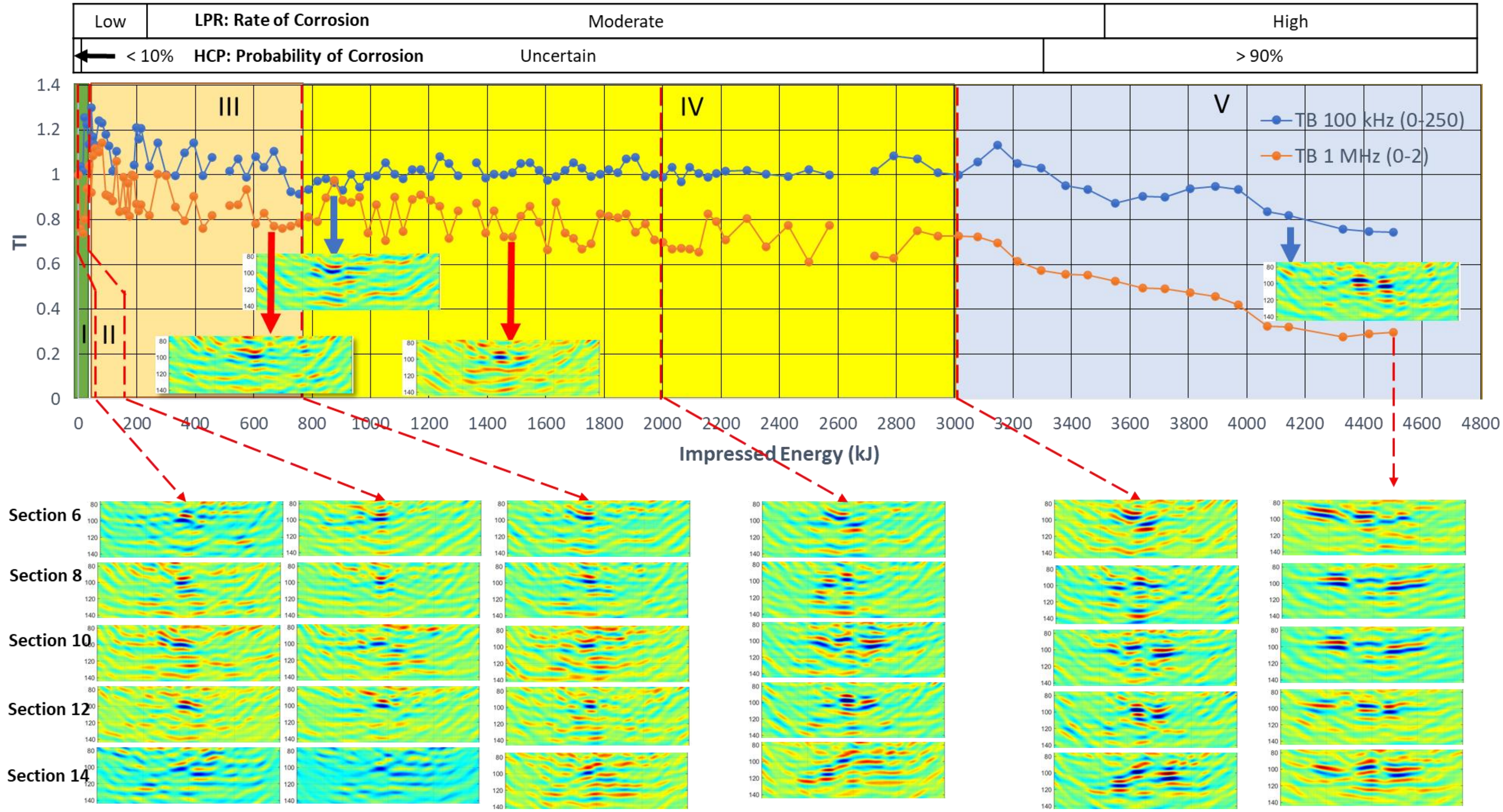

Fig. 7-32 Schematic diagrams of corrosion monitoring using combined NDT techniques: Top bar specimen.

7.4. Discussion and Conclusion

In this chapter, the proposed ultrasonic method was employed to monitor the lifecycle of reinforced concrete specimens, from the bar in air to the bar exposed to air due to corrosion. Contact transducers of carefully selected excitation frequencies were used to excite the desired wave modes. By generating the mode shape of the wave modes, the axial displacement and total energy density distribution along the cross-section of the bar can be reveals. Two wave modes, L (0,1) mode 100 kHz and L (0,7) mode at 1MHz were selected. The axial displacement and total energy density of L (0,1) mode at 100 kHz were concentrated near the surface of the bar. Hence it was sensitive to the change at the bar surface and the change in the bond at the steel-concrete interface. Thus, it was used as the surface-seeking mode to evaluate the change in the steel-concrete bond. The axial displacement and the total energy density of L (0,7) mode at 1 MHz were concentrated around the center of the bar. It was used to evaluate the change in the bar, thus termed the core-seeking mode, aiming to evaluate the change in the bar itself and due to the change in the bond.

Two steel round bars were cast in the concrete at an elevation of 100 mm and 500 mm, aiming to create specimens with and without interfacial void due to top-bar effects. The guided wave-based method was first employed to measure the setting of the reinforced concrete specimen. The pattern of TI of surface-seeking mode and core-seeking mode varied differently. In general, the surface-seeking mode shown high sensitivity to the change in the bond before the final set of the concrete, while the core-seeking mode was more sensitive to the hardening of concrete after the final set. By analyzing the two modes simultaneously, the four stages of hydration of concrete could be clearly identified, which also be validated by the temperature measurements. The TIs in the concrete with top-bar defects were higher than those in the controlled one. However, the difference was not as apparent as that using a PZT wafer-based system. A plateau in the TI was observed between the initial set and final set, which matched with the results of the PZT wafer-based system.

Before conducting a corrosion experiment on the reinforced concrete specimens, a bare bar was subjected to corrosion to evaluate the influence of bar deterioration on surface-seeking mode and core-seeking mode. The TI of core-seeking mode remained steady initially for a short duration and then continued to fall with increasing exposure to corrosion. The TI of surface mode remained steady until a mass loss of 3.8% of the total mass of the bar. A sudden drop in the amplitude of TI was observed, then it remained steady until the end of the experiment. The frequency profile of the L (0,1) mode, on the other hand, continuously changes with corrosion. The high frequency component continuously dropped while the low frequency component increased. A frequency shift was observed. The frequency shift in the L (0,1) showed better sensitivity to corrosion of the bar than the energy profile.

Four techniques were employed simultaneously to monitor the corrosion of reinforced concrete. HCP and LPR measurements indicated the probability of the occurrence of corrosion and the rate of the corrosion process. Although they could not quantify the corrosion process of the reinforced concrete, they served as good indicators to validate that the changes in the guided waves were due to corrosion. Guided waves have been used to monitor the corrosion-induced deterioration of the steel-concrete interface and steel reinforcement using surface-seeking and core-seeking modes, respectively. The pattern of TI of the two modes varied differently with increasing corrosion. The process of corrosion could be evaluated by mapping the guided wave results onto the state of the corrosion process and the three stages cracking model discussed in Chapter 2. The pattern of the guided wave results in reinforced concrete with no top-bar defects matched well with those reported in the literature review. In the presence of top-bar defects, the guided wave results showed a significantly different pattern, especially the surface-seeking mode, which remained steady during stage 3 although corrosion-induced cracking was developed. This might lead to underestimating the severity of corrosion if only guided waves were employed with an assumption of a good bond. This indicated the importance of obtaining prior knowledge of the bond condition. The guided wave-based monitoring algorithm was significantly affected by the bond condition of the concrete. SAFT-based ultrasonic imaging technique has also been employed to reconstruct the images of the cross-section of the specimen, aiming to visualize the location of the rebar and the cracks and to monitor the crack propagation. Although the crack initiation was not identified due to the large wavelength of the probing signal and the cracks near the surface of the concrete was not detected due to lack of scanning points, incipient cracks were clearly detected, and the propagation of the cracks could be monitored long before any corrosion signs appeared on the surface of the concrete. The results of all four techniques were then combined to provide more comprehensive information on the corrosion of the reinforced concrete, comprising rebar deterioration, bond deterioration, and crack generation and propagation.

Chapter 8

8. Conclusions and future works

8.1. Conclusions

Corrosion of reinforcement is a predominant cause that endangers the structural health of reinforced concrete structures. Moistures, especially moistures containing soluble corroding agents, seep into the concrete from the atmosphere, reach the steel reinforcement and initiate corrosion, leading to local pitting corrosion that may significantly reduce the mechanical properties of the rebars. Therefore, ongoing monitoring of the condition of reinforced concrete structures is required to ensure the safety, functionality and integrity of the structures to prevent structural failure that may cause economic and social losses. A brief literature review has been conducted to investigate the current progress in developing the assessment method of concrete corrosion. Several visual and electrochemical techniques have been developed and employed in the field for concrete corrosion *assessment*. However, these techniques cannot assess incipient corrosion and quantify the corrosion process of reinforced concrete. Visual methods can only detect surface defects, while the electrochemical methods can only indicate the corrosion of the reinforcements, but not the change in the bond or the progress of cracking, which are the more severe causes for the degradation of reinforced concrete. A more advanced ultrasonic wave-based technique has been introduced to evaluate concrete corrosion by researchers in recent decades. Several ultrasonic wave-based algorithms have been developed to evaluate the different types of defects in reinforced concrete. All the studies are conducted based on the assumption of a good bond at the steel-concrete interface. Several studies have employed electrochemical methods to evaluate the corrosion of reinforced concrete with interfacial defects owning to the top-bar effect. To the best of the author's knowledge, none has nondestructively detected the presence of top-bar defects and evaluate the corrosion process of reinforced concrete with top-bar defects using ultrasonic methods. Two research gaps have been identified after the literature review, and the completion of this study has filled these gaps:

1. A nondestrcutive method for detecting top-bar defects in reinforced concrete has been developed, and
2. Nondestructive methods for monitoring the corrosion process of reinforced concrete with top-bar defects have been developed.

The following key objectives have been achieved to fill the gaps:

1. To create reinforced concrete with natural top-bar defects.
2. To develop an algorithm for detection of Top-bar defects and monitoring of concrete corrosion.
3. To investigate the feasibility of exciting guided waves using the PZT wafers mounted to the ends of the rebars and use it to evaluate various types of steel reinforcement.
4. To detect top-bar defects in reinforced concrete using guided waves excited by surface-mounted PZT wafers.
5. To monitor the hydration process of cement paste and the setting of reinforced concrete using guided waves excited by surface mounted PZT wafers.
6. To monitor the corrosion process of reinforced concrete using guided waves excited by surface-mounted PZT wafers.
7. To compare the signals and the pattern of signals in reinforced concrete with and without top-bar defects subjected to accelerated corrosion.
8. To develop a combined technique, consisting of electrochemical techniques, ultrasonic guided wave-based technique, and ultrasonic imaging technique, to provide more comprehensive information about the condition of reinforced concrete under chloride attack.

Key conclusions from this study are summarized as follows:

Chapter 4 presents a guided wave-based method for monitoring cement hydration of cement paste and setting of reinforced concrete. PZT wafers are mounted to the ends of the steel reinforcements using superglue. In this way, transverse waves can be excited and propagate through the waveguides. The guided waves are first excited in a 12 mm diameter steel plain bar to evaluate the feasibility of using the proposed configuration to excite guided waves and its ability to monitor concrete setting. The exciting signal is selected based on 3 criteria, the amplitude of the signal, the complexity of the waveform and the mode shape of the modes in the signal. Theoretical solution of the modes and their mode shape can be obtained by generating the dispersion curves using DISPERSE. Two excitation frequencies are selected, which are 240 kHz and 600 kHz. The former one contains two wave modes, F (1,1) and F (1,2), whose axial displacement and total energy density are in the vicinity of the surface of the bar. Hence, the signal at 240 kHz is sensitive to changes in the steel-concrete interface. While the latter one contains one dominant L (0,3) mode, whose axial displacement and total energy density is concentrated around the core of the bar. Hence it is sensitive to the change of the bar. A transmission index (TI) is developed to evaluate the residual energy of the signal during concrete setting. The temperature of the concrete specimen is measured using a needle-type thermometer. The four stages of cement hydration can be identified using temperature measurement. The pattern of TI varies differently in these four stages, in stage 1 the TI of both frequencies drops sharply once the concrete is poured into the mould. In stage 2, the TI of 240 kHz drops sharply while the TI of 600 kHz varies slightly. In stage 3, a rise and fall fluctuation in the TI is observed in both frequencies. In stage 4, the TI of both frequencies remains steady.

The proposed method is extended to monitor the setting of concrete reinforced with 12 mm diameter ribbed bars. Thick double-sided tapes of different lengths are mounted to the bottom surface of the bar to simulate the top-bar defects. Due to the complexity of the geometry of a ribbed bar, dispersion curves cannot be generated. Hence, the selection criteria of the excitation are the complexity and the amplitude of the signal. Frequency sweep is performed to obtain signal at the frequency of 200kHz to 1 MHz. The pattern of the TI at all frequencies is similar, among which the signal at 300 kHz is the strongest. Hence it is used to monitor the concrete setting. A similar pattern of TI is observed regardless of the size of simulated top-bar defects, confirmed the repeatability of the proposed method for concrete setting monitoring. In terms of the size of top-bar defects, the TI of all bars almost match each other, but a significant difference is observed in stage 3, and the rise of TI increases with the size of top-bar defects.

A cast-in transducer is made in the lab to monitor the cement hydration and concrete setting. It consists of two short steel plain bars with PZT wafers mounted to all the ends. The bars are tied together with a fixed spacing using cable ties. In this configuration, both guided waves propagating from one end of the bar to the other end and bulk waves leaking from bar 1 to bar 2 can be obtained.

The transducer is first employed to monitor the hydration of a cement paste specimen. A standard penetration resistance test is performed to detect the setting of the cement, especially identifying the time of initial set and final set. The TI pattern is similar to those of the previous tests, again confirming the repeatability of the proposed method. It is found that the turning point of stage 3 where the TI changes from reduction to increment, occurs just before the final set, and the TI is peaked around the initial hardening of the cement paste. This can be used as a useful indicator to detect the final set and initial hardening of the cement and concrete. The cast-in transducer is then used to monitor the setting of a concrete specimen. A similar pattern of TI is observed.

Chapter 5: presents experimental work on detecting top-bar defects in reinforced concrete using the proposed method. Reinforced concrete wall specimens are cast vertically, aiming to create top-bar defects naturally. The specimen consists of four 12 mm diameter steel plain bars, locating at an elevation of 100 mm, 300 mm, 500 mm, and 700 mm. According to ACI building code 440, the bottom two bars should have a good bond while the top two bars should have the top-bar effect. However, the results obtained from the destructive test reveal that void due to top-bar effects is formed underneath the bar at an elevation of 300 mm and the size of the void increases with the height of the bar. This indicates that the ACI building code 400 underestimates the severity of top-bar effects in this case. Two damage indices (DI) are proposed to detect top-bar effects. A linear DI is proposed to evaluate the change in the total energy of the signal. A nonlinear DI is proposed to evaluate the ratio of the high frequency component (HFC) and the low frequency component (LFC) of the signal with respect to the ratio in the bar in bar scenario. A frequency sweep is performed over a range of 100-500 kHz at a step of 50 kHz. It is found that the signal at 400 kHz is the most suitable excitation as it can generate both strong fundamental and high frequency components and low signal complexity. The linear DI of signal in the bar at 100 mm is the lowest, and the amplitude of linear DI increases with the height of the bars. This is because the void underneath the bars deters the energy leakage from the bar to the surrounding concrete. More energy retains in the bar and being captured, leading to a higher linear DI.

The nonlinear DI can serve as a good indicator of top-bar defects. Initially, HFC exists in signals captured in all bars. The possible cause of the HFC is the instrument nonlinearity, which is generated by the instruments and theoretically changes linearly with the LFC. When bars are embedded in concrete, due to the increment in the properties of the surrounding material (changing from air to concrete), the attenuation of the signal increases. It is well known that the high frequency attenuates much faster than the low frequency. Theoretically, the ratio of HFC and LFC reduces with increasing material properties of the surrounding concrete. Thus the nonlinear DI should be less than 1 or equal to 0 if the HFC is completely attenuated. However, when the concrete is hardened, the nonlinear DI for the bar with a good bond is equal to 0, while the nonlinear DI for the top bars is above 1. The generated nonlinear component in top-bars is believed to be the contact acoustic nonlinearity generated at the top-bar defects due to the opening and closing of the defects. Hence, the nonlinear DI can be used to distinguish top bars from bottom bars with a good bond in reinforced concrete.

Chapter 6: extends the proposed method to monitor the corrosion process of reinforced concrete with and without top-bar defects. Four reinforced concrete specimens, consisting of two controlled specimens with good bond and two specimens with top-bar defects, are subjected to anodic current-induced accelerated corrosion. Each pair of them is corroded to the different milestones of corrosion. Milestone 1 is termed as surface stain. The specimens are corroded until rust stain appears on the surface of the concrete cover. Milestone 2 is termed as concrete cracking. The specimens are corroded until the concrete cover is completely cracked. These two milestones are the common signs of corrosion that visual inspection methods are used to detect. The proposed TI is used to evaluate the residual energy of the signal due to corrosion, hence monitoring the corrosion process. The excitation frequency is 350 kHz as it induces the strongest signal with low complexity. Signal excited at 350 kHz contains two wave modes, F (1,1) and F (1,2), whose axial displacement and total energy density are in the vicinity of the surface. Hence it is sensitive to the change in the steel-concrete interface and shallow surface irregularity of the bar.

For milestone 1, The TI of the controlled specimen shows a 3-stage pattern. In stage 1, the TI continuously falls due to the rust build-up within the steel-concrete interface. The pores around the bar are filled with rust, increasing the contact between the steel and the surrounding concrete. More signals can leak into the surrounding concrete leading to the reduction in the TI. In stage 2, as more rust gets generated, rusts begin to separate the bar from the concrete, which deters the signals from leaking into the surrounding concrete. Therefore, the TI increases until the initiation of cracking. In stage 3, the TI drops again when the cracking propagates from the embedded bar to the surface of the concrete cover. The TI of the top bar specimen first drops slightly about 7% then remains steady for a short duration before it starts to fail continuously until the end of the experiments. Slightly increment in the TI can be observed in between, which denotes the initiation of debonding and cracking. However, no distinguish stages can be observed. Overall, the TI of the top bar specimen is very similar to stage 1 of the TI of the controlled specimen. If the presence of the top-bar defects was unknown at the beginning of the monitoring, it may lead to a false interpretation of the results and thus result in wrong estimation of the severity of the corrosion process.

For milestone 2, the first 3 stages of the TI of the controlled specimen are similar to those in milestone 1, confirming the repeatability of the proposed method for monitoring incipient corrosion in reinforced concrete. In stage 4, the TI first decreases then increases. This is because the guided waves are influenced by bar deterioration which reduces the TI, and debonding due to crack opening, which increases the TI. Initially, the crack is small. It is the bar deterioration that dominates the signal. Hence the TI decreases. When the crack becomes severe, the influence of debonding overcomes the influence of bar deterioration. Therefore, the TI increases. By contrast, the TI of the top-bar specimen continues to drop in stage 4.

All the bars are extracted upon the completion of the experiment. The bottom bars show typical pitting corrosion, while the top bars show a more severe generalized corrosion over the bottom part of the bar where top-bar defects are formed. The maximum mass loss for bottom bars is 0.56%, while the minimum mass loss for top bars is 4.2%. The yield stress and ultimate strength of these bars do not change much, maximum 8.89% and 5.82%, respectively. The ductility of the bars, on the other hand, reduces significantly. The strain reduction for specimen BS and BC is 5.95% and 29.05%. The strain reduction for specimen TS and TC is 45.24% and 52.62%, which is much higher than that of bottom bars.

Chapter 7: four methods, linear polarization resistance, half-cell potential, ultrasonic guided waves and ultrasonic imaging, are used to monitor the corrosion process of reinforced concrete, and the results are combined to provide more comprehensive information on the corrosion process. Half-cell potential measurement indicates that the corrosion of the top-bar specimen initiates immediately once the anodic current is impressed in the specimen. While the corrosion of the bottom bar specimen initiates after 150 kJ of impressed energy. The relative rate of corrosion activity can be obtained using the linear polarization resistance measurement.

Two excitations are selected to excite the guided waves. One is the longitudinal L (0,1) mode at 100 kHz, termed as the surface-seeking mode, whose axial displacement and total energy density is near the surface of the bar. Hence, it is sensitive to the change in the steel-concrete interface. Therefore, it is used to monitor the change in the bond between steel and concrete. The L (0,7) mode at 1 MHz, termed as the core-seeking mode, whose axial displacement and total energy density is concentrated around the core of the bar. It is sensitive to the change in the bar, thus being used to monitor the deterioration of the bar. The TI of both the bottom bar and top bar specimen showed a 5-stage pattern. However, the pattern of TI in the top bar is far different from that in the bottom bar specimen. The condition of the corrosion process, especially the deterioration of the bar and the change in the bond, can be evaluated.

SAFT-based ultrasonic imaging techniques visualized the generation of incipient cracks and the propagation of these cracks. It can be used to measure the size of the cracks and estimate the size of debonding due to concrete cracking. By combining the results, the probability of the corrosion and the corrosion rate for each stage of the corrosion process can be evaluated. The guided waves results can be used to evaluate the deterioration of the bar and the change in the bond, while the images can be used to detect the cracks and monitor their propagation, which helps better interpreting the guided wave results. It is found that the ultrasonic imaging results are compulsory to evaluate the corrosion process of the top-bar specimen, especially in stage 4. The TI of the surface-seeking mode remains steady for a very long duration, and the change in the TI of the core-seeking mode is mild. Based on the guided wave results, it may look like the specimen is intact or the corrosion activity is low. However, the imaging results reveal the generation of severe cracking inside the concrete, although no visual signs can be observed from the surface.

8.2. Limitations of this study

Several limitations of this study have been identified:

1. The results of this study have demonstrated the efficacy of the proposed method for monitoring concrete settings, detecting top-bar defects and monitoring the concrete corrosion with and without top-bar defects. This study is a pilot-scale study in small-scale controlled specimens. To generalize the findings of this study for a potential industry application, the experiments should be evaluated in large-scale specimens and extended to statistically significant specimens.
2. This study is a proof-of-concept study. Only round bars are used as the waveguided to evaluate the efficacy of the proposed method for concrete corrosion monitoring. The experiments should be extended to deformed bars that are commonly used in reinforced concrete.
3. The size of the top-bar defects cannot be accurately measured even after destructive tests. Therefore, the proposed damage index cannot be directly correlated to the size of the top-bar defects.
4. Although the proposed method can successfully monitor the corrosion process of reinforced concrete, the corrosion process cannot be quantified due to the presence of multiple types of defects in corroded reinforced concrete. The TI decreases with the increasing bar deterioration, but the TI increases with the increasing debonding of the steel-concrete interface and cracking of the concrete. The combined effects of these defects make the quantification of the corrosion process a challenging task.

8.3. Recommendations for future work

The work presented in this study notes several possible directions for future works to improve and extend the proposed method. The recommendations are listed below:

1. identify the effects of concrete setting on guided waves, especially the reasons behind the turning point in stage 3 of the setting.
2. Quantify the size of the top-bar defects. The characteristics of guided waves in specimens with simulated top-bar defects, e.g., by attaching double-sided tapes, would be worth investigating to find the relationship between the size of top-bar defects and the proposed linear DI. Simulating the nonlinear zone between the steel and concrete would help find the correlation between the size of the nonlinear zone and the nonlinear DI.
3. Quantify the measured results to the corrosion process of the reinforced concrete to find the relationship between the measured results and the material properties of the bar, such as the mass loss, reduction in the stress and strain due to corrosion.
4. The proposed method should be extended to evaluating the corrosion process of concrete reinforced by the deformed bar.
5. Improve the resolution of the reconstructed images. Scanning should be performed both across the bar and along the bar direction to better investigate the crack propagation. Wedged transducers can be used to focus on a particular depth of the concrete to provide more detailed images.
6. Developing methods to minimize or eliminate the top-bar effect in reinforced concrete.
7. Experiment validations of employing proposed methods to evaluate corrosion in various structure elements and extended to real structures.
8. Develop guidelines to applying the proposed method in various structure elements and real structures.
9. Obtain benchmark of comparison of different methods.